Photo-induced Electron Transfer in Molecular Systems and Nanoparticle Assemblies

by

Brittney M. Graff

B.S., Franklin and Marshall College, 2011

Submitted to the Graduate Faculty of the

Kenneth P. Dietrich School of Arts and Sciences in partial fulfillment

of the requirements for the degree of

Doctor of Philosophy

University of Pittsburgh

2016

UNIVERSITY OF PITTSBURGH

Kenneth P. Dietrich School of Arts and Sciences

This dissertation was presented

by

Brittney M. Graff

It was defended on

November 30, 2016

and approved by

Dr. Geoffrey Hutchison, Assistant Professor, Department of Chemistry

Dr. Sean Garrett-Roe, Assistant Professor, Department of Chemistry

Dr. Bruce A. Armitige, Professor, Department of Chemistry, Carnegie Mellon University

Dissertation Advisor: Dr. David H. Waldeck, Professor, Department of Chemistry

PHOTO-INDUCED ELECTRON TRANSFER IN MOLECULAR SYSTEMS AND NANOPARTICLE ASSEMBLIES

Brittney M. Graff, PhD

University of Pittsburgh, 2016

Charge transfer is a fundamental and extremely important chemical reaction. Fully understanding charge transfer can provide insight into a multitude of emergent technologies (photovoltaics, molecular electronics, etc.). Donor-bridge-acceptor systems are among the most popular methods to study and model photo-induced charge transfer, and this approach is extended to donor and acceptor units that are nanoparticles in work described herein. Various models have been developed to describe charge transfer in molecular donor-bridge-acceptor systems and in nanoparticle assemblies; they can aid in understanding how charge is transferred.

This dissertation describes studies of both molecular donor-bridge-acceptors and nanoparticle assemblies. The first part of this dissertation examines donor-bridge-acceptor systems designed with a molecular cleft that can incorporate a solvent molecule which can facilitate charge transfer. In these studies, the molecular acceptor is modified and this dissertation describes how that modification can alter charge transfer kinetics. The second half of this dissertation describes studies of nanoparticle assemblies. First, the fabrication method and characterization of these well controlled covalently bound nanoparticle assemblies are described and the assemblies' behavior is compared to molecular systems. Finally, this dissertation discusses studies in which a chiral bridge is placed between the donor and acceptor nanoparticles.

TABLE OF CONTENTS

LIST OF TABLES

LIST OF FIGURES

LIST OF EQUATIONS

DEDICATION

This dissertation is dedicated to my beloved Grandmother, Frances Graff.

PREFACE

Over the past few years the help, support, and encouragement I have received was indescribable. I feel truly grateful to have so many wonderful people in my life. First, I would like to thank my advisor, Dr. David Waldeck. He has been extremely supportive, patient, kind, and helpful throughout my time in graduate school. He is a wonderful scientist and a brilliant educator. He was always ready to provide help, advice, or guidance. I am so lucky to have worked with such a kind and intelligent man. In my second year, when I was truly struggling, he sat with me and told me just to keep my head down and keep studying. He promised me that one day I would look up from my books and know more than everyone else. I am so lucky to have a mentor that believed in my abilities and in me, even when I did not. Thank you for that Dave, you will never know how much your encouragement has meant to me.

I am also so thankful to my labmates, including Dr. Prasun Mukherjee, Dr. Emil Wierzbinski, Dr. Yang Wang, Dr. Matthew Kofke, Dr. Xing Yin, Dr. Daniel Lamont, Dr. Brian Bloom, Robin Sloan, Dr. Madu Mendis, Miles Batson, Edward Beall, Arthur Davis, and Simon Wei. They are more than simply co-workers; they are my friends. Dan, thank you for taking the time to teach me everything about optics and answering my phone calls even when I know the timing was not always ideal. Your carefree demeanor forced me to learn how to relax even about the most serious of situations. Dan, you are an excellent co-worker and an even better friend. Brian, thank

you for always challenging my thinking and pushing me to work harder, strive for more, and teaching me how to stand up for my scientific beliefs. It was truly a pleasure to work on so many projects with you. I feel extremely lucky to call myself your colleague and your friend. Xing, thank you for always seeming excited about any question I had, putting up with me even when I was grouchy, and walking me home when I left work late. I feel blessed to have been your co-worker and to be your friend.

I am also thankful to my committee members, Dr. Geoffrey Hutchison, Dr. Sean Garrett-Roe, and Dr. Bruce Armitage. Their support and advice throughout the years has been invaluable. Dr. Garrett-Roe was also the mentor of my research proposal and I was lucky to be able to learn both about proposal writing and ionic liquids from him. Discussions with them throughout the years were so helpful.

I was also lucky to work with several excellent chemists from other institutes. I would like to thank Dr. David Beratan (Duke) and his group, Dr. Catalina Achim (CMU) and her group, especially Selma Ulku, and Dr. Christian Schafmeister (Temple) and his group, especially Dr. Matthew Parker (UC-Irvine).

I also want to express my appreciation to all the staff in the Chemistry Department. I would like to especially thank the individuals who work in the main office. Their understanding and kindness helped me get to this point. I would like to thank the individuals who work in the stockroom. This certainly would not be possible without them. I would like to especially thank the glass blower, Lori, who made custom glassware for me.

To my friends, thank you for putting up with me these last few years. I particularly want to take a moment to thank some of my closest friends: Valerie Perrine, Katie Gares, Ryan Walker, and Dr.

Eric Kratz, you have been amazing friends over this journey. I am so thankful for all the moments we had together: the late nights watching horrible TV shows, the nights out at the bar, and the times spent chatting about science. These moments have helped make this experience worthwhile. Ryan, you were my first friend here and your friendship has meant so much to me. I feel so lucky to have you in my life. Thanks for seeing the quiet girl in the corner and sharing your pretzels with her. Bet you never guessed you would be stuck with me forever!

Last but certainly not the least, I am eternally indebted to my family. My parents, Drs. Bart and Bonnie Graff, have done everything to support me. Over the years they have provided me with everything I have ever needed: an ear to listen, a shoulder to cry on, a pat on the back, and even a swift kick in the butt when needed. My siblings have helped me so much over these last few years. Thank you Bradley, Brooke, Cassie, and Brett Graff. Thanks for always picking up when I called and letting me vent. And thanks for letting me talk with you about things that were not science related. Sometimes, even I needed a break. Knowing you were all there supporting me helped make the tough times better. Thank you so much to my Grandma. You are one of the strongest women I know. You pushed to get a higher degree at a time when women frequently did not go to college. Even though you were not able to see me finish graduate school, I am certain you would be glowing. Sometimes on the tough days during my graduate school career I would listen to the message you left me so many years ago telling me how proud of me you were. Knowing that my hard work has made you proud was exactly what I needed to push through the tough times. I am especially grateful to my loving and supportive husband, Marshall McGoff, who has been my anchor since we met. During the toughest time of my life, he chose to date me, get engaged to me, and marry me. Since the moment I met him he has always been there for me and I just cannot thank him enough for the love and support through all these years!

These words would simply not be enough to truly give him the thanks he deserves. Finally, Lennox, I would like to thank you. These last few years would not have been possible without your evening snuggles, your good morning kisses, and your waggity tail. Marshall and Lennox your sacrifices especially in the loss of our time together, were for me the most humbling of all.

1.0 INTRODUCTION

1.1 OVERVIEW

Charge transfer (CT) is an extremely important chemical reaction that occurs in many fundamental processes in nature;[1] for example, photosynthesis employs CT.[2] Over the last few decades CT has generated a significant amount of interest because of the potential that it has in technologies such as artificial photosynthesis, photovoltaics, and molecular electronics.[3,4,5,6,7] General donor-bridge-acceptor (DBA) molecular systems have been designed to carefully study and manipulate charge transfer. Questions on whether traditional Marcus theory can be extended beyond molecular systems to explain nanoscale assemblies have been raised.[8,9] Semiconductor nanoparticles (NPs) have the potential to be utilized in a variety of applications including photovoltaic cells. Because NPs have size tunable optical and electronic properties, they have been studied in great depth over the past few decades. With syntheses that have become simplified, controlled, and relatively inexpensive, they show great promise for this field.[10]

In this dissertation, general donor-bridge-acceptor systems as well as complex nanoscale assemblies are probed to understand how the transfer of charge differs in these systems. In this introductory chapter, charge transfer theory, basic donor-bridge-acceptor systems that have been designed, and basic features of nanoparticle synthesis and characterization are described.

1.2 BASIC ELECTRON TRANSFER

1.2.1 Classical Marcus Theory

The movement of an electron from a donor molecule D to an acceptor molecule A is defined as electron transfer and can be described by the following chemical equation[11]

$$D + A \rightarrow D^{+} + A^{-}$$ Equation 1.1

Marcus's classical equation, developed in 1956, is the most succinct method for depicting electron transfer. Simply, this can be described as a two parabola model, where the two parabola's potential energy surfaces represent the reactant and product state. The curvature of the parabola is related to the parameter λ, or reorganization energy, and the difference between the two energy minima is the driving force or the Gibb's free energy of reaction, $\Delta_r G$.

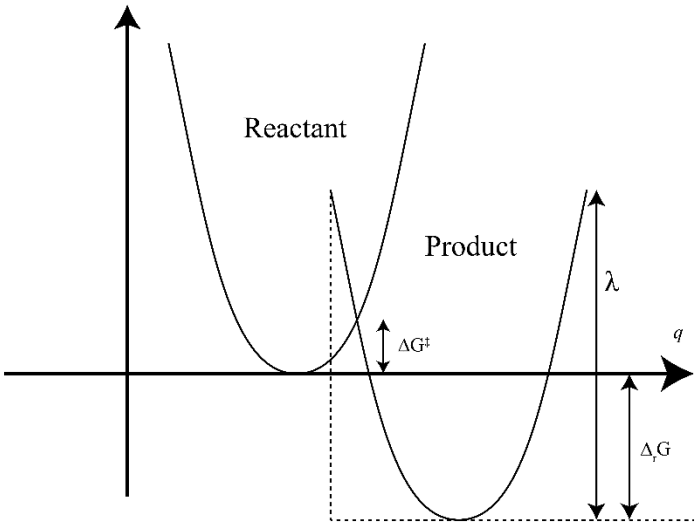

Figure 1.1 - Reaction free energy curves for reactant and product of an electron transfer reaction are shown.

The electron transfer rate is proportional to the probability that charge will transfer from one molecule to the other and can be written[1,12]

$$k_{ET} = A \exp\left(-\frac{(\lambda+\Delta_r G)^2}{4\lambda k_B T}\right) = A \exp\left(-\frac{(\Delta G^{\ddagger})^2}{k_B T}\right) \qquad \text{Equation 1.2 [1]}$$

which defines the activation energy

$$\Delta G^{\ddagger} = -\frac{(\lambda + \Delta_r G)^2}{4\lambda} \qquad \text{Equation 1.3 [1]}$$

The frequency at which the crossing is attempted and the electronic transmission factor yield the exponential prefactor A.[13] The model and these three parameters (λ, $\Delta_r G$, and A) are able to describe a wide range of systems that transfer charge, and classical Marcus theory can be quite

useful particularly as a first approximation for the charge transfer rate (Equation 1.2). Note that Marcus theory predicts the presence of an inverted regime. Equation 1.2 indicates that when $\lambda < \Delta_r G$ the value of k_{ET} will begin to decrease even when the driving force continues to increase. The presence of this inverted regime has been experimentally observed.[14]

1.2.2 Semi-classical Marcus Theory

While the classical Marcus equation (Equation 1.2) can be used to describe a variety of systems, some inconsistencies between experiment and theory still exist. The possibility of traveling from the reactant to the product state without having the classical energy required to reach the transition state is accounted for by introducing a modification into Equation 1.2 that accounts for nuclear tunneling.[1] The Fermi golden rule expression in conjunction with the Franck Condon principle[15] can be applied in the weak coupling limit to yield the following equation

$$k_{ET} = \frac{2\pi}{\hbar}|V|^2\rho(\mathrm{E}) = \frac{2\pi}{\hbar}|V|^2 FCWDS \qquad \text{Equation 1.4}$$

where $|V|$ is the electronic coupling and $\rho(\mathrm{E})$ is the density of electronic states. The Franck-Condon weighted density of states ($FCWDS$) which replaces $\rho(\mathrm{E})$ describes the probability that the system reaches a configuration where the electronic energies of the product and reactant states are equal, so that electron tunneling can occur. When the $FCWDS$ is expanded, the full semi-classical Marcus equation can be expressed via the following equation

$$k_{ET} = \frac{2\pi}{\hbar}|V|^2 \frac{1}{\sqrt{4\pi\lambda_s k_B T}} \left[\sum_{n=0}^{\infty} e^{-S}\left(\frac{S^n}{n!}\right) \exp\left(-\frac{(\lambda_s + \Delta_r G + nh\nu)^2}{4\,\lambda_s k_B T}\right)\right] \qquad \text{Equation 1.5}$$

where k_B is Boltzmann's constant, ν is the frequency of the effective quantized vibrational mode, and S is the Huang-Rhys factor given as the ratio of the inner-sphere reorganization energy, λ_v, to the quantized mode energy spacing, $\frac{\lambda_v}{h\nu}$. The $h\nu$ term refers to the energy of a single effective quantized mode associated with the electron transfer reaction. Note that in contradiction with experimental observations at low temperature, this result predicts that the rate constant goes to zero. This expression has been expanded to include all temperature regimes and can be found in Jortner *et al.*[1,15,16]

1.3 DONOR-BRIDGE-ACCEPTOR SYSTEMS

Rigid covalently linked donor-bridge-acceptor (DBA) molecules have been studied over the last 50 years. These systems are designed such that electron transfer can be probed as a function of donor-acceptor distances and bridge compositions or conformations.[15,17,18] Over the last few decades, cleft or curved DBA molecules have been designed and their electron transfer properties have been studied.[19,20] In these systems, electrons can be transferred through nonbonded contacts such as through solvent or pendent groups that reside in the cleft.[21,22] Here,

electrons can tunnel from the donor molecule to the acceptor molecule through a “line-of-sight” noncovalent linkage between the donor and acceptor.[23]

1.3.1 Linear Donor-Bridge-Acceptor Systems

In linear DBA systems the electron tunnels from the donor to the acceptor through the bridge via a superexchange interaction. As expected, the charge transfer rate is dependent on the nature of the redox centers in linear DBA systems.[24] However, the composition, conformations, and energetic states of the bridge also play a large role on the charge transfer rate.[25] A variety of these DBA systems have been studied to determine how to optimize the charge transfer rate. In general, it has been found that a decrease in bridge length increases the charge transfer rate and that charge transfer through a conjugated bridge is more efficient than through a saturated bridge.[26]

1.3.2 Non-linear Donor-Bridge-Acceptor Systems

A series of studies were completed with U-shaped[27,28] and C-shaped[29,30] DBA systems. In these cases the donor and acceptor are held at fixed distances and charge is transferred between them. In both cases, these systems contain a molecular cleft that lies between the donor and acceptor molecules. For a DBA system of this structure, electrons can tunnel both through the cleft as well as through covalent linkages in the bridge. Other studies show,[31,32] that when a solvent molecule is incorporated into the cleft, the rate of electron tunneling can be more efficient than when the

electron can only tunnel through the bridge. It is believed that the interaction of the donor and acceptor moieties with the solvent molecules enhances the charge transfer rate by enhancing the electronic coupling. A similar concept is utilized when a pendant group is placed inside the cleft. See Figure 1.2 for examples of these types of molecules.

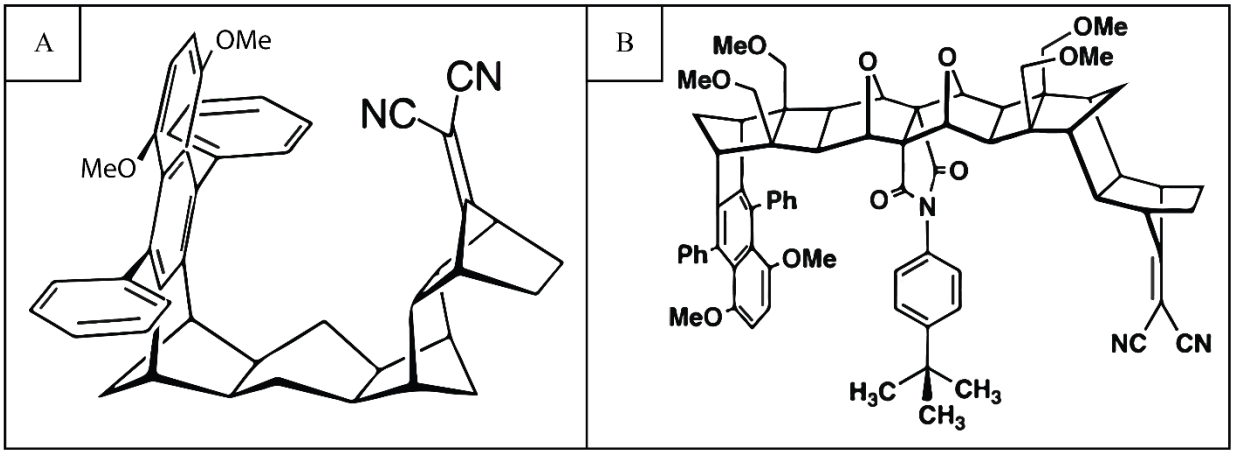

Figure 1.2 – Panel A is an example of a U-shaped DBA system[27] and panel B is an example of a DBA system with a pendant placed in the molecular cleft.[30]

1.4 NANOPARTICLE SYNTHESIS AND CHARACTERIZATION

Because semiconductor NPs have size tunable optical and electronic properties, they have great promise in a variety of applications including bioimaging,[33] sensing,[34] and, for the purposes of this thesis, photovoltaics.[35,36] Over the last few decades, synthesis of semiconductor NPs has become relatively well controlled and inexpensive.

1.4.1 Nanoparticle Nucleation & Growth

While a variety of methods to synthesize NPs exist, two methods are typically utilized to synthesize colloidal NPs in narrow size distributions.[37] One method allows both nucleation and nanoparticle growth to take place over some lengthy period of time at moderate temperatures. This method yields a broad range of sizes, but nanoparticles of different sizes can be isolated from one another. The second method, the hot injection method, separates nucleation from nanoparticle growth. In this case, injection occurs at a high temperature (hot injection) to induce nucleation, and then the temperature is reduced to slow nanoparticle growth. Unlike the previous method, this method yields a narrow distribution of sizes. Because the hot injection method is utilized to synthesize nanoparticles for the studies described in this thesis, a more detailed explanation of its nucleation and growth process follows.

The hot injection method is a thermodynamically driven process, and for spherical nanoparticles the Gibbs energy change is given by

$$\Delta G = -\frac{4}{V}\pi r^3 k_b T ln(S) + 4\pi r^2 \gamma \qquad \text{Equation 1.6 [38]}$$

where V is the volume of the precipitated species, r is the radius of the nanoparticle's nucleus, k_b is Boltzmann's constant, T is the temperature in Kelvin, S is the saturation ratio (precursor concentration v. precursor solubility), and γ is the free energy of the nanoparticle surface per unit area. In Equation 1.6, the first term describes the change in bulk free energy as V, r, and S change.[38,39] The second term describes the surface energy of the nanoparticle. When S is greater than one, the natural log of the saturation ratio becomes positive, the first term as a whole

becomes negative, and the nucleation process becomes favorable. Figure 1.3 depicts the change in free energy as a function of the particle size.

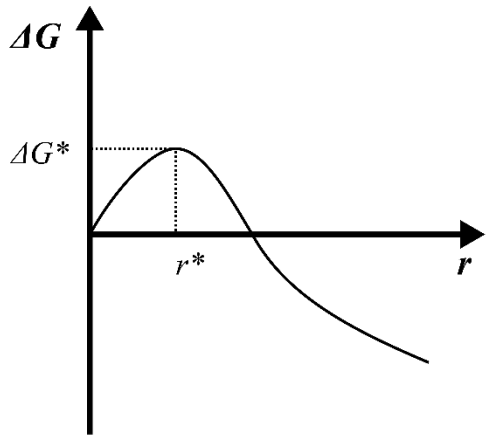

Figure 1.3 - Illustrates the free energy with respect to particle size indicating the activation energy and critical radius necessary for nucleation

The change in Gibb's free energy has a positive maximum at some critical size (r^*). This free energy maximum is the activation energy for nucleation indicating whether the particle will form a nucleus or redissolve into solution.[38,39] The critical radius, r^*, can be determined by defining the point where the derivative of the change in free energy with respect to the nanoparticle radius equals zero ($\frac{dG}{dr} = 0$) as depicted in Figure 1.3. Quantitatively the following equation describes this critical radius

$$r^* = \frac{2V\gamma}{3k_B T ln(S)}$$ Equation 1.7 [38]

As the reagents are depleted, Ostwald ripening can occur. Ostwald ripening is a phenomenon where smaller, more unstable particles, become smaller. The smaller particles can then combine with larger particles to make even more stable, larger particles by minimizing the surface area of

the NP. This phenomenon can be described by monitoring S and r^* - as S becomes smaller r^* becomes larger, forcing any small particles that are smaller than the new critical radius to redissolve into solution.

Nanoparticles can also grow via a secondary growth process – aggregation with other nanoparticles. The rate of growth via aggregation is large because nanoparticles combine to form more stable larger particles.[37] The larger nanoparticles will continue to grow by absorbing smaller and more unstable particles. Because nanoparticles are small and not thermodynamically stable, it is important to counteract the van der Waals attraction to prevent secondary growth via aggregation. Capping agents, such as organic or inorganic ligands, can be utilized to counteract the van der Waals attraction between nanoparticles, manipulating its solubility as well as playing a role in determining the shape of the NP.[36,40,41,42]

1.4.2 Quantum Size Effects in Semiconductor Nanoparticles

Nanoparticles have unique optical properties because their electronic states change with their size. Semiconductor NPs, unlike their bulk counterparts, have a radius comparable to or smaller than the exciton radius; the electron-hole pair and the carriers are, as a result, confined.[43,44,45] The quantum size effect can be described by a particle-in-a-sphere model, which leads to discrete energy levels as opposed to bulk bands. Quantum confinement is a unique property of NPs that also allows the NP's radius to be related to the first exciton energy of the NP. As the NP's radius increases, the particle becomes more similar to the bulk material; thus, the confinement effect lessens, and the exciton energy decreases. Consequently, by controlling the size of the particles,

the optical properties can be controlled as well. Figure 1.4 depicts the absorbance and emission spectra of cadmium telluride (CdTe) NPs taken at various time intervals throughout a reaction. As the reaction time increases, the first excitonic absorbance peak and the corresponding emission peak both redshift indicating both a decrease in band gap and an increase in size of the nanoparticle. The band gap is the energy difference between the highest occupied molecular orbital equivalent, namely the valence band, and the lowest unoccupied molecular orbital equivalent, namely the conduction band.

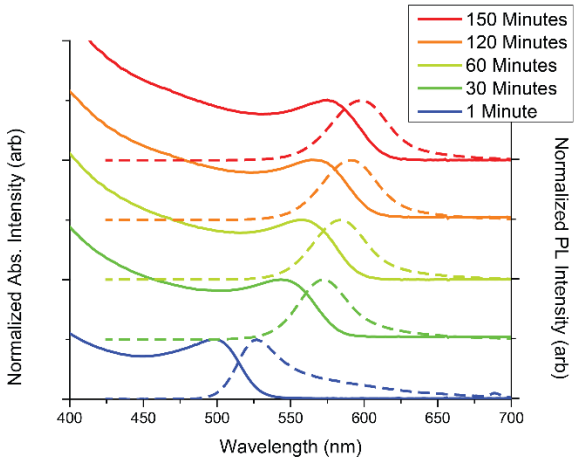

Figure 1.4 - Absorbance (solid) and emission spectra (dashed) of synthesized CdTe nanoparticles depicting the quantum confinement effect. The protocol utilized for this synthesis is described in Zou et. al.[46]

Because NPs have this property in which their energy gap changes with their size, the conduction and valence band energy alignments of nearby nanoparticles have the potential to be particularly interesting, and three typical alignments are possible.[40] Type I alignment, referred to as the straddling gap, is depicted in the left panel of Figure 1.5; A has an energy gap that straddles the gap of B. Type II alignment, the staggered alignment, is when the two sets of band edges are

staggered such that the valence band of A falls within the conduction and the valence bands of B and the conduction band of B falls within the conduction and valence bands of the A (Figure 1.5, middle). Type III alignment, the broken gap, is when the band gap of A does not overlap at all with the band gap of B (Figure 1.5, right). Type II band alignment proves to be useful for charge transfer studies.

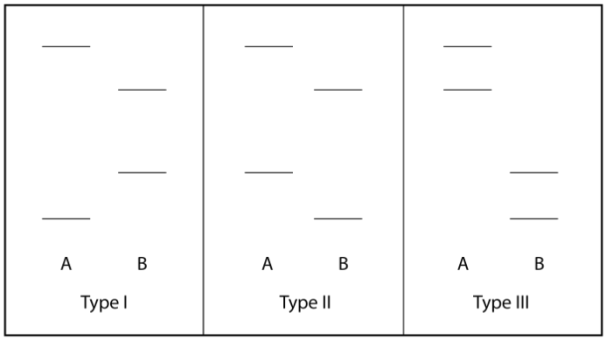

Figure 1.5 - Cartoon describing the three types of band gaps that are commonly observed

In order to regulate which type of band alignment exists in a particular assembly of NPs, the band gap and the band edges (ie. conduction band and valence band) of a NP must be determined. In this thesis, knowing the relative energy positions of the band edges is important to design assemblies that contain a Type II heterojunction and support electron transfer. One commonly used model to predict the band gap of NPs stems from Brus's work in 1984 and uses the effective mass approximation[44,47]

$$E_{gap}^{NC}(r) = \frac{\hbar^2\pi^2}{2r^2}\left[\frac{1}{m_e^*} + \frac{1}{m_h^*}\right] - \frac{1.8e^2}{4\pi\epsilon_0\epsilon_\infty r} + E_{gap}^{bulk} \qquad \text{Equation 1.8 [44,48]}$$

where r is the NP's radius, m_e and m_h are the effective masses of the electrons and holes, and ϵ_∞ is the dielectric constant of the NP. Using this relationship, the following calculation can be used to estimate the conduction band energy minimum.[45]

$$E_{CB}^{NC}(r) = E_{CB}^{bulk} + \left(E_{gap}^{NC} - E_{gap}^{bulk}\right)\left[\frac{m_h^*}{m_e^* + m_h^*}\right] \qquad \text{Equation 1.9 [47]}$$

The valence band can be obtained by subtracting the band gap from the calculated conduction band. Figure 1.6 depicts how the calculated absolute positions of the conduction band and the valance band differ in comparison to experimental cyclic voltammetry measurements for CdSe nanoparticles.[49, 51]

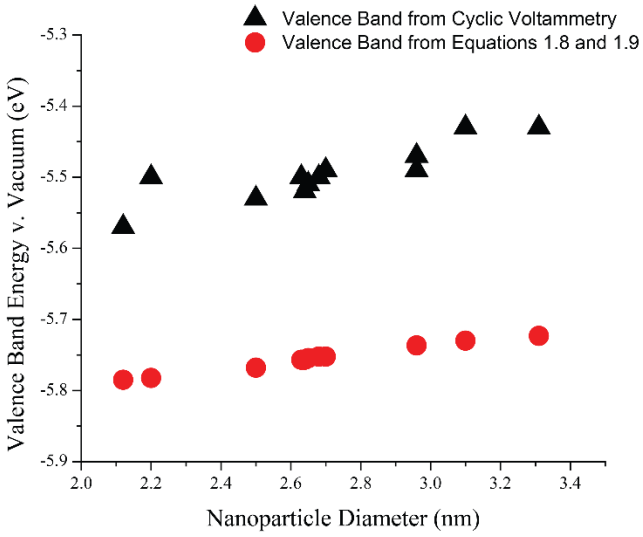

Figure 1.6 - Experimental and theoretical work depicting the valence band for various sizes of CdSe nanoparticles. Cyclic voltammetry measurements were reported in Bloom et. al.[51]

It is evident that this simplified model does not adequately describe the band edge positions. Jasieniak *et. al.*[50] also notes that simple models are not able to wholly predict the changes in the conduction and valence bands. Several other experimental papers have been able to probe these nuances.[51,52,53] For example, Bloom *et. al.*[51] indicates that the functional group of the ligand bound to the surface of the NP can greatly alter the electronic states of the NP. In particular, it should be noted that for thiolated CdSe NPs, the valence band of the CdSe resides on the highest occupied molecular state of the ligand, or on the thiol. Experimentally, it means that the valence band of the thiolated CdSe NP does not change with the size of the NP. Thus, any calculations of the conduction and valence bands should be taken as reasonable approximations.

1.4.3 Nanoparticle Characterization

A commonly utilized technique to characterize NPs is transmission electron microscopy (TEM). TEM is a tool used to analyze samples that display structural features over the micron and nanometer length scales. In this form of characterization, a focused beam of high energy electrons is incident on a thin sample within a high vacuum, and the electrons interact with the sample as they pass through it.[54] On the way through the sample, some parts of the material stop or deflect electrons more than other parts, which modulates the spatial distribution of the electrons that are collected below the sample. In the regions where electrons do not pass through the sample, the image is dark, and where the electrons are unscattered, the image is brighter. After magnifying and focusing, an image can be constructed. The following is a TEM of a sample of CdSe nanoparticles synthesized for this thesis.

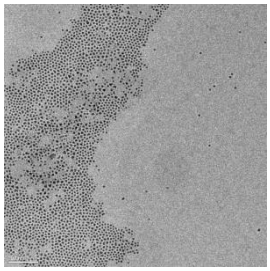

Figure 1.7 - TEM image of CdSe nanoparticles collected by Yang Wang at the University of Pittsburgh Nanoscale Fabication and Characterization Facility.

Absorption and fluorescence spectroscopy of NPs has been well-studied. The absorption maximum of a NP can be used to determine the size of the NPs by correlating the absorbance maxima of the first exciton with TEM data of the size, an example of the empirical equation for CdTe NPs is listed in Equation 1.10 and Equation 1.11[55]

$$D = (9.8127 \times 10^{-7})\lambda^3 - (1.7147 \times 10^{-3})\lambda^2 + (1.0064)\lambda - 194.84 \qquad \text{Equation 1.10 [55]}$$

in which D is the NP diameter in nm and λ is the wavelength of the absorption peak maximum. In addition, Yu *et. al.* [55] found a strong dependence between the extinction coefficient, ε, and the NP size.

$$\varepsilon = 10043\ D^{2.12} \qquad \text{Equation 1.11 [55]}$$

Using the empirical result, the concentration of the sample can then be calculated utilizing the Beer-Lambert law:

$$A = \varepsilon lc$$ Equation 1.12 [56]

where A is the absorbance of the sample, l is the path length of the cuvette, and c is the concentration of the sample. Fluorescence from these NPs results from radiative recombination of an electron from the excited state (conduction band) to the ground state (valence band). Features in the emission spectra can provide insight into NP quality, uniformity, and size distribution.[44] In order to study photo-induced electron transfer, a complete picture of the semiconductor NPs is particularly important. There are a few potential relaxation pathways from the NP's excited state, including radiative energy transfer, non-radiative decay (trap states), and charge transfer.[45] Figure 1.8A depicts some potential relaxation pathways for semiconductor NPs and illustrates the expected band edges of the trap states with respect to the characteristic nanoparticle band edges; because of these surface defects, emission of wavelengths longer than the characteristic nanoparticle bandgap emission (ie. an emission peak to the red) is evident as shown in Figure 1.8B.

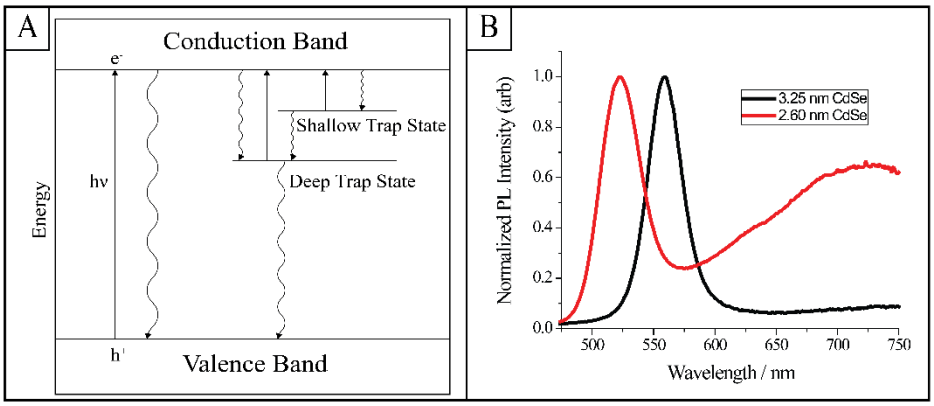

Figure 1.8 - Cartoon describing potential excitation and relaxation pathways in a nanoparticle system. Straight lines indicate excitation pathways and wavy lines indicate relaxation pathways (A). CdSe nanoparticles with prominent surface states (red) are indicated by the broad red-shifted emission, those without promient surface states are also shown (black) (B).

These relaxation pathways can compete with desirable processes, such as charge transfer. Thus, it is important to control these processes by controlling the size and band gap of the semiconductor NP. The potential photoinduced interactions that a NP can have are determined by the relative energy levels. Charge transfer should be energetically favorable when the offset between the conduction band or the valence band is greater than the Coulombic binding energy of the exciton.

The emission peak width can also provide some insight into the nanoparticles' size distribution: typically nanoparticles with broader emission peaks have a broader size distribution. The quantum yield of an NP can be utilized to indicate the success of a synthesis. The relative quantum yield for a NP's (indicated as *x*) emission, as compared to a reference fluorophore (indicated as *r*), is given by Equation 1.13.

$$\frac{\varphi_x}{\varphi_r} = \frac{A_r(\lambda_r) I(\lambda_r) n_x^2 D_x}{A_x(\lambda_x) I(\lambda_x) n_r^2 D_r}$$ Equation 1.13 [57]

where *A* is the absorbance at the excitation wavelength, I is the lamp intensity, n is the refractive index of the solvent, and *D* is the integrated area of the emission. High quantum yields typically indicate that a NP has a well-passivated surface and/or a small number of surface states.

Time-dependent fluorescence spectroscopy, utilizing the time correlated single photon counting method (TCSPC), can be used to provide information on the relaxation pathways of an exciton. TCSPC is a statistical method that measures the delay time of emission photons relative to an excitation pulse.[58] TCSPC makes use of the fact that for low level, high repetition rate signals, the light intensity can be modified so that that the probability of detecting one photon per excitation pulse is much less than one, meaning that the probability of detecting multiple photons per excitation pulse is statistically insignificant. TCSPC can provide information about the average excited state lifetimes of NPs (and molecules) as well as provide some insight into the relative decay pathways in the NP. The excited state lifetime of a species depicts how long the species will remain in the exited state before it relaxes to the ground state.[56] Thus, this method can be used to learn about how surface states, resulting from different syntheses, affect excited state lifetimes.[44,59,60]

Often, the excited state decay law is not exponential, but can be fit by a multi-exponential model, namely

$$I(t) = \sum_{i=1}^{n} \alpha_i e^{-t/\tau_i} \qquad \text{Equation 1.14 [59]}$$

where α is the pre-exponential factor for each component and τ is the decay time for each component. Sometimes, a distribution of decay times rather than discrete decay times are

expected, which is particularly true for systems that are not homogenous, like semiconductor NPs. In this case, the α_i term in Equation 1.14 is replaced by $\alpha(\tau)$. Here, as opposed to looking at discrete decay times that are summed, we look at the integral of this system (Equation 1.15).

$$I(t) = \int_{\tau=0}^{\infty} \alpha(\tau) e^{-t/\tau} \, d\tau \qquad \text{Equation 1.15 [59]}$$

Semiconductor NPs have unique photophysical properties; it has been reported that as the average diameter of CdTe NPs increases the average lifetime will both increase and become more monoexponential in nature (Figure 1.9A). One explanation for this behavior is that the decreased band gap, which correlates with an increase in average diameter, shifts the valence band of the NP above the energy level of the trap states as depicted in Figure 1.9B.[60]

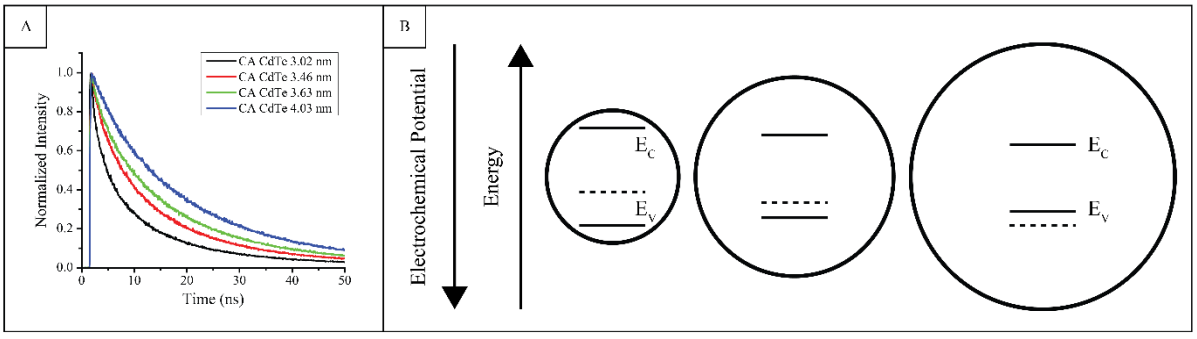

Figure 1.9 - TCSPC measurements collected on CdTe NP as the size of the NP increases (A) Energy digram of CdTe NP as diameter increases and band gap decreases, while trap state energy (dashed) is assumed to be fixed (B).

1.4.4 Ligand Exchange

Once the NP is synthesized, it is possible to alter the surface by ligand exchange. The typical procedure utilized for ligand exchange is a modified version of the procedure described in Soreni-Harari *et. al.*[61] This process begins by placing the NP in a solution of highly concentrated modifying ligand. Mixing should occur as the solution stirs. The binding affinity of the functional group attached directly to the nanoparticle is important for determining the likelihood of a ligand exchange to be successful. It would be difficult for a ligand with low affinity to the surface of the NP to displace a ligand that has a strong affinity to the surface, but it would be relatively easy for a ligand with strong affinity to the surface to displace a ligand with weak affinity to the surface.[49,62] Affinity to the surface of a semiconductor NP typically increases in the following manner: carboxylic acid, amines, phosphonic acid, and sulfur.

Adjusting the concentration ratios or slightly increasing the temperatures are two ways to improve the efficiency of a ligand exchange.[49] A number of problems with ligand exchanges have hampered the approach to controlling NP's surface properties. For example, some ligands are not compatible with filters and do not precipitate out of solution so removing excess ligand may be very difficult. Excess ligand may change the optical properties of the NP. Additionally, while gentle heating can help the ligand exchange proceed, it can also lead to NP growth and could also change the shape of the NP. One useful way to determine the success of a ligand exchange is to change the solubility of the nanoparticle. Figure 1.10 shows such a change in solubility – ODPA (octadecylphosphonic acid) capped CdTe is soluble in toluene, but when the surface ligand is exchanged to MPA (3-mercaptopropionic acid), the NP becomes soluble in

water. Figure 1.10 illustrates the nanoparticles' movement from the hydrophobic phase to the hydrophilic phase when the surface ligand is altered.

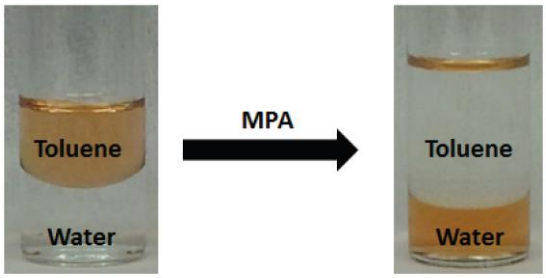

Figure 1.10 - ODPA capped CdTe nanoparticles soluble in toluene (left vial). Following ligand exchange to MPA, the nanoparticles change phases to become soluble in water (right vial). [51]

This technique is a simple way to determine if the ligand exchange was successful; however, it is useful only when the ligand exchange changes the overall polarity of the nanoparticle.

1.5 SPIN SELECTIVE CHARGE TRANSPORT

1.5.1 Chiral Nanoparticles

Recently, it was found that chiral ligands had the ability to imprint their chirality onto the surface of semiconductor NPs yielding a so-called chiral NP. In 2007, the chiro-optical properties of semiconductor NPs were first investigated.[63] L- and D-penicillamine were utilized to cap

colloidal cadmium sulfide (CdS) NPs and the circular dichroism (CD) of the NPs was measured. At the first excitonic peak of the NPs, L- and D-penicillamine induced mirror image CD signatures indicating that the NPs electronic states were chiral. Both experimental studies[64] and quantum mechanical modeling[65] indicate that chirality of a NP's electronic states originates from the chirality of the ligand. Currently, it is believed that the ligand distorts cadmium atoms on the surface of the NP, yielding a chiral NP.

This imprinting of ligand chirality onto the electronic states of CdS NPs has been extended to other NP systems, such as CdSe and CdTe. It was also found that these NPs could be passivated with a variety of different chiral surface ligands, which in turn led to an assortment of CD signatures.[66,67] In addition to directly synthesizing chiral NPs, it was also found that NPs can become chiral post-synthetically.[68] If an achiral NP, or NPs with an achiral capping ligand, are ligand exchanged to a chiral capping ligand, then the NP itself becomes chiral. Figure 1.11 depicts a sample CD signature (top) and corresponding absorbance (bottom) for a post-synthetically modified chiral CdSe NP.[68]

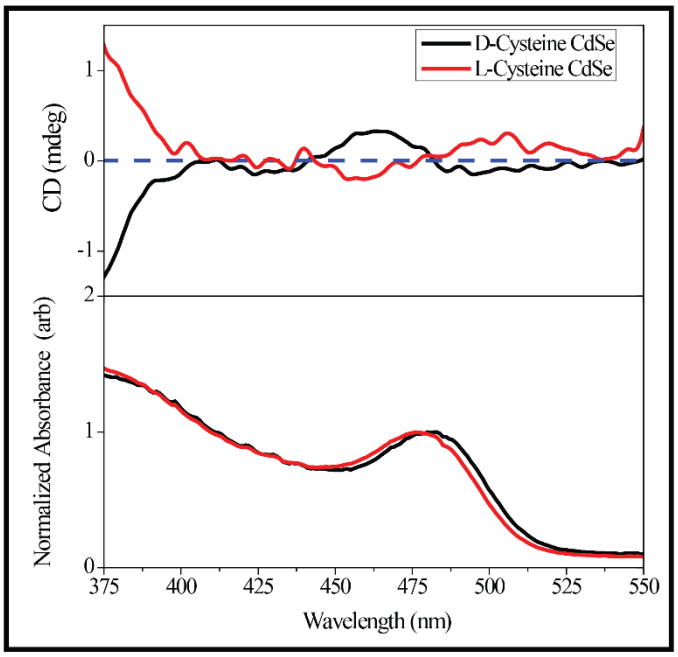

Figure 1.11 - Sample circular dichroism spectra (top) and absorbance spectra (bottom) of L-cysteine CdSe (red) and D-cysteine CdSe (black) nanoparticles, 2.9 nm in diameter.[79]

Fully understanding and controlling chiral NPs is not only interesting fundamentally, but their unique properties have the potential to be utilized in a variety of novel applications including spintronics and spin-selective photovoltaics.

1.5.2 Chiral Induced Spin Selectivity

Spin selective charge transport is an expanding field that currently holds a lot of promise for more efficient charge transport. Simply, spin selective charge transport can inhibit the competing back-transport pathway which would lead to more efficient charge transport. Chiral NPs have the

potential to be implemented in spin selective charge transport systems, assuming the effect named chiral induced spin selectivity (CISS) is present.[69,70]

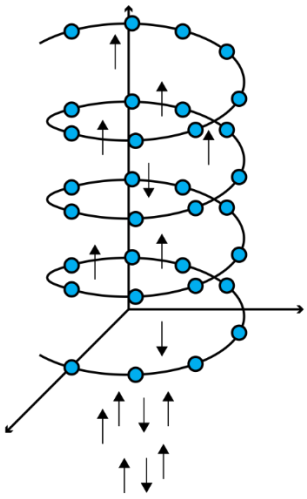

Figure 1.12 - Cartoon of helical molecule (black) assumed to behave as a series of point charges (blue) with electrons going through the helix (arrows).

CISS can be described qualitatively via the cartoon in Figure 1.12 if it is assumed that this helical molecule behaves as series of point charges (blue circles) with a corresponding electric field, $\vec{E}$, associated with the point charges, all directions of the field cancel except for one. An electron traversing through a helical system at some momentum, $\vec{v}$, interacts with the $\vec{E}$ component that has not been cancelled out. This interaction generates a magnetic field, $\overrightarrow{B}$, through the helical system. This effect is shown in Equation 1.16

$$\vec{B} = \frac{\vec{v}}{c^2} \text{ x } \vec{E}$$ Equation 1.16 [70]

where c is the speed of light. The spin of an electron is coupled to its linear momentum, thus the efficiency of charge transport is dependent on the spin of the electron relative to the magnetic field. This effect can generally be depicted by Figure 1.13.

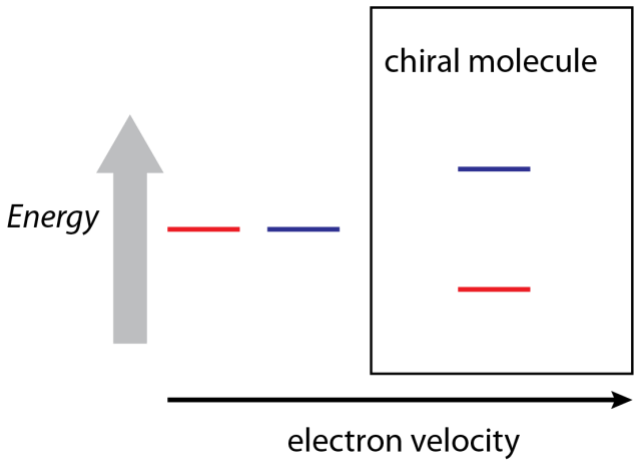

Figure 1.13 - Cartoon of spin state splitting in a chiral molecule.

When the electrons are not in the presence of the chiral molecule, or effective $\overrightarrow{B}$, then the two spin states (red and blue) are degenerate; however, when the electron is going through the chiral molecule, the degeneracy of the spin states breaks and the corresponding difference in energy results from the electron's linear momentum being either parallel or antiparallel to the direction of the magnetic field.[69]

Experimental evidence of the CISS effect was first shown in 1999.[71] A chiral monolayer film (stearoyl lysine) was formed on a gold substrate and the energy of the photoexcited electrons was monitored. It was found that the intensity profile of the emitted photoelectrons was dependent on both the chirality of the film and the orientation of the light polarization. Since these fundamental

experiments, asymmetry indicating spin selective transmission has been shown for helical peptides,[72,73] helical DNA,[74,75,76] other biomolecules,[77,78] and through chiral nanoparticles.[79] Typically, these experiments rely on the magnetization of a spin source (ie. the presence of an external magnetic field).[62] Thus, simply utilizing a polarized light source as a way to selectively produce particular spins would be advantageous. Probing this novel field yields the potential for improving and exploring many applications particularly including photovoltaics and spintronics.

1.6 SCOPE OF DISSERTATION

In order to gain further understanding of electron transfer in both molecular and nanoscale assemblies, this thesis addresses the following questions: 1) How does the hydrophobicity of a molecular cleft affect the electron transfer kinetics of DBA systems and are they controllable? 2) Can donor-acceptor nanoparticle dyads be formed and how do their charge transfer properties compare to molecular systems? 3) In a donor-acceptor NP system, when the acceptor NP is chiral will there be spin selective transport? The goal of this thesis is to study charge transfer in a variety of different donor-acceptor systems, which may be used for a variety of applications including solar cells and spintronics.

Chapter 2 discusses our work studying solvent facilitated charge transfer in DBA systems. Photoluminescence decay measurements and quantum mechanical modelling show that an amide modification to the acceptor molecule, pyrene, greatly alters the size of the interparticle cleft between the donor and acceptor system. The amide modification opens up the cleft and allows

for the incorporation of larger and in some cases more than one solvent molecule. This work demonstrates that small modifications to a DBA system can greatly change the electron transfer properties. This work has been published in the Journal of Physical Chemistry A.[80]

Chapter 3 takes the small modification imposed on the DBA system one step further. In chapter 2, the modification on the pyrene molecule is located as far away from the pyrene's connection to the bridge as possible (in the 6th substituent position). However, in order to further understand the effects of the modification on the DBA system, the amide modification is moved from the 6th substituent position to the 3rd and 8th substituent positions. This chapter further explores the changes in electron transfer properties as the modification has the potential to interact with the bridge subunits.

Chapter 4 discusses our work studying charge transfer between a donor NP and acceptor NP that are templated on a silicon microbead. Time correlated single photon counting is utilized to determine the electron transfer rates in this study. Through careful tuning of the NP's energetics, charge transfer could be monitored. Through a distance dependence study, it was determined that this electron transfer pathway was consistent with electron tunneling. It was also found that Marcus theory was able to describe electron transfer between these organized semiconductor NP dyads. This study introduces a novel approach for the assembly of NP dyads and is able to describe a NP donor-acceptor system analogously to molecular DBA systems. This work has been published in the Journal of the American Chemical Society. [81]

Chapter 5 shows our results for NP dyad assemblies in which the acceptor is a chiral CdSe NP and the donor is an achiral CdTe NP. The NP dyad assemblies are excited with both linearly and circularly polarized light. Circularly polarized light can be utilized to selectively excite either spin up or spin down electrons, while linearly polarized light excites both spins. When an achiral

donor is attached to L-cysteine CdSe, electron transfer is more efficient when counterclockwise circularly polarized light is utilized and less efficient for clockwise circularly polarized light. The reverse effect is observed for the D-cysteine CdSe acceptor. It is found that the chiro-optical properties of the NP correlate with asymmetry observed in the electron transfer rate.

1.7 REFERENCES

1 Jortner J; Bixon, M. Electron Transfer-From Isolated Molecules to Biomolecules, Part 1 and Part 2. John Wiley & Sons, Inc. New York, 1999.
2 Blumberger, *J.; Chem. Rev.*, **2015**, *115*, 11191.
3 Gilbert M.; Albinsson B.; *Chem. Soc. Rev.*, **2015**, *44*, 845.
4 Warren, J. J.; Ener, M. E.; Vlcek, A.; Winkler, J. R.; Gray, H. B.; *Coord. Chem. Rev*., **2012**, *256*, 2478.
5 Hsu, C.; *Acc. Chem. Res.*, **2009**, *42*, 509.
6 Karkas, M. D.; Johnston, E. V.; Verho, O.; Akermark, B.; *Acc. Chem. Res.*, **2014**, *47*, 100.
7 Ward, A. J.; Ruseckas, A.; Kareem, M. M.; Ebenhoch, B.; Serrano, L. A.; Al-Eid, M.; Fitzpatrick, B.; Rotello, V. M.; Cooke, G.; Samuel I. D. W.; *Adv. Mater.*, **2015**, *27*, 2496.
8 Sattler, K. D. Handbook of Nanophysics: Principles and Methods. CRC Press: Boca Raton, FL, 2010; p. 13-1-13-13.
9 Zhu, H.; Yang, Y.; Wu, K.; LIan, T.*; Annu. Rev. Phys. Chem*., **2016**, *67*, 259.
10 Kamat, P. V.; *J. Phys. Chem. C*, **2007**, *111*, 2834.
11 Marcus, R. A.; *J. Chem. Phys*., **1956**, *24*, 966.
12 Marcus, R. A.; *Rev. Mod. Phys*., **1993,** *65*, 599.
13 Bu, Y.; Deng, C.; *J. Phys. Chem*., **1996**, *100*, 18093.
14 Miller, J. R.; Calcaterra, L. T.; Closs, G. L.; *J. Am. Chem. Soc*., **1984**, *106*, 3047.
15 Barbara, P. F.; Meyer, T. J.; Ratner, M. A.; *J. Phys. Chem*., **1996**, *100*, 13148.
16 Jortner, J.; Bixon, M.; *J. Chem. Phys*., **1988**, *88*, 167.
17 Closs, G. L.; Miller, J. R.; *Science*, **1988**, *240*, 440.
18 Paddon-Row, M. N.; *Acc. Chem. Res*., **1994**, *27*, 18.
19 Lokan, N. R.; Craig, D. C.; Paddon-Row, M. N. Synlett. **1999**, 397.
20 Kumar, K,; Kurnikov, I.; Beratan, D.N.; Waldeck, D. H.; Zimmt, M. B.; *J. Phys. Chem. A.*, **1998**, *102*, 5529.
21 Napper, A. M.; Head, N. J.; Oliver, A. M.; Shephard, M. J.; Paddon-Row, M. N.; Read, I.; Waldeck, D. H.*; J. Am. Chem. Soc*., **2002**, *124*, 10171.
22 Liu, M.; Waldeck, D. H.; Oliver, A. M.; Head, N. J.; Paddon-Row, M. N.; *J. Am. Chem. Soc*., **2004**, *126*, 10778.
23 Napper, A. M.; Read, I.; Waldeck, D. H.; Head, N.J.; Oliver, A. M.; Paddon-Row, M. N.; *J. Am. Chem. Soc*., **2000**, *122*, 5220.
24 Oliver, A. M.; Craig, D. C.; Paddon-Row, M. N.; Kroon, J.; Verhoeven, J. W.; *Chem. Phys. Lett*., **1998**, *150*, 366.
25 Albinsson, B.; Martensson, J.; J. *Photochem. Photobio. C: Photochem. Rev*., **2008**, *9*, 138.

26 Ricks, A. B.; Solomon, G. C.; Colvin, M. T.; Scott, A. M.; Chen K.; Ratner, M. A.; Wasielewski, M. R.; *J. Am. Chem. Soc*., **2010**, *132*, 15427.
27 Chakrabarti, S.; Liu, M.; Waldeck, D. H.; Oliver, A. M.; Paddon-Row, M. N.; *J. Am. Chem. Soc*., **2007**, *129*, 3247.
28 Napper, A. M.; Read, I.; Waldeck, D. H.; Head, N. J.; Oliver, A. M.; Paddon-Row, M. N.; *J. Am. Chem. Soc*., **2000**, *122*, 5220.
29 Kaplan, R. W.; Napper, A. M.; Waldeck, D. H.; Zimmt, M. B.; *J. Am. Chem. Soc*., **2000**, *122*, 12039.
30 Chakrabarti, S.; Parker, M. F. L.; Morgan, C. W.; Schafmeister, C. E.; Waldeck, D. H.; *J. Am. Chem. Soc*., **2009**, *131*, 2044.
31 Read, I.; Napper, A.; Zimmt, M. B.; Waldeck, D. H.*; J. Phys. Chem. A*, **2000**, *104*, 9385.
32 Jordan, K. D.; Paddon-Row, M. N.; *Chem. Rev*., **1992**, *92*, 395.
33 Bruchez, M., Jr.; Moronne, M.; Gin, P.; Weiss, S.; Alivisatos, P. A.; *Science*, **1998**, *281*, 2013.
34 Jin, W. J.; Fernandez-Arguelles, M. T.; Costa-Fernandez, J. M.; Pereiro, R.; Sanz-Medel, A.; *Chem. Commun*., **2005**, 883.
35 Talapin, D. V.; Murray, C. B.; *Science*, **2005**, *310*, 86.
36 Maheshwari, V.; Saraf, R. F.; *Science*, **2006**, *312*, 1501.
37 Peng, X.; Wickham, J.; Alivistatos, A. P.; *J. Am. Chem. Soc*., **1998,** *120*, 5343.
38 Burda, C.; Chen, X.; Narayanan, R.; El-Sayed, M. A.; *Chem. Rev*., **2005**, *105*, 1025.
39 Capek, R. K.; Lambert, K.; Dorfs, D.; Smet, P. F.; Poelman, D.; Eychmuller, A.; Hens, Z.; *Chem. Mater*., **2009**, *21*, 1743.
40 Rogach, A. L. Semiconductor Nanocrystal Quantum Dots. Springer: 2008; p. 1-11.
41 Klimov, V. I. Semiconductor and Metal Nanocrystals. Marcel Decker Inc.: 2004; p. 4-35.
42 Peng, X.; Manna, L.; Yang, W.; Wickham, J.; Scher, E.; Kadavanich, A,; Alivisatos, A. P.; *Nature*, **2000**, *404*, 59.
43 Smith, A. M. and Nei, S.; *Acc. Chem. Res*., **2009**, *43*, 193.
44 Zhang, J. Z.; J. *Phys. Chem. B*, **2000**, *104*, 7239.
45 Klimov, V. I. *Nanocrystal Quantum Dots. CRC* Press: 2010; p. 66-74, 247-259.
46 Zou, L.; Gu, Z.; Zhang, N.; Zhang, Y.; Fang, Z.; Zhu, W.; Zhong, X.; *J. Mater. Chem*., **2008**, *18*, 2807.
47 Hetsch, F.; Xu, X.; Wang, H.; Kershaw, S. V.; Rogach, A. L.; *J. Phys. Chem. Lett*., **2011**, *2*, 1879.
48 Hetsch, F.; Xu, X.; Wang, H.; Kershaw, S. V.; Rogach, A. L.; *J. Phys. Chem. Lett*., **2011**, *2*, 1879.
49 Kalyuzhuny, G.and Murrary, R. W.; *J. Phys. Chem. B*., **2005,** *109*, 7012.
50 Jasieniak, J.; Califano, M.; Watkins, S. E.; *ACS Nano*, **2011**, *5*, 5888.
51 Bloom. B. P.; Zhao. L. B.; Wang, Y.; Waldeck. D. H.; Liu, R.; Zhang, P.; Beratan, D.; *J. Phys. Chem. C*, **2013,** *117*, 22401.
52 Boles, M. A.; Ling, D.; Hyeon T.; Talapin, D. V.; *Nat. Mater*., **2016**, *15*, 141.
53 Kilina, S.; Ivanov, S.; Tretiak, S.; *J. Am. Chem. Soc*., **2009**, *131*, 7717.
54 Talapin, D. V.; Lee, J. S.; Kovalenko, M. V.; Shevchenko, E. V.; *Chem. Rev*., **2010**, *110*, 389.
55 Yu. W.; Qu, L.; Guo, W.; Peng, X.; *Chem. Mater*., **2003**, *15*, 2854.
56 Lakowicz, J. R. *Principles of Fluorescence Spectroscopy, 3rd ed*. Springer: 2006; p. 1-61, 97-155, 331-382, 443-475.
57 Brower, A. M.; *Pure Appl. Chem*., **2011**, *83*, 2213.
58 Becker, W., *Advanced Time-Correlated Single Photon Counting Techniques*. Springer: 2005; p. 1-25.
59 Jones, M.; Nedeljkovic, J.; Ellingson, R. J.; Nozik, A. J.; Rumnles, G.; *J. Phys. Chem. B*, **2003**, *107*, 11346.
60 Wuister, S. F.; Donega, C; Meijerink, A.; *J. Phys. Chem. B*., **2004**, *108*, 17393.
61 Soreni-Harai, M.; Yaacobi-Gross, N.; Steiner, D.; Aharoni, A.; Banin, U.; Millo, O.; Tessler, N.; *Nano. Lett*., **2008,** *8*, 678.
62 Perro, A.; Reculusa, S.; Ravaine, S.; Boourgeat-Lami, E.; Duguet, E.; *J. Mater. Chem*., **2005**, *15*, 3745.
63 Moloney, M. P.; Gun'ko, Y. K.; Kelly, J. M.; *Chem. Commun*., **2007**, 3900.
64 Nakashima, T.; Kobayashi, Y.; Kawai, T.; *J. Am. Chem. Soc*. ,**2009**, *131*, 10342.
65 Elliott, S. D.; Moloney, M. P.; Gun'ko, Y. K.; *Nano Lett*., **2008**, *8*, 2452.
66 Zhou, Y.; Zhu, Z.; Huang, W.; Liu, W.; Wu, S.; Liu, X.; Gao, Y.; Zhang, W.; Tang, Z.; *Angew. Chem*., **2011**, *123*, 11658.

67 Tohgha, U.; Deol, K. K.; Porter, A. G.; Bartko, S. G.; Choi, J. K.; Leonard, B. M.; Varga, K.; Kubelka, J.; Muller, G.; Balaz; *ACS Nano*, **2013**, *7*, 11094.
68 Tohgha, U.; Varga, K.; Balaz, M.; *Chem. Commun*., **2013**, *49*, 1844.
69 Naaman, R.; Waldeck, D. H.*; J. Phys. Chem. Lett*., **2012**, *3*, 2178.
70 Naaman, R.; Waldeck, D. H.; *Annu. Rev. Phys. Chem*., **2015**, *66*, 263.
71 Ray, K.; Ananthavel, S. P.; Waldeck, D. H.; Naaman, R.; *Science*, **1999**, *283*, 814.
72 Mtangi, W.; Kiran, V.; Fontanesi, C.; Naaman, R.; *J. Phys. Chem. Lett*,. **2015**, *6*, 4916.
73 Kettner, M.; Göhler, B.; Zacharias, H.; Mishra, D.; Kiran, V.; Naaman, R.; Fontanesi, C.; Waldeck, D. H.; Sęk, S.; Pawłowski, J.; Juhaniewicz, J.; *J. Phys. Chem. C*, **2015**, *119*, 14542.
74 Peer, N.; Dujovne, I.; Yochelis, S.; Paltiel, Y.; *ACS Photonics*, **2015**, *2*, 1476.
75 Göhler, B.; Hamelbeck, V.; Markus, T. Z.; Kettner, M.; Hanne, G. F.; Vager, Z.; Naaman, R.; Zacharias, H.; *Science*, **2011**, *331*, 894.
76 Ray, S. G.; Daube, S. S.; Leitus, G.; Vager, Z.; Naaman, R.; *Phys. Rev. Lett*., **2006**, *96*, 036101.
77 Mondal, P. C.; Fontanesi, C.; Waldeck, D. H.; Naaman, R.; *ACS Nano*, **2015**, *9*, 3377.
78 Mishra, D.; Markus, T. Z.; Naaman, R.; Kettner, M.; Göhler, B.; Zacharias, H.; Friedman, N.; Sheves, M.; Fontanesi, C.; *Proc. Natl. Acad. Sci*., **2013**, *110*, 14872.
79 Bloom, B. P.; Kiran, V.; Varada, V.; Naaman, R.; Waldeck, D. H.; *Nano Lett*., **2016**, *16*, 4583.
80 Graff, B. M.; Lamont, D. N.; Parker, M. F. L.; Bloom, B. P.; Schafmeister, C. E.; Waldeck, D. H.; *J. Phys. Chem. A.*, **2016**, *120*, 6004.
81 Graff, B. M.; Bloom, B. P.; Wierzbinski, E.; Waldeck, D. H. *J. Am. Chem. Soc*. **2016**, *138*, 13260.

2.0 THROUGH SOLVENT TUNNELING IN DONOR-BRIDGE-ACCEPTOR MOLECULES CONTAINING A MOLECULAR CLEFT

This work has been published as Graff, B. M.; Lamont, D. N.; Parker, M. F. L.; Bloom, B. P.; Schafmeister, C. E.; Waldeck, D. H. The thesis author performed all of the photophysical studies and co-wrote the manuscript with D.N.L. The supporting information for this chapter is provided in Appendix A, Chapter 7.0. This chapter was published previously as Graff, B. M.; Lamont, D. N.; Parker, M. F. L.; Bloom, B. P.; Schafmeister, C. E.; Waldeck, D. H. *J. Phys. Chem. A*, **2016**, *120*, 6004. and is reprinted with permission.

Photoinduced electron transfer is used to investigate the solvent mediated electron tunneling between electron donor and acceptor groups in polar solvents. Bis-peptide scaffolds are used to control the spatial positioning of electron donor and acceptor groups and create a molecular cleft. The photoinduced electron transfer is studied for two different cleft sizes and the electronic coupling is found to be controlled by the nature of the solvent and the ability of the molecular cleft to accommodate it, as well as interact directly with it. These studies demonstrate the importance of electron tunneling through non-bonded contacts and reveal a strategy for examining such tunneling pathways in polar solvents.

2.1 INTRODUCTION

Electron-transfer (ET) reactions are essential to many chemical and biological transformations. A nonzero electronic coupling $|V|$ between an electron donor (D) and acceptor (A) unit is a prerequisite for electron-transfer reactions. As detailed by Marcus and others,[82] the strength of the electronic coupling is generally used to categorize ET reactions into a strong coupling or adiabatic charge-transfer regime for which $|V| >> kT$, an intermediate regime for which $|V|$ is comparable to kT, and a weak coupling/ nonadiabatic regime for which $|V| < kT$; the latter is relevant to the systems discussed herein. In the nonadiabatic limit the ET rate constant may be written as

$$k_{ET} = \frac{2\pi}{\hbar} \cdot |V|^2 \cdot FCWDS \qquad \text{Equation 2.1}$$

where FCWDS is the Franck-Condon factor, which contains parameters related to molecular structure and environmental variables. The electronic coupling magnitude may be mediated by covalent and/or noncovalent interactions and depends on the electronic features of the medium through which the electron tunnels. Although often weaker than bond-mediated coupling pathways, electron-transfer involving solvent molecules in the electron tunneling pathway is likely to play an important role for intermolecular electron transfer reactions; consequently, the solvent's electronic structure can play an important role in the ET kinetics.

Over the past three decades the study of well-defined synthetic donor-bridge-acceptor (DBA) systems has led to a better understanding of ET mechanisms and kinetics in nonpolar solvents. Investigations of conformationally restricted linear DBA molecules[83,84,85,86,87] have demonstrated

the distance dependence of bond-mediated coupling. Analogous studies with cleft containing molecules have demonstrated electron tunneling through non-bonded contacts. For C-shaped DBA molecules, in which the D and A units are separated by a solvent-accessible cleft;[88,89,90,91] such coupling appears to be strongest when a single solvent molecule occupies the cleft. The dependence of |V| on the molecular orbital energetics of the solvent molecule involved in the electron tunneling event has been studied using both C-shaped DBA molecules[90] and U-shaped DBA systems, for which a pendant group is fixed inside the cleft.[92,93] The U-shaped systems have been used to tune the electronic coupling from the weak (nonadiabatic) limit to the strong (adiabatic) limit and to examine the important role played by solvent dynamics.[94,95] DBA systems, which demonstrate the influence of macromolecular structural fluctuations on ET rates, have been studied as well.[96,97,98] The studies reported here are distinguished from these earlier studies by examining solvent mediated coupling in water and polar solvents.

While early studies examined through-solvent coupling in frozen media, conformationally restricted DBA systems provide a way to examine solvent mediated ET in fluid media. The use of rigid C-shaped molecules facilitates the study of solvent-mediated electron transfer by limiting the conformational freedom of the D and A moieties. In many rigid DBA systems, the rate of the DBA systems' structural fluctuations that might affect |V| is fast compared to k_{et}; so that an average value for $|V|^2$ can be used to describe the electronic coupling. In a previous study,[91] the shape of a DBA bis-amino acid oligomer was tailored to produce a well-defined cleft with a line-of-sight donor-acceptor distance that was just large enough to accommodate a single water molecule. The observed electron-transfer rate constant in water was significantly higher than in DMSO and was attributed to water molecule(s) in the cleft between the donor and acceptor to mediate the electronic coupling.

This study explores how the photoinduced ET rates of two rigid C-shaped DBA bis-amino acid oligomers are affected by polar solvents. The two compounds have similar donor and acceptor groups but different topologies caused by chiral inversions of two bridge stereocenters. The DBA system D-SSS-A, **1**, forms a molecular cleft with a distance of about 6 Å between the donor and acceptor; whereas the D-RSS-A, **2**, molecule has a more open and flexible cleft (see Figure 2.1 for a molecular structure). These two molecules are similar to the DBA systems reported in a previous study,[91] but they display different cleft properties and redox energetics by variation of the acceptor unit. The bis-amino acid bridge units and electron donor moiety, dimethylaniline (DMA), are unchanged from the earlier study. The acceptor unit is attached to the bridge, via a carboxamide moiety, however a methylacetamide substitution is made at the C-6 of the pyrene in an attempt to shift the reaction energetics and modulate the properties of the cleft. This feature allows the reaction Gibbs energy to be extracted from the kinetic data directly and to examine how cleft site polarity affects the solvent mediated electron transfer.

2.2 EXPERIMENTAL

2.2.1 Synthesis

Compounds **1**, **2**, and **3** were prepared using solid phase peptide chemistry utilizing a 2-chlorotrityl chloride resin similar to that which is described in Chakrabarti et. al.[91] Due to the hydrophilic nature of the compounds, they were liberated from the resin with all protecting

groups intact and purified using HPLC, followed by deprotection and subsequent HPLC purification. The final compounds were assessed for identity and purity using NMR and LCMS techniques. The functional pyrene carboxylic acid used to make compounds **1-4** was synthesized in 5 synthetic steps and isolated from a mixture of regioisomers. The regiochemistry of the isomer was confirmed using 2D-NMR (See Appendix A, Chapter 7.4). All other components used to assemble compounds **1-4** were obtained from commercial sources or have been previously described.[91] Compound **4** was prepared using standard solution phase acylation conditions from the same pyrene precursor. See Appendix A, Chapter 7.1 for more detail on the synthesis and molecule characterization.

Fmoc-Lys(Boc)-OH and Fmoc-Gly-OH were purchased from Novabiochem. O-(7-azabenzo-triazole-1-yl)-N, N,N'N'-tetramethyluronium hexafluorophosphate (HATU) and 2-Chlorotrityl chloride resin were purchased from Genscript. Hexafluoro-2-propanol was purchased from Oakwood. All other reagents were purchased from Sigma Aldrich.

An ISCO CombiFlash Companion was utilized to perform flash chromatography. The cartridges were filled with Bodman 32-63 D grade silica gel. A Waters Xterra MS C18 column (3.5 um packing, 4.6 mm x 100 mm) was utilized with a Hewlett-Packard Series 1200 for HPLC-MS analysis. The solvent system of acetonitrile/water (0.1% formic acid) had a flow rate of 0.8 mL/min. A Waters Xterra column (5um packing, 19 mm X 100 mm) was utilized with the Varian Prostar Prep HPLC system to carry out preparatory scale HPLC purification. The solvent system of acetonitrile/water (0.1% formic acid) had a flow rate of 12 mL/min. A Bruker 500 MHz NMR was utilized to perform NMR experiments. The chemical shifts (δ) reported are relative to the residual solvent peak of the solvent utilized; either DMSO-d_6 or $CDCl_3$.

HRESIQTOFMS (high resolution quadrupole time of flight mass spectrometry) analysis was performed at Ohio State University.

2.2.2 Photophysics

Water used in all experiments was purified by a Barnstead Nanopure system, and its resistance was 18.2 MΩ-cm at 25 °C. Dimethyl sulfoxide (99.9+ %), n-methyl-2-pyrrolidone (99.5 %), chloroform (99.8 %), 3-methyl-1-butanol (98+ %), 1-butanol (99.8 %), 1-propanol (99.7 %), ethanol (99.5 %), methanol (99.8 %), citric acid monohydrate (99.0+ %), and sodium phosphate dibasic (99.95 %) were purchased from Aldrich and used without further purification. Samples of **1**-**3** were readily soluble in DMSO, NMP, methanol, ethanol, and propanol and **4** was readily soluble in chloroform and DMSO. Samples of **1**-**3** were sonicated and heated to 40 °C for two hours to increase solubility in butanol and 3-methyl-1-butanol.

Samples of **1**, **2**, **3**, and **4** were characterized via absorption and steady-state fluorescence spectroscopy. UV-Vis spectra were collected on a model 8453 Agilent spectrometer and fluorescence spectra were collected on a JY-Horiba Fluoromax-3 spectrofluorometer. Fluorescence spectra were collected at various excitation wavelengths, with 0.34 mm slits and a 0.1 s integration time.

Solutions of **1**, **2**, **3**, and **4** were prepared with an optical density of approximately 0.25 at the absorption peak maximum. All of the solutions, aside from the aqueous solutions, were prepared with molecular sieves in the cuvette. Each solution was freeze-pump-thawed a minimum of three times. The samples were back-filled with argon to reduce evaporation at the higher experimental

temperatures and kept moderately above atmosphere by a balloon filled with argon. A temperature cell was constructed from aluminum and controlled using a NESLAB RTE-110 chiller.

Time resolved fluorescence measurements of **1**, **2**, **3**, and **4** were measured using the time correlated single photon counting (TSCPC) technique with a PicoHarp 300 TCSPC module (PicoQuant GmbH).[99] The samples were excited at 375 nm using a picosecond diode laser (PiL037) at a 1 MHz repetition rate. All measurements were made at the magic angle polarization geometry. The data were collected until a maximum count of 20,000 was observed at the peak channel. The instrument response function was measured using colloidal $BaSO_4$, in every case the instrument response function had a full-width-at-half-maximum of ≤96 ps. Emission from the samples was collected on the red side of the emission maximum. The decay curves were fit to a distribution of lifetimes by a convolution and compare method using Edinburgh Instruments fluorescence analysis software technology (FAST).[100]

2.3 RESULTS

2.3.1 Photophysical Model

The donor-bridge-acceptor oligomers in this study form an intramolecular exciplex in polar solvents. The formation of this exciplex is described by a photophysical model that involves a

locally excited state and a charge separated state. This model is used to analyze the kinetics and calculate an electron transfer rate.

Figure 2.1 depicts the steady state emission spectra of **1**, **2**, and **3**. Clearly, the spectra of **1** and **2** display a second red-shifted emission that becomes more prominent as the excitation shifts to the red; whereas compound **3** does not. Because **1** and **2** both have the donor (dimethylaniline, DMA) present, but **3** does not; the second red-shifted emission is assigned to the formation of a charge separated state (intramolecular exciplex). While the absorbance spectra of **1**-**3** appear to be the same on the red edge, the excitation spectra show a weak tail on the red edge of the excitation, when the emission is monitored at 525 nm, as compared to 450 nm. Figure 7.1 depicts these two excitation spectra for a solution of **1** in pH 7 buffer. When exciting at 375 nm (wavelength used in the kinetic studies) the emission from the 'red' species is a small fraction of that observed from the locally excited state; nonetheless both emissions are accounted for in the analysis.

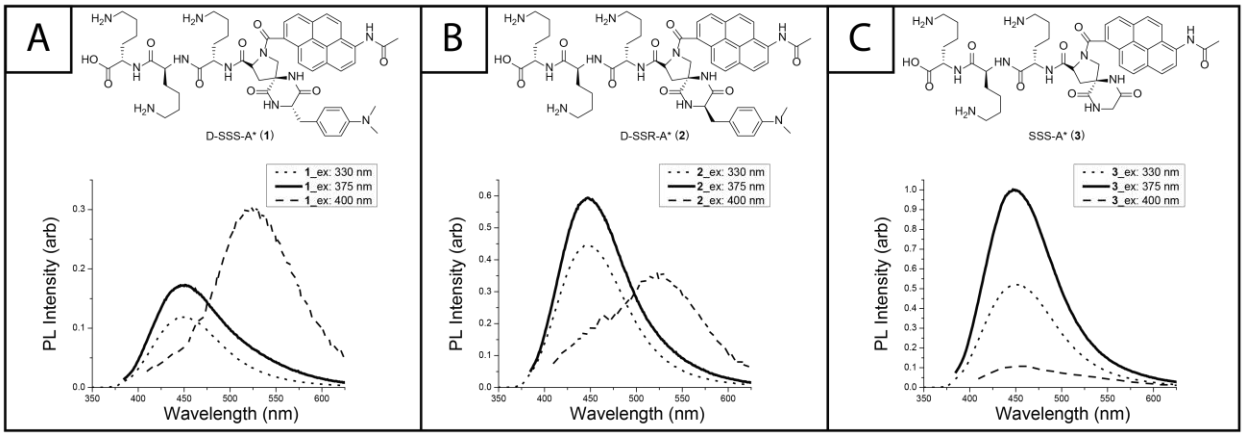

*Figure 2.1 - The figure shows photoluminescence (PL) spectra for aqueous solutions of **1** (A), **2** (B), and **3** (C) at excitation wavelengths of 330 nm (dotted), 375 nm (solid), and 400 nm (dashed). Molecular structures for **1**, **2**, and **3** are shown in the upper portion of each panel. The spectra have been OD corrected and the emission intensity has been scaled for convenience; note that the relative magnitudes of the emission intensity between the panels are accurately reflected by the intensity scale.*

In an effort to confirm exciplex formation, studies were performed to examine the lower energy emission peaks observed in **1** and **2** and rule out excimer formation. Pyrene is known to readily form excimers in solution when the concentration of pyrene is high enough.[101,102] Thus, to confirm or exclude excimer formation, **1** and **3** in pH 7 buffer were monitored over a concentration range of 2.3×10^{-5} M to 2.2×10^{-6} M (see Figure 7.2). The shape of both the absorbance and emission spectra of **3** did not change with concentration and no red-shifted emission was observed, even in the most concentrated sample of **3**. In contrast, sample **1** displayed a red-shifted emission over the entire concentration range. The intensity of this red-shifted emission did not increase in intensity, nor in proportion to that of the blue (pyrene monomer) emission, at higher concentrations. These data indicate that the red-shifted emission arises from an intramolecular process and is not associated with excimer formation or solute aggregation.

In order to explore whether the red-shifted emission is consistent with charge transfer interactions between the pyrene (acceptor) unit's excited state and the dimethylaniline (DMA) unit (donor), DMA was added to solutions of **3** and to solutions of the N-(6-(pyrrolidine-1-carbonyl)pyren-1-yl)acetamide, denoted **4** (see Figure 7.3 for the molecular structure). If the charge transfer interaction between the DMA and the pyrene excited state is strong enough, then an intermolecular exciplex can be formed at high enough DMA concentrations.[103,104,105,106] Literature suggests that an exciplex should form when the DMA and pyrene, or similar systems, are in close proximity to one another (approximately between 3 and 8 Å).[107,108,109,110,111] For deoxygenated solutions of **4** in chloroform (5.6×10^{-6} M) an exciplex emission is clearly evident for DMA concentrations in excess of 2.6×10^{-4} M (Figure 7.4). In contrast, DMSO solutions of **4** yielded no resolvable red emission, presumably because the stabilized exciplex is able to

dissociate into a solvent separated ion pair, thus quenching the exciplex emission. Note that the excitation spectra for the monomer emission and the exciplex emission are similar, indicating that any ground state association of the pyrene and DMA (Figure 7.1) is weak. These data support the assignment of the red-shifted emission in compounds **1** and **2** to the formation of a charge separated state (or intramolecular exciplex); the red tail observed in the excitation spectrum, monitored at 525 nm, suggests that a small percentage of the solution's ensemble of DMA/pyrene conformations may exist in an 'exciplex-like' geometry.

Another feature that supports the formation of a charge separated state is the red shift of the emission peak position (Figure 2.2A) with solvent polarity.[110] Donor-acceptor systems were studied in a series of alcohols, and Figure 2.2B shows a Lippert-Mataga plot made from these data, namely a plot of the solvatochromic spectral shift, $\Delta\nu$, versus the Pekar factor Δf.[106,112] Δf provides a measure of the solvent polarity and is defined by Equation 2.2 [112]

$$\Delta f = \frac{\varepsilon - 1}{2\varepsilon + 1} - \frac{n^2 - 1}{2n^2 + 1} \qquad \text{Equation 2.2}$$

where ε is the static dielectric constant and n is the refractive index of the solvent. The plot reveals a roughly linear correlation between the spectral shift and the solvent polarity.[112,113,114] The Lippert-Mataga slope can be used to calculate the dipole moment of the donor acceptor system assuming that there is a sphere encompassing the donor and acceptor moieties. If one assumes a 9.2 Å and 8.5 Å radius spherical cavity for **1** and **2** respectively,[115] then the slopes of 19100 cm^{-1} and 37000 cm^{-1} from this plot give an effective dipole moment of 38 D for **1** and 43 D for **2**. This approximation is not always accurate; however the differences between the

encompassing ellipsoid and sphere are moderate for **1** and **2** (See Appendix A, Chapter 7.7); *vide infra*.

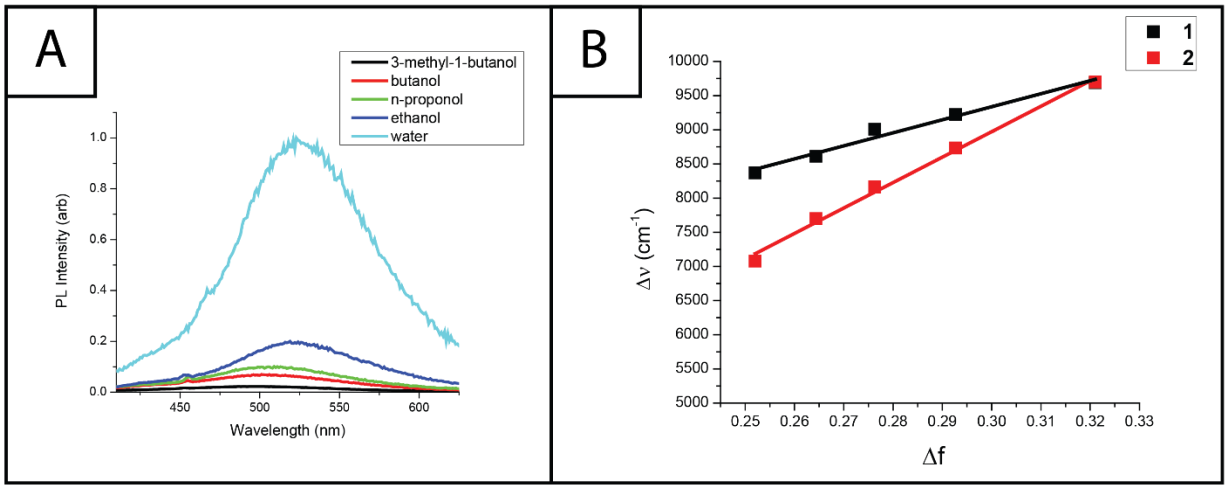

*Figure 2.2 - Panel A shows emission spectra (optical density corrected) of **1** in a variety of different solvents - 3-methyl-1-butanol (black), butanol (red), propanol (green), ethanol (blue), and pH 7 buffer (cyan). In panel B a Lippert-Mataga plot is shown for **1** and **2** in a series of normal alcohols. An analysis of the correlation between solvent polarity and the emission band red-shift is consistent with a 38 D dipole moment for **1** and a 43 D dipole moment for **2**; see text for details.*

The red-edge emission from **1** is consistent with the formation of an intramolecular exciplex. The featureless charge transfer band is red-shifted from the pyrene locally excited (LE) state's emission. The intensity and existence of the charge transfer emission relative to the LE state emission is dependent on the presence and concentration of donor (dimethylaniline) when the donor and acceptor are free in solution. When the donor and acceptor are attached as in **1** or **2**, the charge transfer emission is not enhanced relative to the LE state emission by increasing the concentration, which indicates that the charge transfer emission results from intramolecular donor-acceptor interactions. Furthermore, the second emission red-shifts (charge separated state becomes more stable) with solvent polarity.

Interestingly, the charge transfer emission peak of **1** is most prominent in water (Figure 2.2A). In a traditional exciplex reaction scheme, the excited state complex, or contact ion pair, is stabilized as the solvent polarity increases; [112,113,116,117] and it eventually dissociates. For the intramolecular case ion pair dissociation does not occur; rather, the molecule can undergo back electron transfer to the locally excited state or it can relax back to the ground electronic state by either radiative or nonradiative relaxation (Figure 2.3). The charge separated (CS) state is stabilized by solvent polarity (ie., the emission redshifts with increasing solvent polarity). As the CS state energy becomes lower in energy than the locally excited (LE) state, the probability of back electron transfer to the LE state decreases. Thus, stabilization of the CS state relative to the LE state can increase the CS state's quantum yield of emission because the back electron transfer to the LE state is slower; however, the stabilization of the CS state decreases the energy gap to the ground electronic state and increases the internal conversion rate. The balance of these competing effects determines the polarity at which the CS state's emission will be the strongest. The kinetic scheme shown in Figure 2.3 is consistent with the spectral data and can be used to rationalize the excited state photophysics; below it is used to extract rate constants from the excited state decay law.

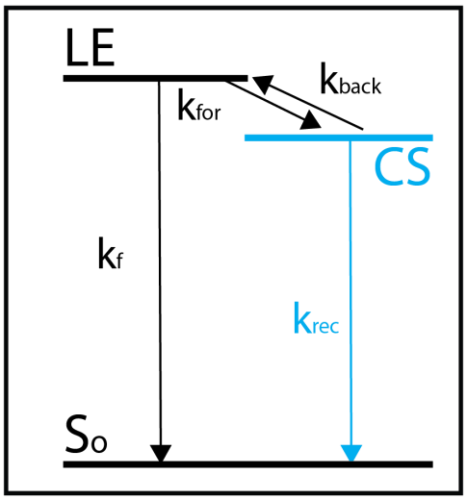

Figure 2.3 - The diagram depicts the kinetic scheme for the intramolecular exciplex, charge separated state (CS), formation.

2.3.2 Kinetic Analysis

The time-correlated single photon counting method was used to measure the fluorescence intensity decay of molecules **1**, **2**, and **3** in aqueous buffer at pH=7, dimethylsulfoxide (DMSO), and N-methylpyrrolidone (NMP). All samples were excited by 375-nm radiation. Fluorescence decay profiles were fit using the discrete component analysis, and the distribution of lifetime algorithms provided by the Edinburgh Instruments FAST™ software package. Fluorescence decay profiles of **1** and **2**, which were collected at the steady-state LE fluorescence emission maximum, produced discrete exponential fits of three or more distinct components, and lifetime distributions with complex shape. This behavior has been attributed to interactions arising from the bridge pendant groups that are added for solubility purposes (see Appendix A, Chapter 7.6). When the observed fluorescence emission band was red-shifted from the LE emission maximum towards the CS emission, the lifetime distributions displayed a bimodal character and a discrete component analysis consisting of two exponential terms could be used. In addition, single mode

lifetime distributions were observed for the bridge-acceptor only compound, **3**. For these reasons the observation window was chosen to be 525 nm.

The kinetic scheme proposed in (Figure 2.3) assumes that the photo-excitation of the modified pyrene carboxamide acceptor populates the LE state, the initial population of the CS state is zero, and the observed fluorescence signal arises from a combination of LE → S_0 and CS → S_0 radiative emission. In this scheme k_{for} is the forward electron-transfer rate constant, k_{back} is the backward or reverse electron transfer rate constant, and k_{rec} is the rate constant for recombination from the CS state to the ground electronic state. The difference between the assumptions of this model and of the model reported in previous works[88,89,90] is the observation of fluorescence originating from two states (see Chapter 7.0). Solving the differential equations for this kinetic model, a decay law with a double exponential form is obtained.

$$I(t) = I(0) \cdot [a_+ \, exp\,(-k_+ t) \; + \; (1 - a_+) \, exp(-k_- t)] \qquad \text{Equation 2.3}$$

where a_+ is the fraction of fluorescence decaying with the fast rate constant k_+ , k_- is the rate constant of the slow fluorescence decay, α is the fraction of fluorescence arising from LE → S_0 emission, and β is the fraction from the CS → S_0. The parameters in this decay law can be used to obtain the primary rate constants

$$k_{for} = \left(a_+(k_+ - k_-) + k_- - k_f\right)\left[\frac{\alpha}{\alpha - \beta}\right] \qquad \text{Equation 2.4}$$

$$k_{back} = \frac{(k_+ - k_-)^2 - \left[2 \cdot \left(k_{for} + k_f\right) - (k_+ + k_-)\right]^2}{4k_{for}}$$ Equation 2.5

and

$$k_{rec} = k_+ + k_- - k_f - k_{for} - k_{back}$$ Equation 2.6

The intrinsic fluorescence decay rate k_f is the decay rate given by the control molecule, the bridge-acceptor compound **3**, for which the electron transfer pathway is not possible.

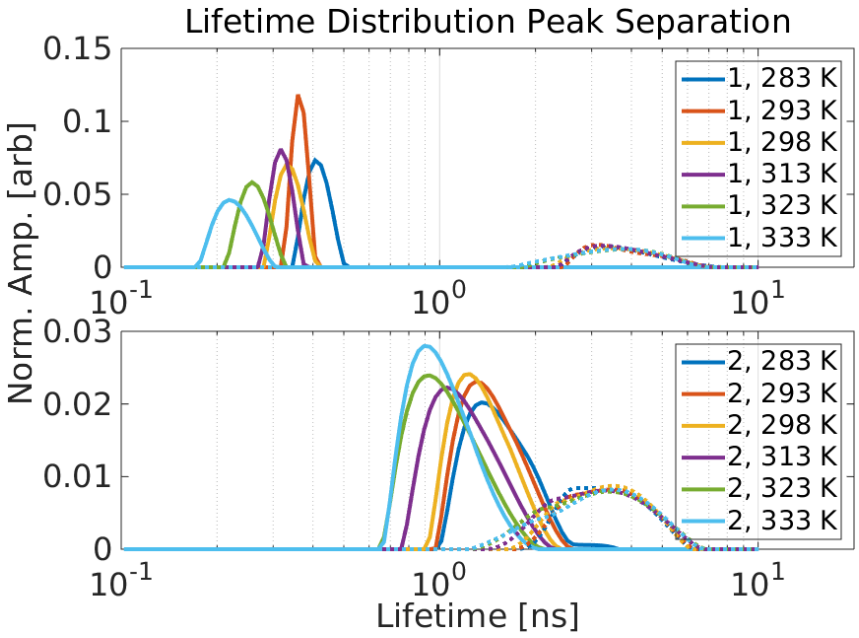

*Figure 2.4 - The top panel shows the lifetime distribution for **1** in pH=7 buffer, and the bottom panel shows the lifetime distribution for **2** in pH=7 buffer. In each case the lifetime distributions could be separated into short-time (solid lines) and long-time (dashed lines) components.*

In order to relate the predicted decay law to the observed lifetime distributions, a distribution fitting protocol was developed. This protocol splits a bimodal distribution into a short-time

distribution and a long-time distribution, and it calculates the distribution statistics used to parametrize the predicted decay law. Two kinds of bimodal distributions were observed for the data (see Figure 2.4). In the first kind, the short-time and long-time distributions are clearly separated. The well separated short-time distributions typically demonstrate a constant positive slope from its onset to 90% of the maximum amplitude value, and a segment of constant negative slope after the maximum amplitude followed by an exponentially decreasing segment. Well separated distributions were observed for molecule **1** at temperatures below 333 K. In the second kind of distribution, the short-time and long-time distribution components overlap with each other. Here the two segments of constant slope near the amplitude maximum were used to isolate the short-time and long-time distributions. After separation of the two distribution components, normalized distribution amplitudes were used to weight the sampling of each distribution. Short and long time distributions were sampled 1000 times and the 25th, 50th, and 75th percentiles were calculated. The 50th percentile value of the short and long time distributions were used to determine k+ and k-, respectively, see Figure 2.5.

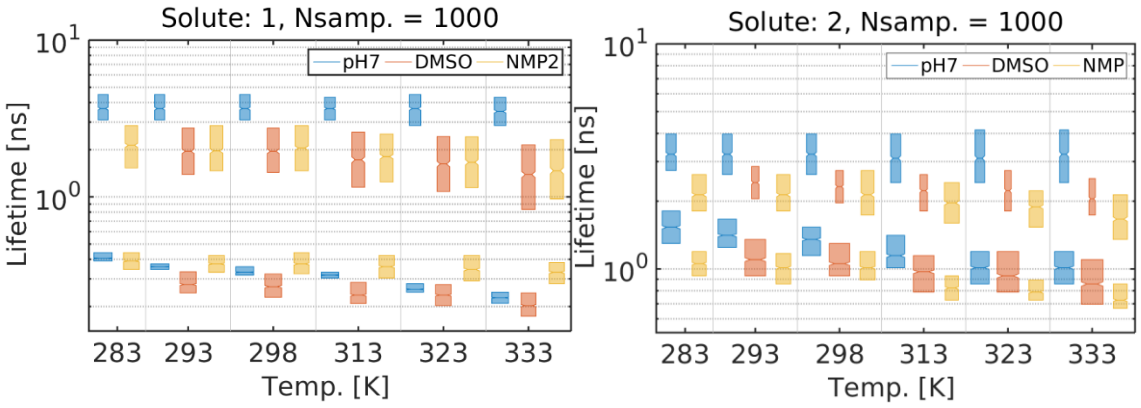

*Figure 2.5 - This figure shows a box plot representation for separation of the fluorescence decay lifetime distribution into short-time and long-time components. The left panel shows the lifetime distribution for **1**, and the right panel shows the lifetime distribution for **2**. The central line of each box represents the median value. Edges of the boxes represent the 25th and 75th percentiles.*

The temperature dependence of the forward and backward electron transfer rate constants are shown in Figure 2.6. Because of the double exponential character of the excited state decay law, it is possible to determine the reaction Gibbs energy directly from the rate constants as described in Equation 2.7; see Table 2.1. The free energy of the LE → CS reaction, $\Delta_r G$, is given by

$$\Delta_r G = -\mathrm{RT} \ln\left(\frac{k_{for}}{k_{back}}\right) \qquad \text{Equation 2.7}$$

Figure 7.5 plots the reaction free energy as a function of temperature and shows that the dependence on temperature is very weak. In fact, the free energies observed over the temperature range in each solvent are smaller than the spread in the k_+ and k_- caused by the inherent width of the lifetime distributions. In Table 2.1, $\Delta_r G$ values for each solvent are reported at T = 298 K.

*Table 2.1 - Reaction free energy $\Delta_r G$ for the DBA oligomers **1** and **2** in different solvents, in eV*

Solvent	ε_s	n^2	$\Delta_r G$ of **1**	$\Delta_r G$ of **2**
Water (pH7)	*80.1*	*1.77*	*-0.013*	*-0.023*
DMSO	*46.7*	*2.19*	*-0.012*	*-0.036*
NMP	*32.3*	*2.16*	*-0.0082*	*-0.021*

DMSO is dimethylsulfoxide and NMP is N-methylpropionamide

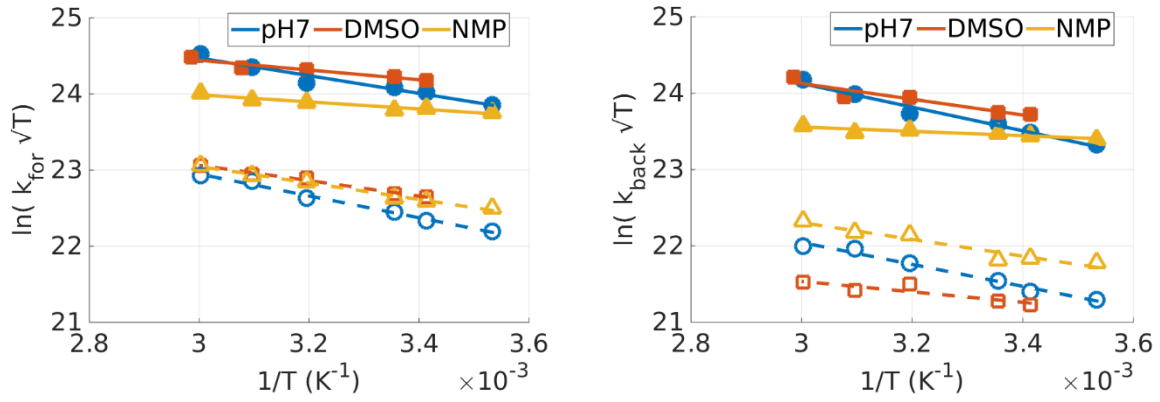

*Figure 2.6 - The temperature dependence of the forward (left panel and back (right panel) electron transfer rate constant of **1**, DsssA, (filled symbols) and **2**, DsrrA, (open symbols) are shown.*

2.3.3 Electron Transfer Rate Analysis

The electron transfer rate constant analysis used a semi-classical version of the Marcus expression.[90,118,119,120,121] For a single effective quantum mode, the rate constant k_{ET} can be written as

$$k_{ET} = \frac{2\pi}{\hbar}|V|^2 \frac{1}{\sqrt{4\pi\lambda_s k_B T}} \sum_{n=0}^{\infty} e^{-S}\left(\frac{S^n}{n!}\right) \exp\left(-\frac{(\lambda_s + \Delta_r G + nh\nu)^2}{4\lambda_s k_B T}\right) \qquad \text{Equation 2.8}$$

where k_B is the Boltzmann's constant, $|V|$is the electronic coupling matrix element, $\Delta_r G$ is the reaction free-energy, λ_s is the outer-sphere or solvent reorganization energy, ν is the frequency of the effective quantized vibrational mode, and S is the Huang-Rhys factor given as the ratio of the inner-sphere reorganization energy, λ_v, to the quantized mode energy spacing, $\frac{\lambda_v}{h\nu}$. The $h\nu$ term refers to the energy of a single effective quantized mode associated with the electron transfer reaction; it is specific to the solute vibrational manifold and is not very sensitive to solvent and temperature. Thus, $h\nu$ and λ_v are fixed at values appropriate for the donor and acceptor, and they are not changed as the bridge, solvent, and temperature change.

The lines of best fit in Figure 2.6 represent fits to the semi-classical electron-transfer rate equation (Equation 2.8). The data reveal that the forward (and backward) electron transfer rate for **1** in the three solvents are significantly higher than that of **2** in the same three solvents. Given that **1** and **2** have the same donor and acceptor units and the two bridges are diastereomers of one another, the difference in the electron transfer rate occurs because of the different spatial positioning of the donor and acceptor with respect to each other. In this analysis, 1400 cm^{-1} was used as the value for the single effective quantized mode and 0.30 eV for the inner-sphere reorganization energy. These values are the same as those used in previous work on donor-bridge-acceptor systems having the same donor and a similar acceptor group; note that this frequency value is typical of that for carbon-carbon stretching frequencies in aromatic ring systems.[91,118,122] While roughly the same values for $h\nu$ and $\lambda_v$were assumed as in Chakrabarti, et. al.,[91] these values may have some variation because the pyrene moiety was modified in this set of experiments. Although an error in the internal reorganization energy affects the absolute magnitude of the electronic coupling that is extracted from fits to the semiclassical equation (Equation 2.8), the relative values of the coupling for the same solute in different solvents is not

sensitive to the choice of internal reorganization energy.[122] Note that the redox potential of the pyrene is changed by the amide modification, and it is expected to decrease the reduction potential of pyrene.[123,124]

The slopes of the plots in Figure 2.6 are largely determined by the Gibbs reaction energy and the reorganization energy for the electron transfer, whereas the intercepts depend largely on the electronic coupling. If one considers only the first term (n=0) in Equation 2.8, the classical Marcus expression is obtained and the activation Gibbs energy may be obtained directly from the slope of the graph. The solvent reorganization (λ_s,empirical) and the electronic coupling ($|V|$, empirical) that are obtained from best fits of Equation 2.8 to the data are reported in Table 2.2, along with the activation Gibbs energy that is extracted from the slope. Note that the electronic coupling values which are obtained by fits of the data to Equation 2.8 are weakly dependent on λ_S; see Figure 7.6-Figure 7.12 in Appendix A.

*Table 2.2 - The activation Gibbs energy ($\Delta G^{\ddagger}$), solvent reorganization energy (λ_s), and electronic coupling ($|V|$) of **1** and **2** in different solvents at 298 K.*

Sample	$\Delta G^{\ddagger}$ **(eV)** classical limit	λ_s **(eV)** empirical	λ_s **(eV)** ellipsoid model	$\|V\|$ **(cm^{-1})** empirical	$\|V\|$ **(cm^{-1})** ellipsoidal model
1 pH 7	0.10	0.42	0.42	32 ± 8	34
1 DMSO	0.05	0.23	0.23	12 ± 2	9
1 NMP	0.04	0.16	0.16	7 ± 1	5
2 pH 7	0.12	0.52	0.53	22 ± 7	26
2 DMSO	0.09	0.40	0.40	12 ± 3	8
2 NMP	0.09	0.40	0.40	13 ± 3	8

*** Note that the reaction Gibbs energies are reported in Table 2.1.*

To assess better the trends observed in the reorganization energy and electronic coupling parameters, the data were analyzed in the framework of a continuum dielectric model. The reorganization energy λ_S was modeled by treating the change in the DBA molecule's electrostatic charge distribution by a dipole moment within a symmetric ellipsoidal cavity; namely

$$\lambda_S = \frac{\Delta\mu^2}{2cb^2}\left(\frac{1}{n^2} - \frac{1}{\varepsilon_S}\right)\sum_{n=1}^{n=\infty} X_n = \frac{\Delta\mu^2}{2cb^2}\left(\frac{1}{n^2} - \frac{1}{\varepsilon_S}\right)\Sigma \qquad \text{Equation 2.9}$$

in which c and b are the ellipsoid's radii and $\sum$ is a shape factor that can be evaluated numerically. In order to parametrize this model, the semiempirical molecular orbital package MOPAC2012 was used to study the molecular structures of **1** and **2**. Using the PM7 Hamiltonian, optimized molecular geometries and molecular orbitals were determine for cases in which DBA molecule clefts contained 0, 1, or 2 solvent molecules. The results of these calculations were visualized and analyzed using the three-dimensional chemical structures package Jmol.[125,126,127] Prolate spheroids approximately circumscribing the solvent excluded surface of the optimized solvent-DBA systems (see Figure 7.21 to Figure 7.27) were used to determine the ellipsoidal radii. Assuming a full charge moves from the donor to the acceptor; the calculated distances between the nitrogen atom of the donor moiety and the carbon atoms of the pyrene ring were used to obtained $\Delta\mu$.

Table 2.3 - Parameters for the CS state dipole moment and solute-solvent complex geometries

Solvent	**Solute**	r_{sphere} (Å)	c (Å)	a (Å)	V_{sphere} (Å^3)	$V_{spheriod}$ (Å^3)	**Σ (scale)**	μ (D)	μ_{min} (D)
H_2O	**1**	9.2	10.0	7.0	3263	2053	0.86	30.9	28.5
NMP	**1**	9.0	9.5	7.1	3054	2006	1.20	35.1	31.5
DMSO	**1**	9.5	9.5	8.1	3591	2611	1.14	42.1	38.2
H_2O*	**2**	8.0	8.7	8.7	2145	1786	0.91	33.5	24.7
H_2O	**2**	8.5	9.0	9.0	2572	2235	0.95	39.5	30.5
NMP	**2**	8.5	9.5	9.5	2572	2421	0.95	41.1	34.0
DMSO	**2**	8.5	9.3	9.5	2572	2619	0.98	43.5	35.8

*** indicated the lowest energy configuration of 2 with two H_2O molecules.**

The solvent reorganization energy was calculated using the dipole moments given in Table 2.3, however the ellipsoid's volume was adjusted to give a good fit with the data; see Figure 2.6. The dipole moments (μ) were calculated using the average distance between the donor ring nitrogen and the acceptor ring carbons, and the μ_{min} were calculated in a similar manner using the minimum distance. Note that the change in the dipole moment through the solvent series correlates with the size of the molecule in the cleft. The dipole moments calculated using the spheroid model (Table 2.3) closely mimic the dipole moments that were calculated using the Lippert-Mataga plot (Figure 2.2), which approximate the molecular cleft by an effective sphere of radius r_{sphere} ($V_{sphere} = \frac{4}{3}\pi r_{sphere}^{\ 3}$). By keeping the ellipsoid shape fixed (namely the shape factor Σ) but adjusting its volume ($V_{spheriod} = \frac{4}{3}\pi ca^{\ 2}$), to fit the experimental data in Figure 2.6, the solvent reorganization energies reported in Table 2.2 (as λ_s, ellipsoidal model) were obtained. Using these reorganization energies, one finds the electronic coupling parameters reported as |V|, ellipsoidal model in Table 2.2. These values are in reasonable agreement with those found by an empirical fit of the data in which the reorganization is varied as a free parameter.

Note that the scaling factor Σ for **1** in water is quite different from the scaling factor for solute **1** in the other solvents (NMP and DMSO) and the "loose-cleft" forming systems, **2**, in all solvents. Water has the most interaction with the cleft, as suggested by the electron transfer data. The solvent water facilitates electron transfer most efficiently in DBA solute **1**, as indicated by the large coupling parameter (see Table 2.2). Because water has the most interaction with the cleft, particularly in **1**, the scaling factor is less predictable. In system **2** multiple waters can fit into the cleft, thus an individual water molecule does not have as significant interaction with the cleft.

2.4 DISCUSSION

These studies build on the earlier work of Chakrabarti et. al.[91] by investigating an amide substituted acceptor unit which can interact favorably with a hydrogen bonding solvent. The donor unit used in both systems is the same. Although amide modification has a small effect on the overall molecular volume, the cleft size changes somewhat with the solvent type, *vide infra*. In addition, amide modification causes a red-shift in the absorption spectrum, decreases the excited stated lifetime, and alters the energetics of the electron transfer reaction. In particular, the $\Delta_r G$ for the amide modified pyrene system is significantly smaller than that of the unmodified pyrene system. This decrease in the $\Delta_r G$ facilitates the equilibrium between the locally excited state and the charge separated state and allows for a significant charge transfer emission to be

observed; in contrast to the unsubstituted case of Chakrabarti et. al. for which no charge transfer emission could be seen.

The time resolved fluorescence of **1** and **2** was collected at the red edge of the emission spectrum because it displayed a double exponential decay law. The decay law at more blue emission wavelengths had a third component, which was traced to a direct interaction between the solubilizing lysine groups on the bridge and the acceptor (see Appendix A). The red edge emission arises from both the locally excited state and the charge separated state; however this could be modeled quantitatively in the kinetic scheme for the reaction. This kinetic scheme, shown in Figure 2.3, was used to extract the $\Delta_r G$ for the reaction directly from the kinetic data.

The $\Delta_r G$ values for **1** and **2** are significantly different from the $\Delta_r G$ that were used to model the electron transfer for the corresponding donor-bridge structure and unsubstituted pyrene acceptor, which were reported to be -0.66 eV and -0.54 eV in water.[91] Most of the shift in the $\Delta_r G$ arises from the amide functionality that has been added to the pyrene. This fact was confirmed by performing ultraviolet photoelectron spectra (UPS) of the bridge-acceptor molecules (see Figure 7.14), and it is supported by literature data on similar systems.[123,124] The $\Delta_r G$ for **1** and **2** are the same within experimental error; in contrast the 'tight' and 'loose' cleft molecules reported on by Chakrabarti[91] differed by 0.1 eV. These facts support a view that the amide modification changes both the intrinsic reduction potential of the acceptor and the solvation of the acceptor, as compared to the unsubstituted pyrene system. The amide substitution may open the cleft and reduce the hydrophobic interaction between the donor and acceptor; potentially, allowing it to incorporate multiple solvent molecules.

This view of the cleft is consistent with the difference in solvent reorganization energy found for this system as compared to that reported by Chakrabarti[91] for the unsubstituted case. In the

unsubstituted case, the π-π and hydrophobic interactions control the solvation environment of the cleft, so that a large solvent reorganization occurs upon formation of the charge separated state. For DBA systems **1** and **2** the cleft environment is already somewhat polar. Note that the reaction Gibbs energy and reorganization parameters in the semi-classical equation are highly coupled, and Chakrabarti[91] was unable to experimentally determine $\Delta_r G$ in the donor-bridge-acceptor system; hence the absolute difference in the reorganization energies should not be interpreted too strictly.

In order to examine the features of the molecular cleft more quantitatively, quantum chemistry (PM7) simulations of **1** and **2** with solvent were performed. These calculations showed that the cleft in **1** and **2** was able to adapt to the size of the solvent molecules studied (water, DMSO, and NMP). For the case of DMSO and NMP (see Appendix A) only one solvent molecule was able to fit in the cleft of **2**, and similarly only one solvent molecule could fit in the cleft of **1**. The contact surfaces and the donor to acceptor distances for these cleft/solvent systems were similar, and this finding is compatible with the similar reorganization energies and electronic couplings reported for these systems.

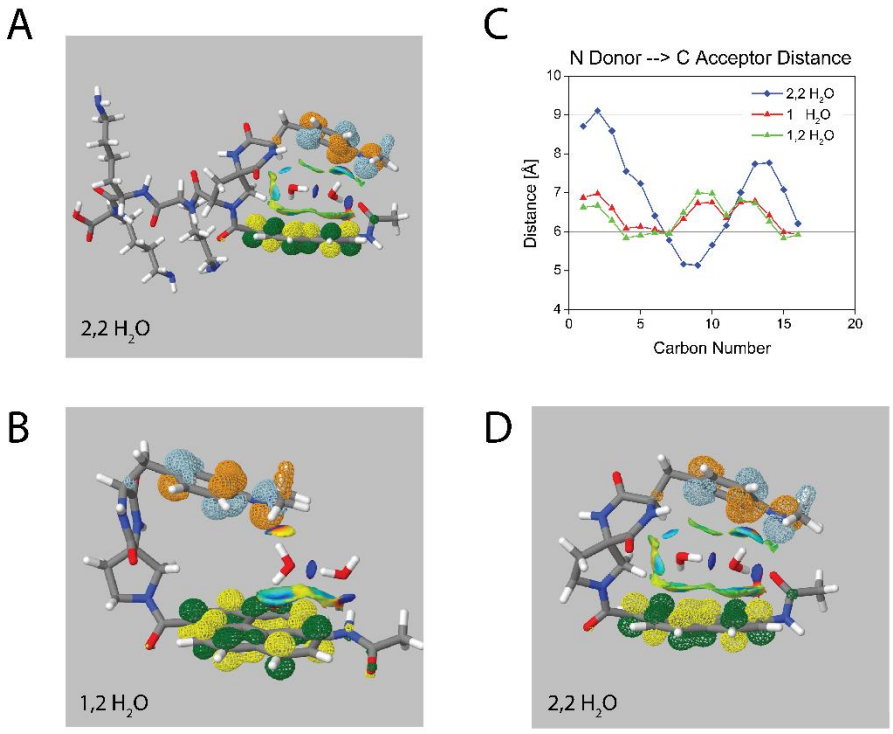

Figure 2.7 - Frontier HOMO(orange/grey) and LUMO(yellow/green) molecular orbitals are shown for the two DBA molecules with water. In panel A the entire DBA structure is displayed. Panel C shows a plot of the distance between the nitrogen atom of the donor and the carbon atoms of the pyrene ring at the optimized geometry. In the expanded view in panels (B) and (D), the lysine moieties have been removed to facilitate observation of the DBA cleft region. The interaction surface of the solvent molecules is shown, as well.

Simulations of **1** and **2** with water solvent were performed for both one and two solvent molecules in the cleft (see Figure 2.7 and Appendix A). For both solutes the cleft could accommodate one water molecule; however the loose cleft (**2**) had a better van der Waals contact with two water molecules present than with one. Figure 2.7B shows the energy minimum for two water molecules in the cleft of **2** and Figure 2.7D shows the energy minimum for two water molecules in the cleft of **1**. The tight cleft does not let the water molecules fill it, whereas the loose cleft does. Figure 2.7C shows plots of the distance between the donor N atom and the different C atoms of the pyrene acceptor for the tight cleft (**1**) with one and two water molecules and the loose cleft (**2**) with two water molecules; note that the loose cleft with one water

molecule had no clear energetic minimum. Note that the tight cleft's distances change only slightly in accommodating more than one water molecule, and that these distances range from 6 to 7 Å depending on ring location. In contrast the loose cleft shows a broader range of distances (5 to 9 Å) and it has some regions of the ring closer to the donor N. These data underscore the different cleft geometries, yet are consistent with the similar electronic couplings that are found for water. Namely, the electron tunneling is controlled by distance and although the loose cleft has a small area of the acceptor placed closer to the donor, most of it is farther from the donor than the distances for the tight cleft. The calculations show that the contact interaction with the solvent controls the donor to acceptor distance. Although **2** has a few 5Å contact interactions, its average contact distance is 7 Å; whereas molecule **1** has an average of 6.4 Å. The net result appears to be a similar coupling for the two cases.

If the electron transfer occurs through solvent then this means that the electronic coupling is mediated by the solvent in the cleft. Because the donor to acceptor spacing of **1** and **2** is smaller with the water solvent than it is with the DMSO and NMP solvents, one expects that the electronic coupling would be higher for the case of water than the other cases, in agreement with the fits to the data; see Table 2.2. NMP and DMSO both facilitate electron transfer, however the rate constant is smaller because the donor to acceptor distance is larger and hence it has a smaller electronic coupling. Because the cleft spacings are similar for **1** and **2** with DMSO and NMP, the electronic couplings are found to be similar. Thus, the ability of the cleft to accommodate different sizes and numbers of solvent molecules gives rise to a behavior that is more rich than that found for the strictly hydrophobic donor-acceptor system reported by Chakrabarti.[91]

2.5 CONCLUSION

The amide substitution on the pyrene in the donor-bridge-acceptor system changes both the reaction Gibbs energy for the photoinduced electron transfer and the hydrophilicity of the molecular cleft. The less negative $\Delta_r G$ allows one to observe the charge separated emission, under appropriate solvent conditions as compared to the system reported earlier for the unsubstituted pyrene. The increased hydrophilicity of the cleft impacts its ability to accommodate solvent and change the interaction between the donor (DMA) and acceptor (pyrene). As with the earlier study for the unsubstituted pyrene acceptor, in which water was able to lodge in the cleft and mediate the electron tunneling, the amide substituted pyrene forms a cleft that can accommodate water molecules. In contrast to the earlier study, the cleft for **1** and **2** appears to be able to accommodate larger solvent molecules (and multiple water molecules). This feature suggests that substitution of the pyrene ring might be used to tune the cleft's solvation characteristics and the size of the tunneling gap.

2.6 ACKNOWLEDGEMENT

DHW acknowledges support from the US National Science Foundation via CHE-0718755 and DMR-1412030. CS acknowledges support from the National Science Foundation under Grant No. 1300231 and the NIH/NIGMS GM067866.

2.7 REFERENCES

82 Jortner J; Bixon, M. Electron Transfer-From Isolated Molecules to Biomolecules, Part 1 and Part 2; John Wiley & Sons, Inc. New York, 1999.

83 Paddon-Row, MN Orbital Interactions and Long-Range Electron Transfer. *Adv. Phys Org. Chem.*, 2003, *38*, 1-85.

84 Gilbert M, Albinsson B. Photoinduced Charge and Energy Transfer in Molecular Wires. *Chem. Soc. Rev.*, 2015, *44*, 845-886.

85 Natali M., Campagna S., Scabndola, F. Photoinduced Electron Transfer Across Molecular Bridges: Electron-and Hole-Transfer Superexchange Pathways. *Chem. Soc. Rev.*, 2014, *43*, 4005-4018.

86 Weiss, E.A., Wasielewski, M. R., Ratner, M.A. Molecules as Wires: Molecule-Assisted Movement of Charge and Energy. *Top. Curr. Chem*., 2005, *257*, 103-133.

87 Gu, Y.; Kumar, K.; Lin, Z.; Read, I.; Zimmt, M. B.; Waldeck, D. H. Studies into the Character of Electronic Coupling in Electron Transfer Reactions. *J. Photochem. Photobio. A: Chem.*, 1997, *105*, 189 - 196.

88 Read, I.; Napper, A.; Kaplan, R.; Zimmt, M. B.; Waldeck, D. H. Solvent-Mediated Electronic Coupling: The Role of Solvent Placement. *J. Am. Chem. Soc.*, 1999, *121*, 10976-10986.

89 Nadeau, J. M.; Liu, M.; Waldeck, D. H. and Zimmt, M. B. Hole Transfer in a C-Shaped Molecule: Conformational Freedom Versus Solvent-Mediated Coupling. *J. Am. Chem. Soc.*, 2003, *125*, 15964-15973.

90 Zimmt, M. B. and Waldeck, D. H. Exposing Solvent's Roles in Electron Transfer Reactions: Tunneling Pathway and Solvation. *J. Phys. Chem. A*, 2003, *107*, 3580-3597.

91 Chakrabarti, S.; Parker, M. F. L.; Morgan, C. W.; Schafmeister, C. E.; Waldeck, D. H. Experimental Evidence for Water Mediated Electron Transfer Through Bis-Amino Acid Donor- Bridge- Acceptor Oligomers. *J. Am. Chem. Soc.*, 2009, *131*, 2044-2045.

92 Napper, A. M.; Head, N. J.; Oliver, A. M.; Shephard, M. J.; Paddon-Row, M. N.; Read, I.; Waldeck, D. H. Use of U-shaped Donor-Bridge-Acceptor Molecules to Study Electron Tunneling Through Nonbonded Contacts. *J. Am. Chem. Soc.*, 2002, *124*, 10171-10181.

93 Chakrabarti, S.; Liu, M.; Waldeck, D. H.; Oliver, A. M.; Paddon-Row, M. N. Competing Electron-Transfer Pathways in Hydrocarbon Frameworks: Short-Circuiting Through-Bond Coupling by Nonbonded Contacts in Rigid U-Shaped Norbornylogous Systems Containing a Cavity-Bound Aromatic Pendant Group. *J. Am. Chem. Soc.*, 2007, *129*, 3247-3256.

94 Liu, M.; Ito, N.; Maroncelli, M.; Waldeck, D. H.; Oliver, A. M.; Paddon-Row, M. N. Solvent Friction Effect on Intramolecular Electron Transfer. *J. Am. Chem. Soc.*, 2005, *127*, 17867–17876

95 Chakrabarti, S.; Liu, M.; Waldeck, D. H.; Oliver, A. M.; Paddon-Row, M. N. Solvent Dynamical Effects on Electron Transfer in U-Shaped Donor-Bridge-Acceptor Molecules. *J. Phys. Chem. A*, 2009, *113*, 1040-1048.

96 Beratan, D. N.; Skourtis, S. S.; Balabin, I. A.; Balaeff, A.; Keinan, S.; Venkatramani, R.; Xiao, D. Steering Electrons on Moving Pathways. *Acc. Chem. Res.*, 2009, *42*, 1669–1678.

97 Skourtis, S. S.; Waldeck, D. H.; Beratan, D. N. Fluctuations in Biological and Bioinspired Electron-Transfer Reactions. *Annu. Rev. Phys. Chem.*, 2010, *61*, 461–485.

98 Bingöl, B.; Durrell, A. C.; Keller, G. E.; Palmer, J. H.; Grubbs, R. H.; Gray, H. B. Electron Transfer Triggered by Optical Excitation of Phenothiazine-tris(*meta*-phenylene-ethynylene)-(tricarbonyl)(bpy)(py)rhenium(I). *J. Phys. Chem. B*, 2013, *117*, 4177–4182.

99 Yin, X.; Kong, J.; De Leon, A.; Li Y.; Ma Z.; Wierzbinski, E.; Achim, C.; Waldeck, D. H. Luminesence Quenching by Photoinduced Charge Transfer between Metal Complexes in Peptide Nucleic Acids. *J Phys. Chem. B*, 2014, *118*, 9037-9047.

100 McGuinness, C. D.; Nishimura, M. K. Y.; Keszenman-Pereyra, D.; Dickinson, P.; Campbell, C. J.; Bachmann, T. T.; Ghazalb, P.; Crainac, J. Detection of Single Nucleotide Polymorphisms Using DNA Holliday Junction Nanoswitch – a High-Throughput Fluorescence Lifetime Assay. *Mol. BioSyst.*, 2010, *6*, 386-390.

101 Reis e Sousa, A. T.; Castanheira, E. M. S.; Fedorov, A.; Martinho J. M. G. Polystyrene Cyclization Using Excimer Formation. Effect of Feminate Pairs in Good Solvents. *J. Phys. Chem. A*, 1998, *102*, 6406-6411.

102 Haedler, A. T.; Misslitz, H.; Buehlmyer, C.; Albuquerque, R. Q.; Kohler, A.; Schmidt, H.-W. Controlling the π-Stacking Behavior of Pyrene Derivatives: Influence of H-Bonding and Steric Effects in Different States of Aggregation. *ChemPhysChem*, 2013, *14*, 1818-1829.
103 Gilbert, A.; Baggott, J. *Essentials of Molecular Photochemistry;* Blackwell Scientific Publications: Oxford, England, 1991; pp 91-175.
104 Gordon, M.; Ware, W. R. *The Exciplex;* Academic Press Inc.: New York, 1975; pp 1-23.
105 Bichenkova, E. V.; Douglas, K.T.; Sardarian, A. Exciplexes. U.S. Patent WO2001046121 A2, June 28, 2001; http://www.google.com/patents/WO2001046121A2?cl=en (accessed Oct 1,2014).
106 Mataga, N.; Kubota, T. *Molecular Interactions and Electronic Spectra;* Marcel Dekker, Inc.: New York, 1970. pp. 411-485.
107 Verhoeven, J. W.; Scherer, T.; Willemse, R. J. Solvent Effects on the Structure of Fluorescent 'Exciplexes' in Rigidly-, Flexibly-, and Non-Bridged Donor-Acceptor systems. *Pure Appl.Chem.*, 1993, *65*, 1717-1722.
108 Verhoeven, J. W. Electron Transport via Saturated Hydrocarbon Bridges: 'Exciplex' Emission from Flexible, Rigid and Semiflexible Bichromophores. *Pure Appl.Chem*., 1990, *62*, 1585-1596.
109 Okada, T., Fujita; T., Kubota, M.; Masaki, S.; Mataga, N. Intramolecular Electron Donor-Acceptor Interactions in the Excited State of (Anthracene)-(CH2)*n*-(N,N-dimethylaniline) Systems. *Chem. Phys. Lett.*, 1972, *14*, 563-568.
110 Lewis, F. D. Formation and Reactions of Stilbene Exciplexes. *Acc. Chem. Res.*, 1978, *12*, 152-158.
111 Borsarelli, C. D.; Cosa, J. J.; Previtali, C. M. Exciplex Formation Between Pyrene Derivatives and N,N-dimethylaniline in Aerosol OT Reversed Micelles. *Langmuir*, 1992, *8*, 1070-1075.
112 Lakowicz, J. R. *Principles of Fluorescence Spectroscopy, 3rd ed.;* Springer: Baltimore, Maryland, 2006; pp 205-232.
113 Kuzmin, M. G. Exciplex Mechanism of the Fluorescence Quenching in Polar Media. *Pure & Appl. Chem.*, 1993, *65*, 1653-1658.
114 Van Haver, Ph.; Helsen, N.; Depaemelaere, S.; Van der Auweraer, M.; De Schryver, F. C. The Influence of Solvent Polarity on the Nonradiative Decay. *J. Am. Chem. Soc.*, 1991, *113*, 6849-6857.
115 These radii were calculated using the circumscribed sphere (Figure 7.21 and Figure 7.24).
116 Gould, I. R.; Ege, D.; Moser, J. E.; Farid, S. Efficiencies of Photoinduced Electron-Transfer Reactions: Role of the Marcus Inverted Region in Return Electron Transfer within Geminate Radical-Ion Pairs *J. Am. Chem. Soc.*, 1990, *112*, 4290-4301.
117 Marcus, R. A. Relation Between Charge Transfer Absorption and Fluorescence Spectra and the Inverted Region. *J. Phys. Chem.* 1989, *93*, 3078-3086.
118 Barbara, P. F.; Meyer, T. J.; Ratner, M. A. Contemporary Issues in Electron Transfer Research. *J. Phys. Chem.*, **1996**, *100*, 13148-13168.
119 Van Voorhis, T.; Kowalczyk, T.; Kaduk, B.; Wang, L.-P.; Cheng, C.-L.; Wu, Q. The Diabatic Picture of Electron Transfer, Reaction Barriers, and Molecular Dynamics. *Annu. Rev. Phys. Chem*., **2010**, *61*, 149-170.
120 Gratzel, M. *Heterogeneous Photochemical Electron Transfer;* CRC Press, Inc.; Boca Raton, Florida, 1989. pp. 5-20.
121 Jortner J; Bixon, M. *Electron Transfer-From Isolated Molecules to Biomolecules*; John Wiley & Sons, Inc. New York, 1999. pp. 553-601.
122 Kumar, K.; Kurnikov, I.; Beratan, D.; Waldeck, D. H.; Zimmt, M. B. Use of Modern Electron Transfer Rate Theories to Determine Electronic Coupling Matrix Elements in Intramolecular Systems. *J. Phys. Chem. A*, **1998**, *102*, 5529-5541.
123 Feldman, K. S.; Hester, D. K.; Goldbeck, J. H. A Relationship Between Amide Hydrogen Bond Strength and Quinone Reduction Potential: Implications of Photosystem I and Bacterial Reaction Center Quinone Function. *Bioorg. Med. Chem. Lett.*, **2007**, *17*, 4891-4894.
124 Kerr, C. E.; Mitchell, C. D.; Headrick, J.; Eaton, B. E.; Netzel, T. L. Synthesis and Photophysics of 1-Pyrenyl Substituted 2'-Deoxyuridine-5-Carboxamide Nucleoside: Electron Transfer Products as CIS INDO/S Excited States. *J Phys Chem B*, **2000**, *104*, 1637-1650.
125 MOPAC2012, James J. P. Stewart, Stewart Computational Chemistry, Version 15.229L web: *HTTP://OpenMOPAC.net*
126 Maia, J. D. C.; Carvalho, G. A. U.; Mangueria, C. P.; Santana, S. R.; Cabral, L. A. F.; Rocha, G. B. GPU Linear Algebra Libraries and GPGPU Programming for Accelerating MOPAC Semiempirical Quantum Chemistry Calculations. *J. Chem. Theory Comput.*, **2012**, *8*, 3072-3081.

127 JSmol: an open-source HTML5 viewer for chemical structures in 3D. Web: http://wiki.jmol.org/index.php/JSmol.

3.0 THE EFFECT OF THE POSITION OF AN AMIDE MODIFICATION ON A PYRENE ACCEPTOR MOIETY IN A DONOR-BRIDGE-ACCEPTOR SYSTEM

This work has not been published but the following people contributed to this work: Graff, B. M.; Yin, X.; Parker, M. F. L. P; Schafmeister, C. E.; Waldeck, D. H. The thesis author performed all of the photophysical studies and wrote the manuscript. The supporting information for this chapter is provided in Appendix B.

Solvent mediated electron tunneling between a dimethylaniline donor and an amide modified pyrene acceptor was studied in dimethyl sulfoxide and water. The amide modification was located on the third, sixth, or eighth substituent position of the pyrene ring. Electron transfer in these bis-amino acid donor-bridge-acceptor systems was studied as a function of the amide modification for two different cleft sizes. It was found that the small cleft molecules, **1**, have a faster rate constant than the large cleft molecules, **2**. It was also determined that while the position of the amide modification plays a significant role in the inherent pyrene recombination kinetics, the electron transfer kinetics were only slightly affected.

3.1 INTRODUCTION

Electron transport is an essential chemical and biological process, and solvent (especially water) can play a large role in influencing electron transport properties, particularly in biological systems.[128,129] The effect that solvent has on electron transfer can be studied in well-defined molecular donor-bridge-acceptor (DBA) systems. Generally, the electron transfer rate constant can be written as[130]

$$k_{ET} = \frac{2\pi}{\hbar} \cdot |V|^2 \cdot FCWDS \qquad \text{Equation 3.1 [130]}$$

where the Frank-Condon weighted density of states (FCWDS) accounts for environmental variables including the solvent's orientation with respect to the donor and acceptor. Frequently, in DBA systems, electrons are transferred through bond; however, when electron transfer is less favorable through bond (the through bond electronic coupling, $|V|$, is small) electrons can be transferred through the solvent. In this situation, the role of the solvent becomes central to the transport kinetics.

Conformationally restricted DBA systems provide a means for studying solvent effects on electron transfer in the liquid phase rather than in frozen media, which was the earliest approach to studying electron tunneling through solvent.[131,132,133] Studies of conformationally restricted linear DBA systems,[134,135,136,137,138] which tunnel through bond, and those forming molecular clefts,[139,140,141,142,143] which tunnel through space, have probed electron transport properties as a function of solvent, $|V|$, distance, etc. Over the past few decades, DBA molecules have been studied in an effort to better understand electron transfer kinetics in both polar and nonpolar

solvents. There have been many studies in nonpolar solvents,[144,145,146] but those in polar systems,[142,143] such as water, are less frequent.

This work studies the photo-induced electron transfer for C-shaped DBA bis-amino acid oligomers in two polar solvents, water and dimethyl sulfoxide (DMSO). The DBA systems have the same donor and acceptor moieties, but one of the stereocenters on the bridge is inverted, yielding two distinct molecules: D-SSS-A, **1**, and D-RSS-A, **2**. These isomers vary in the size of their molecular cleft. In this study, the amide modification on the pyrene acceptor is located on either the third (**A**), sixth (**B**), or eighth (**C**) position on the pyrene ring, and the electron transfer rate is studied in polar solvents as a function of this substituent position.

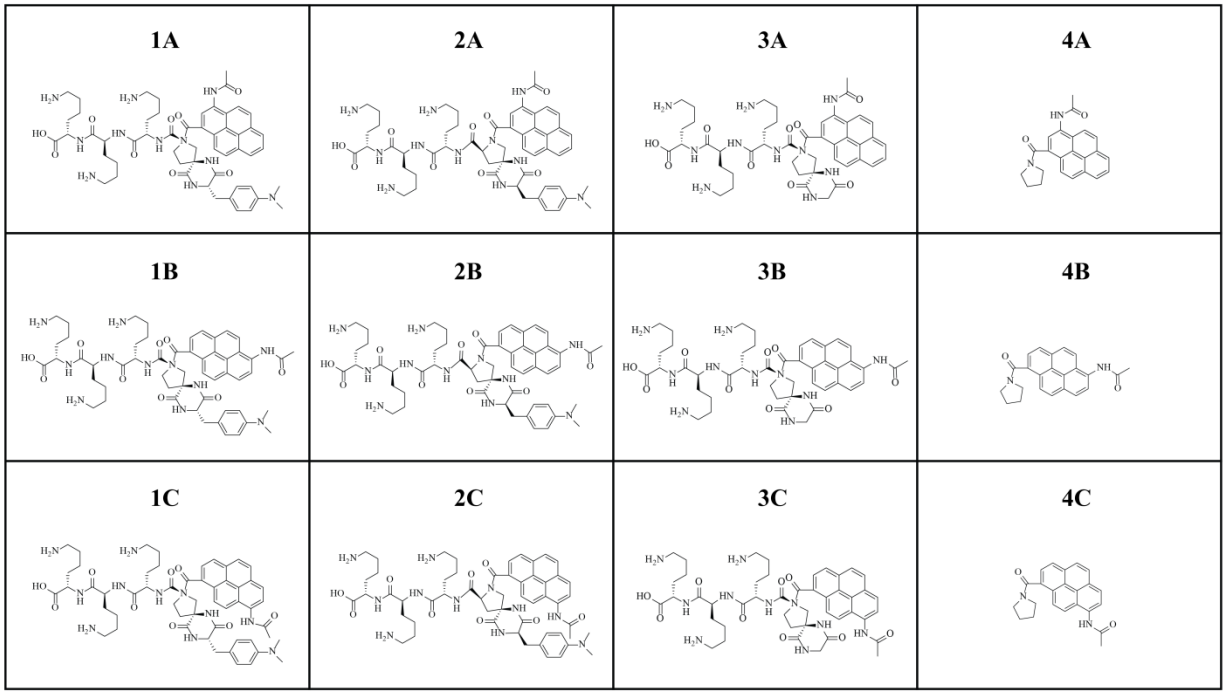

*Figure 3.1 - Molecular structures for **1**, **2**, **3**, and **4** are shown. The small cleft system is **1**, the large cleft system is **2**, the bridge-acceptor molecule is **3**, and **4** is the modified pyrene. The amide modification to the pyrene acceptor moiety is located on either the third (**A**), sixth (**B**), or eighth (**C**) position on the pyrene ring*

3.2 EXPERIMENTAL

3.2.1 Synthesis

Solid phase peptide chemistry was used to prepare compounds **1**, **2**, **3,** and **4** (Figure 3.1), and the procedure is identical to that which is described in Graff *et. al.*[143] In the synthesis described there, 1,3 (**A**), 1,6 (**B**), and 1,8 (**C**) substituted pyrene molecules were all reaction products, and they were purified by HPLC. For more details on the synthesis and purification see Appendix A.

3.2.2 Photophysics

A Barnstead Nanopure system with a resistance of 18.2 MΩ-cm at 25 °C was used to produce the deionized water in these experiments. Citric acid monohydrate (99.0+ %), sodium phosphate dibasic (99.95 %), and dimethyl sulfoxide (99.9+ %) were purchased from Aldrich and used without further purification. While samples of **1-3** were readily soluble in water and DMSO, sample **4** was only readily soluble in DMSO.

Samples of **1**, **2**, **3**, and **4** were characterized via absorption and fluorescence spectroscopy. The UV-Vis spectra were collected on a Model 8453 Agilent spectrometer and fluorescence spectra were collected on a JY-Horiba Fluoromax-3 spectrofluorometer. While the fluorescence spectra were collected at various excitation wavelengths, the following parameters were always used: 0.34 mm slits and 0.1 s integration time.

Photoluminescence decay data were measured via the time correlated single photon counting (TCSPC) technique using a PicoHarp 300 TCSPC module (PicoQuant GmbH). [147] Samples were excited at 375 nm using a picosecond diode laser (PiL037), at a 1MHz repetition rate, and the measurement was performed at the magic angle polarization geometry. At the peak channel, 20,000 counts were collected. The instrument response function was measured using colloidal $BaSO_4$, and the instrument response function had a full-width-at-half-maximum of $\leq$96 ps. Emission from the samples was collected on the red edge of the emission maximum unless noted otherwise. Edinburgh Instruments fluorescence analysis software technology (FAST)[148] was used to fit the photoluminescence decays to a distribution of lifetimes or a sum of exponentials via the convolution and compare method.

All solutions of **1**, **2**, **3**, and **4** have an approximate optical density of 0.25 at the S1 absorption band maximum of the pyrene. Each solution was freeze-pump-thawed a minimum of three times; samples dissolved in DMSO had molecular sieves in the cuvettes to ensure that no water was present. The samples were also back-filled with argon. A temperature cell was controlled using a NESLAB RTE-110 chiller.

3.2.3 Computation

Both ground state geometry optimization and potential energy surface (PES) scans were performed at the B3LYP/6-31G(d) level using Gaussian 09.[149] The solvent environment (DMSO or water) was simulated with the Polarizable Continuum Model (PCM) model.[150]

Molecules **4A**, **4B** and **4C** contain non-standard amino acid residues, which are not included in the standard AMBER force fields. The missing atom types in ff14SB[151] were complemented with GAFF.[152] Partial charges were determined using the Restrained Electrostatic Potential (RESP) fit[153] for the equilibrium geometries at B3LYP/6-31G(d) level while the electrostatic potentials were calculated at HF/6-31G(d) level. All other missing parameters were obtained from the GAFF atom types, equilibrium geometries and partial charges with the help of antechamber.[154]

Initial input structures for molecular dynamics (MD) were built using xleap with the above extended ff14SB[151] force fields. The structures were then solvated in a TIP3P[155] water box, such that the distance between the walls of the box and the closest solute atom was at least 12 Å. After 100 ns energy minimization and equilibration, the solvated structures were subjected to a 300 ns MD production run. All MD simulations were performed with the "pmemd" module of AMBER 14[156] at T = 300 K and P = 1 atm, with periodic boundary conditions.

3.3 RESULTS AND DISCUSSION

3.3.1 Effect of Substituent Pattern on Control Compounds **3** and **4**

The acceptor molecule, pyrene, was modified with an amide substituent (Figure 3.1) at either position 3 (**A**), 6 (**B**), or 8 (**C**) of the pyrene ring. The absorbance spectra of the bridge acceptor (**3**) and modified pyrene only (**4**) system in dimethyl sulfoxide, DMSO, are nearly identical and do not differ much as the position of the amide modification is changed (Figure 3.2A & Figure 3.2B). Distinct differences appear in the steady state photoluminescence (PL) spectra of the bridge acceptors in DMSO (Figure 3.2C), however. Both **3B** and **3C** show a broad unfeatured emission centered at 427 nm, while **3A** has an emission profile that is more characteristic of a pyrene locally excited state. The PL spectrum of **3A** is not as broad as **3B** and **3C**; note that the vibronic structure present in **3A** are more similar to the emission shown in Chakrabarti *et. al.*[142] in which no amide modification is present.

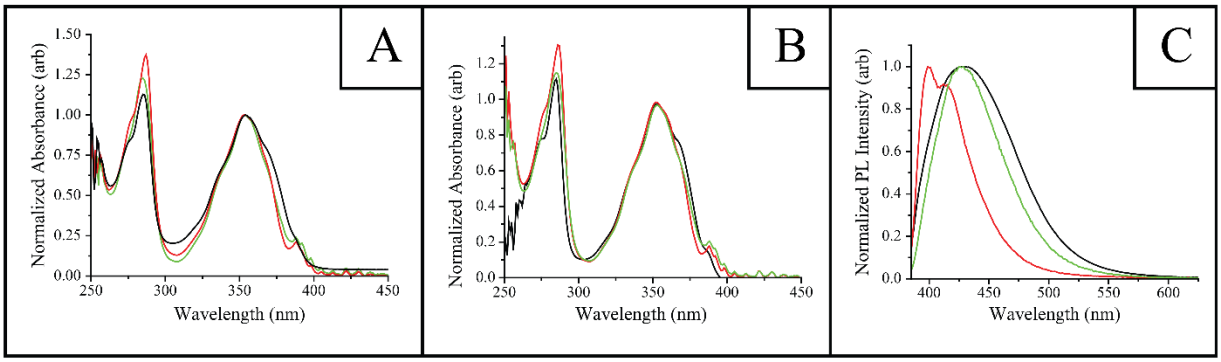

*Figure 3.2 - Panels A and B show absorbance spectra for solutions of **3A, 3B,** and **3C** (A) and **4A, 4B,** and **4C** (B). Panel C shows photoluminescence (PL) spectra of **3A, 3B,** and **3C** in DMSO. The PL spectra were obtained by exciting the molecules at 375 nm. In all cases **A** is red, **B** is black, and **C** is green*

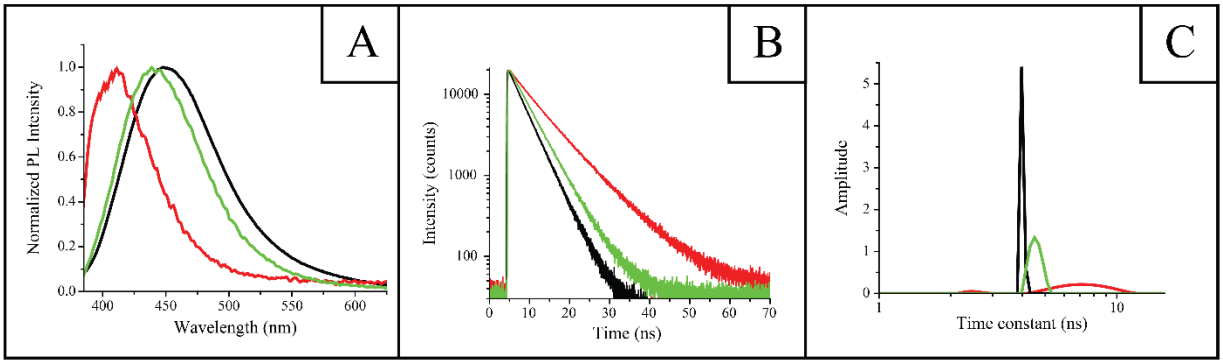

*Figure 3.3 - The figure shows photoluminescence (PL) spectra (A), PL decays (B), and the distribution of lifetime components (C) that are obtained by fitting the PL decay (C) for solutions of **3A, 3B,** and **3C** in pH 7 aqueous buffer. The PL spectra were obtained by exciting the molecules at 375 nm. In all cases **A** is red, **B** is black, and **C** is green.*

Figure 3.3 summarizes the luminescence spectra and lifetime data for the bridge-acceptor control compounds **3A**, **3B**, and **3C**. In Figure 3.3A, the emission spectra of **3A**, **3B**, and **3C** in pH 7 aqueous buffer are shown. Note that all three substitution patterns show similar photoluminescence characteristics (ie. the vibronic structure that is observed for **3A** in DMSO is less apparent), but there are shifts in the emission peak maxima of the molecules. Again, **3B** and **3C** are more similar, while **3A** differs notably. Panel B of Figure 3.3 shows the

photoluminescence decay of **3A, 3B,** and **3C** in pH 7 buffer. Note that the lifetime of the pyrene varies noticeably with the substitution position. In Chakrabarti *et. al.,*[142] the lifetime of the bridge acceptor for an unmodified pyrene system at room temperature is approximately 6 ns longer than for the longest lived systems (**3A**) in this study. When the substituent is near the bridge, far from the molecular cleft, as in the case of **3A**, the lifetime of the pyrene is the longest and is most similar to what is reported in Chakrabarti *et. al.*[142] Note that the pyrene lifetime is the shortest for **3B**, where the amide substituent is farther from the bridge, closest to the molecular cleft, and generates the most polar system (ie. largest Stokes shift). Compound **3C** has an excited state lifetime that is in between **3A** and **3B**. Quantum chemistry calculations in Graff *et. al.*[143] indicate that the presence of an amide substituent on the pyrene acceptor can disrupt the π-π interaction between the donor, dimethylaniline (DMA), and the acceptor.

The differences in the characteristic steady state emission spectra of the bridge-acceptor control systems helps to explain the variance that is observed in the experimental electron transfer rates. As anticipated, the photoluminescence (PL) decays of the bridge-acceptor controls vary. It is found that the lifetime of the excited state differs for all three substituents measured; however, **3B** and **3C** behave very similarly in water (Figure 3.3B & Figure 3.3C). When fit with a distribution of lifetime components, it was found that the bridge-acceptor system could be fit to a single time constant for **3B** and **3C** (Figure 3.3C); however, this was not the case for **3A**. The bridge-acceptor system **3A** could only be fit reasonably to two time constants. The distribution of the dominant time constant was both longer lived and broader than what was observed for **3B** and **3C**; this time constant is more similar to what was observed in Chakrabarti *et. al.*[142]. Note that there is a second lifetime component observed in **3A**. In summary, the PL decay of **3B** and

3C are described well by an exponential decay law, but the PL decay of **3A** requires two exponentials.

In order to ensure that the difference in the PL decay properties for pyrene does not arise as a result of pyrene bridge interactions, **3** was directly compared to **4**. Recall, **3** contains the bridge unit, but **4** does not. Because **4** does not contain the water-soluble bridge subunit, it is not soluble in water, but is soluble in DMSO. For direct comparison, both **3** and **4** were dissolved in DMSO and the photoluminescence decay was fit using a distribution of time constants. The distribution fits for **3** and **4** for all three substitution positions are shown in Figure 3.4. Note that both **3A** and **4A** contained two distinct time constants while **3B**, **4B**, **3C**, and **4C** can be fit by a single time constant. These data indicate that the second time constant observed in **3A** and **4A** arise from the amide substituent position on the pyrene chromophore rather than the bridge pyrene interaction. This difference is discussed further in Appendix B.

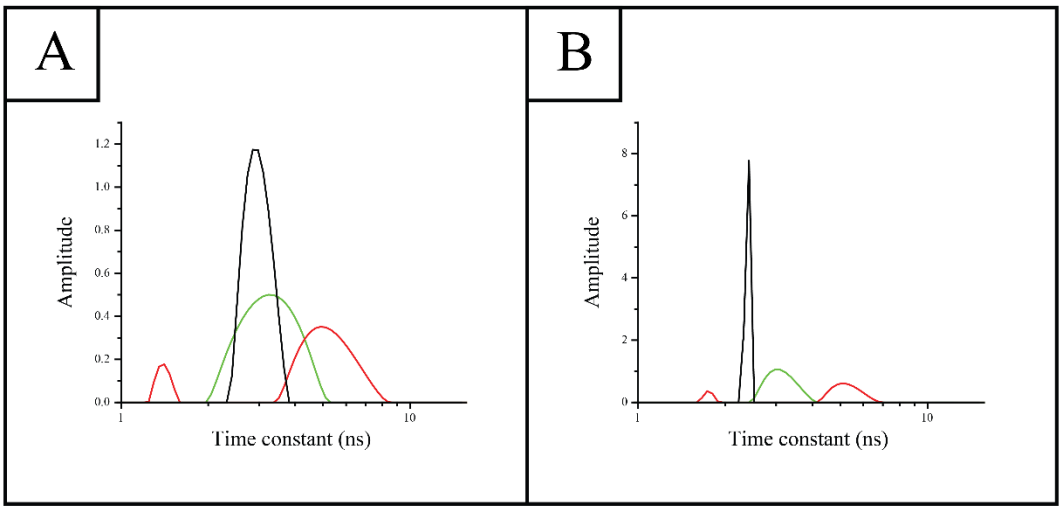

*Figure 3.4 - The figure shows the distribution of lifetime components that are obtained from fitting the photoluminescence (PL) decay of **3** (A) and **4** (B) in DMSO at 25 ℃. The PL spectra were obtained by exciting the molecules at 375 nm. In both cases **A** is red, **B** is black, and **C** is green.*

These data show that the substituent position of the amide on the pyrene moiety changes the intrinsic decay of the pyrene, and it must be considered when determining the electron transfer rate for **1** and **2**.

3.3.2 Electron Transfer Rates for **1** and **2**

The electron transfer rates of molecules **1** and **2** were calculated using the kinetic scheme shown in Figure 3.5A. This scheme is the same kinetic scheme that was used in Graff *et. al.;*[143] DBA molecules **1** and **2** form intramolecular exciplexes which can either undergo relaxation to the ground state (k_{rec}) or back electron transfer to the locally excited state (LE). The charge separated (CS) state is more stable in polar solvents leading to a redshift in the emission of the exciplex. The kinetic scheme depicted in Figure 3.5A rationalizes the excited state photophysics and accounts for the presence of a second red-shifted emission peak when the donor is present (Figure 3.5B & Figure 3.5C). The PL decays were collected in the CS emission band, to the red of the LE state peak maximum (Figure 3.5B). In each case, the PL decays were collected at the peak maximum of the emission depicted in Figure 3.5C; ie. 535 nm for **1A**, 525 nm for **1B**, and 515 nm for **1C**.

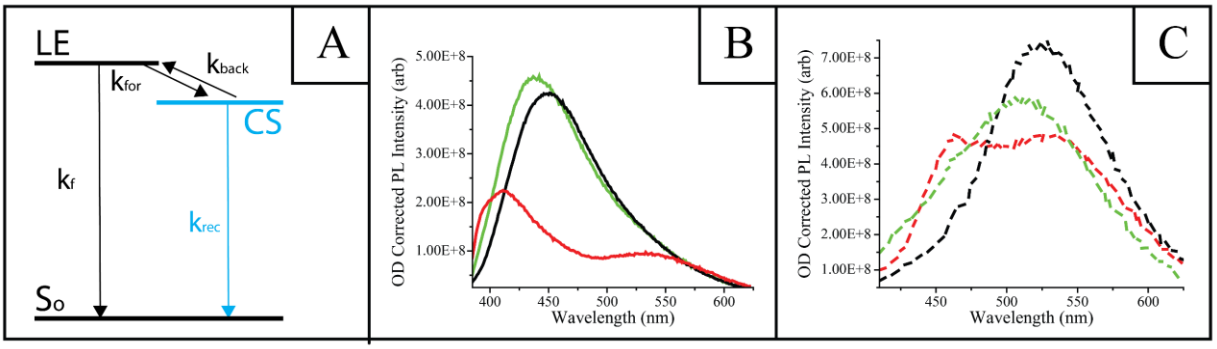

*Figure 3.5 - The diagram depicts the kinetic scheme for the charge separated state (CS) formation (A). Panels B and C show CS emission spectra that were obtained for excitation at 375 nm (Panel B), the wavelength used in the PL decay measurements, and at 400 nm for molecule **1** (Panel C). In both cases **A** is red, **B** is black, and **C** is green.*

Excitation of the modified pyrene acceptor populates the LE state. When the donor is present, the fluorescence signal that arises is a combination of emissions resulting from two transitions: LE → S_0 and CS → S_0. For this kinetic model, a decay law with a double exponential form is obtained[139,140,141,143]

$$I(t) = I(0) \cdot [a_+ \exp(-k_+ t) + (1 - a_+) \exp(-k_- t)] \qquad \text{Equation 3.2}$$

where a_+ is the fraction of fluorescence decaying with the fast rate constant, k_+, and k_- is the rate constant of the slow fluorescence decay. From this equation, the forward electron transfer rate constant, k_{for}, the backward electron transfer rate constant, k_{back}, and the rate constant associated with recombination from the CS state to the ground state, k_{rec}, can be determined. For details describing the determination of k_{for}, k_{back}, and k_{rec}, see Graff *et. al.*[143] and Appendix B. Because two components were observed in the control system, **3A**, it was assumed that the intermediate time constant present in DBA molecules **1** and **2** did not participate in electron transfer (see Appendix B for a full discussion on the exclusion of this time constant). The use of this kinetic model allows for the direct calculation of the Gibb's free energy, $\Delta_r G$,

$$\Delta_r G = -\mathrm{RT}\ln\left(\frac{k_{for}}{k_{back}}\right) \qquad \text{Equation 3.3}$$

The electron transfer rate was determined at various temperatures. By analyzing these data and using the $\Delta_r G$ values, the activation energy, $\Delta G^{\ddagger}$, and the electronic coupling, $|V|$, can be directly determined by way of the semi-classical Marcus equation (Equation 3.4).[130]

$$k_{ET} = \frac{2\pi}{\hbar}|V|^2 \frac{1}{\sqrt{4\pi\lambda_s k_B T}} \sum_{n=0}^{\infty} e^{-S}\left(\frac{S^n}{n!}\right) \exp\left(-\frac{(\lambda_s + \Delta_r G + nh\nu)^2}{4\lambda_s k_B T}\right) \qquad \text{Equation 3.4}$$

where k_B is Boltzmann's constant, $|V|$is the electronic coupling, $\Delta_r G$ is the reaction free-energy, λ_s is the solvent reorganization energy, ν is the frequency of the effective quantized vibrational mode, and S is the Huang-Rhys factor, which is the ratio of the inner-sphere reorganization energy, λ_v, to the quantized mode energy spacing, $\frac{\lambda_v}{h\nu}$. In this analysis, 1400 cm^{-1} was used as the value for the single effective quantized mode and 0.30 eV for the inner-sphere reorganization energy. These values are the same as those used in previous work with the same donor and a similar acceptor.[142]

In an effort to self-consistently analyze the electron transfer rates, the intermediate time constant observed for **3A** was excluded; ie. this time constant is assumed to arise from a molecular conformer that is not involved in the electron transfer process. Appendix B and Chapter 8.3, provide a more detailed discussion of this point. Figure 3.6 shows an Arrhenius-like plot for the temperature dependence of the electron transfer rates (k_{for}) in both pH 7 aqueous buffer and DMSO.

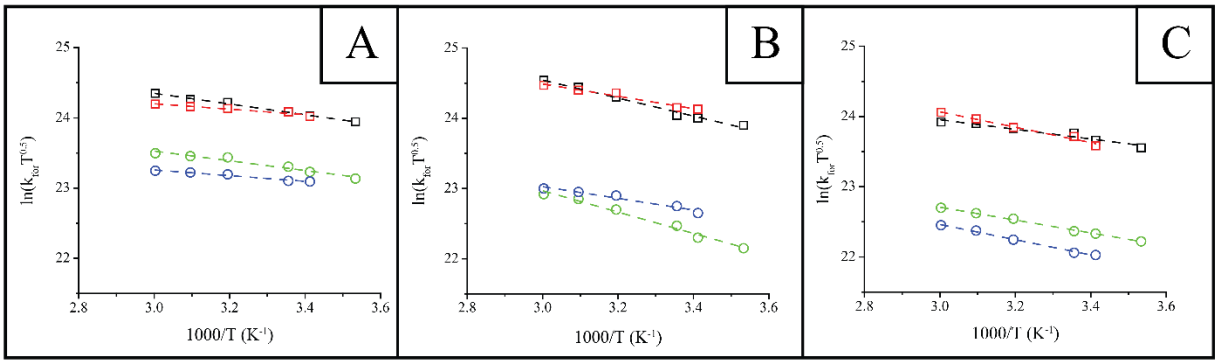

*Figure 3.6 - The temperature dependence of the electron transfer rate constant of **1A**, (squares) and **2A**, (circles) are shown in panels A, **1B** (squares) and **2B** (circles) are shown in panel B, and **1C** (squares) and **2C** (circles) are shown in panel C for pH 7 buffer (black, green) and DMSO (red, blue). The details of the error in the electron transfer rate constant are in described in the Supplemental Information (S4).*

Experimentally, it is observed that the electron transfer rates reported for the small cleft molecules, **1**, in both DMSO and water are similar (Figure 3.6A, Figure 3.6B, & Figure 3.6C) for all substituent positions studied; however, the large cleft molecules show a solvent dependence, which is different in **B** than in **A** and **C**. The best fit lines in Figure 3.6 represent fits to the semi-classical electron-transfer rate equation for a single effective quantum mode (Equation 3.4).[130] $|V|$ and $\lambda_s$were determined through these fits and their values in water are also reported in Table 3.1.

*Table 3.1 - The reaction Gibbs energy ($\Delta_r G$), solvent reorganization energy (λ_s), and electronic coupling (|V|) of **1** and **2** with different substituent patterns at 298 K.*

Sample	pH 7 buffer			DMSO		
	$\Delta_r G$ (eV)	λ_s (eV)	$\|V\|$ (cm^{-1})	$\Delta_r G$ (eV)	λ_s (eV)	$\|V\|$ (cm^{-1})
1A	-0.025	0.31	20	-0.014	0.25	9
1B	-0.013	0.42	32	-0.012	0.23	12
1C	-0.028	0.29	17	-0.014	0.41	18
2A	-0.023	0.28	12	-0.034	0.35	6
2B	-0.023	0.52	22	-0.036	0.40	12
2C	-0.064	0.44	12	-0.040	0.45	8

There are some clear differences in the electron transfer rate between molecules **1** and **2** as a function of the substituent position (**A**, **B**, **C**) and their solvent (DMSO, pH 7 buffer). While the presence of an amide modification does not drastically change the molecular volume, it can change the cleft size. [143] The change in cleft size can modify the size and type of solvent that can be incorporated into the cleft to facilitate electron transfer. It was found through quantum mechanical calculations in Graff *et. al.*[143] that when the amide substituent is present, water, DMSO, and even larger solvents can be incorporated into the cleft for the tight binding cleft, **1**, and facilitate electron transfer.

The $\Delta_r G$ values reported in Table 3.1 are much smaller than what would be anticipated for a dimethylaniline-pyrene system.[142] Using ultraviolet photoelectron spectroscopy measurements Graff *et. al.*[143] showed that the amide modification on the pyrene leads to a less favorable redox

potential than an unmodified pyrene. In most cases, the solvent reorganization energy was larger for those systems in water than those in DMSO. This similar trend was reported in Chakrabarti *et. al.* [142] Note, that system **1B**, which has the highest emission for the charge separated state (Figure 3.4C), also has the largest solvent reorganization energy. Because both cleft sizes and all substituent positions can incorporate both DMSO and water, it is reasonable that the reorganization energies are similar. The quantum mechanical calculations reported on in Graff *et. al.*[143] indicate that the similarity in electronic coupling between the tight and loose binding cleft systems is expected. The calculations note that the clefts in **1** and **2**, as a result of the more polar amide modification, were able to adapt to the size of the solvent molecules.

3.3.3 Origin of Spectator Pathway

In an effort to provide an explanation as to the origin of the spectator pathway, a coarse potential energy scan (PES) was calculated by rotating the pyrrolidone (PDN) group for **4A**, **4B**, and **4C**. Molecule **4A** was modelled rather than **3A** because it was smaller and had two distinct time constants also (Figure 3.1 & Figure 3.4). The calculations *in vacuo* showed that **4A** has a higher barrier height than the other isomers, **4B** and **4C** (Figure 3.7). Figure 3.7 indicates that **4A** could have more rigid conformers than **4B** and **4C**, which could lead to the additional relaxation pathway observed for **3A** (Figure 3.4). However, Figure 8.6 shows that when solvent molecules were incorporated into the calculation, the differences noted in Figure 3.7 are less apparent.

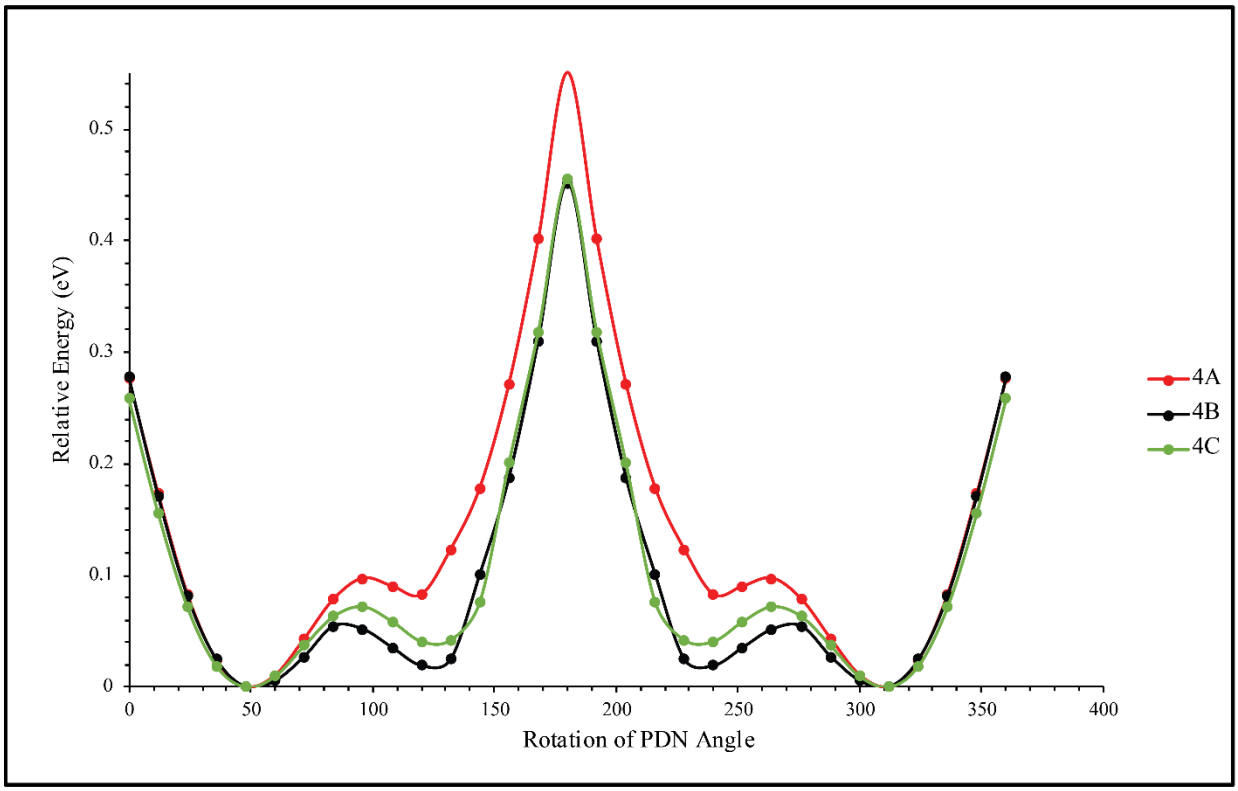

*Figure 3.7 - Potential energy scan in vacuum of molecules **4A** (red), **4B** (black), and **4C** (green) while rotating the pyrrolidone group.*

From the above Figure 3.7, note that the rotation barrier is large for PDN; *in vacuo* it is ~0.6 eV, and in solvent it is ~ 0.5 eV (~ 20 times larger than $k_B T$). The magnitude of this barrier indicates that the interchange on the excited electronic state timescale (tens of ns) is very unlikely. Therefore, the PDN conformers stay either "above" or "below" the pyrene plane. The differences among the PES curves are caused by the pyrrolidone-acetyl (PDN-ACE) interaction. **4A**, with the largest rotation barrier, would also have the strongest PDN-ACE interaction. Within the potential well, there are two distinct minima with a local maximum. The local maximum has the largest barrier height for the case of **4A** (~0.1 eV) and the smallest barrier height for **4B** (~0.05 eV). Thus, even when the rotation between the two wells is unlikely, the lower energy rotation is significantly more favorable for the case of **4B** or **4C** than for **4A**. While these differences are

reduced after the inclusion of solvent molecules (Figure 8.6), **4A** still has the largest barrier between the two minima within a single well. Note that for the case of the calculations reported on in this study, the bridge subunits were not present. It is possible that the presence of the bridge could sterically hinder the rotation angles of the PDN and favor certain conformers over others.

3.4 CONCLUSIONS

The position of the amide substitution on the pyrene in the donor-bridge-acceptor system modestly modifies the electron transfer rate kinetics. The reaction Gibbs energy for the photoinduced electron transfer and the hydrophilicity of the molecular cleft are affected by the position of the amide substituent. Substitution at positions 6 and 8 are similar and generate a less hydrophobic molecular cleft, while substitution at position 3 behaves more like an unmodified pyrene molecule, but also displays a time constant that does not seem to participate in electron transfer. When utilizing only time constants that participate in electron transfer to determine the electron transfer rates, all three substituent positions have similar electron transfer rate kinetics. Similar to an earlier study, the amide modification on the pyrene ring allows the incorporation of both small polar solvents (water) and larger polar solvents (DMSO) into the molecular cleft.

3.5 REFERENCES

[128] Beratan, D. N.; Onuchic, J. N. *Protein Electron Transfer*; Bendall, D. S., Ed.; BIOS Scientific Publishers Ltd.: Oxford, 1996; p 23.
[129] Page, C. C.; Moser, C. C.; Chen, X.; Dutton, P. L.; *Nature* **1999**, *402*, 47.
[130] Jortner J; Bixon, M. *Electron Transfer-From Isolated Molecules, Part 1 and Part 2*; John Wiley & Sons, Inc. New York, 1999.
[131] Miller, J. R.; *J. Phys. Chem.* **1975**, *79*, 1070.
[132] Wenger, O. S.; Leigh, R. M.; Villahermosa, H. B.; Gray, H. B.; Winkler, J. R.; *Science* **2005**, *307*, 99.
[133] Ponce, H. B.; Gray, H. B.; Winkler, J. R.; *J. Am. Chem. Soc.*, **2000**, *122*, 8187.
[134] Paddon-Row, M. N.; *Adv. Phys Org. Chem.*, **2003**, *38*, 1.
[135] Gilbert M, Albinsson B.; *Chem. Soc. Rev*., **2015**, *44*, 845.
[136] Natali M., Campagna S., Scabndola, F., *Chem. Soc. Rev.*, **2014**, *43*, 4005.
[137] Weiss, E.A., Wasielewski, M. R., Ratner, M.A.; *Top. Curr. Chem*., **2005**, *257*, 103.
[138] Gu, Y.; Kumar, K.; Lin, Z.; Read, I.; Zimmt, M. B.; Waldeck, D. H.; *J. Photochem. Photobio. A: Chem.*, **1997**, *105*, 189.
[139] Read, I.; Napper, A.; Kaplan, R.; Zimmt, M. B.; Waldeck, D. H.; *J. Am. Chem. Soc.*, **1999**, *121*, 10976.
[140] Nadeau, J. M.; Liu, M.; Waldeck, D. H. and Zimmt, M. B.; *J. Am. Chem. Soc.*, **2003**, *125*, 15964.
[141] Zimmt, M. B. and Waldeck, D. H'. *J. Phys. Chem. A*, **2003**, *107*, 3580.
[142] Chakrabarti, S.; Parker, M. F. L.; Morgan, C. W.; Schafmeister, C. E.; Waldeck, D. H.; *J. Am. Chem. Soc.*, **2009**, *131*, 2044.
[143] Graff, B. M.; Lamont, D. N.; Parker, M. F. L.; Bloom, B. P.; Schafmeister, C. E.; Waldeck, D. H.; *J. Phys. Chem. A.*, **2016**, *120*, 6004.
[144] Beratan, D. N.; Skourtis, S. S.; Balabin, I. A.; Balaeff, A.; Keinan, S.; Venkatramani, R.; Xiao, D.; *Acc. Chem. Res.*, **2009**, *42*, 1669.
[145] Skourtis, S. S.; Waldeck, D. H.; Beratan, D. N. *Annu. Rev. Phys. Chem.*, **2010**, *61*, 461.
[146] Bingöl, B.; Durrell, A. C.; Keller, G. E.; Palmer, J. H.; Grubbs, R. H.; Gray, H. B.; *J. Phys. Chem. B*, **2013**, *117*, 4177.
[147] Yin, X.; Kong, J.; De Leon, A.; Li Y.; Ma Z.; Wierzbinski, E.; Achim, C.; Waldeck, D. H.; *J Phys. Chem. B*, **2014**, *118*, 9037-9047.
[148] McGuinness, C. D.; Nishimura, M. K. Y.; Keszenman-Pereyra, D.; Dickinson, P.; Campbell, C. J.; Bachmann, T. T.; Ghazalb, P.; Crainac, J.; *Mol. BioSyst.*, **2010**, *6*, 386-390.
[149] Frisch, M. J.; Trucks, G. W.; Schlegel, H. B.; Scuseria, G. E.; Robb, M. A.; Cheeseman, J. R.; Scalmani, G.; Barone, V.; Mennucci, B.; Petersson, G. A.; Nakatsuji, H.; Caricato, M.; Li, X.; Hratchian, H. P.; Izmaylov, A. F.; Bloino, J.; Zheng, G.; Sonnenberg, J. L.; Hada, M.; Ehara, M.; Toyota, K.; Fukuda, R.; Hasegawa, J.; Ishida, M.; Nakajima, T.; Honda, Y.; Kitao, O.; Nakai, H.; Vreven, T.; J. A. Montgomery, J.; Peralta, J. E.; Ogliaro, F.; Bearpark, M.; Heyd, J. J.; Brothers, E.; Kudin, K. N.; Staroverov, V. N.; Keith, T.; Kobayashi, R.; Normand, J.; Raghavachari, K.; Rendell, A.; Burant, J. C.; Iyengar, S. S.; Tomasi, J.; Cossi, M.; Rega, N.; Millam, J. M.; Klene, M.; Knox, J. E.; Cross, J. B.; Bakken, V.; Adamo, C.; Jaramillo, J.; Gomperts, R.; Stratmann, R. E.; Yazyev, O.; Austin, A. J.; Cammi, R.; Pomelli, C.; Ochterski, J. W.; Martin, R. L.; Morokuma, K.; Zakrzewski, V. G.; Voth, G. A.; Salvador, P.; Dannenberg, J. J.; Dapprich, S.; Daniels, A. D.; Farkas, O.; Foresman, J. B.; Ortiz, J. V.; Cioslowski, J.; Fox, D. J. Gaussian 09, Revision C.01 **2010**.
[150] Tomasi, J.; Mennucci, B.; Cammi, R. *Chem. Rev.* **2005**, *105*, 2999.
[151] Maier, J. A.; Martinez, C.; Kasavajhala, K.; Wickstrom, L.; Hauser, K. E.; Simmerling, C. *J. Chem. Theory Comput.* **2015**, *11*, 3696.
[152] Wang, J. M.; Wolf, R. M.; Caldwell, J. W.; Kollman, P. a; Case, D. a *J. Comput. Chem.* **2004**, *25*, 1157.
[153] Bayly, C. I.; Cieplak, P.; Cornell, W.; Kollman, P. A. *J. Phys. Chem.* **1993**, *97*, 10269.
[154] Wang, J.; Wang, W.; Kollman, P. A.; Case, D. A. *J. Mol. Graph. Model.* **2006**, *25*, 247.
[155] Jorgensen, W. L.; Chandrasekhar, J.; Madura, J. D.; Impey, R. W.; Klein, M. L. *J. Chem. Phys.* **1983**, *79*, 926.

156 Case, D. A.; Babin, V.; Berryman, J. T.; Betz, R. M.; Cai, Q.; Cerutti, D. S.; Cheatham, T. E. I.; Darden, T. A.; Duke, R. E.; Gohlke, H.; Goetz, A. W.; Gusarov, S.; Homeyer, N.; Janowski, P.; Kaus, J.; Kolossváry, I.; Kovalenko, A.; Lee, T. S.; LeGrand, S.; Luchko, T.; Luo, R.; Madej, B.; Merz, K. M.; Paesani, F.; Roe, D. R.; Roitberg, A.; Sagui, C.; Salomon-Ferrer, R.; Seabra, G.; Simmerling, C. L.; Smith, W.; Swails, J.; Walker, R. C.; Wang, J.; Wolf, R. M.; Wu, X.; Kollman, P. A. AMBER 14 2014.

4.0 ELECTRON TRANSFER IN NANOPARTICLE DYADS ASSEMBLED ON A COLLOIDAL TEMPLATE

This work has been published as Graff, B. M.; Bloom, B. P.; Wierzbinski, E.; Waldeck, D. H. The thesis author designed and executed nanoparticle assembly fabrication, collected all absorbance and fluorescence measurements, determined all electron transfer rates, developed a system specific two-state model for describing electron transfer in nanoparticle dyad systems, and wrote the manuscript. The supporting information for this chapter is provided in Appendix C. This chapter was published previously as Graff, B. M.; Bloom, B. P.; Wierzbinski, E.; Waldeck, D. H. *J. Am. Chem. Soc.,* **2016**, *138*, 13260. and is reprinted with permission.

This work shows how to create covalently bound nanoparticle dyad assemblies on a colloidal template and studies photoinduced charge transfer in them. New results are reported for how the electron transfer rate changes with the inter-nanoparticle distance and the energy band offset of the nanoparticles (reaction Gibbs energy). The experimental findings show that the distance dependence is consistent with an electron tunneling mechanism. The dependence of the rate on the energy band offset is found to be consistent with Marcus theory, as long as one performs a sum over final electronic states. These results indicate that our understanding of electron transfer

in molecular donor-bridge-acceptor assemblies can be translated to describe nanoparticle-bridge-nanoparticle assemblies.

4.1 INTRODUCTION

Electron transfer reactions are ubiquitous in nature, and their control is important for many technologies. This work explores fundamental aspects of photoinduced electron transfer between semiconductor nanoparticles, which are one promising material for use in new types of solar cells and solid-state lighting technologies.[157] In particular, bulk heterojunction solar cells are a low-cost photovoltaic technology,[158,159,160] however, the best bulk heterojunction solar cells currently have an efficiency of 8-10%, which is less than their predicted maximum efficiency of 15-18%.[161] Organic-inorganic nanoparticle composites offer one strategy for improving the performance of such inexpensive self-assembling photovoltaic structures but better control over the optical properties and the charge separation and recombination kinetics is required for its realization. This work develops our understanding of how to manipulate semiconductor nanoparticle properties, in particular their charge transfer and recombination kinetics, to yield efficient charge separation.

Over the past few decades, the study of electron transfer in donor-bridge-acceptor (DBA) supermolecules has provided a platform for examining fundamental features of electron transfer between molecular units. [162,163,164,165] Experimental electron transfer studies in molecular DBA systems have allowed for the detailed and rigorous examination of the predictions made by the

Marcus electron transfer model and its extensions. These studies have elucidated the dependence of electron transfer on reaction Gibbs energy and reorganization energy, as well as their dependence on molecular and solvent structure. Through the examination of different bridging units, the importance of bridge architecture, electronic structure, and connectivity have been revealed.[166,167,168,169,170,171,172] This understanding has allowed for the extension of these models to examine the role of solvent polarization[173] and solvent mediated electron tunneling.[174,175] The current study introduces an analogous platform with the aim of examining electron transfer between nanoparticles; i.e., donor and acceptor molecular units are replaced by semiconductor nanoparticles. The ability to vary the optical and electronic properties of semiconductor nanoparticles by varying their size[176] provides a strategy for examining whether or not Marcus theory and our understanding of electron transfer in molecules can be directly translated to nanostructures or whether they need to be modified.[177,178] This work provides a novel protocol for preparing donor-bridge-acceptor nanoparticle structures and examining electron transfer rates in them.

Charge transfer at semiconductor heterojunctions and interfaces has been studied since the middle of the twentieth century and it is well known that a staggered, or Type II, band alignment facilitates charge transfer.[179,180,181] The same energy level structure is important for charge transfer in semiconductor nanoparticles and a number of earlier works have demonstrated charge transfer for such nanomaterials. A recent review provides an up-to-date and comprehensive discussion for charge transfer involving nanoparticles,[182] including the importance of how donor-acceptor ratios, donor-acceptor distance, and environmental factors can affect observed electron transfer rates. As the current study examines charge transfer in cadmium selenide/cadmium telluride (CdSe/CdTe) heterojunctions this discussion focuses on the earlier work for these

materials. Scholes and coworkers have examined charge transfer in CdTe/CdSe heterostructure nanorods and core/shell nanoparticles. [183,184] They confirmed the presence of a charge transfer band from which they were able to quantify the reorganization energy, λ, and reaction Gibbs free energy, $\Delta_r G$. They found a very small reorganization energy which is consistent with the nanoscale size of the donor and acceptor. Several groups have studied charge transfer in CdSe and CdTe nanoparticle aggregates that are linked together electrostatically or covalently, and charge transfer rates in these systems range from picoseconds to nanoseconds.[185,186] It is likely that these assemblies contain a large variation in charge transfer rates because of their distribution of sizes, interparticle distance, and band energy differences. Additionally, because the nanoparticle aggregates that have been studied do not have uniform donor to acceptor molar ratios there can be large variations in the measured charge transfer rate.[185,187] While nanoparticle aggregates of this sort are highly relevant for understanding charge transfer in bulk heterojunction materials, more precise assemblies are needed to understand how the structural features impact charge separation and recombination kinetics, enabling the design of better bulk heterojunction materials.

This work describes electron transport kinetics of nanoparticle assemblies, approximately nanoparticle dyads, that have a more well-defined architecture than randomly formed aggregates of nanoparticles in solution. Preparation of such assemblies was accomplished by utilization of a colloidal template and stepwise formation of a designed nanoparticle composite architecture. Figure 4.1 shows a general scheme for the nanoparticle assembly formation and their anticipated structure.

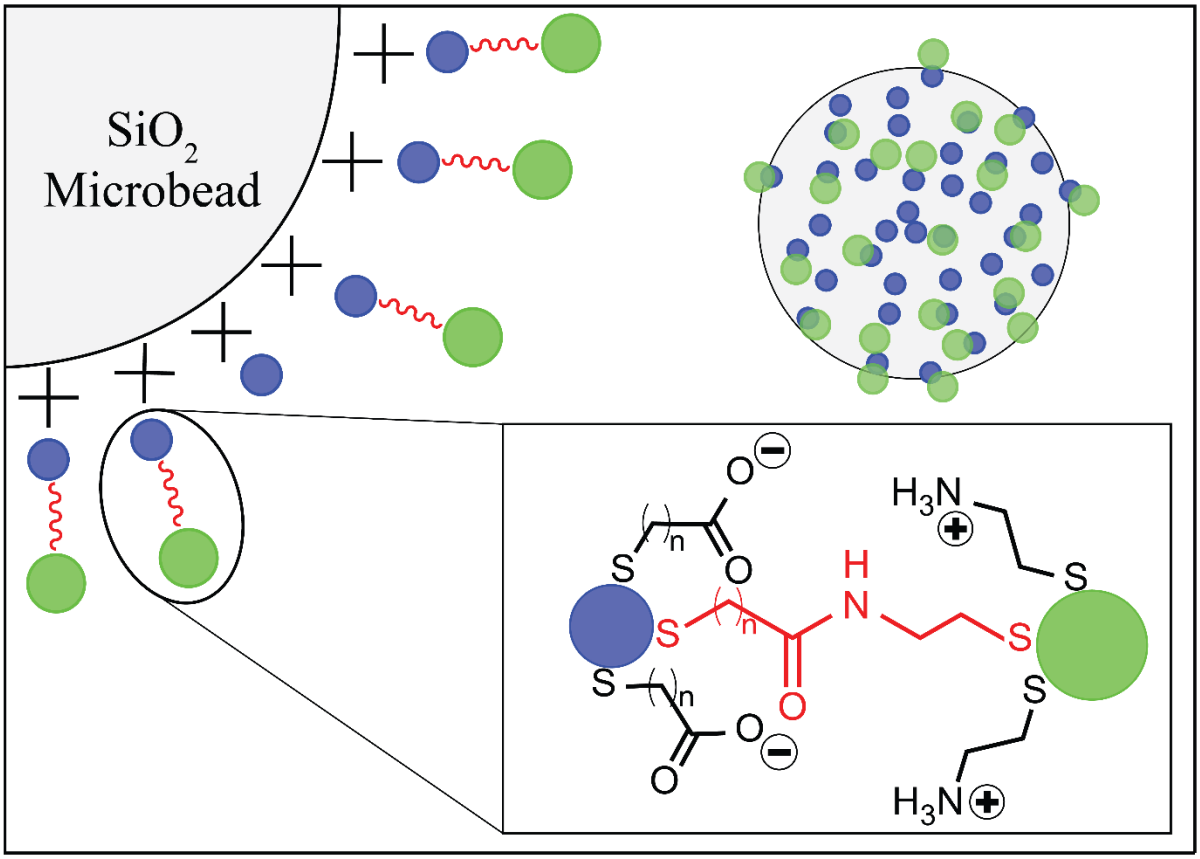

Figure 4.1 - Cartoon describing the attachment of the nanoparticles on a microbead. The acceptor nanoparticle (blue) is electrostatically attached to a SiO_2 template and covalently linked (red) to a donor nanoparticle (green) yielding a nanoparticle dyad on the microbead (2NPA). The upper left corner of the image depicts a cartoon of a single microbead with many nanoparticles on the surface. The upper left hand corner zooms in on one section of the microbead containing many nanoparticle dyads and the lower right hand corner zooms in on a single dyad. The capping ligand on the donor nanoparticles were always cysteamine (CA), but the acceptor nanoparticles had a variety of different surface ligands. The number of methylene units, n, in the cartoon indicate the various ligands utilized in these experiments (n=1 TGA, n=3 MBA, n=5 MHA, n=7 MOA, n=10 MUA). Note that in the zoomed in image, ligand sizes are dramatically exaggerated with respect to the size of the nanoparticle.

Covalent linkage of the nanoparticles by way of organic capping ligands on the nanoparticles provides good control over the interparticle distance and enables independent manipulation of the nanoparticle size. By studying the relationship between the electron transfer rate and the interparticle distance, changed by variation of the number of methylene groups in an amide linker chain, we demonstrate that the natural log of the electron transfer rate falls off linearly with the length of the interparticle bridge. By studying the electron transfer rate as a function of

the reaction driving force (Gibbs free energy, $\Delta_r G$) we demonstrate that the electron transfer rate increases as $\Delta_r G$ becomes more negative, and this dependence can be modeled using semi-classical Marcus theory. These findings imply that our understanding of electron transfer in molecular systems can be translated to describe electron transfer in inorganic semiconductor nanoparticle systems.

4.2 RESULTS

4.2.1 Demonstration of Nanoparticle Dyad Assemblies

The formation of nanoparticle assemblies on a 500 nm diameter silicon dioxide (SiO_2) sphere has been confirmed by fluorescence, zeta potential, and electron microscopy measurements. An excess of thioglycolic acid coated cadmium telluride nanoparticles (TGA-CdTe) were added to a solution of amine coated SiO_2 microspheres, and it was left to shake for one hour. After one hour, the assembly was purified by filtration through a 100 nm porous filter, see Appendix C for a more detailed description of the purification protocol. The assembly is driven by the electrostatic attraction of the negatively charged nanoparticle for the positively charged microsphere.

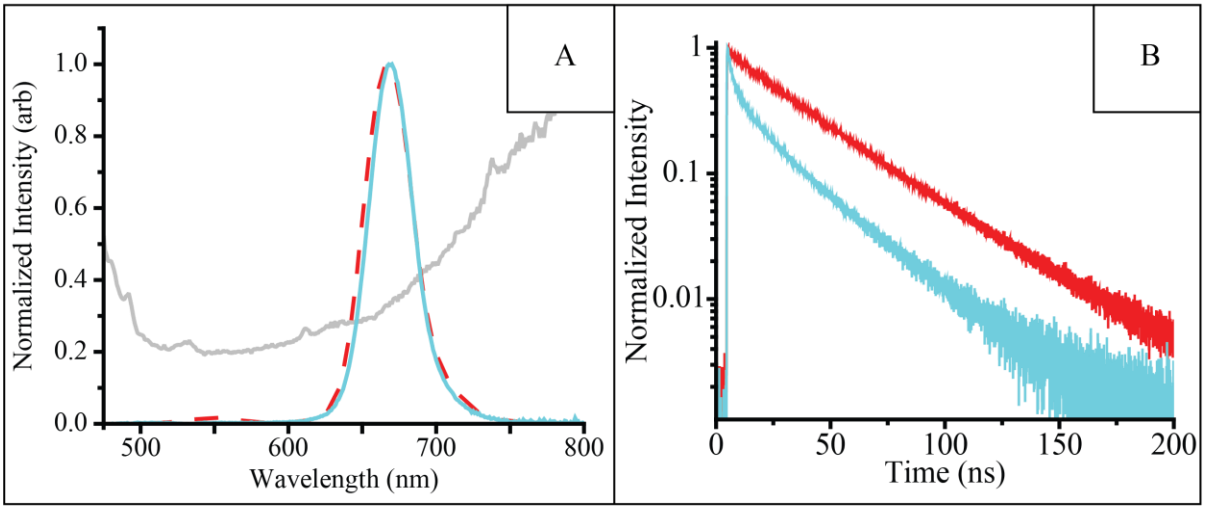

Figure 4.2 - Panel A shows normalized steady state fluorescence spectra of the TGA-CdTe in solution (red dashed) and assembled on the colloidal microspheres (1NPA) in solution (blue) (λ_{ex}: 440 nm, 0.7 nm resolution, 0.1 s integration time). Note that the microsphere scattering is subtracted from the 1NPA spectrum. The scattering from the microsphere (grey) is shown and is amplified by 25 times compared to that of the 1NPA spectrum. Panel B shows photoluminescence decays of the TGA-CdTe in solution (red) and the 1NPA (blue) in solution.

Figure 4.2A and Figure 4.2B show spectral data confirming the loading of negatively charged CdTe nanoparticles onto the silica beads, 1NPA assemblies. The spectra in Figure 4.2A show the characteristic emission peak from the TGA-CdTe (red dashed) in solution and when it is bound onto the microbead (blue). Figure 4.2B shows the photoluminescence decay for the nanoparticle on the microbead (blue) and compares it to that of the nanoparticle in solution (red). Note that the fluorescence decay for the 1NPA differs from that of the free nanoparticle in solution. The electron transfer analysis accounts for this effect (*vida infra*); however, its origin will be reported on elsewhere. When the nanoparticle is removed from the microsphere, however, the photoluminescence decay recovers to that obtained before bead loading (see Figure 9.5).

After the first nanoparticle layer was successfully assembled, a second nanoparticle could be attached to the first one, either through electrostatic interactions or by covalent bonding. These two nanoparticle assemblies (2NPA) on the microsphere were confirmed by zeta potential

(electrokinetic potential) and fluorescence energy transfer measurements. After the addition of each oppositely charged layer a zeta potential measurement was taken. A change in the sign of the zeta potential indicated the presence of an oppositely charged layer on the surface of the microbead. The fluorescence of the filtrate, 1NPA, and 2NPA were monitored. The decrease in the filtrate emission intensity after each successive filtration indicated that no free nanoparticle was left in solution. Additionally, the existence of an emission peak from each nanoparticle in the 2NPA was indicative of their attachment. In the studies reported herein, a positively charged cysteamine-coated CdTe (CA-CdTe) nanoparticle was covalently attached to a TGA-CdTe through the formation of an amide bond, facilitated by the catalysts 1-ethyl-3-(3-dimethylaminopropyl)carbodiimide (EDC) and N-hydroxysulfosuccinimide (sulfo-NHS). The purification of the reaction mixture was the same as that used for the 1NPA. Throughout this series of experiments, the ratio between the donor and acceptor nanoparticles was maintained at **3** donor: **4** acceptor. We refer to these assemblies as nanoparticle dyads.

Formation of the 1NPA and 2NPA was further confirmed by electron microscopy. Because of instrumental limitations it was necessary to change the relative sizes of the particles in the assemblies and to increase the microbead loading so that they could be imaged; however, the chemistry and procedures were kept the same. For the images shown in Figure 4.3 the microspheres were approximately 150 nm; the CdSe nanoparticle was 5.5 nm, and the CdTe nanoparticle was 4.0 nm. Note that the smaller microsphere reduced charging effects in the scanning transmission electron microscopy (STEM) measurement, but it caused the filtration procedure to be less effective. Figure 4.3A shows an example STEM image of a colloidal silica template with a nominal diameter of 150 nm. The beads composed of the template are characterized by a spherical shape with a surface that is devoid of any distinguishable features.

The 1NPAs (Figure 4.3B) show distinguishable features (ca. 5 nm) that are uniformly distributed on the template's surface. These dark spots in Figure 4.3B are assigned to the 4.0 nm CdTe nanoparticles and they show a typical separation of several nanometers along the surface. Presumably, the nanoparticles form a sparse monolayer rather than a compact film because of their electrostatic repulsion. The 2NPA (see Figure 4.3C) is less evenly distributed than the 1NPA; nevertheless, a bi-layer type surface film is formed in certain parts of the template surface, rather than large aggregates of the nanoparticles. Please note that while there are acceptor nanoparticles (inner layer) that do not have any donor nanoparticles (outer layer) attached to them, only the donor nanoparticles are photoexcited. Details in the structures of 1NPA and 2NPA are somewhat more distinguishable on the images digitally processed with an FFT bandpass filter,[188] which improves the image contrast at the edges of the beads (see insets in Figure 4.3A-C). Additional examples of STEM images of 1NPA and 2NPA and particles size analysis based on microscopy data are provided in Appendix C.

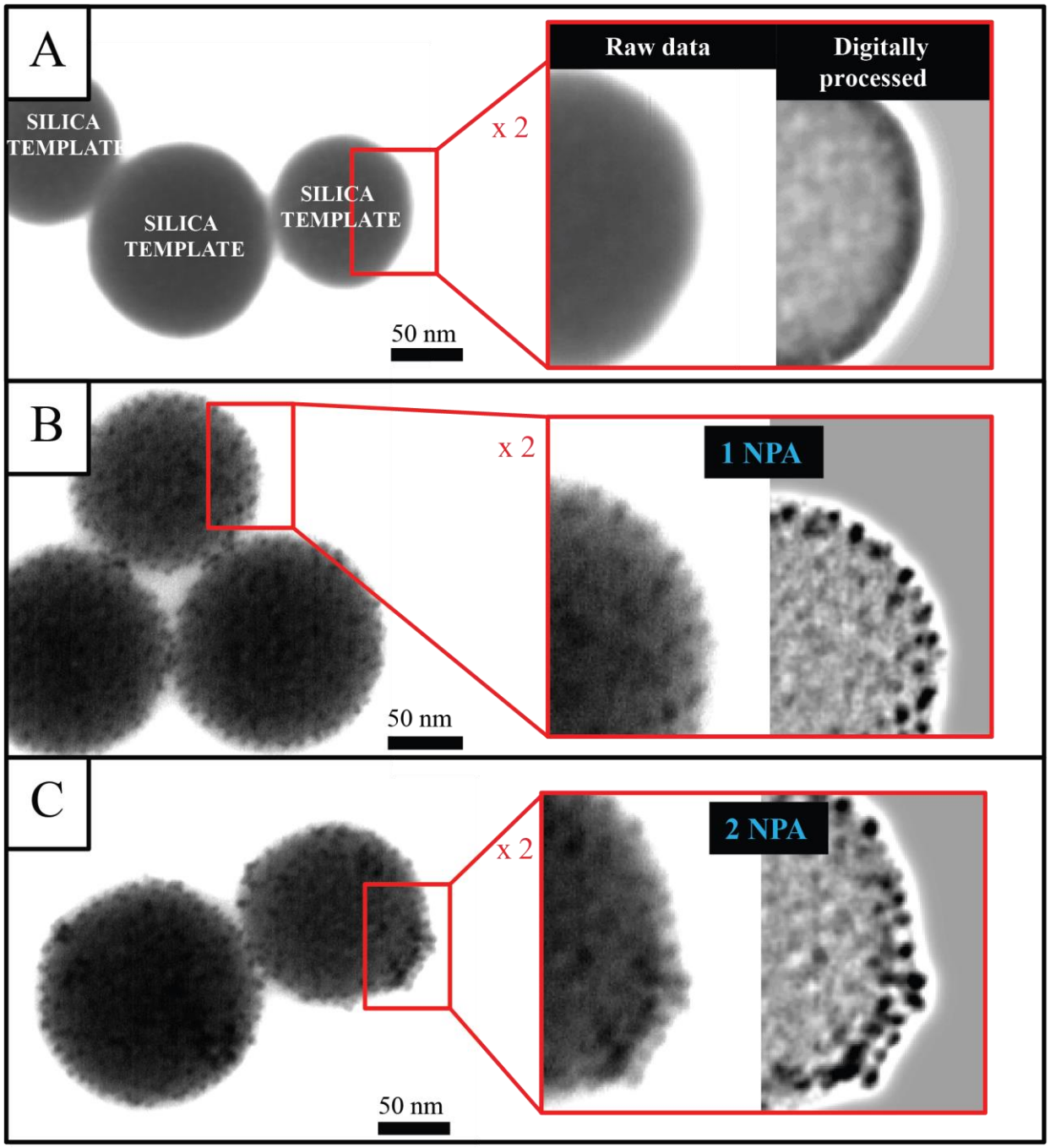

Figure 4.3 - Electron Microscopy Characterization. Panel A shows the micrograph of the silica sphere used as a template for the nanoparticle assembly. Panel B shows an example of the 1NPA composed of CA-CdTe on silica beads. Panel C presents an image for 2NPA assemblies obtained after further modification of the 1NPA with MPA-CdSe. Insets in A-C show digitally two-fold magnified fragments of the original micrographs together with images processed with an FFT bandpass filter. Contrast of the features outside of the c.a. 1.5 - 7 nm diameter range was suppressed by the bandpass filter (right panels in the insets). Note that the diameter of the silica spheres template and the size of the nanoparticles differs significantly from the parameters used in electron transfer studies. See text for details.

Additional data that confirm the fabrication of 1NPAs and 2NPAs are provided in Appendix C.

4.2.2 Mechanism of Fluorescence Quenching

The mechanism of fluorescence quenching in the nanoparticle dyads can be controlled by manipulating the energy bands of the individual nanoparticles. Figure 4.4A shows a Type I system which has an energy level structure that allows both charge transfer and Förster energy transfer if the wider bandgap nanoparticle is excited; the spectral overlap integral between the donor emission (green, CA-CdTe) and the acceptor absorption (red, TGA-CdTe) was maximized (Figure 4.4C). In contrast, if the smaller bandgap nanoparticle, TGA-CdTe, is excited, then both charge transfer and Förster energy transfer are blocked. Figure 4.4B shows a Type II, or staggered, energy band offset. In this case, if only the wider bandgap semiconductor (TGA-CdSe) is excited both Förster energy transfer and hole transfer to the smaller band gap nanoparticle (CA-CdTe) are allowed. In contrast, excitation of the smaller bandgap nanoparticle allows only electron transfer from the smaller bandgap CA-CdTe to the larger bandgap TGA-CdSe.

The electronic state energies of the CdSe and CdTe nanoparticles reported in Figure 4.4 and Figure 4.5 are inferred from previous experimental measurements. For CdSe nanoparticles functionalized with a thiol linker it was shown that the valence band maximum does not shift greatly with size.[189] The conduction band minimum was then determined by using the optical band gap and exciton binding energy of the nanoparticle.[190] For CdTe nanoparticles the valence and conduction band energies reported by Jasieniak et. al.[191] were utilized. Although a different

passivating ligand was used in their experiments than in the nanoparticle assemblies studied here, electrochemical measurements were performed on a 4.1 nm CA-CdTe nanoparticle, and they showed that the valence band maxima are in good agreement with Jasieniak et. al.[191] (Figure 9.6).

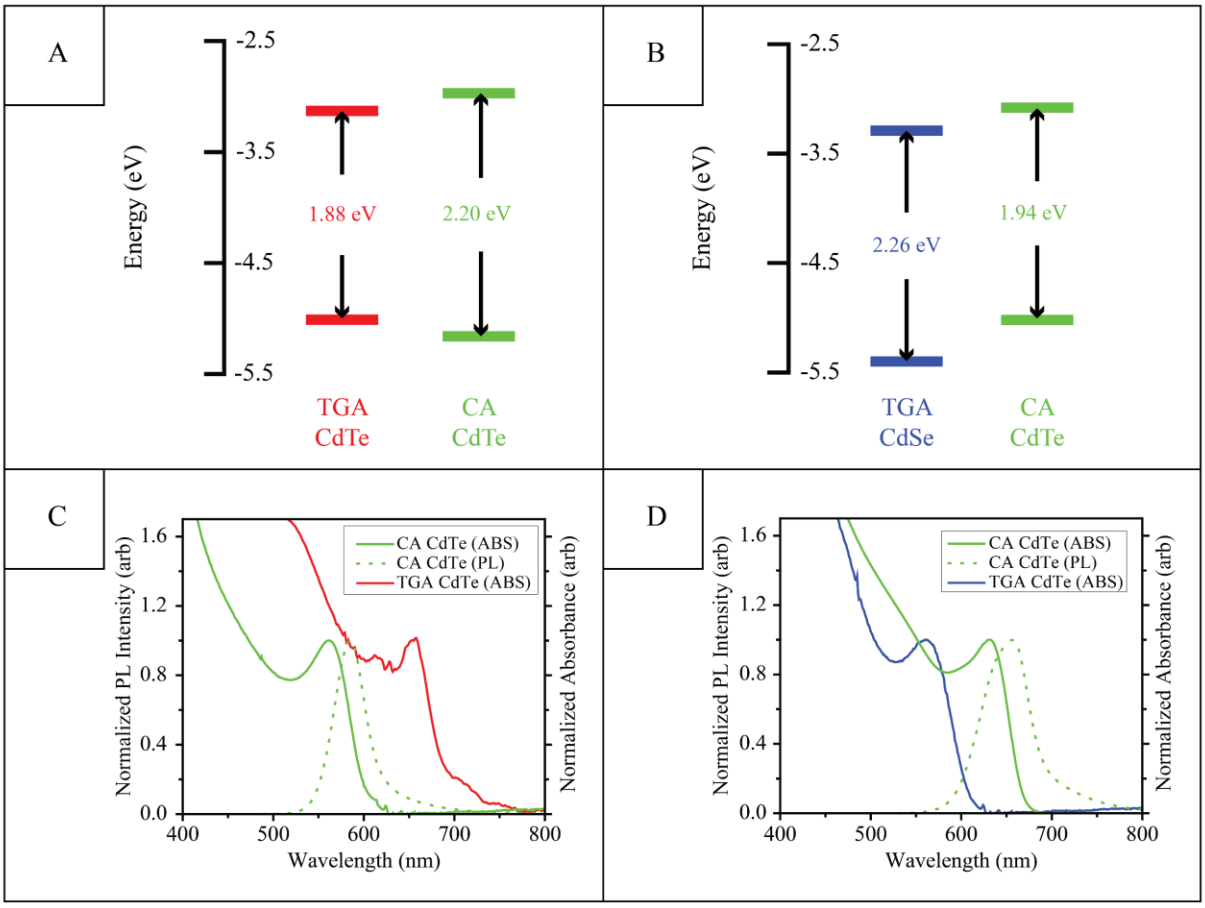

Figure 4.4 - Energy schemes and optical spectra are shown for the nanoparticle assemblies under investigation. Panels A and B show the donor (green) and acceptor (red/blue) energy levels for the case of Förster energy transfer (A) and electron transfer (B). Panels C and D show the normalized absorbance (solid) and photoluminescence (dashed) in the Förster energy transfer (C) and electron transfer case (D).

Time-resolved photoluminescence (PL) measurements were used to monitor the quenching rate of the donor, CA-CdTe, for the two assemblies shown in Figure 4.4. In each case the fluorescence decay profiles were non-exponential, but could be well characterized by a distribution of lifetime components. To ensure a consistent analysis the nanoparticle assemblies

were also fit to a sum of exponentials. Examples of the fluorescence decay data and the fitting are provided in Figure 9.8. For this survey study, the fluorescence decay rate of the CA-CdTe free in aqueous solution was used as a reference system for extracting the quenching rate constants.

Two interparticle distances, obtained by changing the number of methylene groups in the capping ligand for the acceptor nanoparticle, were studied for the Type I and Type II nanoparticle assemblies (see Table 4.1). For the short linker, thioglycolic acid (TGA) was used; and for the long linker, mercaptoundecanoic acid (MUA) was used. For the Type I assemblies both distances were found to have a quenching rate of about 1.65×10^{9} s^{-1}, and for the Type II assemblies the donor nanoparticle was quenched nine times more strongly for the shorter interparticle distance than for the longer distance case (See Table 4.1). The difference in fluorescence quenching rate is consistent with the difference in distance dependences that are expected for energy transfer and electron transfer; and it substantiates the nanoparticle dyad energy band alignments of Figure 4.4. If one approximates the nanoparticles as dipole absorbers, the Förster energy transfer model gives a Förster radius of 50 Å which is consistent with the weak distance dependence. Electron transfer rates are expected to decay more rapidly than Förster energy transfer rates as a function of distance, which indicates that the Type II heterojunction assemblies undergo electron transfer.[185]

Table 4.1 - The dyad assemblies (2NPA) and their corresponding quenching rate, kquench

Type	**I**	**I**	**II**	**II**
Distance (Å)	6.2	12.2	6.2	12.2
$\boldsymbol{k_{quench}}$ **(ns^{-1})**	1.7 ± 0.1	1.6 ± 0.1	3.6 ± 0.08	0.4 ± 0.08
X	TGA	MUA	TGA	MUA

a - Type I assemblies are Microsphere/X-CdTe/CA-CdTe and the Type II assemblies are Microsphere/X-CdSe/CA-CdTe. X is the capping ligand on the acceptor QD; TGA is thioglycolic acid and MUA is mercaptoundecanoic acid. The error in k_{quench} was calculated from the width of the lifetime distribution peak; see SI for more detail.

Note that the quenching rates in Table 4.1 overestimate the actual electron transfer rate, because this analysis does not account for the fact that the nanoparticles experience some intrinsic quenching on the microbead assembly (see Figure 4.2B). In order to provide a more realistic reference system for the quantitative studies of the electron transfer rate that are described below, a Type I system for which Förster energy transfer and electron transfer are blocked was used as the reference system (*vide infra*).

4.2.3 Distance Dependent Electron Transfer Study

The electron transfer rate was examined as a function of the inter-nanoparticle distance by using five acceptor ligand lengths, differing by the number of methylene groups. Because the nanoparticle's proximity to the microsphere causes some quenching (Figure 4.2B), a Type I nanoparticle assembly, in which a larger bandgap nanoparticle replaces the electron acceptor nanoparticle, was used as a reference system (see Figure 4.5A). The Type I system was chosen as the reference because it maintains the same assembly structure, just with a larger bandgap (smaller in size) CdSe acceptor nanoparticle. In every case, the donor CA-CdTe has a smaller

band gap so that Förster energy transfer is not significant. Additionally, only the donor nanoparticle is excited to ensure that electron transfer rather than hole transfer is observed.[192] The relative conduction and valence bands for the Type I and Type II systems utilized in this distance dependent study were calculated in a manner similar to that described above.

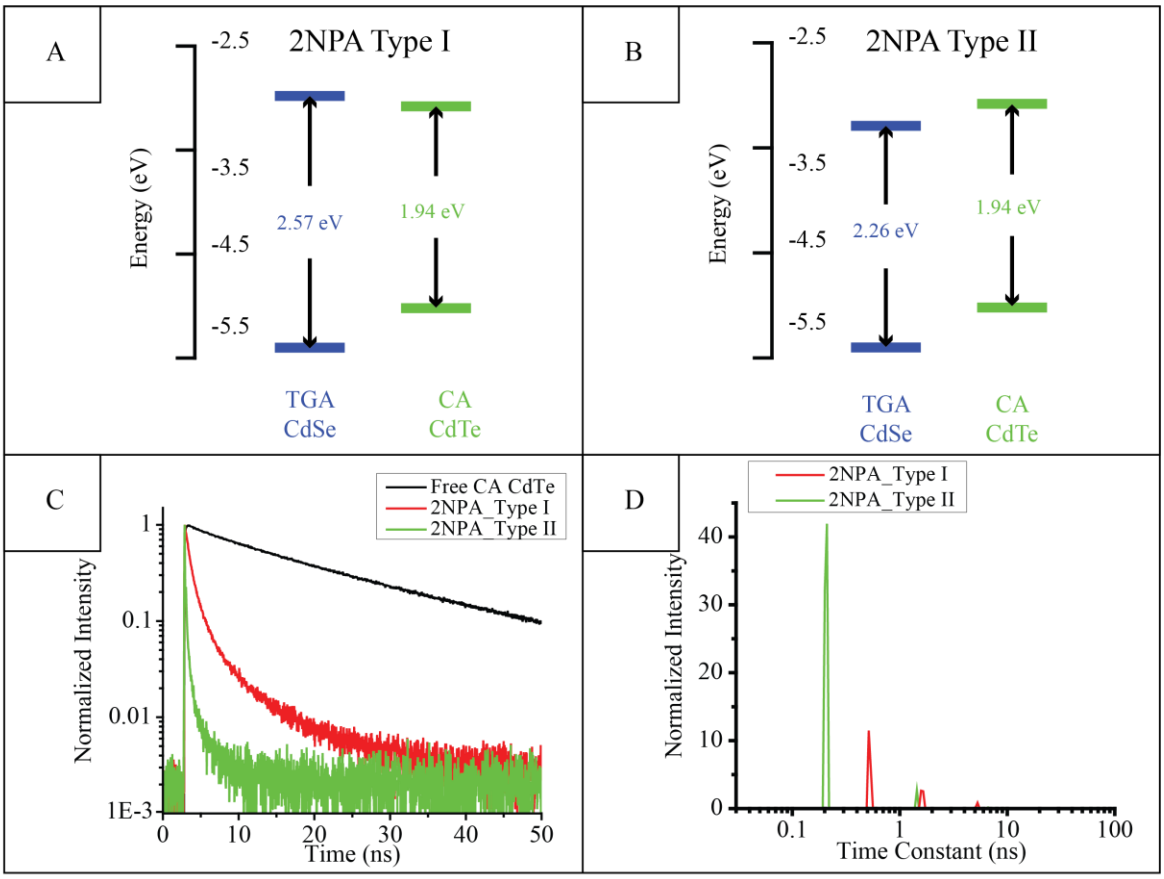

Figure 4.5 - Band diagrams are shown for the nanoparticle assemblies used in the electron transfer rate measurements; in each case the smaller band gap nanoparticle, CA-CdTe, is photoexcited. The energy scheme in panel A depicts the band edges for the Type I reference system, and the scheme in panel B depicts the band edges for the photoinduced electron transfer. Photoluminescence decays are shown in panel C and the lifetime distribution fitting results are shown in panel D; for the CA-CdTe free in solution (black), the Type I 2NPA (red), and the Type II 2NPA (green). The donor emission is quenched most dramatically in the Type II nanoparticle dyad assembly

Figure 4.5 provides an example of the fluorescence decay data and the lifetime distribution analysis for the two different types of assemblies. Figure 4.5C shows fluorescence decays for the

free donor nanoparticle in solution (black), the Type I 2NPA (red), and the Type II 2NPA (green). Comparison of the free donor in solution to the Type I system shows that the microsphere assembly introduces some quenching; however, a significant increase in the quenching of the donor occurs when the Type II acceptor is present. Figure 4.5D shows the lifetime distributions that are obtained by fitting the fluorescence decays of the Type I and Type II assemblies in Figure 4.5C. These distributions show that the long lifetime components (τ_{long}) have low amplitude and do not change significantly in shape or position between the two assemblies; however, the short lifetime components change dramatically. Thus, it was assumed that the short lifetime component (τ_{short}) provides an accurate measure of the electron transfer. The electron transfer rate was determined from the difference in the two short lifetime rate constants ($k = \frac{1}{\tau_{short}}$); namely

$$k_{Type\ II} - k_{Type\ I} = k_{et} \qquad \text{Equation 4.1}$$

The error in the electron transfer rate constant has both systematic and random contributions. Systematic errors can arise from the use of the Type I reference system and the focus on the short time constant to obtain the rate. Because the Type I reference system accounts for electrostatic field effects on the photoluminescence and includes possible surface state quenching pathways, it is most similar to the Type II system, while blocking the electron transfer from the band edge of the donor to the bands of the acceptor. Note that a dendrimer, PAMAM Dendrimer G1.5 Carboxylate Sodium Salt (Figure 9.11), control was also used and gives results similar to those found for the Type I TGA-CdSe system (see Appendix C). In order to ensure that the method of

analysis utilized was accurately describing the relationships reported in this study, the average lifetime of the decay was compared to the short time constant of each decay and it was found that there is a linear relationship between the short time constant and the average lifetime. This indicates that while the magnitude of the electron transfer rates may vary from the reported values the relationships that are described herein persist. The random error was estimated by using the full-width-at-half maximum of the short-lived lifetime components from the lifetime distribution fits and then propagating the error. For more discussion of these analyses and detailed k_{et} evaluation see Appendix C.

Figure 4.6 shows a plot of the natural log of the electron transfer rate constants versus the number of methylene units in the nanoparticle linker. These data show the results from multiple trials involving different batches of both donor (CA-CdTe) and acceptor (CdSe) nanoparticles as well as different nanoparticle coverages on the microsphere. Note that k_{et} does not change significantly with coverage, for the range studied. The ratio of donor to acceptor nanoparticles was kept consistent; even when the coverage of nanoparticle dyads on the surface of the microsphere was varied over a factor of three. The data in Figure 4.6 are well described by a linear dependence on the number of methylene groups (n) in the ligand, namely

$$k_{et} = k_{et}\,(n = 0) \cdot \exp(-\beta n) \quad \text{or} \quad \ln(k_{et}) = -\beta n + \ln(k_{et}(n = 0)) \qquad \text{Equation 4.2}$$

where k_{et} is the electron transfer rate constant and β is the tunneling decay constant per methylene unit. Note that for the number of methylene groups, n, it has been assumed that all of the linkages between the donor and acceptor (from thiol to thiol) including the amide bond

behave akin to a methylene group. For tunneling through a self-assembled monolayer of alkanes, workers[193,194] have reported β values ranging from 0.9 to 1.1 per methylene, however a β of 0.68 was observed in this study. Explanations for rationalizing this difference in distance dependence are described in the discussion section.

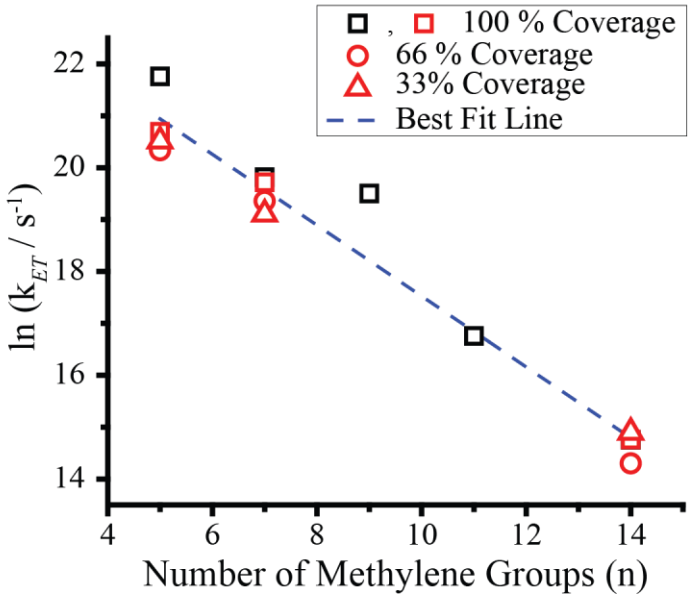

Figure 4.6 - The natural log of the electron transfer rate constant is plotted against the number of methylene groups. The blue dashed line shows a best fit by Equation 4.2 and it has a slope of 0.68 ± 0.04 (error determined via least-squares fitting). The black and red symbols indicate different batches of donor and acceptor nanoparticles. Various coverages for the same batch of nanoparticles were studied and are distinguished by their symbol: maximum coverage is a square (□), two-thirds maximum coverage is a circle (○), and one-third maximum coverage is a triangle (△). In all cases the donor to acceptor ratio was maintained.

4.2.4 Dependence on $\Delta_r G$

The electron transfer rate in the nanoparticle dyad systems was studied as a function of the reaction Gibbs energy, $\Delta_r G$, by changing the size of the acceptor nanoparticle (CdSe) which changes the conduction band offsets. In all cases the interparticle distance was fixed by using

cysteamine (CA) as the ligand shell for the donor nanoparticle and mercaptohexanoic acid (MHA) as the ligand shell for the acceptor nanoparticle, ~ 14.8 Å. Experimentally it is observed that as the reaction free energy becomes more favorable, the electron transfer rate increases in a monotonic manner (Figure 4.7).

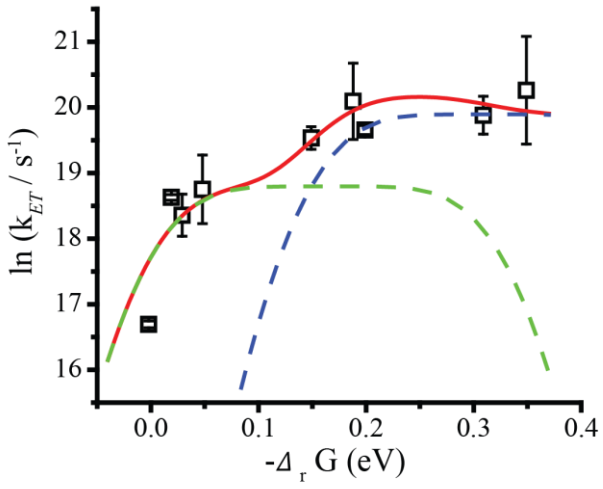

Figure 4.7 - The natural log of the electron transfer rate constant is plotted against the negative $\Delta_r G$ for the experimental data (black squares). The red curve shows a fit by the semi-classical Marcus equation with a sum over electronic final states for the first two energetic states of the acceptor (solid red); the dashed lines indicate using only the first excited state (green) or the second excited state (blue); see text for details.

The experimental data are well described by the traditional semi-classical Marcus equation (Equation 4.3), as long as one includes the two possible final electronic states; the S_e and P_e that reside in the acceptor's conduction band. The S_e state of CdSe is taken to be the conduction band edge and the difference in energy between the S_e and P_e state was fixed at 0.15 eV in keeping with earlier reports.[195] While use of the S_e or P_e state alone was not able to reproduce the data (see dashed curves), summing over the first two electronic states of the acceptor was able to represent the experimental data accurately (Figure 4.7, red). More details on the determination of the conduction and valence bands are provided in the SI. The energy offset of these two discrete

electronic states are what cause the Marcus curve to display a second rise at approximately -0.15 eV. For $\Delta_r G$ near zero the S_e state dominates, but as $\Delta_r G$ becomes more negative the P_e state contributes more to the reaction rate. Equation 4.3 shows the explicit form of the semiclassical equation[173]

$$k_{ET} = \frac{2\pi}{\hbar}|V|^2 \frac{1}{\sqrt{4\pi\lambda_s k_B T}}\left[\sum_{n=0}^{\infty} e^{-S}\left(\frac{S^n}{n!}\right)\exp\left(-\frac{(\lambda_s + \Delta_r G(S_e) + nh\nu)^2}{4\,\lambda_s k_B T}\right)\right. \\ \left. + 3\sum_{n=0}^{\infty} e^{-S}\left(\frac{S^n}{n!}\right)\exp\left(-\frac{(\lambda_s + \Delta_r G(P_e) + nh\nu)^2}{4\,\lambda_s k_B T}\right)\right] \quad \text{Equation 4.3}$$

where k_B is Boltzmann's constant, $|V|$is the electronic coupling matrix element, $\Delta_r G$ is the reaction free-energy, λ_s is the outer-sphere or solvent reorganization energy, ν is the frequency of the effective quantized vibrational mode, and S is the Huang-Rhys factor given as the ratio of the inner-sphere reorganization energy, λ_v, to the quantized mode energy spacing, $\frac{\lambda_v}{h\nu}$. The $h\nu$ term refers to the energy of a single effective quantized mode associated with the electron transfer reaction, and in this analysis it was taken to correspond to the longitudinal optical phonon frequency of the acceptor (207 cm^{-1} for CdSe).[196] The solvent reorganization energy was approximated by using a two-sphere model in a dielectric continuum; namely[173]

$$\lambda_S = \frac{e^2}{4\pi\varepsilon_0}\left(\frac{1}{D_{OP}} - \frac{1}{D_S}\right)\left(\frac{1}{2r_D} + \frac{1}{2r_A} - \frac{1}{R}\right) \quad \text{Equation 4.4}$$

where D_{OP} is the optical dielectric constant, D_S is the static dielectric constant, $r_D$is the donor nanoparticle radius, r_A is the acceptor nanoparticle radius (which is changing in this system), and R is the interparticle distance. The two sphere model predicts that the value of the solvent reorganization energy, λ_s, should lie between 0.005 eV and 0.05 eV; and the fit to the experimental data was constrained to have a λ_s over this range. In addition to λ_s, the electronic coupling parameter and the inner-sphere reorganization energy, λ_v, were floated to minimize the residuals. The best fit curve is indicated by the red line in Figure 4.7. The best fit parameters were found to be $\lambda_s = 0.029$ eV, $\lambda_v = 0.009$ eV, and $|V| = 2.7$ cm^{-1}.

Note that Equation 4.3 assumes that the quantized vibrational mode is significantly larger than k_BT; however this assumption is not strictly valid. A more appropriate model is available for cases in which $hv \approx k_BT$,[197] and it gives a similarly good fit to the data, however the best fit value of the electronic coupling is 0.3 cm^{-1} rather than 2.7 cm^{-1}. See the discussion and Appendix C for more details.

4.3 DISCUSSION

4.3.1 Electron Transfer Kinetics

These studies build upon the earlier work of Wu et. al.,[185] that investigated electrostatically bound semiconductor nanoparticle aggregates of variable size, by studying covalently bound semiconductor nanoparticle donor-acceptor dyads. The donor nanoparticle was photoexcited at

the first excitonic peak maximum (635 nm); and to minimize the effect from scattering by the microspheres, the nanoparticle fluorescence was collected at the red edge of the emission spectrum. The photoluminescence decays were fit using a lifetime distribution analysis. The difference in quenching between the Type II system which promotes electron transfer and the Type I control system was used to determine the electron transfer rate (Equation 4.1). Comparison of the lifetime distributions shows that the dominant change in the lifetime distribution is a shift in the value of the shortest lifetime component, and it was used to calculate an electron transfer rate (See Equation 4.1).

The ability to use a single lifetime component to extract an electron transfer rate differs significantly from what other groups have observed.[198,199,200,201] Frequently, electron transfer rates are calculated as a difference between the average lifetime of a control system (where electron transfer is not favored) and the investigated system (where electron transfer is favored). However, this process provides an effective electron transfer rate that is an average over a nanoparticle distribution that is not necessarily known or well defined. In the absence of a charge transfer band it has been difficult to attribute electron transfer as arising from a single time constant in these complex assemblies.[202] For example, if we mimic the type of system designed by Wu et. al.[185] and fabricate covalently bound nanoparticle aggregates in solution, the fit to the experimental photoluminescence decays are significantly less clear and the electron transfer rates are not able to be determined as previously described in this study. Figure 4.8 shows data from such a system in which it can be seen that the long lived lifetime components are not fixed in shape and position in the presence of the acceptor nanoparticle. Additionally, the amplitude of the long-lived lifetime components are much larger than that which is reported in

Figure 4.4D. Thus, the nanoparticle dyad assemblies studied here represent an advancement toward the sort of system homogeneity found in molecular dyads.

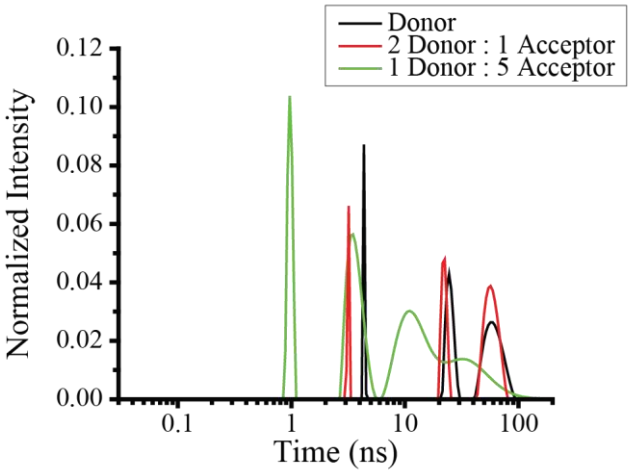

Figure 4.8 - Sample of the PL distribution fitting for the Type II covalently bound nanoparticle assemblies. The free donor in solution, MPA CdTe, (black) 2 Donor: 1 Acceptor (red), and 1 Donor : 5 Acceptor (green) are depicted here. The prefactors before donor and acceptor are molar ratios.

4.3.2 Electron Transfer Rate as a Function of Interparticle Distance

The data in Figure 4.6 report how charge transfer changes with the distance between two semiconductor nanoparticles that form a dyad. Over the last two decades a number of closely related studies have been performed; other research groups have investigated how electron transfer rates in semiconductor nanoparticles attached to either molecular/polymer[203] or metal/metal oxide[202,204] systems change as a function of donor-acceptor distance. In the metal and metal oxide systems, the semiconductor quantum dots have been linked through a molecular bridge, and electron transfer between a semiconductor quantum dot and a metal oxide[202] was studied as a function of interparticle distance yielding a decay parameter of 0.94 per methylene.

This is similar, but is somewhat larger than the β value of 0.68 per methylene found for the 2NPAs. Tagliazucchi et. al.,[203] studied electron transfer between CdSe nanoparticles and poly(viologen) for varying viologen units, and found β to be 0.8 per Å, and if one assumes the length of a methylene unit is 1.26 Å,[205] then the value of β for this work is determined to be 0.54 per Å. Thus, the decay parameter for the CdSe-polymer system[203] is similar to the value determined for these CdTe-CdSe dyad systems.

For traditional alkane self-assembled monolayers the distance dependence for alkane chains is reported to range from 0.9 to 1.1 per methylene.[193,194] There are a few explanations for why the distance dependence for this system would be less than the value of 1.0 per methylene. The current system has an amide linkage, and others report that amide groups can enhance the electron transfer efficiency and yield a β that is less than 1.0.[204,206,207] Additionally, when the molecules in a SAM are not oriented normal to the surface, both 'through bond' superexchange and 'through space' superexchange can contribute to the electron tunneling. For example, alkanethiol SAMs on indium phosphide with a 55 degree tilt angle were shown to have a β value of 0.49 per methylene.[194,208] It is likely that the packing of the ligands on the surface of the nanoparticles is not perfect, thus as the chain length increases there is likely some variation in the effective donor-acceptor distance. Since it is unlikely that the ligands on the nanoparticle surface are entirely perpendicular to the surface or perfectly packed on the surface and the fact that they contain an amide group in the middle of the chain, the β value reported for the dyads seems reasonable.

In complex nanoscale systems, where electron transfer is studied as a function of distance, slopes that are much less than one are frequently reported.[168,209,210,211,212,213] Gilbert et. al.[168] describes molecular wires in which electrons can hop along the bridge, as well as tunnel through it,

yielding smaller β values. In complex two nanoparticle systems separated by "alkane-like" linkers β values have been reported to be 0.42[212] and 0.08[213] per Å. For the current system, very shallow slopes are not observed, which is consistent with an electron tunneling mechanism by way of a covalent pathway of saturated C-C bonds. Lastly, we note that the magnitude of the electron transfer rate for the shortest linker, TGA, falls within the regime of reported electron transfer rates in the literature for dyes directly attached to a nanoparticle.[202,203,214,215]

4.3.3 Free Energy Dependence of the Electron Transfer

Other groups have observed an increase in electron transfer rate with an increase in driving force, even in locations where the inverted regime is expected.[177,216,217,218,219] Figure 4.7 and Figure 4.9 show plots of the electron transfer rates versus $-\Delta_r G$, as well as fits by different versions of the Marcus model. As noted earlier, $h\nu$ was fixed at 207 cm^{-1} [196] and λ_s was restricted to lie in the range of 0.005 eV to 0.05 eV. The longitudinal optical (LO) phonon of the acceptor, CdSe, used for the quantized mode, ν, is known to be important for the carrier relaxation in the CdSe conduction band. It is reported in the literature to be 207 cm^{-1} over the size regime studied.[196] As a caveat, it should be noted the value of the LO phonon does change as a function of nanoparticle size, particularly for very small nanoparticle diameters; however, the change is small ~ 5 cm^{-1}, and does not affect the fit quality. An appropriate range for the solvent reorganization energy, λ_s, was chosen by using a two-sphere model.[220] In a CdSe-CdTe nanorod heterostructure reported on by Scholes et. al.[220], a charge transfer band was present and the reorganization energy of 0.02 eV

was calculated directly using the shape of the free energy curves. Thus, the best fit value of 0.029 eV seems quite reasonable.

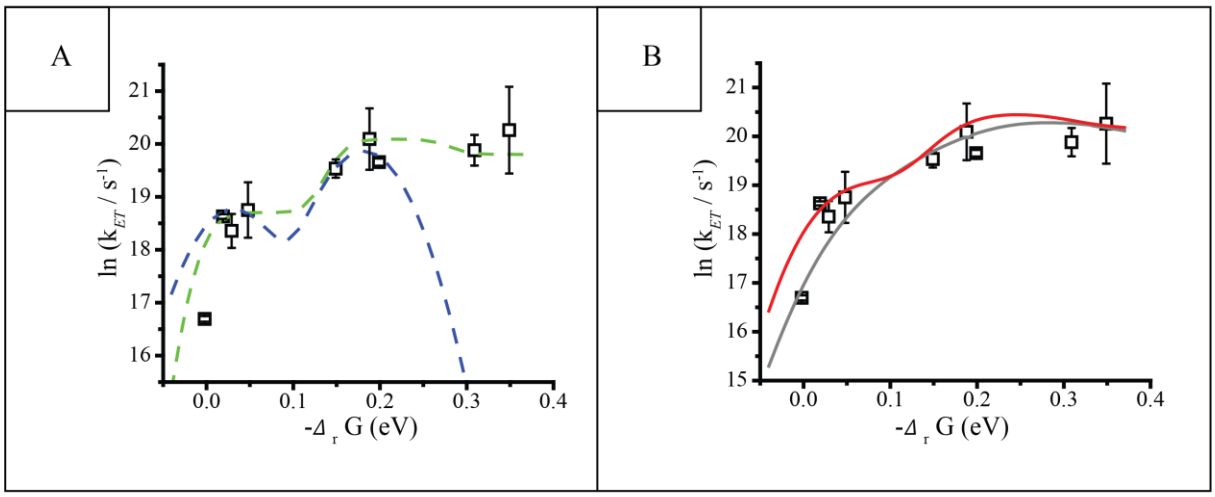

Figure 4.9 - The natural log of the electron transfer rate constant is plotted against the reaction Gibbs energy, - $\Delta_r G$, for the experimental data (black squares). The left panel shows best fits to the classical Marcus theory (blue) and a semi-classical Marcus theory at intermediate temperature ($h\nu \sim k_B T$, green). The right panel shows best fits to the data by the semiclassical equation (Equation 4.3) (red curve) and by Equation 4.3 while accounting for the size distribution in the nanoparticles (grey) (see text).

Figure 4.9 compares the predictions of different models for describing the experimental data for the $\Delta_r G$ trend. The classical Marcus theory (blue dashed curve, left panel), without quantized nuclear modes, fails to adequately describe the data, even with the inclusion of more than two product energy levels. The incorporation of the vibrational states (i.e., longitudinal optical phonon mode) in the semi-classical Marcus theory ($k_B T > h\nu$) helps to broaden the Marcus curve and describes the system well over the $\Delta_r G$ regime investigated (red, right panel). If we incorporate the fact that $h\nu \approx k_B T$, however, we can utilize a more appropriate model and obtain a similarly good fit to the data (dashed green line, left panel). The best fit model parameters change somewhat; most notably the value of the electronic coupling is 0.3 cm^{-1} rather than 2.7 cm^{-1}. Note that the model used here to describe the charge transfer is fundamentally

related to the multiphonon emission model for charge carrier trapping in deep traps of a semiconductor.[221] We note that an Auger-assisted electron transfer mechanism,[222] which has been used to describe hole transfer in the deeply inverted Marcus regime, does not need to be invoked to generate a good fit to the data. Thus, the best fit, with the most realistic physical parameters, is found by using the semi-classical Marcus equation, (aka, multiphonon emission model), either at high or intermediate temperature, over a sum of the two final states.

These model fits predict a step, or rise, in the electron transfer rate as the reaction free energy becomes large enough to include the second excited state, P_e; however the experimental data do not display such a rise. Given that the nanoparticles have a distribution of sizes and have a distribution of $\Delta_r G$ values, this feature in the model is likely to be masked in the data. To illustrate this effect, the gray curve shows a fit by the semiclassical model (with the same parameters as in the red curve) that is convoluted with a Gaussian-shaped nanoparticle size distribution of 0.070 eV. The 0.070 eV width of the Gaussian was estimated from the width in the absorbance spectra of the nanoparticles, and its inclusion 'smears' the resolution in the model prediction, giving an excellent fit to the data. Figure 9.12 provides a contour plot, which shows the dependence of the fit quality on values of V and λ_s.

In an effort to assess whether the high frequency limit or the intermediate frequency model more accurately describes the data, the value of the electronic coupling at contact between the nanoparticles was obtained by extrapolating to a zero distance, using the distance dependence from Figure 4.6. Two limits were considered for contact, direct contact between nanoparticle atoms, as in a core-shell material, and a disulfide bond linkage.[223] For the fit by Equation 4.3 (red curve) we obtain a 197 meV electronic coupling for direct contact and an 80 meV electronic coupling for the disulfide linkage; whereas for the fit by Equation 9.5 (green curve) we find $|V|$

= 22 meV at direct contact and 8.7 meV for a disulfide linker. For CdSe-CdTe nanorod heterostructures Scholes et. al. [220] reports 50 meV, for CdTe-CdTe aggregates (via a quantum mechanical calculation) a value of 40 meV[224] is reported, and for dye molecules directly bound to a semiconductor nanoparticle electronic couplings in the range of 10 to 10^3 meV have been reported. Although both models give reasonable coupling strengths, the intermediate frequency limit is more consistent with the known phonon properties of the nanoparticle.

4.4 CONCLUSIONS

A controlled covalently linked nanoparticle dyad system on a template was fabricated. The band edges of the nanoparticles in these systems were designed in a manner such that electron transfer could be studied as a function of interparticle distance and driving force. The electron transfer rate between the nanoparticles changed exponentially with distance and the electron tunneling decay length for a hydrocarbon bridge is similar to that found for molecular dyads and for molecules tethered to an electrode surface. The semi-classical Marcus theory was able to accurately describe the relationship between electron transfer and $\Delta_r G$, as long as one performs a sum over the manifold of final states. Important differences between the nanoparticle dyads and molecular dyads arise from the small reorganization energies in the nanoparticles (because of their size and rigidity) and the ability to tune the free energy difference by changing the nanoparticle size. These findings imply that much of the knowledge gained from studies in molecular systems can be readily translated to the case of nanoparticle quantum dots and should

prove useful for understanding, controlling, and designing bulk heterojunction solar cells that transfer charge using semiconductor nanoparticles.

4.5 EXPERIMENTAL DETAILS MATERIALS AND METHODS

Selenium powder (99.999%), tellurium powder (99.999%), cadmium chloride ($CdCl_2$; 99%) sodium borohydride ($NaBH_4$; 98%), CdO (99.999%), thioglycolic acid (TGA), 4-mercaptobutyric acid (MBA), 6-mercaptohexanoic acid (MHA), 8-mercaptooctanoic acid (MOA), 11-mercaptoundecanoic acid (MUA), 1-ethyl-3-(3-dimethylaminopropyl)carbodiimide (EDC), *N*-hydroxysulfosuccinimide (S-NHS), and phosphate buffered saline tablets (PBS), Oleic Acid (OA), trioctylphosphine oxide (99%) were purchased from Sigma-Aldrich. trioctylphospine was purchased from Strem Chemicals. Octadecylphosphonic acid (ODPA, >99%) and tetradecylphosphonic acid (TDPA, >99%) were purchased from PCI Synthesis. Silica microbeads, both amine coated and bare, 150 nm and 500 nm diameter were purchased from Polysciences, Inc. All reagents and solvents were used as received. Water used in all experiments was purified by a Barnstead Nanopure system, and its resistance was 18.2 MΩ-cm at 25 °C.

4.5.1 Carboxylic acid terminated Cadmium Selenide (CdSe)

Octadecylphosponic acid (ODPA) CdSe nanoparticles, < 2.5 nm, as well as oleic acid (OA) CdSe nanoparticles, > 2.5 nm, were synthesized following previously published methodologies.[225,226] The purified nanoparticles were ligand exchanged to TGA, MBA, MHA, MOA, or MUA by stirring the ligand in a solution whose concentration was 1000 times in excess to that of the nanoparticle. The mixture was stirred overnight in a 4.0 mL 50% water (pH=11) 50% chloroform solution. The exchanged nanoparticles were then isolated from the water phase and purified through syringe and centrifugal filtration. For synthesis of larger, 5.5 nm, OA CdSe nanoparticles a multiple injection of the selenium precursor was utilized.

4.5.2 Amine terminated CdSe

ODPA-CdSe, 2.2 nm, and OA-CdSe, 3.1 nm, stock solutions were ligand exchanged to cysteamine (CA) through a precipitation process, demonstrated previously by Strekal et. al. for CdSe/ZnS core-shell nanoparticles.[227] The precipitation was performed through the addition of 200 μL of a 20 mg/mL concentration cysteamine/methanol solution to a 2.0 mL NP stock solution. The nanoparticle solutions were isolated through centrifugation and dried. The nanoparticles could then be dissolved in water and purified through syringe and centrifugal filtration

4.5.3 Amine terminated Cadmium Telluride (CdTe)

CA-CdTe nanoparticles, 3.3 nm, 4.0 nm, and 4.1 nm were synthesized by an adaptation of a procedure by Wang et. al.[228] Briefly, 1.145 g $CdCl_2$ and 0.8521 g CA were dissolved in 20.0 mL of water and the pH was adjusted to be approximately 5.75. This solution was then heated to 90.0 °C and deoxygenated for approximately 20 min. Reduced tellurium was made by dissolving 127.5 mg Te and 94.5 mg $NaBH_4$ in 5.0 mL of water and heated under argon to 70.0 °C. The reduced tellurium precursor (2.5 mL) was injected into the cadmium solution and refluxed until the desired size was reached. The nanoparticles were purified through syringe and centrifugal filtration.

4.5.4 Carboxylic acid terminated CdTe

Carboxylic acid terminated CdTe nanoparticles, 4.1 and 4.4 nm, were synthesized through a two part process. First, large tetradecylphosphonic acid (TDPA) capped CdTe nanoparticles were synthesized following a multiple injection approach using the synthesis developed by Peng et al.229 Next, the TDPA-CdTe nanoparticles were ligand exchanged to either TGA or MUA following a procedure similar to that published by Wang et al.[192] A 10.0 mL solution of water containing 0.1 mmol $CdCl_2$ and 0.2 mmol TGA or MUA at pH 11.5 was degassed with argon at 80°C for 10 min. Then, 0.5 mL of the TDPA-CdTe nanoparticle chloroform solution was injected and. the heating was continued until all the chloroform was boiled off. The solution was then brought to 100 °C and refluxed for 3 hours. The resulting solution was purified by

centrifugation and syringe filters to remove any non-soluble nanoparticles and unreacted precursors.

4.5.5 Assembly Formation

Nanoparticle dyads were formed by templating on a SiO_2 microsphere. The first step in a one nanoparticle assembly (1NPA) was to attach a nanoparticle to an amine coated SiO_2 microsphere, approximately 500 nm in diameter. Approximately 30 mg of SiO_2 microspheres (zeta potential = 41.91 ± 0.60 mV) were dispersed in 1 mL of water. An excess of oppositely charged (carboxylic acid terminated) nanoparticles was added to the microsphere solution and the total volume was adjusted to equal 3 mL. Then, it was shaken for one hour. During this process, nanoparticles bind electrostatically to the surface of the microsphere. The assembly was purified using a stirred ultrafiltration cell with a 100 nm pore size cellulose nitrate membrane filter (Whatman). The "free" nanoparticles (< 5 nm) go through the filter, but those that are attached to the SiO_2 template do not and are captured by the filter. The pressure used in the filtration was 50 psi and filtrate samples were collected. After filtration, the solid on the filter paper was suspended in 4 mL of water. An additional two to three rounds of filtrations were performed on this sample and the 1NPA was suspended in 3 mL of water. The zeta potential for a sample 1NPA was -19.66 ± 2.49 mV.

The nanoparticle dyads (2NPA) were assembled by forming an amide bond between the exposed carboxylic acid group of the 1NPA and the solvent exposed terminus of an amine terminated nanoparticle (Figure 4.1). The catalyst 1-ethyl-3-(3-dimethylaminopropyl)carbodiimide (EDC)

sulfo-NHS was used to promote this reaction. By choosing the second nanoparticle to be larger than that in the 1NPA the reaction is biased to create dyads. The 1NPA and EDC were added to a 500 mM PBS buffer solution in a 1:1000 ratio,[230] and stirred for 15 minutes. Then the amine terminated nanoparticles were added to the solution and it was stirred overnight. The sample was cooled to 4 ^{o}C to quench the excess EDC and then purified using the same methodology as described above for the 1NPA. The zeta potential for a resulting 2NPA was 9.35 ± 1.45 mV. A more detailed description of this procedure can be found in Appendix C.

4.5.6 Steady-State Spectroscopy

Steady-state absorption spectra were measured on an Agilent 8453 spectrometer, and the steady-state emission spectra were measured on a Horiba J-Y Fluoromax 3 fluorescence spectrophotometer.

4.5.7 Time-Dependent Fluorescence Spectroscopy

Time resolved fluorescence measurements of the nanoparticle assemblies were measured using the time correlated single photon counting (TSCPC) technique with a PicoHarp 300 TCSPC module (PicoQuant GmbH).[231] The samples were excited at 635 nm using a synchronously pumped dye laser. All measurements were made at the magic angle. Measurements were collected using a 1 MHz repetition rate, 32 ps resolution, and until a maximum count of 10,000 was observed at the peak channel. The instrument response function was measured using

colloidal $BaSO_4$ and in every case the instrument response function had a full-width-at-half-maximum of ≤96 ps. The decay curves were fit to a distribution of lifetime components by a convolution and compare method using Edinburgh Instruments fluorescence analysis software technology (FAST)[232] namely (Equation 4.5)[233]

$$I(t) = \int_{\tau=0}^{\infty} \alpha(\tau) \cdot \exp\left(-t/\tau\right) \mathrm{d}\tau \qquad \text{Equation 4.5}$$

4.5.8 Zeta Potential Measurements

Zeta potential measurements were performed at room temperature in a 90° geometry with a 532 nm laser (Brookhaven Instrument Co.). The electrophoretic mobility measurements were performed on the same instrument at room temperature with an electrical field strength of 16 V/cm and a field frequency of 2.00 Hz by using a Zeta Plus zeta potential analyzer.

4.5.9 Scanning Transmission Electron Microscopy (STEM)

Samples for electron microscopy characterization were drop casted on a carbon film on a copper transmission microscopy grid (Ted Pella Inc.). The measurements were performed using a ZEISS Sigma 500 VP Scanning Electron Microscope equipped with a STEM detector. The images were collected in bright field mode, with an electron beam acceleration voltage of 24-28 keV, 10 μm aperture, and working distance of about 2.5 mm.

4.6 ACKNOWLEDGEMENTS

This work was funded by the U.S. Department of Energy (Grant No. ER46430). B. P. B. is grateful for additional financial support from the R.K. Mellon foundation.

4.7 REFERENCES

157 Shami, S.; *IJSTR*, **2015**, *4*, 165.
158 Yu, G.; Gao, J.; Hemmelen, J. C.; Wudl, F.; Heeger, A. J.; *Science*, **1995**, *270*, 1789-1791.
159 Huynh, W. U.; Dittmer, J. K.; Alivisatos, A. P.; *Science*, **2002**, *295*, 2425-2427.
160 Park, S. H.; Roy, A.; Beaupre´, S.; Cho, S.; Coates, N.; Moon, J. S.; Moses, D.; Leclerc, M.; Lee, K.; Heeger, A.; *J. Nat. Photon*, **2009**, *3*, 297-302.
161 You, J.; Dou, L.; Yoshimura, K.; Takehito, K.; Ohya, K.; Moriarty, T.; Emery, K.; Chen, C.; Gao, J.; Gang, L.; Yang, Y.; . *Nat. Commun.*, **2013**, *4*, 1446.
162 Marcus, R. A.; Sutin, N.; *Biochim. Biophys. Acta.*, **1985**, *811*, 265-322.
163 Sanders, A. M.; Magnanelli, T. J.; Bragg, A. E.; Tovar, D. J.; *J. Am. Chem. Soc.*, **2016**, *138*, 3362-3370.
164 Chen, P.; Meyer, T. J.; *Chem. Rev.*, **1998**, *98*, 1439-1478.
165 Jortner J; Bixon, M. Electron Transfer-From Isolated Molecules to Biomolecules, Part 1 and Part 2; John Wiley & Sons, Inc. New York, 1999.
166 a) Paddon-Row, M.N.; *Adv. Phys Org. Chem.* **2003**, *38*, 1-85; b) Oevering, H.; Paddon-Row, M. N.; Heppener, M.; Oliver, A. M.; Cotsaris, E.; Verhoeven, J. W.; Hush, N. S.; *J. Am. Chem. Soc*., **1987**, *109*, 3258-3269.
167 Lawson, J. M.; Paddon-Row, M. N.; Schuddeboom, W.; Warman, J. M.; Clayton, A. H. A.; Ghiggino, K. P.; *J. Phys. Chem.* **1993**, *97*, 13099-13106.
168 Gilbert M, Albinsson B.; *Chem. Soc. Rev.*, **2015**, *44*, 845-886.
169 Bixon, M.; Jortner, J.; *J. Chem. Phys.*, **1997**, *107*, 5154-5170.
170 Natali M.; Campagna S.; Scandola, F.; *Chem. Soc. Rev.*, **2014**, *43*, 4005-4018.
171 Weiss, E.A., Wasielewski, M. R., Ratner, M.A.; *Curr Chem* **2005**, *257*, 10-3-133.
172 Gu, Y.; Kumar, K.; Lin, Z.; Read, I.; Zimmt, M. B.; Waldeck, D. H.; *J. Photochem. Photobio. A: Chem.*, **1997**, *105*, 189 - 196.
173 Liu, M.; Waldeck, D. H.; Oliver, A. M.; Head, N. J.; Paddon-Row, M. N.; *J. Am. Chem Soc.*, **2004**, *126*, 10778-10786.
174 Chakrabarti, S.; Parker, M. F. L.; Morgan, C. W.; Schafmeister, C. E.; Waldeck D. H.; *J. Am. Chem. Soc.*, **2009**, *131*, 2044-2045.
175 Zimmt, M. B. and Waldeck, D. H.; *J. Phys. Chem. A*, **2003**, *107*, 3580-3597.

176 Smith, A. M.; Nie, S.; *Acc. Chem. Res.*, **2010**, *43*, 190-200.
177 Zhu, H.; Yang, Y.; Hyeon-Deuk, K.; Califano, M.; Song, N.; Wang, Y.; Zhang, W.; Prezhado, O. V.; Lian T.; *Nano. Lett.*, **2014**, *14*, 1263-1263-1269.
178 Olshansky, J. H.; Ding, T. X.; Lee, Y. V.; Leone, S. R.; Alivisatos, A. P.; *J. Am. Chem. Soc.*¸ **2015**, *137*, 15567-15575.
179 Sze, S. M.; Kwok, N. K.; *Physics of Semiconductor Devices Nanomaterials: 2nd Edition;* John Wiley & Sons Inc. Publishing: Hoboken, New Jersey, 2007.
180 Komsa, H.; Krasheninnikov, A.; *Phys. Rev. B*, **2013,** *88* 1-7.
181 Kang, J.; Tongay, S.; Zhou, J.; Li, J.; Wu, J.; *Appl. Phys. Lett.*, **2013**, *012111*, 22-25.
182 Vokhmintcev, K. V.; Samokhvalov, P. S.; Nabiev, I.; *Nanotoday*, **2016**, *11*, 189-211.
183 Chuang, C-H.; Doane, T. L.; Lo, S. S.; Scholes, G. D.; Burda, C.; *ACS Nano*, **2011**, *5*, 6016.
184 a) Scholes, G. D.; *Adv. Funt. Mater.*, **2008**, *18*, 1157-1172; b) Lo, S. S.; Mirkovic, T.; Chaung, C-H.; Burda, C.; Scholes, G. D.; *Adv. Mater.*, **2011**, *23*, 180-197.
185 Wu, M.; Mukherjee, P.; Lamont, D. N.; Waldeck, D. H.; *J. Phys. Chem. C,* **2010**, *114*, 5751-5759.
186 a) Sellers, D. G.; Button, A. A.; Nasca, J. N.; Wolfe, G. E.; Chauhan S.; Watson, D. F.; *J. Phys. Chem. C*, **2015**, *119*, 27737-27748; b) Gross, D.; Susha, A. S.; Klar, T. A.; Da Como, E.; Rogach, A. L.; Feldmann, J.; *Nano Lett.*, **2008**, *8*, 1482-1485.
187 Wang, D.; Zhao, H.; Wu, N.; Khakani, M. A. E.; Ma, D.; *J. Phys. Chem. Lett.* **2010**, *1*, 1030-1035.
188 Rasband, W.S., ImageJ, U. S. National Institutes of Health, Bethesda, Maryland, USA, http://imagej.nih.gov/ij/, 1997-2016
189 Bloom, B. P.; Zhao, L.-B.; Wang, Y.; Waldeck, D. H.; Liu, R. ; Zhang, P.; Beratan, D. N.; *J. Phys. Chem. C*, **2013**, *117*, 22401-22411.
190 Meulenberg, R. W.; Lee, J. I. R.; Wolcott, A.; Zhang, J. Z.; Terminello, L. J.; van Buuren, T.; *ACS Nano*, **2009**, *3*, 325-330.
191 Jasieniak, J.; Califano, M.; Watkins, S. E.; *ACS Nano*, **2011**, *5*, 5888-5902.
192 Wang, Y.; Liu, K.; Mukherjee, P.; Hines, D. A.; Santra, P.; Shen, H. Y.; Kamat, P.; Waldeck, D. H.: *Phys. Chem. Chem. Phys.* **2014**, *16*, 5066-5070.
193 Smalley, J. F.; Feldberg, S. W.; Chidsey, C. E. D.; Linford, M. R.; Newton, M. D.; Liu, Y.-P.; *J. Phys. Chem.*, **1995**, *99*, 13141-13149.
194 Slowinski, K.; Chamberlain, R. V.; Miller, C. J.; Majda M.; *J. Am. Chem. Soc.*, **1997**, *119*, 11910-11919.
195 Norris, D. J.; Bawendi, M. G.; *Phys. Rev. B.*, **1996**, *53*, 16338-16346.
196 Lin, C.; Gong, K.; Kelley, D. F.; Kelley, A. M.; *ACS Nano*, **2015**, *9*, 8131-8141.
197 Jortner, J.; *J. Chem. Phys.*, **1976**, *64*, 4860-4867.
198 Robel, I.; Kuno, M.; Kamat, P. V.; *J. Am. Chem. Soc.*, **2007**, *129*, 4136-4137.
199 Yang, J.; Oshima, T.; Yindeesuk, W.; Pan, Z.; Zhong, X.; Shen Q.; *J. Mater. Chem. A*, **2014**, *2*, 20882-20888.
200 Xu, Z.; Cotlet, M.; *Agnew. Chem. Int. Ed.*, **2011**, *50*, 6079-6083.
201 Dibbell, R. S.; Watson, D. F.; *J. Phys. Chem. C*, **2009**, *113*, 3139-3149.
202 Morris-Cohen, A. J.; Frederick, M. T.; Cass, L. C.; Weiss, E. A.; *J. Am. Chem. Soc.*, **2011**, *133*, 10146-10154.
203 Tagliazucchi, M.; Tice, D. B.; Sweeny, C. M.; Morris-Cohen, A. J.; Weiss, E. A.; *ACS Nano*, **2011**, *5*, 9907-9917.
204 Wang, H.; McNellis, E. R.; Kinge, S.; Bonn, M.; Canovas, E.; *Nano. Lett.*, **2013,** *13*, 5311-5315.
205 Wasserman, S. R.; Tao, Y.-T.; Whitesides, G. M.; *Langmuir*, **1989**, *5*, 1074-1087.
206 a)Slowinski, K.; Majda, M.; *J. Electroanal. Chem.*, **2000**, *491*, 139-147; b) Sek, S.; Misicka, A.; Bilewicz, R.; *J. Phys. Chem. B*, **2000**, *104*, 5399-5402; c) Sek, S.; Palys, B.; Bilewicz, R.; *J. Phys. Chem. B*, **2002**, *106*, 5907-5914; d) Slowinski, K.; Fong, H. K. Y.; Majda, M.; *J. Am. Chem. Soc.*, **1999**, *121*, 7257-7261.
207 Kai, M.; Takeda, K.; Morita, T.; Kimura, S.; *J. Pept. Sci.*, **2008**, *14*, 192-202.
208 Yamamoto, H. and Waldeck, D. H.; *J. Phys. Chem. B*, **2002**, *106*, 7469-7473.
209 Bradbury, C. R.; Zhao, J.; Fermin, D. J.; *J. Phys. Chem. C*, **2008**, *112*, 10153-10160.
210 Shein, J. B.; Lai, L. M. H.; Eggers, P. K.; Paddon-Row, M. N.; Gooding, J. J.; *Langmuir*, **2009**, *25*, 11121-11128.
211 Gotesman, G.; Guliamov, R.; Naaman, R.; *Beilstein. J. Nanotechnol.*, **2012**, *3*, 629-636.
212 Hines, D. A.; Forrest, R. P.; Corcelli, S. A.; Kamat, P. V.; *J. Phys. Chem. B.*; **2015**, *119*, 7439-7446.
213 Ji, X.; Wang, W.; Mattoussi, H.; *Phys. Chem. Chem. Phys.*, **2015**, *17*, 10108-10117.

214 Haung, J.; Haung, Z.; Yang, Y; Zhu, H.; Lian, T.; *J. Am. Chem. Soc.*, **2010**, *132*, 4858-4864.
215 Haung, J.; Stockwell, D.; Haung, Z.; Mohler, D.; Lian, T.; *J. Am. Chem. Soc.*, **2008**, *130*, 5632-5633.
216 Chakrapani, V.; Tvrdy, K.; Kamat, P. V.; *J. Am. Chem. Soc.*, **2010**, *132*, 1228-1229.
217 Sellers, D. G.; Watson, D. F.; *J. Phys. Chem. C*, **2012**, *116*, 19215-19225.
218 Heyon-Deuk, K.; Kim, J.; Prezhdo, O. V.; *J. Phys. Chem. Lett.*, **2015**, *6*, 244-249.
219 Olshansky, J. H.; Ding, T. X.; Lee, Y. V.; Leone, S. R.; Alivisatos, A. P.; *J. Am. Chem. Soc.*, **2015**, *137*, 15567-15575.
220 Scholes, G. D.; Jones, M.; Kumar, S.; *J. Phys. Chem. C*, **2007**, *111*, 13777-13785.
221 a) Krasikov,D.N.; Scherbinin, A. V.; Knizhnik, A. A.; Vasiliev, A. N.; Potapkin, B. V.; Sommerer, T. J. ; *J. Appl. Phys.* **2016**, *119*, 085706 ; b) Henry, C. H. ; Lang, D. V.; Phys Rev B *1977* **15** 989.
222 Zhu, H.; Yang, Y.; Wu, K.; Lian, T.; *Annu. Rev. Phys. Chem.*, **2016**, *67*, 259.
223 a) Boles, M. A.; Ling, D.; Hyeon, T.; Talapin, D. V.; *Nat. Mater.*, **2016,** *15*, 141-356.; b) Dubois, L. H.; Nuzzo, R. G.; *Annu. Rev. Phys. Chem.*, **1992**, *43*, 437-463.
224 Koole, R.; Liljeroth, P.; Donega, C. d. M.; Vanmaekelbergh, D.; Meikjerink, A.; *J. Am. Chem. Soc.*, **2006,** *128*, 10436-10441.
225 Kalyuzhuy, G.; Murray, R. W. *J. Phys. Chem. B*, **2005** *109*, 7012-7021.
226 Yu. W. W.; Peng, X.; *Agnew. Chem. Int. Ed.*, **2002**, *41*, 2368-2371.
227 Strekal, N.; Kulakovich, O.; Belyaev, A.; Stsiapura, V.; Maskevich, S.; *Opt. Spectrosc.* **2011**, *104*, 50-56.
228 Wang, R.; Wang, Y.; Feng, Q.; Zhou, L.; Gong, F.; Lan, Y.; *Mater. Lett.*, **2012**, *66*, 261-263.
229 Yu, W. W.; Wang, Y. A.; Peng, X.: *Chem. Mater.* **2003**, *15*, 4300-4308.
230 Hoppe, K.; Geidel, E.; Weller, H.; Eychmuller, A. *Phys. Chem. Chem. Phys.*, **2002**, *4*, 1704-1706.
231 Yin X.; Kong, J.; De Leon, A.; Li Y.; Ma Z.; Wierzbinski, E.; Achim, C.; Waldeck, D. H. *J Phys. Chem. B*, **2014**, *118*, 9037-9047
232 McGuinness, C. D.; Nishimura, M. K. Y.; Keszenman-Pereyra, D.; Dickinson, P.; Campbell, C. J.; Bachmann, T. T.; Ghazalb, P.; Crainac, J. *Mol. BioSyst.*, **2010**, *6*, 386-390.
233 Lakowicz, J. R. *Principles of Fluorescence Spectroscopy, 3rd ed.*; Springer: Maryland. 2006; p. 1-61, 97-155, 331-382, 443-475.

5.0 SPIN SELECTIVITY IN ELECTRON TRANSFER TO CHIRAL SEMICONDUCTOR QUANTUM DOTS

This work is in preparation for submission as Bloom, B. P.; Graff, B. M.; Waldeck, D. H. The thesis author performed nanoparticle assembly fabrication, collected fluorescence measurements, determined electron transfer rates, and wrote the manuscript in collaboration with B. P. B. The supporting information for this chapter is provided in Appendix D.

This work shows that electron transfer to chiral quantum dots (QDs) is spin selective. The spin selectivity in the electron transfer was investigated by using the light's polarization to control the helicity of the electron donor QD and then examining how the photoinduced electron transfer rate constant changes with the acceptor QD's chirality. These experiments reveal a difference in the electron transfer rate of more than fifteen-fold and show that it correlates with the chirality of the acceptor QD's and the strength of its circular dichroism spectrum. This work contributes to a deeper understanding of spin dependent charge transport in QD assemblies, which promise to play an important role in nanoscale spintronic and optoelectronic devices.

5.1 MAIN TEXT

Understanding and controlling an electron's spin orientation in charge transfer and charge transport is essential for a deeper understanding of redox processes[234,235] and for realizing new spintronics technologies.[236,237] Existing approaches to spintronics, which rely on spin injection from magnetic electrodes and/or semiconductors with large spin-orbit coupling, have significant limitations.[238] Semiconductor quantum dots (QDs) are good candidates for optoelectronic spin driven devices because they have long spin decoherence times at room temperature and the spin polarization can be controlled by photoexcitation with circularly polarized light.[239,240] One such example for the control of spin transport is in double QD solid-state platforms in which the occupancy of the electronic states and the singlet-triplet energy splitting that generates a Pauli spin blockade is gated with external electric and magnetic fields, in order to rectify the current. [241] Recently chiral molecules have been shown to act as spin filters in electron transfer via the chiral induced spin selectivity (CISS) effect.[242] CISS does not require an external magnetic field, rather it arises from an effective magnetic field that breaks the degeneracy of the electron spin states upon propagation through a chiral structure.[243,244] Consequently, electron transport is favored for one spin direction over the other; where the preference for spin direction depends on the handedness of the chiral molecule and the momentum of the electron. This study examines the extension of CISS to inorganic QDs and the control of charge transport in QDs by spin selectivity filters.

The emergence of chiral QDs[245,246] has enabled the replacement of organic spin filters with inorganic spin filters.[247] Previous optical experiments have shown that electron transmission from achiral QDs photoexcited with circularly polarized light through chiral biomolecules

strongly depends on the light polarization.[248,249,250] In these studies, spin selective electron transport is controlled by the chirality of the molecule and the QD is only used for preferentially exciting one particular spin type. More recently, magnetic conductive probe atomic force microscopy measurements and magnetoresistance measurements have shown that the efficiency of electron transport through films of chiral CdSe QDs is dependent upon the chiroptical properties of the QD.[247] In those experiments the spin selectivity was found to be ~15%, and was limited, presumably, because of the weak chiroptical properties of the QDs. Here, we report on the spin-dependent photoinduced electron transfer kinetics between QDs templated on a silica microbead.[251] Excitation of the achiral donor QD with circularly polarized light creates a spin polarized electron-hole pair distribution [252,253] and the subsequent donor quenching, arising from electron transfer to the chiral QD,[251] is monitored using time-resolved fluorescence. The spin dependence of the electron transfer rates is calculated for clockwise ($k_{et}(CW)$) and counterclockwise ($k_{et}(CCW)$) circularly polarized light by way of a polarization parameter *P*, defined as

$$P = \frac{k_{et}(CW) - k_{et}(CCW)}{k_{et}(CW) + k_{et}(CCW)} \qquad \text{Equation 5.1}$$

We find that the sign of the polarization correlates with the sign of the acceptor QDs CD signal, and the magnitude of *P* correlates with the strength of the CD response. Polarizations as high as $P = 0.88$ (i.e., a fifteen-fold difference in electron transfer rate) are observed.

A two nanoparticle QD assembly was fabricated using a protocol like that reported previously. [251] The schematic diagram in Figure 5.1A shows the architecture of the QD, 'dyad', assembly

and the inset in the top right corner shows an energy diagram for the corresponding Type - II heterojunction.

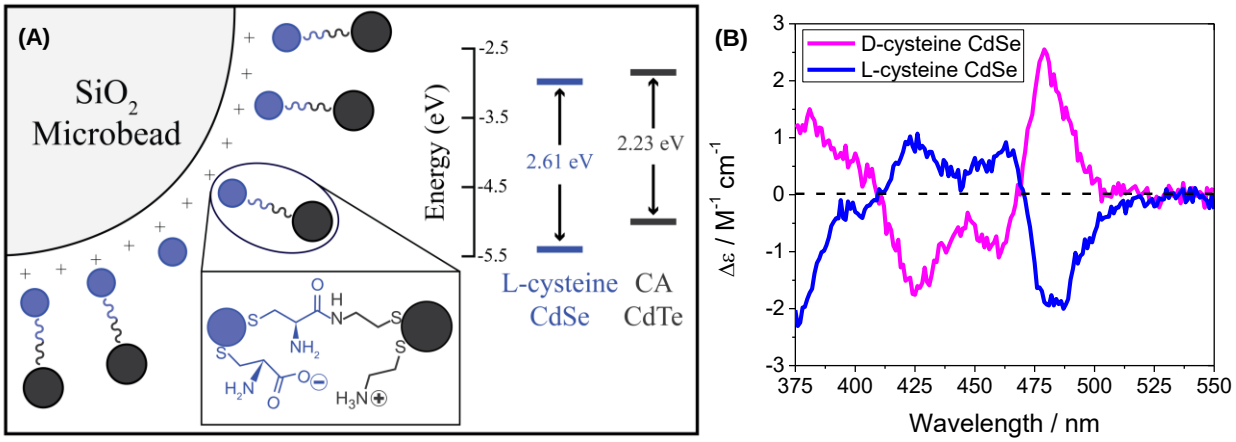

Figure 5.1 Panel A is a cartoon of the assembly of an achiral donor QD (black) and chiral acceptor QD (blue) assembled onto a silica microbead. The top right image in the cartoon shows an energy diagram of the QD assembly and the bottom right shows the covalent attachment between their two ligands. Note that the ligand sizes are exaggerated in this cartoon. Panel B shows circular dichroism spectra of the acceptor QD, L-cysteine capped CdSe (blue), and its enantiomer D-cysteine capped CdSe (magenta).

The acceptor QD was made chiral by ligand exchanging an achiral QD with cysteine and the donor QD was achiral. This QD dyad architecture provides a reproducible method for controlling the donor QD – acceptor QD interaction and prevents ill-controlled aggregation and subsequent flocculation of the QD dyads. The assemblies also orient the QD dyads so that the circularly polarized light more strongly illuminates the QD dyads on the front surface of the microbead than on the back surface, giving rise to a spin-polarized, photoexcited carrier population (in the lab frame). The electron transfer rate, k_{et} $(= 1/\tau_{et})$, is found by comparing the donor QD's population lifetime, τ_{QDA}, in the dyad assembly to its lifetime, $\tau_{D'}$ in comparable assemblies where electron transfer is blocked; thus,

$$k_{et} = \frac{1}{\tau_{et}} = \frac{1}{\tau_{QDA}} - \frac{1}{\tau_D} \qquad \text{Equation 5.2}$$

In the current study, a dendrimer that does not accept an electron was used to replace the acceptor QD; however it is also possible to use another QD with a type 1 band alignment.[251]

Figure 5.1B shows mirror image CD spectra, in units of molar extinction, of L-cysteine (blue) and D-cysteine (magenta) passivated CdSe in the absorbance maximum region (475 nm) of the QDs. The circular dichroism spectra display considerable batch-to-batch variability in their intensity and this is believed to reflect differences in the extent of ligand exchange and cysteine surface coverage in the CdSe accepter QDs. The chirality of the acceptor CdSe is very sensitive to the structure of the ligand shell on the surface of the QD. Adjacent ligands on the surface of the QD can chelate in opposite orientations, *cis* and *trans*, which have been shown computationally to result in a flip of the sign of the circular dichroism spectrum.[256] For very small QDs more disorder in the ligand shell is expected, arising from the high surface curvature, and a weaker CD signal intensity is observed. In extreme cases, where the *trans* conformer dominates the surface structure, the sign of the CD spectrum for the QD ensemble can flip entirely.[254] The dependence of the CD signal strength on the extent of ligand exchange was confirmed by purposeful variation of the amount of chiral capping ligand (*vide infra*).

Figure 5.2A-Figure 5.2C show examples of the photoluminescence decays for QD dyad assemblies that contain different acceptor QDs: D-cysteine (left), MPA (middle), and L-cysteine (right) passivated CdSe acceptor QDs. In each panel, the fluorescence decay is shown for three different light polarizations used to excite the achiral CdTe donor QD; they are linear (black), CW (red), and CCW (green) polarized light. Each of the decay curves was fit to a distribution of lifetime components, and the differences in the decays could be attributed to significant changes in the short lifetime component. Figure 5.2D to Figure 5.2F show the distribution of the short time constant components for the photoluminescence decays in panels Figure 5.2A to Figure

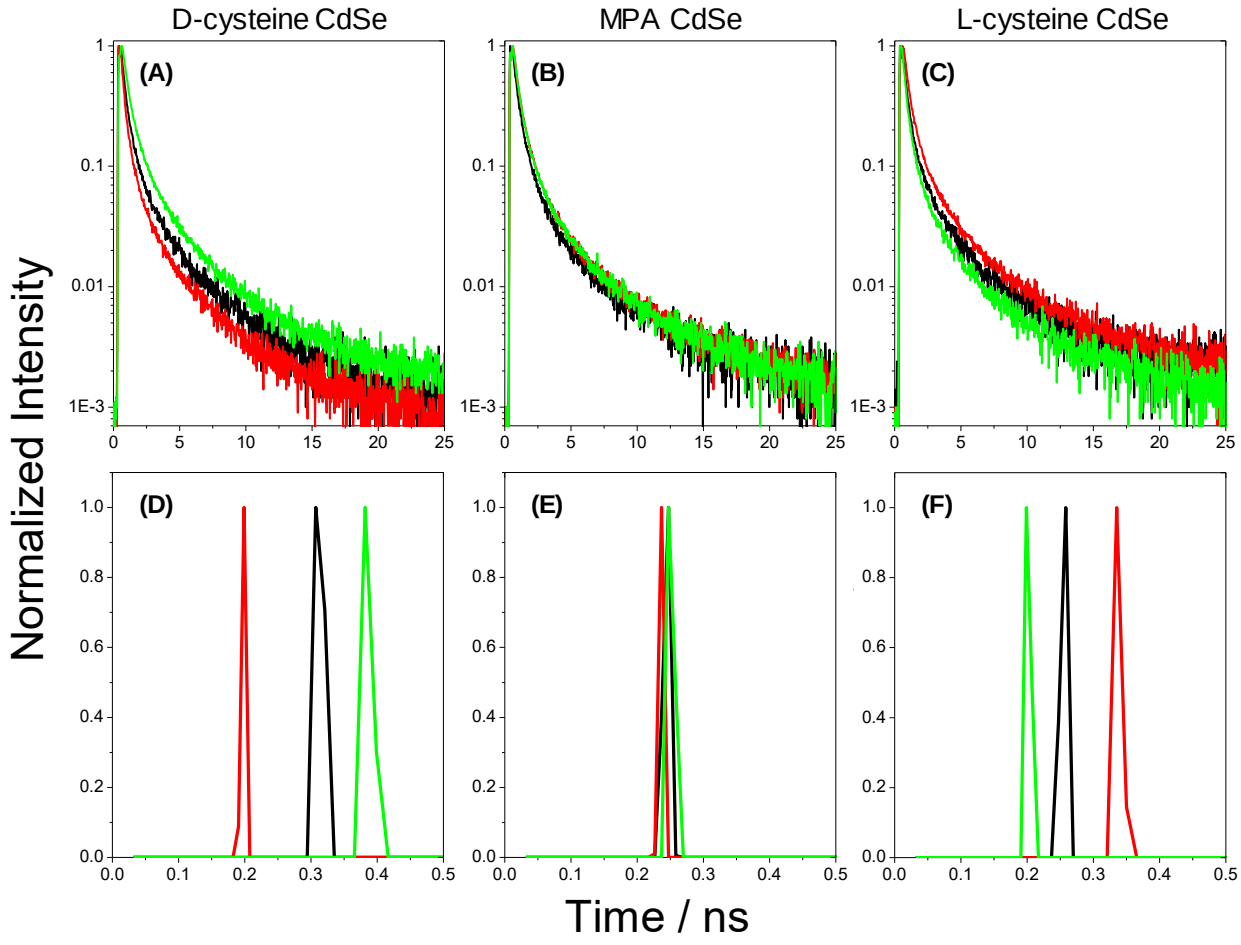

Figure 5.2 - The photoluminescence decays (A, B, C) and the distribution fittings (D, E, F) for QD assemblies containing various acceptors: D-Cysteine CdSe (left) MPA CdSe (middle), and L-Cysteine CdSe (right). The excitation light polarization in each case is indicated by a different color; linear (black), CW (red), and CCW (green).

5.2C. These fast time constants lie in the few hundred picosecond regime which is faster than the electron spin decoherence time reported for photoexcited QDs at room temperature.[254] For the dyad assemblies, with chiral acceptor QDs, large differences in the short time constants were observed for the different light polarizations; whereas for the assembly with an achiral acceptor (MPA-CdSe) the fluorescence decay does not change considerably with light polarization (see Figure 5.2E).

The dyad assemblies with chiral acceptor QDs show a significant change in the short time constant with the light polarization. For the D-cysteine capped CdSe acceptor QD the fastest decay law is observed for CW circularly polarized light, intermediate for linearly polarized light, and longest for CCW circularly polarized light, indicating faster to slower electron transfer rates respectively (Figure 5.2D). The reverse is true for assemblies with L-cysteine capped CdSe acceptor QDs; the shortest time constant was found for CCW polarized light, intermediate for linear polarized light, and the longest time constant was found for CW polarized light (Figure 5.2F). Moreover, the decay rate for the linear polarizations was similar in every assembly. Such changes in electron transfer rates with chirality and light polarization in QD assemblies is unprecedented, however this behavior can be rationalized by the CISS effect.[243,244]

Figure 5.3 shows the relationship between the polarization in the electron transfer rate of the QD dyads and the magnitude of the acceptor QDs' circular dichroism spectrum. In every case shown, the $\Delta_r G$ of the reaction is -0.18 eV. The magenta squares correspond to D-cysteine capped CdSe, the dark blue circles correspond to L-cysteine capped CdSe, and the light blue triangles correspond to L-acetylcysteine capped CdSe; the red sigmoidal line is a guide to the eye. Note that the majority of L-cysteine CdSe QDs have negative $\Delta\varepsilon$ values, however one data point occurs at 1.04 M^{-1} cm^{-1}, presumably because of a switch in the ligand's binding geometry on the

QD surface. Interestingly, the sign of the polarization *P* coincides with this change in sign of the acceptor QD's circular dichroism. This behavior suggests that the spin selectivity in electron transport is related to the chirality of the acceptor QDs' electronic state and not the molecular chirality of the individual ligands. Figure 5.3 shows that the magnitude and sign of the polarization correlates with the intensity and direction of the chiroptical response of the chiral acceptor QDs.

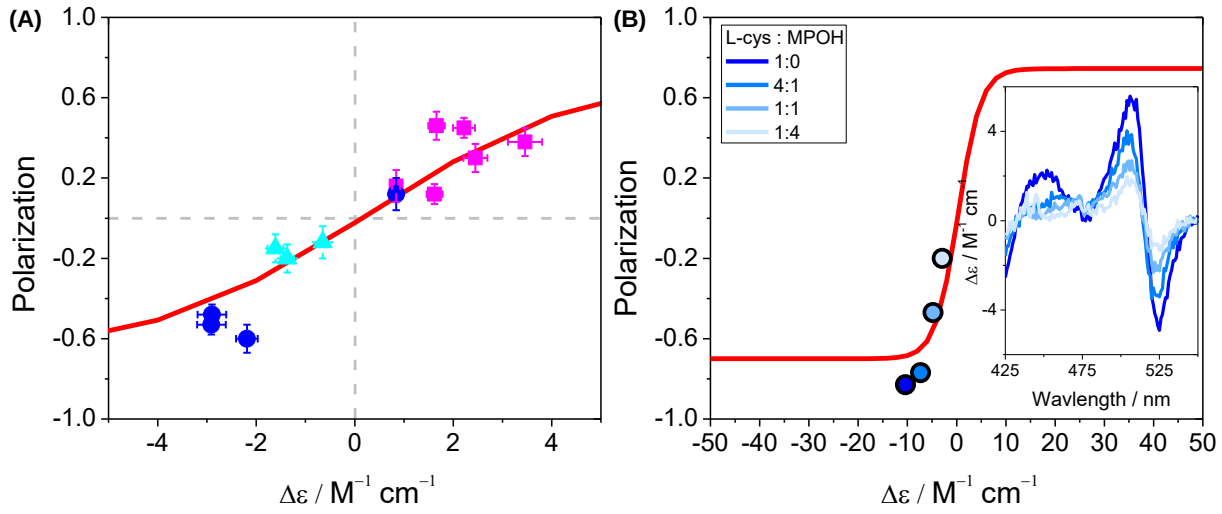

Figure 5.3 - The calculated polarization in the electron transfer rate is plotted against the corresponding peak to trough magnitude of the acceptor QDs circular dichroism spectrum. Each data point represents a different QD assembly. In Panel A the symbol type characterizes the ligands on the acceptor QD; D-cysteine (magenta, square), L-cysteine (dark blue, circle), and L-acetylcysteine (light blue, triangle). Panel B shows the spin polarization of different assemblies in which the CdSe acceptor QDs are passivated with a 1:0, 4:1, 1:1, and 1:4 ratio of L-cysteine : MPOH ligands. The inset shows the circular dichroism spectra of the QDs. The red line in both panels is a sigmoidal fit to the data and is the same curve in both plots.

In addition to the use of L and D cysteine as a capping ligand, L-acetylcysteine was also used as a capping ligand on the acceptor QD. Unlike the experiments by Balaz *et al.*,[255] the orientation of the circular dichroism for the L-acetylcysteine capped CdSe was found to be in the same direction as that for L-cysteine capped CdSe; the bisignate peak at the absorption maximum of the QD goes from negative to positive in the low energy to high energy direction. Interestingly, the Cotton effects for the L-acetylcysteine capped CdSe are in agreement with the works of

Balaz *et al.*,[256] but both the L-cysteine and D-cysteine capped CdSe QDs have opposite Cotton effects to that reported in their study. Because the QDs' CD spectrum is sensitive to the binding geometry of the ligand on the surface, it is reasonable that a different method for synthesizing the acceptor QDs could give rise to differences in the CD spectrum. Previous experiments have shown that an inversion in the CD spectra of trioctylphosphine oxide (TOPO) capped CdSe and oleic acid (OA) capped CdSe, when ligand exchanged to cysteine, occurs even under the same experimental conditions.[257] When the QDs with OA native ligands are exchange to L-cysteine the bisginate peak at the absorption maximum of the QD goes from positive to negative in the low energy to high energy direction. Conversely, the opposite dependence was found for QDs passivated with TOPO native ligands.[257]

The relationship between the polarization *P* and CD intensity could reflect the ensemble nature of the measurements. The measured CD sepectrum is an average over the individual QDs in solution. For example, some QDs could possess all *cis* ligand chelation that gives rise to an intense (+) CD signal; whereas other QDs could have multiple *trans* ligand conformations that result in the individual QD having a lower net chirality, or even the opposite chirality orientation (-). The lifetime measurements are performed using an ensemble of chiral acceptor QDs and therefore the degree of homogeneity in the surface structure will dictate the polarization; if the ratio of (+) to (-) is high then both a more intense CD spectrum and a larger polarization will be observed. To test this hypothesis, we performed experiments in which the chirality of the acceptor QD was purposefully decreased by diluting the chiral cysteine ligand shell with achiral 3-mercapto-1-propanol ligands (MPOH).

Figure 5.3B shows the calculated spin polarizations plotted against the magnitude of their CD spectra for CdSe acceptor QDs in which the ligand shell was prepared using different ratios of L-

cysteine and MPOH surface capping ligands; 1:0, 4:1, 1:1, and 1:4. The inset in Figure 5.3B corresponds to the CD spectrum for each data point and the red line is the same sigmoidal curve used in panel A. The corresponding photoluminescence decays and distribution fitting to the short component of the measurements for the QD assemblies with the different ligand coverages are shown in the Supplemental Information. The spectra show a systematic decrease in intensity of the CD spectra but no significant spectral shift as the coverage of achiral ligands is increased. Because the donor CdTe can only be covalently attached to the L-cysteine ligand on the acceptor CdSe (MPOH does not have the right chemical functional group) the bridge composition is equivalent in every QD assembly. Thus, if the spin polarization is associated only with the chirality localized on the bridge the same polarization ought to be observed, independent of the L-cysteine surface concentration. From this figure, it is evident that the polarization changes greatly with the chirality of the QD and therefore does not manifest solely from the bridge architecture.

Previous studies have shown that it is necessary to account for both the S_e and P_e electronic states in the conduction band of the acceptor QD to accurately describe electron transport in a donor-acceptor QD assembly.[251] By changing the size of the acceptor QD, the driving force (Δ_rG) for the electron transfer reaction can be altered, and with it the electronic state contribution to the overall electron transfer. For a Δ_rG of -0.18 eV used in the above experiments, the electron transport to the S_e and P_e states is approximately equal. For a less favorable Δ_rG the majority of electron transfer is to the S_e states and for a more favorable Δ_rG the electron transfer to the P_e electronic states dominate; see Graff *et al*. for more details.[251]

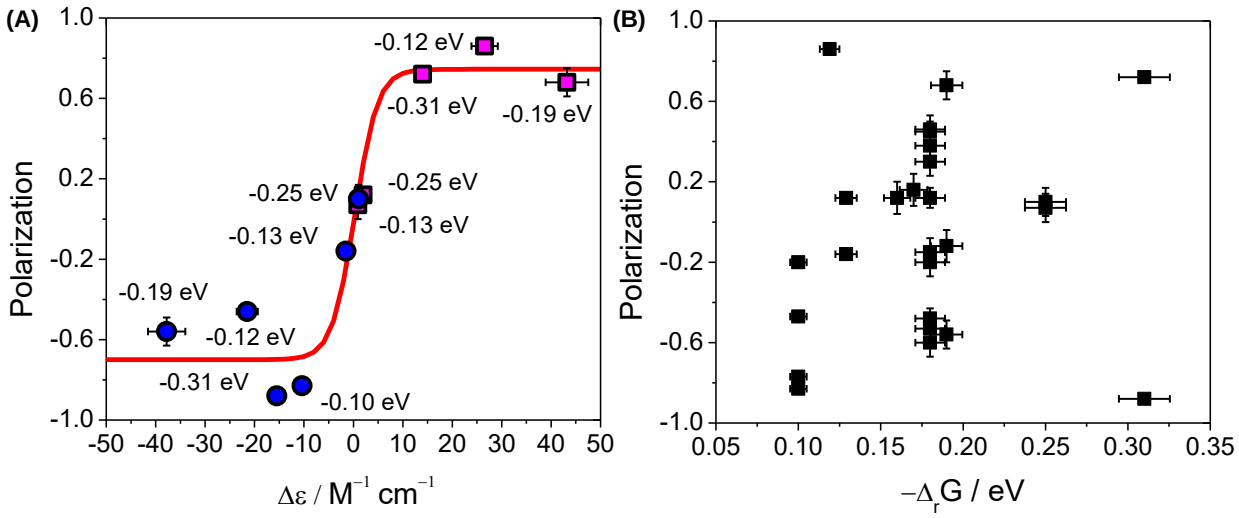

Figure 5.4 - Panel A shows the spin polarization of different QD assemblies in which the symbol type characterizes the ligand on the acceptor QDs; D-cysteine (magenta, square) and L-cysteine (blue, circle). The labeling above each data point represents the Δ_rG. See main text for more details. The red line is a sigmoidal fit used as a guide to the eye. It is the same distribution as that used in Figure 3. Panel B shows the lack of a correlation between reaction free energy and polarization for all of the QDs studied.

Figure 5.4A shows data for experiments in which the energy offset between the donor and acceptor QDs was varied. Here, Δ_rG values more negative than -0.18 have more favorable transport and Δ_rG more positive than -0.18 are less favorable. Data in which Δ_rG = -0.18 are removed for clarity. Figure 5.4B is a plot of the polarization at all of the different reaction free energies measured. It is clear from Figure 5.4 that, despite large differences in the driving force, the most significant parameter for predicting the polarization is the CD strength of the acceptor QD. The correlation between polarization and chirality, independent of Δ_rG, has two important implications: 1) the spin operates equally over both electronic levels on the acceptor QD and 2) the polarization is associated with a change in the electronic coupling between the donor and acceptor QDs. The data from the three different sets of experiments (a change in acceptor ligand chirality, controlled density of chiral ligands on the acceptor QD, and changes in reaction free energy between donor and acceptor QDs) are summarized in Figure 5.5A. It is interesting to note that all of the data qualitatively fall along the sigmoidal curve used in Figure 5.3 and indicate that

the chiroptical properties of the QD is the majority contributor for the manifestation of a spin polarization.

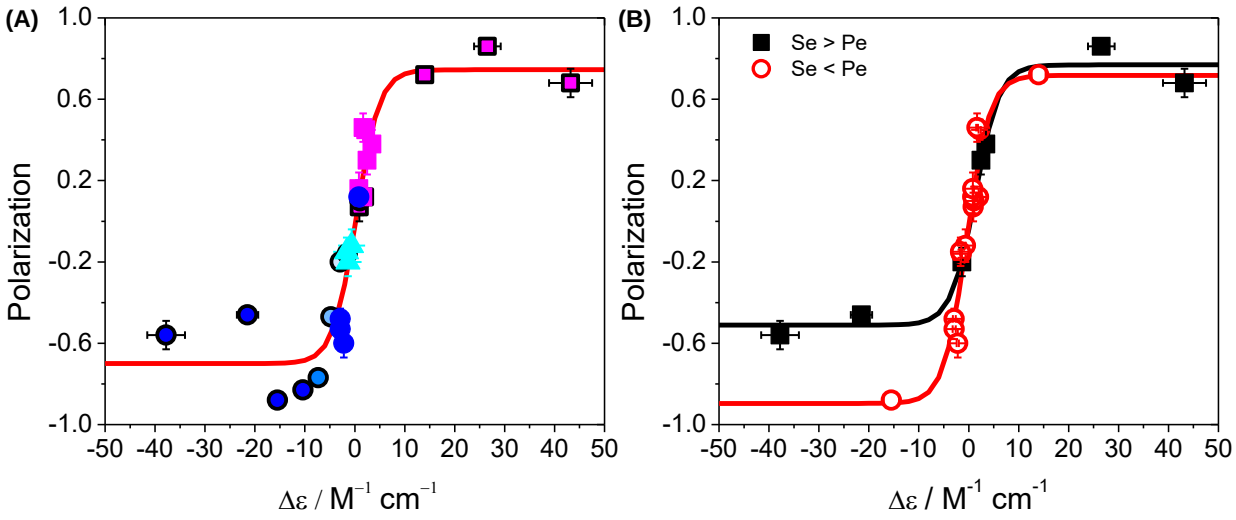

Figure 5.5 - The calculated polarization for each QD assembly is plotted against the corresponding peak to trough magnitude of the circular dichroism spectrum. Each data point represents a different QD assembly and the symbol type characterizes the ligands on the acceptor QD; D-cysteine (magenta, square), L-cysteine (dark blue, circle), and L-acetylcysteine (light blue, triangle). Symbols outlined with a black box represent an assembly with a different energy offset between donor and acceptor. The red line in panel A is the same sigmoidal curve used in the other plots. Panel B shows the same data but separated by electronic state intensity of the S_e and P_e states in the CD spectra; S_e electronic transitions more intense than the P_e transitions (black) and S_e transitions less intense than P_e (red). A new sigmoidal curve was then used to fit the two different data sets.

The plot in Figure 5.5A shows more scatter in the polarization at high values of $\Delta\varepsilon$ and may be caused by differences in the electronic structure of the QDs. The magnitude of $\Delta\varepsilon$ is calculated using only the bisignate peak appearing in the first excitonic region of the QD however, higher order electronic transitions are not always consistent. For some QD samples the $1S_{3/2} \rightarrow S_e$ electronic transition has a higher intensity in the CD spectrum than the $1P_{3/2} \rightarrow P_e$ electronic transition, whereas in other QD samples the reverse is true. Figure 5.5B shows how the data set follows two different distinct line shapes when separated based on their relative intensities. While the reason for the differences in the CD spectrum isn't wholly clear, it may have roots in the higher order electronic transitions interacting to form non-degenerated coupled oscillators or

slight asymmetry in the spherical QDs (prolate or oblate). A better understanding of the origin of this effect synthetically may allow for more reproducibly high polarizations in the large $\Delta\varepsilon$ limit.

In previous work, we showed that chiral QDs have inherent differences in the spin specific conduction of electrons through chiral QD layers in the dark.[247] In a series of magnetoresistance measurements on devices and magnetic conductive probe atomic force microscopy measurements on thin films it was shown that the conduction through D-cysteine capped CdSe QDs was more favorable for spin up (parallel to propagation direction) electrons than for spin down (antiparallel to the propagation) electrons. The opposite preference was observed for L-cysteine capped CdSe layers. In this study, the photoexcitation of CdTe QDs with CW circularly polarized light (from the front surface of the microbead) creates a majority of spin up electrons.[258] When the acceptor QD is D-cysteine, faster quenching is observed when the donor CdTe QD is excited with CW polarized light (red trace) than for CCW polarized light (green trace), Figure 5.2D. This suggests that, when the acceptor QD is D-cysteine capped CdSe, the electron transfer for spin up electrons is more favorable than for spin down electrons and is in agreement with the spin dependent conduction preference previously demonstrated for chiral QDs.

The work reported here establishes two important new facts about for chiral QDs in spin-based electronics. First, the correlation between polarization and the CD strength of a QDs exciton transition imply that the CD strength can be used to predict the spin filtering performance of a chiral QD. Second, the spin degree of freedom in electron transport can be controlled through the QDs chirality alone. These findings may lead to new design principles for the creation of circularly polarized luminescence and spin light emitting diode type technologies without the need of a permanent magnet. Moreover, the spin selective properties of chiral QDs may find

practicality in spintronic applications where gate voltage pulses to form Pauli spin blockades would no longer be necessary.

5.2 REFERENCES

234 K. Michaeli, N. Kantor-Uriel, R. Naaman, D. H. Waldeck, *Chem. Soc. Rev., ASAP* (2016) DOI: 10.1039/C6CS00369A.
235 P. C. Mondal, C. Fontanesi, D. H. Waldeck, and R. Naaman *Accts. Chem. Res* **49** 2560 (2016).
236 a) R. Hanson, L.P. Kouwenhoven, J.R. Petta, S. Tarucha, L.M.K. Vandersypen, *Rev Mod. Phys.* **79** 1217 (2007).
237 D. D. Awschalom, M. E. Flatte *Nature Physics* **3** 153 (2007).
238 E. I. Rashba, *Physica E* **34**, 31 (2006).
239 M. Ouyang, D. D. Awschalom, *Science* **301**, 1074 (2003).
240 F. Liu *et al., Phys. Rev. B.* **89**, 115306 (2014).
241 K. Ono, D. G. Austing, Y. Tokura, S. Tarucha, *Science* **297**, 1313 (2002)
242 K. Ray, S. P. Ananthavel, D. H. Waldeck, R. Naaman, *Science* **283**, (1999)
243 R. Naaman, D. H. Waldeck, *J. Phys. Chem. Lett.* **3**, 2178 (2012).
244 R. Naaman, D. H. Waldeck, *Annu. Rev. Phys. Chem.* **66**, 263 (2015).
245 M. P. Moloney, J. Govan, A. Loudon, M. Mukhina, Y. K. Gun'ko, *Nat. Protoc.* **10**, 558 (2015).
246 F. P. Milton, J. Govan, M. V. Mukhina, Y. K. Gun'ko, *Nanoscale Horiz.* **1**, 14 (2016).
247 B. P. Bloom, V. Kiran, V. Varade, R. Naaman, D. H. Waldeck, *Nano Lett*. **16**, 4583 (2016).
248 M. Eckshtain-Levi *et al., Nat. Commun*. **7**, 10744 (2016).
249 P. Roy *et al. ACS Nano*. **10**, 4525 (2016).
250 O. B. Dor, N. Morali, S. Yochelis, L. T. Baczewski, Y. Paltiel, *Nano Lett*. **14**, 6042 (2014).
251 B. M. Graff, B. P. Bloom, E. Wierzbinski, D. H. Waldeck, *J. Am. Chem. Soc.* **138**, 13260 (2016).
252 R. Hanson, D. D. Awschalom, Nature 453, 1043 (2008).
253 D. D. Awschalom, J. M. Kikkawa, *Phys. Today* **52**, 33 (1999).
254 J. A. Gupta, D. D. Awschalom, X. Peng, A. P. Alivisatos, *Phys. Rev. B*. **59**, 10421 (1999)
255 J. K. Choi et al. ACS Nano 10, 3809 (2016).
256 J. Kyu *et al. ACS Nano* **10**, 3809 (2016).
257 U. Tohgha *et al. ACS Nano* **7**, 11094 (2013).
258 R. Winkler, *Handbook of Magnetism and Advanced Magnetic Materials*, John Wiley & Sons, New York (2007).

6.0 CONCLUSIONS

This dissertation has explored electron transfer in molecular systems and nanoparticle assemblies. Chapter 2 described the experimental determination of the electron transfer rate of an amide modified pyrene donor-bridge-acceptor system. It was found that the presence of the amide modification decreased the redox potential of the pyrene acceptor moiety. Consequentially, the amide substituent led to a change in the driving force of the electron transfer reaction as well as the electronic coupling when compared to an unmodified pyrene moiety. As a result of the amide modification, the hydrophobicity of the molecular cleft was decreased by altering the strength of the π-π interaction between the donor and acceptor moiety. Thus, the amide modification caused the molecular cleft to increase in size allowing for larger solvent molecules and multiple water molecules to fit into the cleft and facilitate charge transfer. These findings indicate that an amide modification can be utilized to tune the tunneling gap.

Chapter 3 further explored the effects of an amide modification to a pyrene acceptor moiety. The amide modification was placed on either the third, sixth, or eighth substituent position on the pyrene. It was found that when the amide substituent was placed closer to the bridge (more removed from the molecular cleft), the acceptor moiety behaved more similarly to an unsubstituted pyrene molecule. The amide modification on the third substituent position of the pyrene led to a new radiative recombination pathway that did not participate in electron transfer.

So, while the electron transfer kinetics did not change significantly with the position of the amide substituent, the radiative decay of the pyrene itself did change with the amide modification.

Chapter 4 described electron transfer in a donor-bridge-acceptor semiconductor nanoparticle assembly. The design of a well-defined nanoparticle dyad architecture was fabricated and characterized. Simply by modifying the surface ligand of the acceptor nanoparticle, the interparticle distance between the donor and acceptor nanoparticle was varied. Experimentally determined electron transfer rates showed that the mechanism of electron transport is electron tunneling. Electron transfer rates were also studied as a function of driving force, $\Delta_r G$. This study was accomplished by modifying the size of the acceptor nanoparticle, which changes the energetics of the acceptor nanoparticle. Similar to a molecular donor-bridge-acceptor, these semiconductor donor-acceptor nanoparticle assemblies can also be described via the semi-classical Marcus equation. Thus, the knowledge gained over the last few decades for molecular donor-acceptor systems can be used to understand these semiconductor nanoparticle assemblies.

Chapter 5 described donor-acceptor semiconductor nanoparticle assemblies where the acceptor nanoparticle was chiral. This system design allowed for a careful study of the relationship between the chiroptical properties of the acceptor and the effective spin filtering capabilities or polarization. It was found that the polarization correlated well with the chiroptical properties of the acceptor, indicating that the spin selectivity of electron transport could be predicted by the chiroptical properties of the acceptor. Note that circularly polarized light alone was found to generate near-unity control over spin selectivity, which could prove to be useful in designing technologies that are spin selective but do not require a permanent magnet.

The molecular and nanoparticle systems presented in this dissertation were utilized to study electron transfer; these studies apply to particular systems, but their findings can be generalized

and applied to future works where the separation of charge is necessary. Chapter 2 and 3 studies how small modifications to the pyrene acceptor moiety in a donor-bridge-acceptor system can modify the electron transfer kinetics. This work can be utilized to predict how modification to acceptor moieties in donor-bridge-acceptor systems can affect electron transfer pathways. Chapters 4 and 5 describe how a novel design architecture for a donor nanoparticle-acceptor nanoparticle system can be utilized to quantitatively predict charge transport and spin selectivity in nanoparticle dyads. A current area of interest is further probing what role nanoparticles play in spin selective charge transport (ie. position of chiral center with respect to the nanoparticle) and these well-defined nanoparticle dyads provide an excellent architecture for such studies. Hopefully, the findings in this thesis will help future researchers better predict charge transport properties of molecular and nanoparticle systems.

7.0 APPENDIX A

7.1 SOLUTION PHASE SYNTHESIS

7.1.1 Methyl 6-aminopyrene-1-carboxylate (S-1)

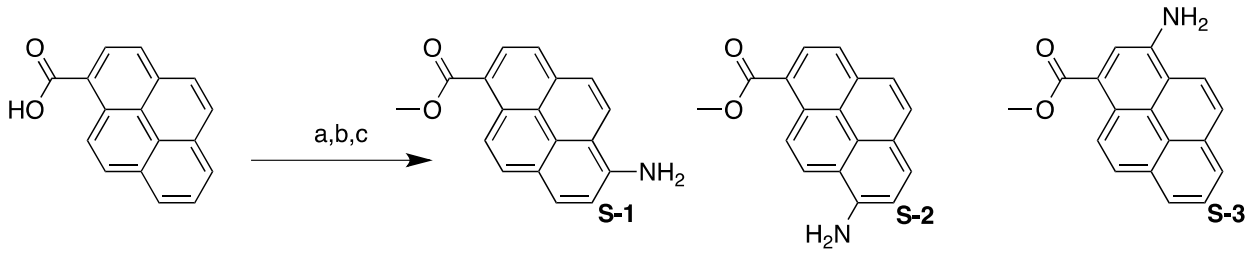

Pyrene-1-carboxylic acid a) Na_2CO_3, MeI, DMF; b) HNO_3, Ac_2O; c) Pd/C, H_2, THF

Sodium carbonate, Na_2CO_3, (215 mg, 2.04 mmol, 2 equiv) followed by methyl iodide, MeI (70 uL, 1.12 mmol, 1.1 equiv) was added to pyrene-1-carboxylic acid (250 mg, 1.02 mmol) in N,N-dimethylformamide, DMF, (10 mL). After stirring overnight, the mixture was added dropwise to a stirred solution of water (100 mL) at 0℃. A precipitate formed, was collected, and was5 washed with cold water. After the solid was resuspended in acetic anhydride, Ac_2O, (10 mL) a 0.4 M nitric acid, HNO_3, solution in Ac_2O (5 mL, 2,04 mmol, 2 equiv) was added. After heating to 70℃, the reaction was stirred overnight and concentrated under reduced pressure. Pd/C (30

mg) was added after the residue was resuspended in THF (20 mL). The sample was then degassed, charged with H_2 *(g),* and stirred overnight. The reaction mixture was then chromatographed on silica, with isocratic elution of PhMe. The desired fractions were collected, combined, and concentrated to yield a solid (118 mg, 429 umol, 42 % yield). ^{1}H NMR (500 MHz, rt, $CDCl_3$): δ 9.03 (d, J=9.1 Hz, 1H), 8.56 (d, J=8.3 Hz, 1H), 8.07 (m, 3H), 8.01 (d, J=8.3 Hz, 1H), 7.98 (d, J=9.1 Hz, 1H), 7.41 (d, J=8.3 Hz, 1H), 4.08 (s, 3H); ^{13}C NMR (125MHz, rt, CDCl3): δ 168.8, 141.8, 135.2, 134.9, 132.3, 128.6, 126.3, 125.7, 125.3, 124.5, 123.0, 122.6, 122.2, 121.1, 117.1, 116.1, 114.3, 52.2; HRESIQTOFMS calcd for $C_{18}H_{13}NO_2$ ($M + H^+$) 276.1019, measured 276.1013 (1.9ppm).

7.1.2 Methyl 8-aminopyrene-1-carboxylate (S-2)

Isolated during the purification of **S-1**, and the procedure used here was the same as used in **S-1**. The desired fractions were combined and concentrated to yield a solid (53 mg, 193 umol, 19 %). ^{1}H NMR (500 MHz, rt, $CDCl_3$): δ 9.25 (d, J=10.0 Hz, 1H), 8.57 (d, J=8.6 Hz, 1H), 8.14 (d, J=10.0 Hz, 1H), 8.03 (m, 3H), 7.83 (d, J=8.6 Hz, 1H), 7.40 (d, J=8.6 Hz, 1H), 4.08 (s, 3H); ^{13}C NMR (125MHz, rt, $CDCl_3$): δ 168.5, 142.3, 135.5, 131.9, 129.9, 128.7, 127.9, 125.5, 124.4, 123.8, 123.4, 122.2, 121.4, 115.9, 114.1, 52.1; HRESIQTOFMS calcd for $C_{18}H_{13}NO_2$ ($M + H^+$) 276.1019, measured 276.1012 (2.3ppm).

7.1.3 Methyl 3-aminopyrene-1-carboxylate (S-3)

Isolated as a mixture of isomers during the purification of **S-1**.

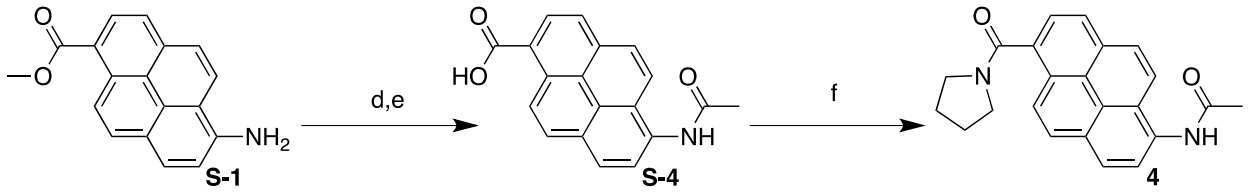

d) Ac_2O, DIPEA, DCM; e) KOTMS, DCM; f) Pyrrolidine, HATU, NMP

7.1.4 6-acetamidopyrene-1-carboxylic acid (S-4)

To **S-1** (100 mg, 400 umol) in DCM (8 mL) was added Ac_2O (1 mL) and then DIPEA (1 mL). The reaction was concentrated under reduced pressure after stirring overnight. Potassium trimethylsilanolate, KOTMS, (513 mg, 4 mmol, 10 equiv) was added to the residue diluted in THF (20 mL) and stirred overnight. Reverse-phase chromatography with a gradient elution from water (0.1% formic acid) to acetonitrile, MeCN, in water (0.1% formic acid over 18 column volumes. The desired fractions were collected, combined, and freeze-dried to yield a powder (910 mg, 300 umol, 75 % yield).^{1}H NMR (500 MHz, rt, DMSO-D6): δ 10.41 (s, 1H), 9.18 (d, J=9.0 Hz, 1H), 8.59 (d, J=9.0 Hz, 1H), 8.46 (d, J=9.0, 1H), 8.33 (m, 5H), 2.26 (s, 3H); ^{13}C NMR (125MHz, rt, $CDCl_3$): δ 167.7, 133.6, 130.4, 128.9, 128.7, 127.4, 126.8, 126.1, 124.9, 124.4, 123.9, 123.7, 123.0; HRESIQTOFMS calcd for $C_{19}H_{13}NO_3$ ($M + H^+$) 304.0968, measured, 304.0985 (3.1 ppm).

7.1.5 N-(4-(pyrrolidine-1-carbonyl)pyrenyl)acetamide (4)

S-4 (30 mg, 100umol) in NMP (500 uL) was added to HATU (38 mg, 100umol) and pyrrolidine (25uL) was added. The reaction was stirred for 1hr then immediately purified on reverse phase HPLC with gradient elution over 30 minutes from water (0.1% formic acid) to MeCN (0.1% formic acid). Fractions containing the product were combined and freeze-dried to yield a powder (27 mg, 76umol, 76% yield). Purity was assessed with analytical HPLC-MS; mobile phase, (gradient elution over 30 minutes from water (0.1% formic acid) to 100% acetonitrile (0.1% formic acid) UV detection at 274nm, tR = 18.3. HRESIQTOFMS calculated for $C_{23}H_{21}N_2O_2$ (M + H+) 357.1598 measured 357.1586 (3.3ppm).

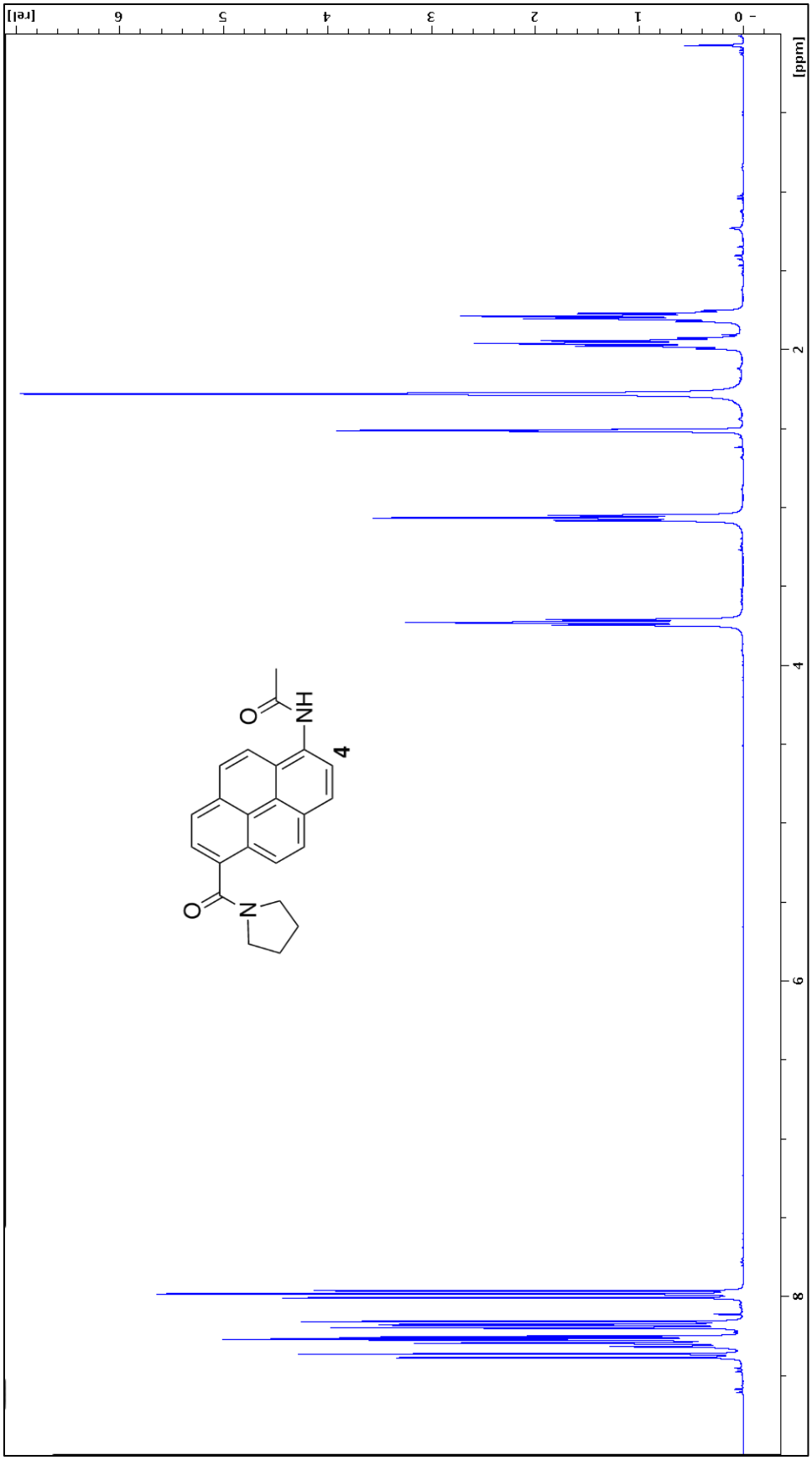

1H NMR (500 mHz, DMSO-D6 + 7.5uL TFA, 333K) of Compound 4

7.2 SOLID PHASE SYNTHESIS

7.2.1 General procedure (A): Attachment to Trityl resin

DIPEA (5 equiv) was added to the amino acid (10 equiv) in DCM (3mL/mmol). The resin in the solid phase reactor was exposed to the reaction mixture, and the mixture was stirred for 4 hours. The resin was filtered and washed with DMF, DCM, isopropyl alcohol (IPA), DCM and DMF.

7.2.2 General procedure (B): O-(7-azabenzotriazol-1-yl)-tetramethyluronium hexafluorophosphate, HATU, coupling

DIPEA (6 equiv) was added to a solution of amino acid (3 equiv) and HATU (3 equiv) in NMP (5 mL/mmol amino acid). The solid phase reactor of the resin was pre-swelled with DMF. After 5 minutes of agitation the reaction mixture was added to the resin and stirred for 45 minutes. The resin was filtered and washed as described in procedure **A**.

7.2.3 General procedure (C): Fluorenylmethyloxycarbamate, Fmoc, deprotection

After the solid phase reactor of the resin was pre-swelled with DMF a solution of 20% piperidine in DMF (15 mL/mmol) was added to this portion of the resin and stirred for 15 minutes. The resin was filtered and washed as described in procedure **A**.

7.2.4 General procedure (D): Allyloxycarbamate, Alloc, deprotection

Within the solid phase reactor the resin was pre-swelled with DMF a borane:dimethylamine complex (6 equiv) in DCM (10 mL/mmol) was added to this portion of the resin and stirred for 5 minutes.A solution of tetrakis(triphenylphosphine)palladium(0) (0.1 equiv) in DCM (10mL/mmole) was added to borane:dimethylamine complex solution and stirred for 1 hour. The resin was filtered and washed as described in procedure **A**.

7.2.5 General procedure (E): Liberation from Trityl resin

After washing the resin with DCM and MeOH and drying under vacuum, a solution of 33% HFIP in DCM was added to the resin and stirred for 4 hours. After rinsing and filtering the resin with additional aliquots of the HFIP solution, the filtrate was concentrated. The residue was redissolved in DMSO and purified on reverse phase HPLC with gradient elution over 30 minutes

from water (0.1% formic acid) to MeCN (0.1% formic acid). Fractions containing the product were combined and freeze-dried to yield a powder.

7.2.6 General procedure (F): tert-Butylcarbamate, Boc, deprotection

The powders are treated with TFA for 4 hours and concentrated. The residue was redissolved in H_2O and and purified on reverse phase HPLC with gradient elution over 30 minutes from water (0.1% formic acid) to MeCN (0.1% formic acid). Fractions containing the product were combined and freeze-dried to yield a powder.

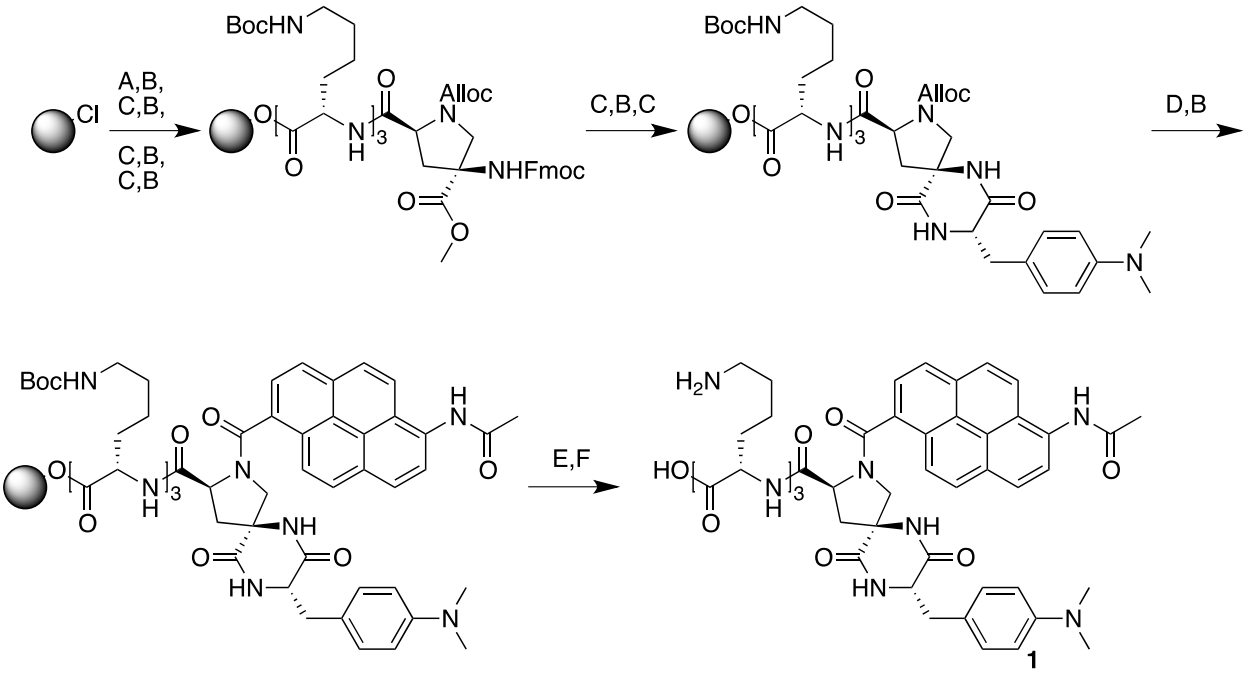

7.3 SOLID PHASE SYNTHESIS SCHEME

7.3.1 D-SSS-A* (1)

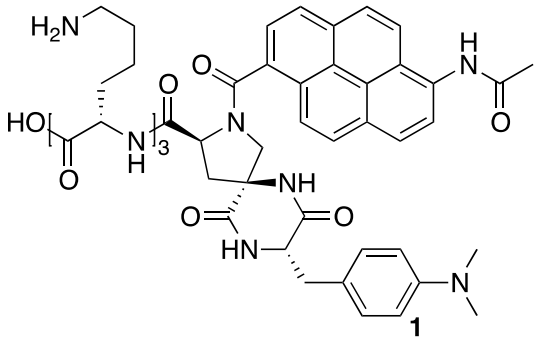

Trityl resin (100 mg, 100 umol) was placed in a 4 mL solid phase reactor. According to general procedure **A** using DCM (4.5 mL) and DIPEA (116 uL, 750 umol) Fmoc-Lys(Boc)-OH (703 mg, 1.5 mmol) was attached to the resin. As described in procedure **C**, the terminal Fmoc group was removed using 20% piperdine in DMF (2.25 mL). Using HATU (171 mg, 450 umol), NMP (2.25 mL), and DIPEA (156 uL, 900 umol) and procedure **B** Fmoc-Lys(Boc)-OH (211 mg, 450 umoles) was attached. The terminal Fmoc group was again removed using procedure **C** as described previously. Fmoc-Lys(Boc)-OH was coupled according to procedure **B** as described previously. The terminal Fmoc group was removed according to procedure **C**.

Using procedure **B**, Pro4ss (223 mg, 450 umol) was coupled using HATU (171 mg, 450 umol), NMP (2.25 mL) and DIPEA (156 uL, 900 umol). The terminal Fmoc group was removed according to procedure **C** described previously. Fmoc-L-DMA-OH was coupled according to procedure **B** as described previously. The terminal Fmoc group was removed according to procedure **C** and the reaction time was extended to 2 hours. Using procedure **D** a borane dimethylamine complex (53 mg, 900 umol) in DCM (2.5 mL) and

tetrakis(triphenylphosiphine)palladium(0) (17mg, 15umoles) in DCM (2mL) was used to remove the Alloc group. Using procedure **B** previously described sample **S-4** (136 mg, 450 umol) was coupled.

Using procedure **E**, 3.75 mL of the cleavage mixture was utilized to remove sample **V** from the resin. After suspension in 50% MeCN in water (0.1% formic acid) the residue was purified by reverse-phase chromatography with gradient elution over 30 minutes from water (0.1% formic acid) to 50% MeCN in water (0.1% formic acid). Fractions containing the product were combined and freeze-dried to yield a powder. Purity was assessed with analytical HPLC-MS; mobile phase, (gradient elution over 30 minutes from water (0.1% formic acid) to 50% acetonitrile (0.1% formic acid) in water (0.1% formic acid). UV detection at 274nm, tR = 9.8. HRESIQTOFMS calculated for $C_{54}H_{70}N_{11}O_9$ (M + H+) 1016.5352 measured 1016.5310 (4.1ppm).

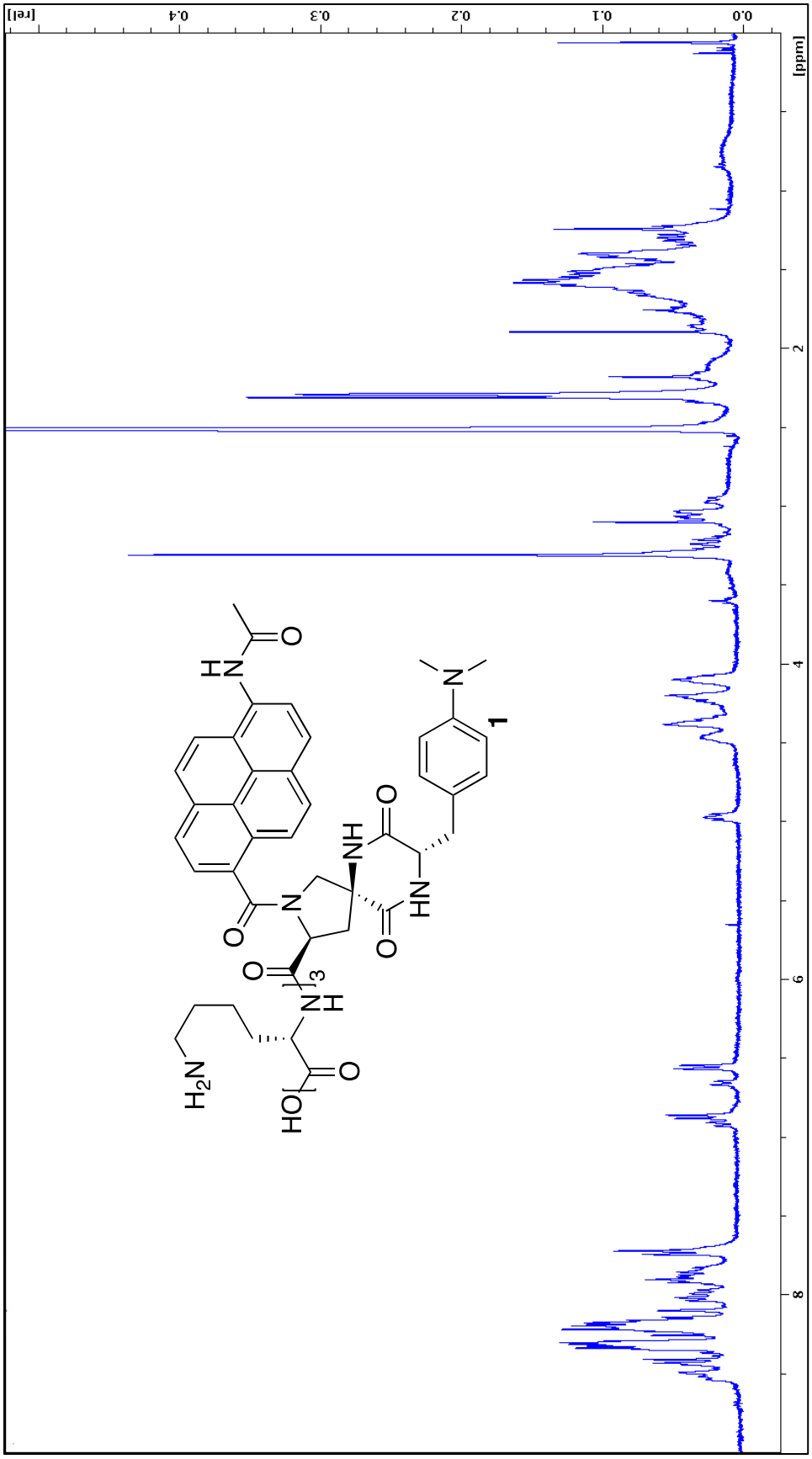

1H NMR (500 mHz, DMSO-D6 + 7.5uL TFA, 333K) of Compound 1

7.3.2 D-RSS-A* (1)

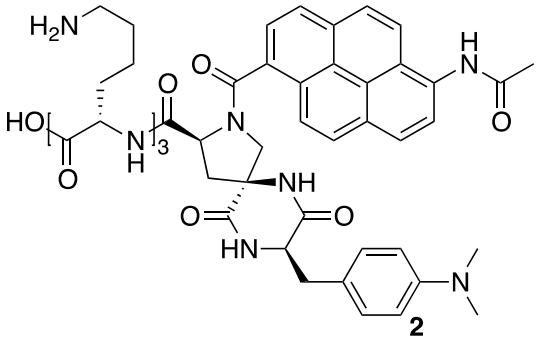

Trityl resin (100 mg, 100 umol) was placed in a 4 mL solid phase reactor. According to general procedure **A** using DCM (4.5 mL) and DIPEA (116 uL, 750 umol) Fmoc-Lys(Boc)-OH (703 mg, 1.5 mmol) was attached to the resin. As described in procedure **C**, the terminal Fmoc group was removed using 20% piperdine in DMF (2.25 mL). Using HATU (171 mg, 450 umol), NMP (2.25 mL), and DIPEA (156 uL, 900 umol) and procedure **B** Fmoc-Lys(Boc)-OH (211 mg, 450 umoles) was attached. The terminal Fmoc group was again removed using procedure **C** as described previously. Fmoc-Lys(Boc)-OH was coupled according to procedure **B** as described previously. The terminal Fmoc group was removed according to procedure **C**.

Using procedure **B**, Pro4ss (223 mg, 450 umol) was coupled using HATU (171 mg, 450 umol), NMP (2.25 mL) and DIPEA (156 uL, 900 umol). The terminal Fmoc group was removed according to procedure **C** described previously. Fmoc-R-DMA-OH was coupled according to procedure **B** as described previously. The terminal Fmoc group was removed according to procedure **C** and the reaction time was extended to 2 hours. Using procedure **D** a borane dimethylamine complex (53 mg, 900 umol) in DCM (2.5 mL) and tetrakis(triphenylphosiphine)palladium(0) (17mg, 15umoles) in DCM (2mL) was used to remove

the Alloc group. Using procedure **B** previously described sample **S-4** (136 mg, 450 umol) was coupled.

Using procedure **E**, 3.75 mL of the cleavage mixture was utilized to remove sample **V** from the resin. After suspension in 50% MeCN in water (0.1% formic acid) the residue was purified by reverse-phase chromatography with gradient elution over 30 minutes from water (0.1% formic acid) to 50% MeCN in water (0.1% formic acid). Fractions containing the product were combined and freeze-dried to yield a powder. Purity was assessed with analytical HPLC-MS; mobile phase, (gradient elution over 30 minutes from water (0.1% formic acid) to 50% acetonitrile (0.1% formic acid) in water (0.1% formic acid). UV detection at 274nm, tR = 9.8. HRESIQTOFMS calculated for $C_{54}H_{70}N_{11}O_9$ (M + H+) 1016.5352 measured 1016.5338 (3.8ppm).

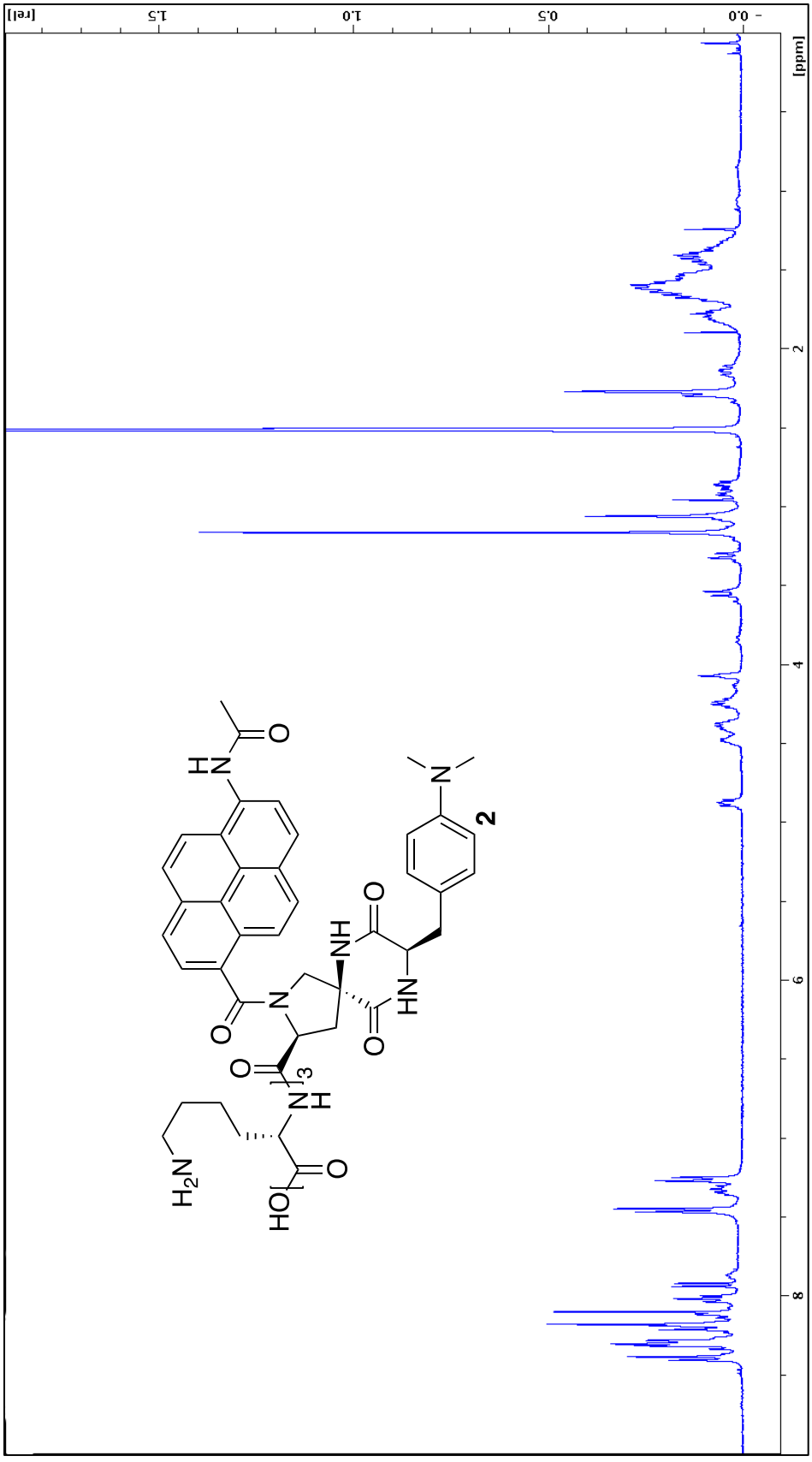

1H NMR (500 mHz, DMSO-D6 + 7.5uL TFA, 333K) of Compound 2

7.3.3 SS-A* (1)

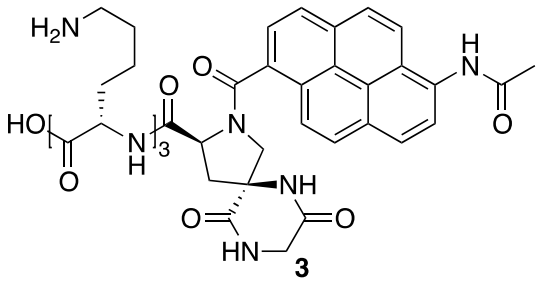

3

Trityl resin (100 mg, 100 umol) was placed in a 4 mL solid phase reactor. According to general procedure **A** using DCM (4.5 mL) and DIPEA (116 uL, 750 umol) Fmoc-Lys(Boc)-OH (703 mg, 1.5 mmol) was attached to the resin. As described in procedure **C**, the terminal Fmoc group was removed using 20% piperdine in DMF (2.25 mL). Using HATU (171 mg, 450 umol), NMP (2.25 mL), and DIPEA (156 uL, 900 umol) and procedure **B** Fmoc-Lys(Boc)-OH (211 mg, 450 umoles) was attached. The terminal Fmoc group was again removed using procedure **C** as described previously. Fmoc-Lys(Boc)-OH was coupled according to procedure **B** as described previously. The terminal Fmoc group was removed according to procedure **C**.

Using procedure **B**, Pro4ss (223 mg, 450 umol) was coupled using HATU (171 mg, 450 umol), NMP (2.25 mL) and DIPEA (156 uL, 900 umol). The terminal Fmoc group was removed according to procedure **C** described previously. Fmoc-Gly-OH was coupled according to procedure **B** as described previously. The terminal Fmoc group was removed according to procedure **C** and the reaction time was extended to 2 hours. Using procedure **D** a borane dimethylamine complex (53 mg, 900 umol) in DCM (2.5 mL) and tetrakis(triphenylphosiphine)palladium(0) (17mg, 15umoles) in DCM (2mL) was used to remove the Alloc group. Using procedure **B** previously described sample **S-4** (136 mg, 450 umol) was coupled.

Using procedure **E**, 3.75 mL of the cleavage mixture was utilized to remove sample **V** from the resin. After suspension in 50% MeCN in water (0.1% formic acid) the residue was purified by reverse-phase chromatography with gradient elution over 30 minutes from water (0.1% formic acid) to 50% MeCN in water (0.1% formic acid). Fractions containing the product were combined and freeze-dried to yield a powder. Purity was assessed with analytical HPLC-MS; mobile phase, (gradient elution over 30 minutes from water (0.1% formic acid) to 50% acetonitrile (0.1% formic acid) in water (0.1% formic acid). UV detection at 274nm, tR = 10.5. HRESIQTOFMS calculated for $C_{54}H_{70}N_{11}O_9$ (M + H+) 883.4461 measured 883.4428 (3.7ppm).

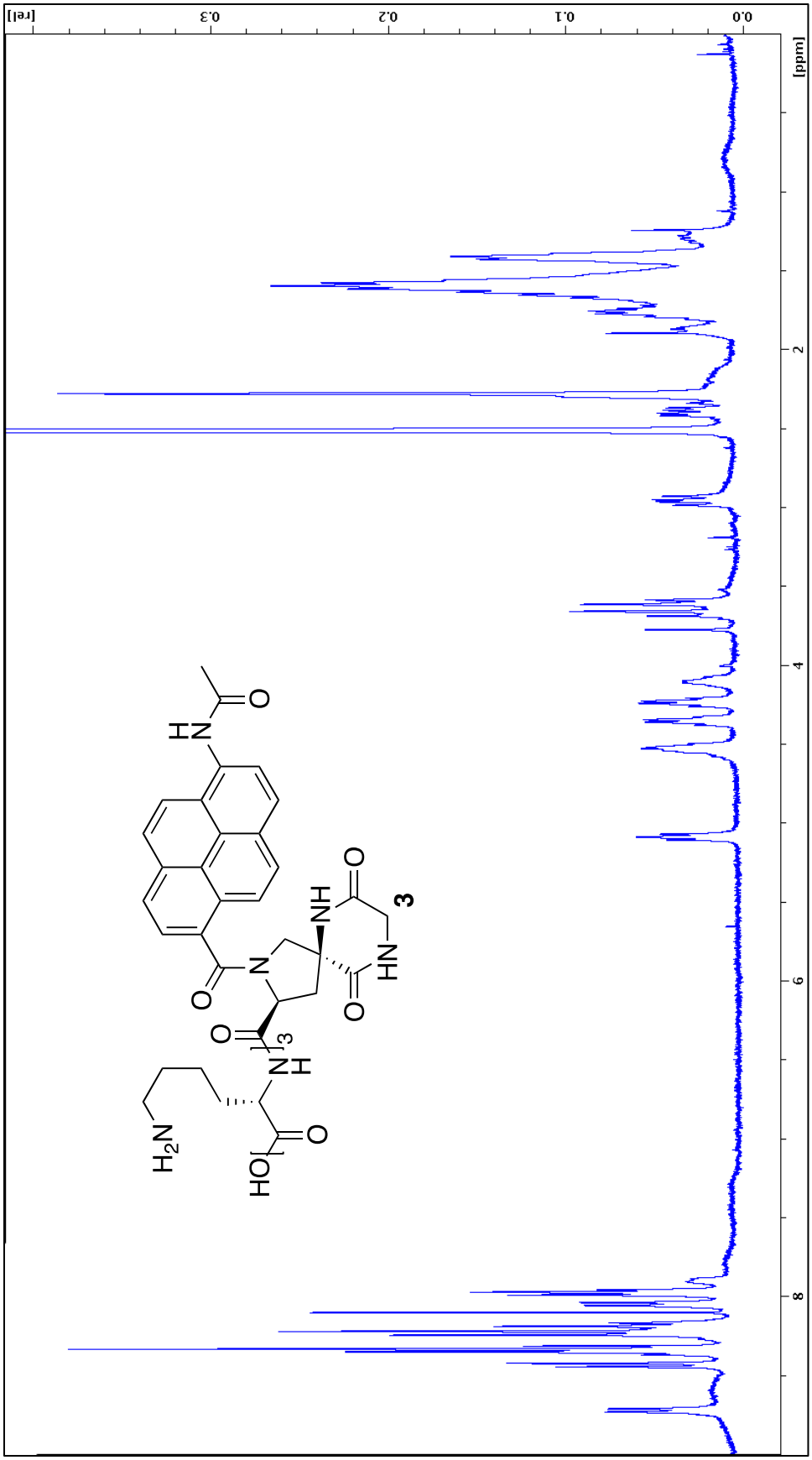

1H NMR (500 mHz, DMSO-D6 + 7.5uL TFA, 333K) of Compound 3

7.4 NMR ANALYSIS FOR REGIOCHEMISTRY ASSIGNMENTS OF COMPOUNDS S-1, S-2, AND S-3

Through 1H NMR analysis the 2H and 10H can easily be assigned and combined with the information from COSY spectra of each isomer, the four isolated spin system pairs can be assigned and arbitrarily labeled as A, B, C, and D. From the HSQC and HMBC NMR spectra, the aniline carbon can be easily identified. The couplings observed clearly show that for Isomer 1, the nitrogen is at the C6 position corresponding to compound S-1 and for Isomer 2, the nitrogen is at the C8 position corresponding to compound S-2.

1H NMR (500 mHz, $CDCl_3$ 298K) of Isomer 1, Isomer 2, Pyrene-carboxylic Acid Stacked

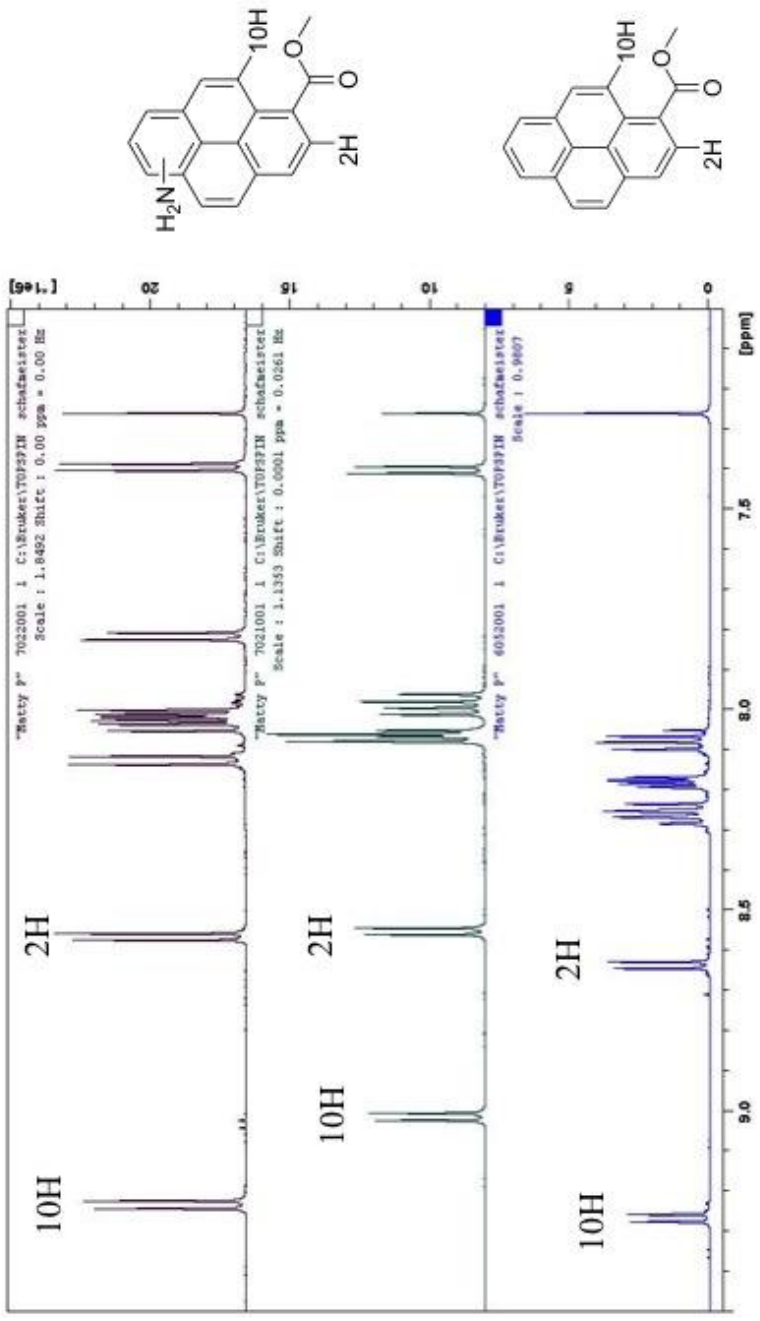

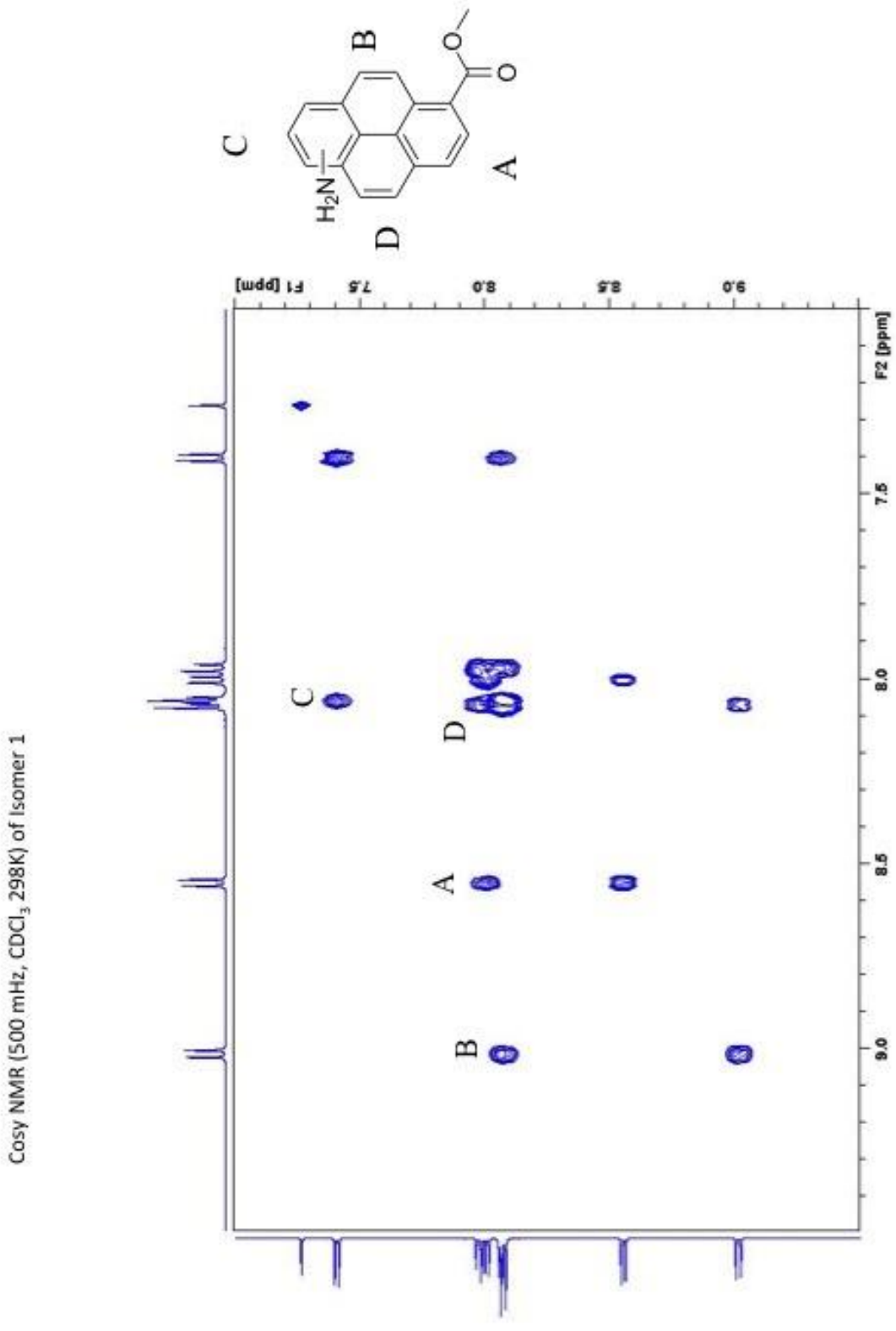

Cosy NMR (500 mHz, $CDCl_3$ 298K) of Isomer 1

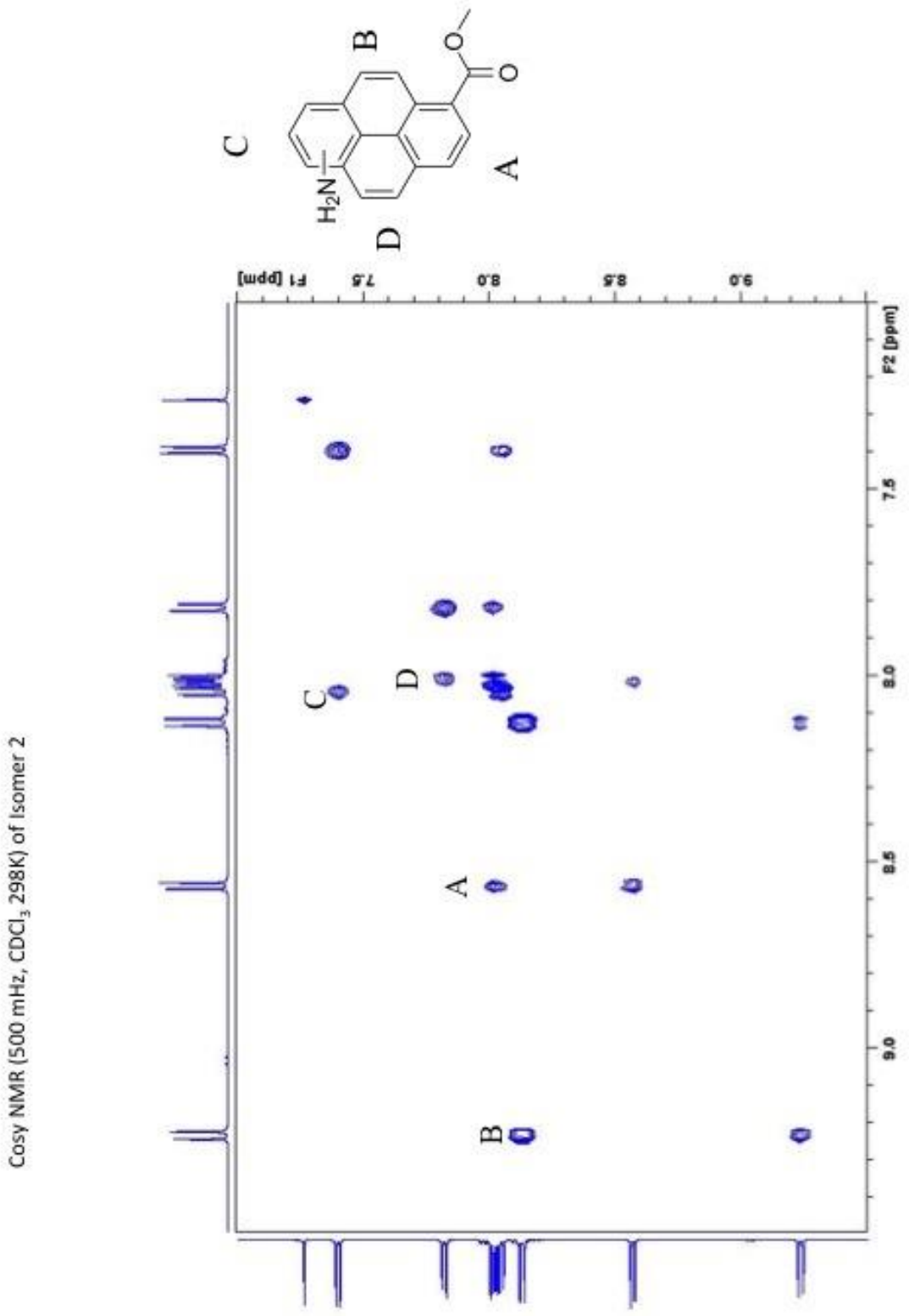
Cosy NMR (500 mHz, $CDCl_3$ 298K) of Isomer 2
A
B
C
D
H_2N
O
O
F1 [ppm]
F2 [ppm]
7.5
8.0
8.5
9.0

HSQC & HMBC NMR (500 mHz, $CDCl_3$ 298K) of Isomer 1 overlayed

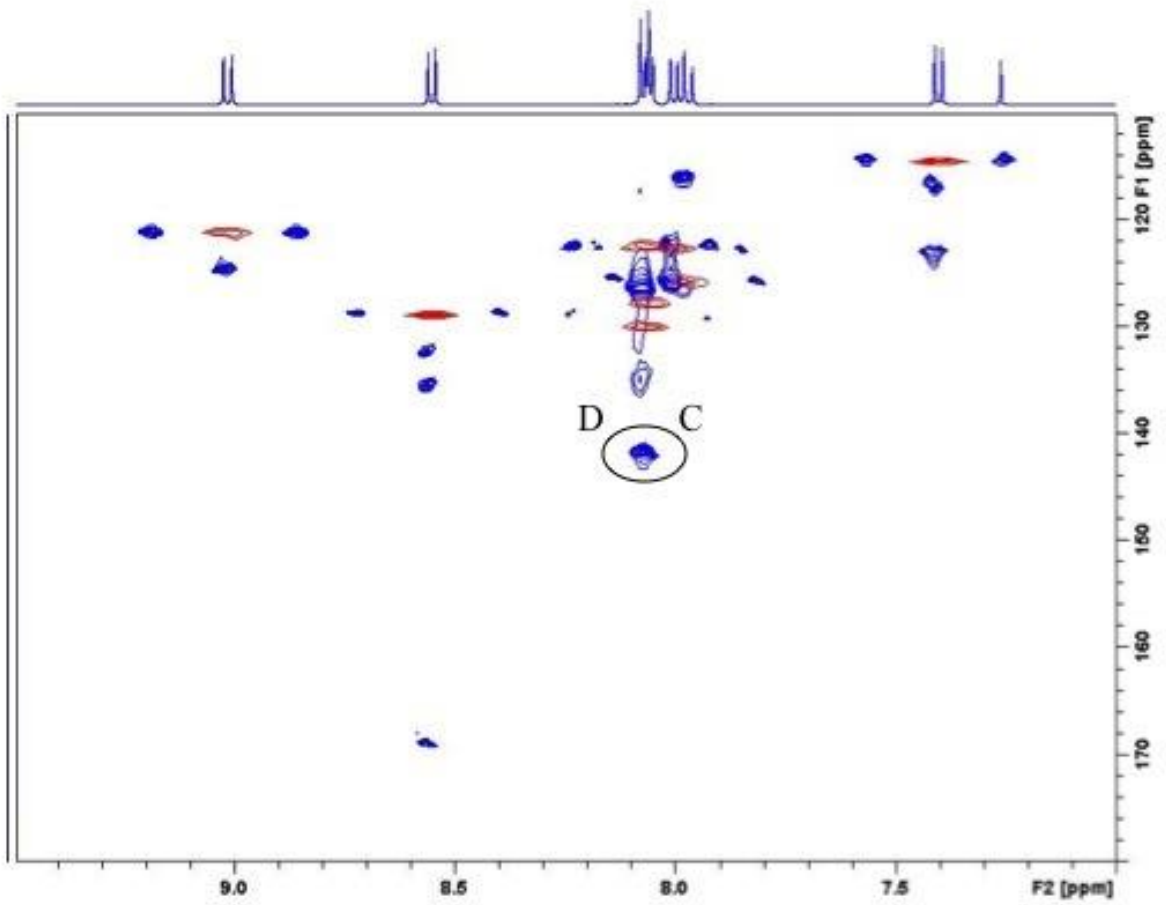

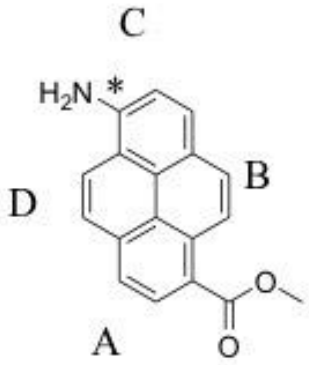

HSQC & HMBC NMR (500 mHz, $CDCl_3$ 298K) of Isomer 2 overlayed

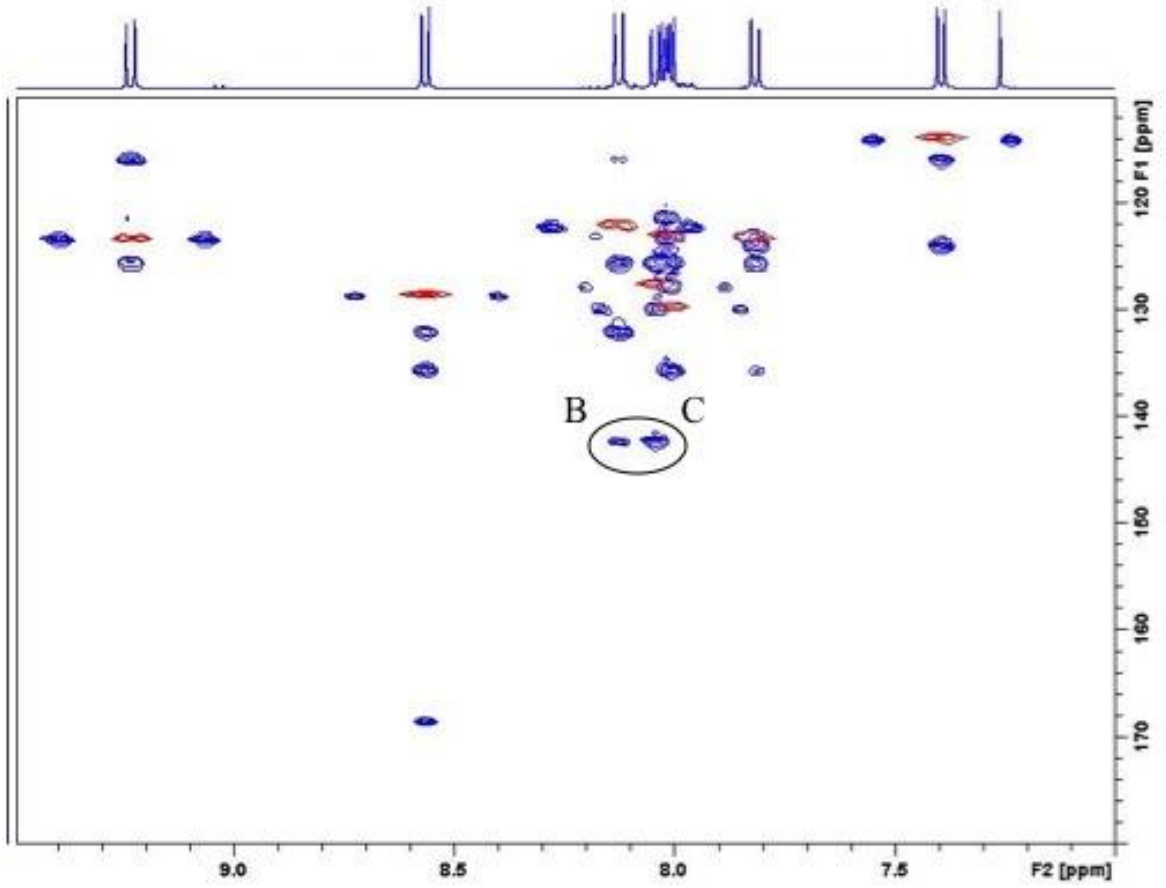

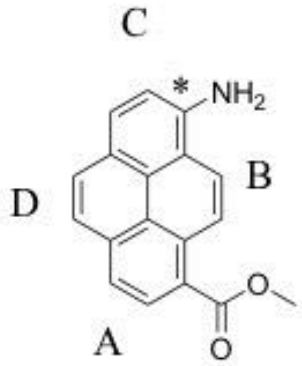

HMBC NMR (500 mHz, $CDCl_3$ 298K) of Isomer 1 & Isomer 2 overlayed

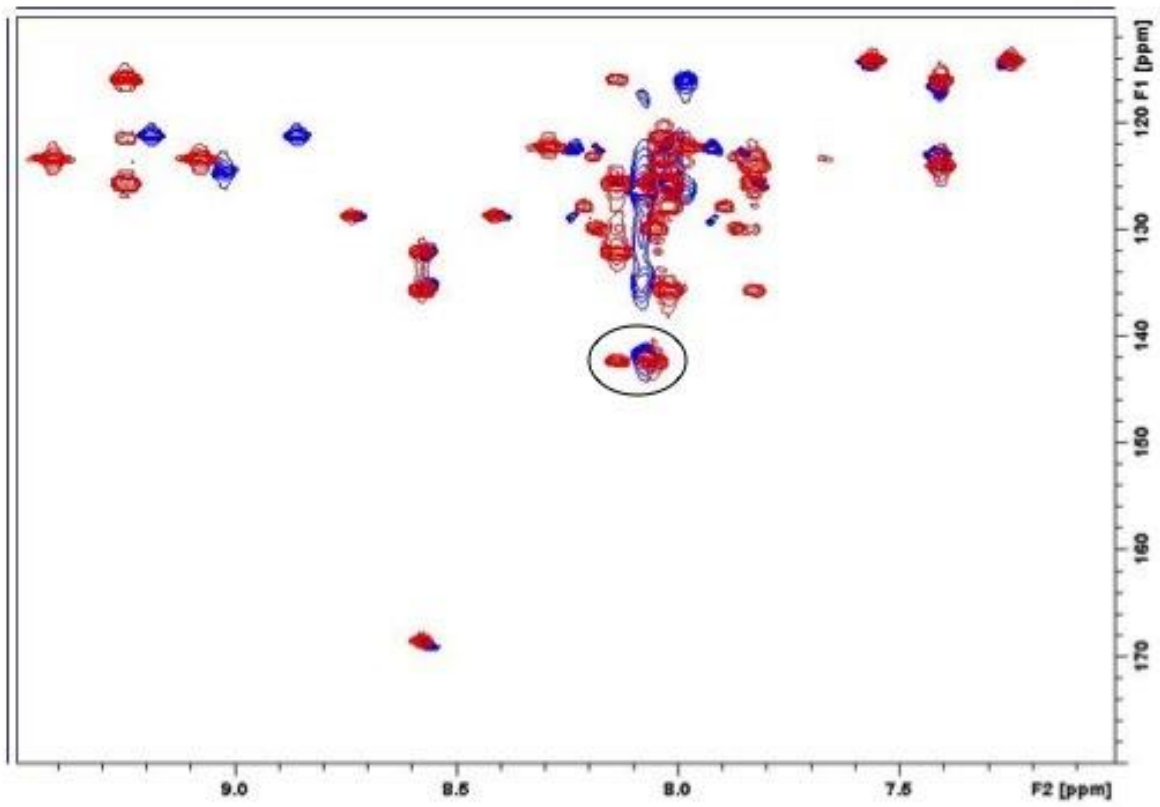

Isomer 1

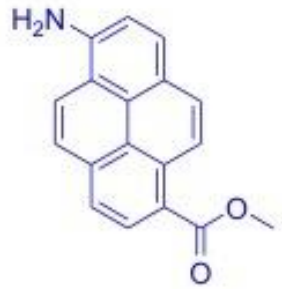

Isomer 2

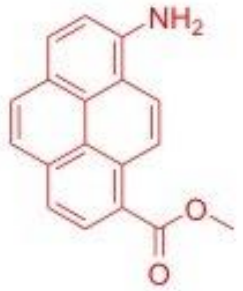

7.5 SPECTRA IN SUPPORT OF THE PHOTOPHYSICAL MODEL

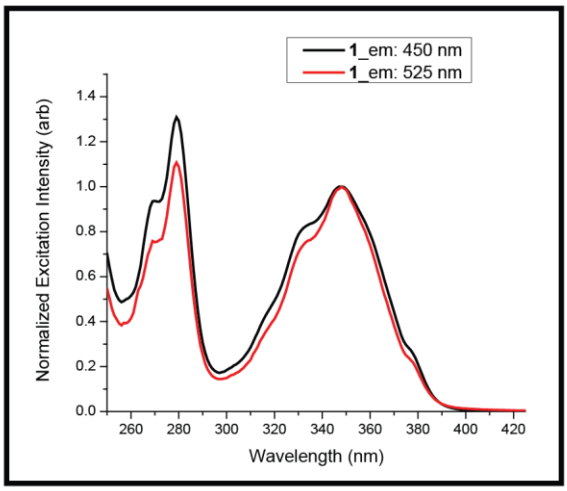

*Figure 7.1 - Excitation spectra are shown for sample **1** in pH=7 buffer. The spectra were taken while observing emission at the monomer maximum (450 nm) and the exciplex emission (525 nm) - 0.17 mm slits and 0.1s integration time.*

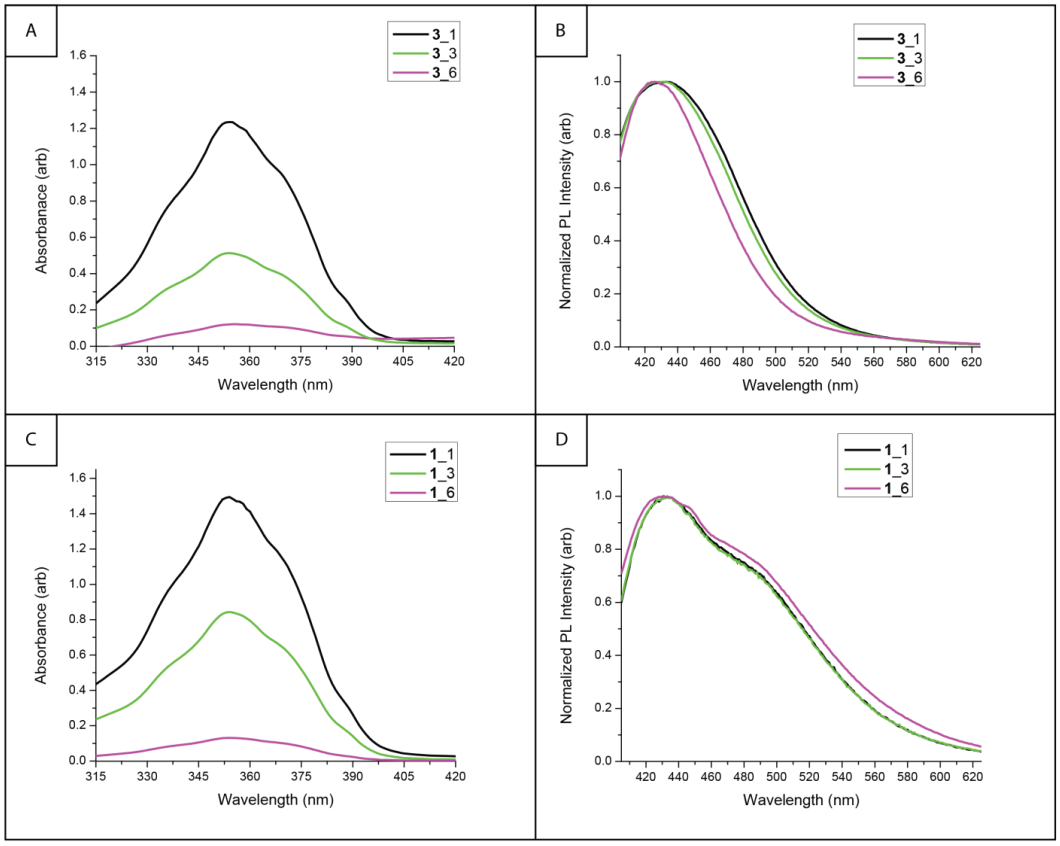

*Figure 7.2 - Absorbance (A) and normalized photoluminescence (PL) spectra (B) are shown for excitation at 385 nm (0.34 mm slits and 0.1s integration time) at varying concentrations of **3** in pH=7 buffer. Panels C and D show absorbance and normalized PL spectra for excitation at 385 nm (0.34 mm slits and 0.1s integration time) at varying concentrations of **1** in pH=7 buffer.*

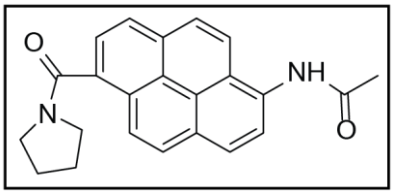

*Figure 7.3 - Molecular structure for the acceptor only compound, **4**.*

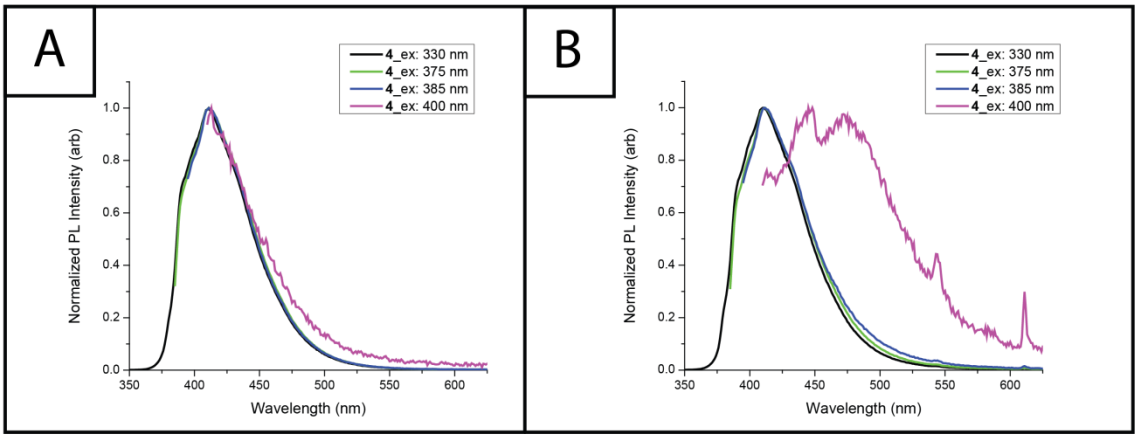

*Figure 7.4 - This figure shows normalized photoluminescence spectra of **4** in chloroform with no DMA (A) and 100 uM DMA (B) at various excitation wavelengths after deoxygenation (0.34 mm slits and 0.1s integration time).*

7.6 KINETIC MODEL WITH EMISSION FROM BOTH LE AND CS STATES

Equation 7.1 and Equation 7.2 describe the kinetic model illustrated in Figure 7.3.

$$\frac{dC_{LE}}{dt} = -(k_f + k_{for})C_{LE} + k_{back}C_{CS} = -k_{LE}C_{LE} + k_{back}C_{CS} \qquad \text{Equation 7.1}$$

$$\frac{dC_{CS}}{dt} = -(k_{rec} + k_{back})C_{CS} + k_{for}C_{LE} = -k_s C_{CS} + k_{for}C_{LE} \qquad \text{Equation 7.2}$$

where $k_{LE} = k_f + k_{for}$ and $k_s = k_{rec} + k_{back}$. Solution of these equations gives

$$C_{LE}(t) = a'_+ e^{-\lambda_+ t} + a'_- e^{-\lambda_- t} \text{ and } a'_+ + a'_- = C_{LE}(0)$$

and

$$C_{CS}(t) = b'_{+}e^{-\lambda_{+}t} + b'_{-}e^{-\lambda_{-}t} \text{ and } b'_{+} + b'_{-} = C_{CS}(0)$$

which can be rearranged to give

$$C_{LE}(t) = \left\{a'_{+}e^{-\lambda_{+}t} + (C_{LE}(0) - a'_{+})e^{-\lambda_{-}t}\right\} \text{ and } C_{CS}(t) = \left\{b'_{+}e^{-\lambda_{+}t} + (C_{CS}(0) - b'_{+})e^{-\lambda_{-}t}\right\}.$$

The eigenvalues are given by

$$\lambda_{\pm} = \frac{1}{2}(k_{LE} + k_S) \pm \frac{1}{2}\sqrt{(k_{LE} + k_S)^2 + 4k_{back}k_{for}}$$

By substitution into Equation 7.1, one can show that

$$b'_{+} = \frac{k_{for}}{(\lambda_{-} - \lambda_{+})}C_{LE}(0) + \frac{(\lambda_{-} - k_S)}{(\lambda_{-} - \lambda_{+})}C_{CS}(0) \text{ and } a'_{+} = \frac{(k_S - \lambda_{+})}{(\lambda_{-} - \lambda_{+})}C_{LE}(0) + \frac{(\lambda_{-} - k_S)(k_S - \lambda_{+})}{(\lambda_{-} - \lambda_{+})}C_{CS}(0)$$

These expressions are equivalent, via substitution for λ_{-} and λ_{+}.

7.6.1 Special Case

For the pyrene systems with $\lambda_{ex} = 375\,nm$, one can make the approximation that $C_{CS}(0) \sim 0$. Then one finds

$$a_{+} \approx \frac{(k_S - \lambda_{+})}{(\lambda_{-} - \lambda_{+})}C_{LE}(0) \text{ and } b_{+} \approx \frac{k_{for}}{(\lambda_{-} - \lambda_{+})}C_{LE}(0)$$

so that

$$C_{LE}(t) = C_{LE}(0)\left[\frac{(k_S - \lambda_{+})}{(\lambda_{-} - \lambda_{+})}e^{-\lambda_{+}t} + \frac{(\lambda_{-} - k_S)}{(\lambda_{-} - \lambda_{+})}e^{-\lambda_{-}t}\right]$$

and

$$C_{CS}(t) = C_{LE}(0)\left[e^{-\lambda_+ t} - e^{-\lambda_- t}\right]\left(\frac{k_{for}}{(\lambda_- - \lambda_+)}\right)$$

Depending on λ_{em}, one observes

$$I(t) = \alpha C_{LE}(t) + \beta C_{CS}(t)$$

where the parameters α and β account for the wavelength dependence of the charge transfer and locally excited state emission bands. Hence, one finds that

$$I(t) = C_{LE}(0)e^{-\lambda_+ t}\left[\alpha\frac{(k_s - \lambda_+)}{(\lambda_- - \lambda_+)} + \beta\frac{k_{for}}{(\lambda_- - \lambda_+)}\right] + C_{LE}(0)e^{-\lambda_- t}\left[\alpha\frac{(\lambda_- - k_s)}{(\lambda_- - \lambda_+)} - \beta\frac{k_{for}}{(\lambda_- - \lambda_+)}\right]$$

or

$$I(t) = \alpha C_{LE}(0)\left\{\left[\frac{k_s - \lambda_+ + \frac{\beta k_{for}}{\alpha}}{(\lambda_- - \lambda_+)}\right]e^{-\lambda_+ t} + \left[\alpha\frac{\lambda_- - k_s - \frac{\beta k_{for}}{\alpha}}{(\lambda_- - \lambda_+)}\right]e^{-\lambda_- t}\right\}$$

Note that

$$\lambda_+ + \lambda_- = k_s + k_{LE}$$

$$\lambda_+ - \lambda_- = \sqrt{(k_s + k_{LE})^2 + 4k_{for}k_{back}}$$

Using algebra and the expression for λ_+, λ_-, and a_+one can show that

$$k_{for} = \{a_+(\lambda_+ - \lambda_-) + \lambda_- - k_f\}\frac{\alpha}{\alpha - \beta}$$

$$k_{back} = \frac{(\lambda_+ - \lambda_-)^2 - \left[2\left(k_{for} + k_f\right) - (\lambda_+ + \lambda_-)\right]^2}{4k_{for}}$$

$$k_{rec} = \lambda_+ + \lambda_- - k_f - k_{back} - k_{for}$$

Note that k_{for} differs by $\frac{\alpha}{\alpha-\beta}$ but the other expressions are identical to that reported earlier.

- Temperature dependent delta G

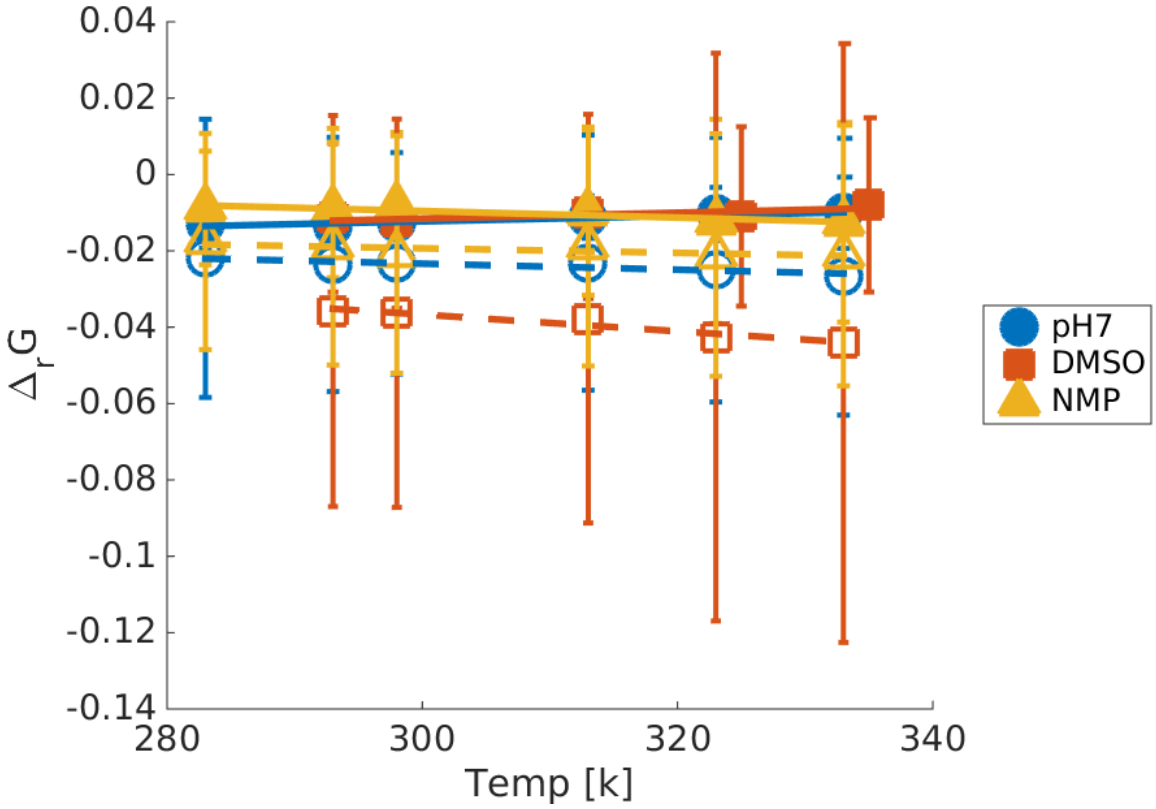

*Figure 7.5 - The temperature dependence of the $\Delta_r G$, experimentally determined via the kinetic model, is shown for **1**, DSSSA, (filled symbols) and **2**, DSRRA, (open symbols). Error bars are shown which indicate that the $\Delta_r G$ is essentially independent of temperature in this range.*

7.7 FEATURES OF THE FITTING OF RATE DATA TO THE SEMICLASSICAL MODEL

7.7.1 Contour plots and parameter coupling

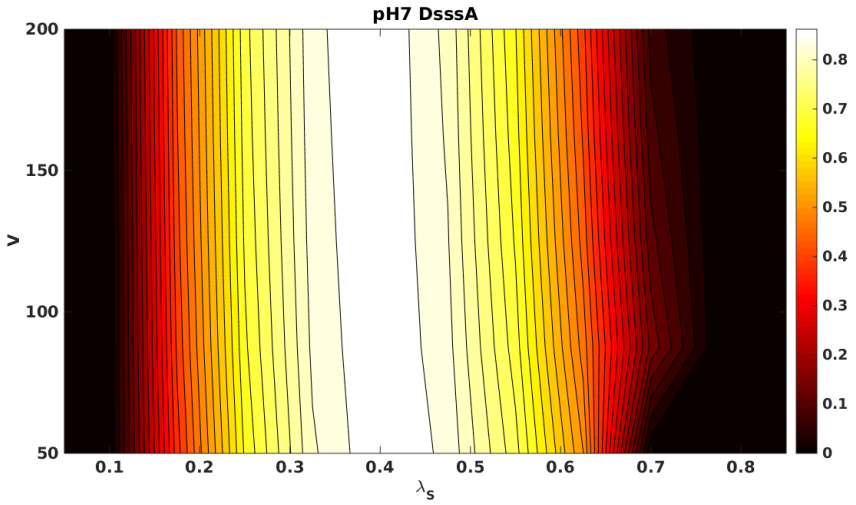

*Figure 7.6 - Contour plot of fitting parameters V and λ_s for DBA system **1** in pH=7 buffer. The magnitude of the contour plot gives the R^2 values that are obtained by fitting the semi-classical equation.*

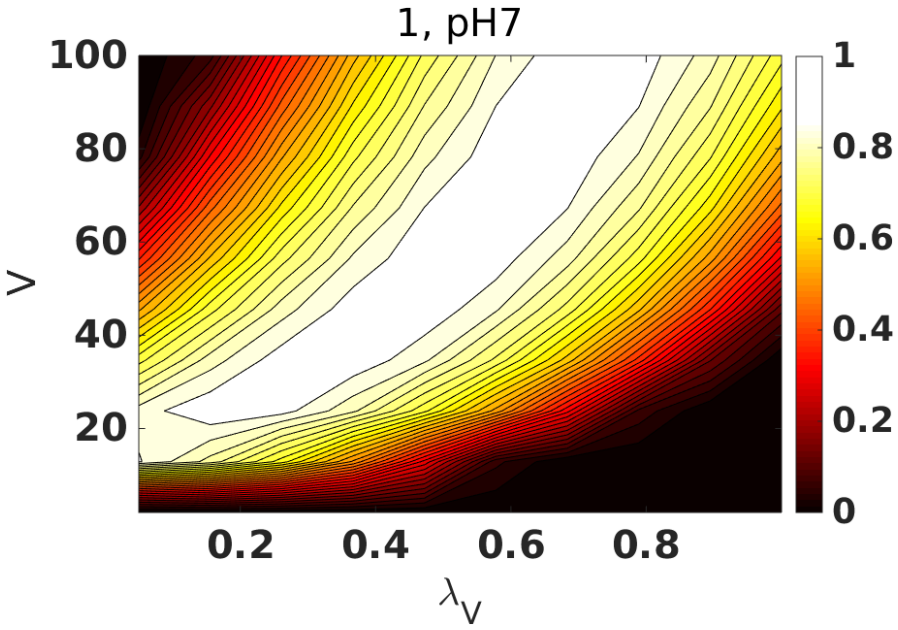

*Figure 7.7 - Contour plot of fitting parameters V and λ_v for DBA system **1** in pH=7 buffer. The magnitude of the contour plot gives the R^2 values that are obtained by fitting the semi-classical equation.*

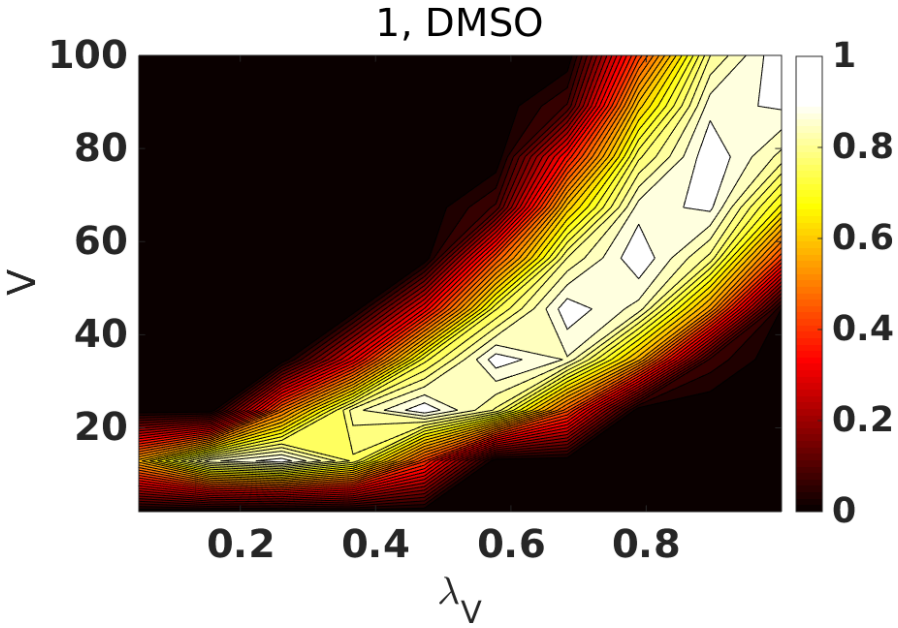

*Figure 7.8 - Contour plot of fitting parameters V and λ_v for DBA system **1** in DMSO. The magnitude of the contour plot gives the R^2 values that are obtained by fitting the semi-classical equation.*

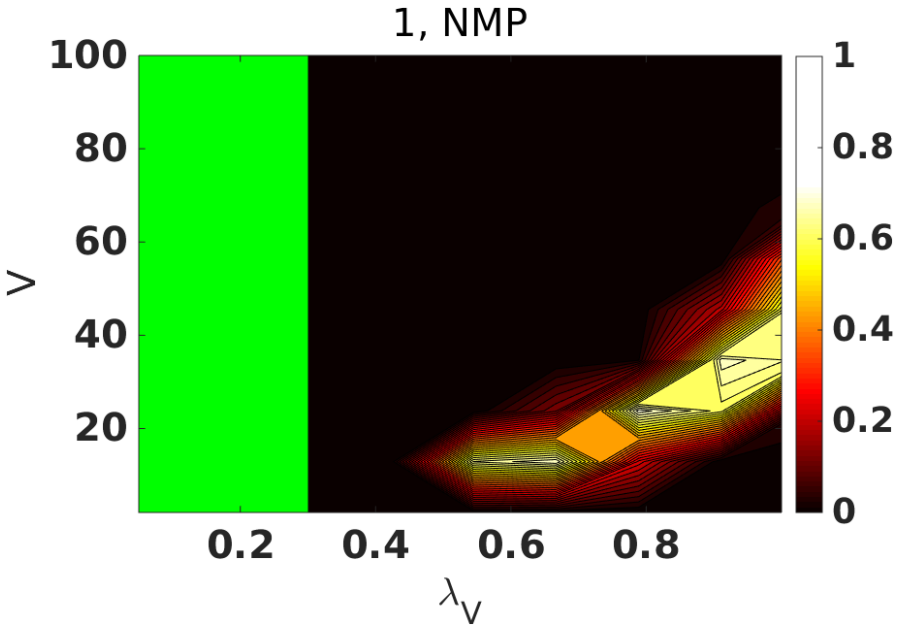

*Figure 7.9 - Contour plot of fitting parameters V and λ_v for DBA system **1** in NMP. The magnitude of the contour plot gives the R^2 values that are obtained by fitting the semi-classical equation. No data was collected in area shaded in green.*

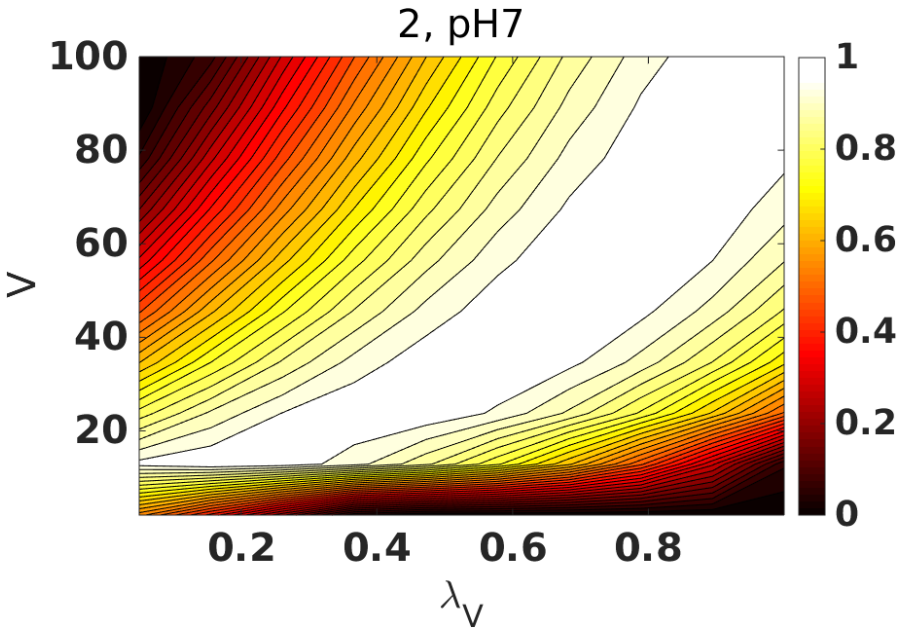

*Figure 7.10 - Contour plot of fitting parameters V and λ_v for DBA system **2** in pH=7 buffer. The magnitude of the contour plot gives the R^2 values that are obtained by fitting the semi-classical equation.*

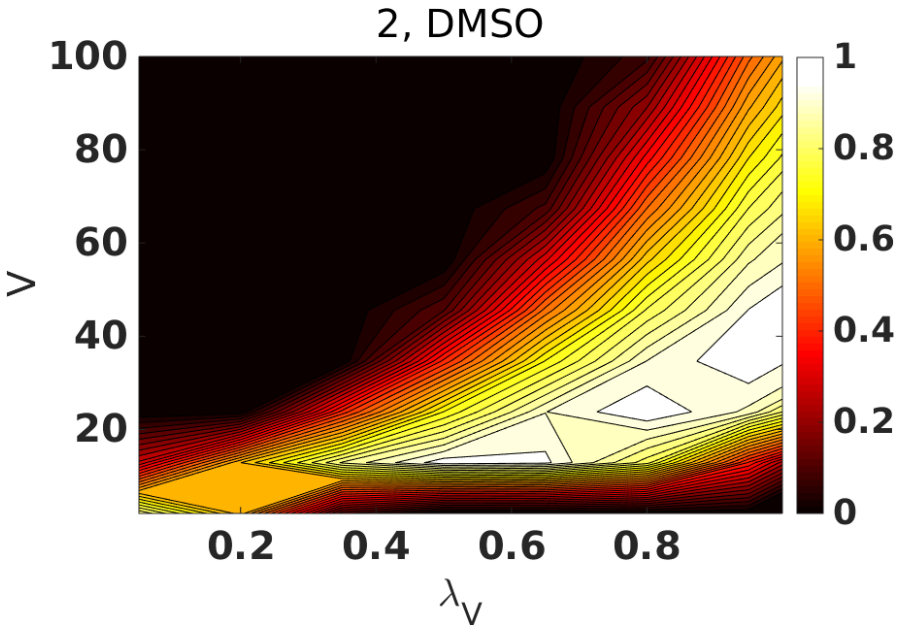

*Figure 7.11 - Contour plot of fitting parameters V and λ_v for DBA system **2** in DMSO. The magnitude of the contour plot gives the R^2 values that are obtained by fitting the semi-classical equation.*

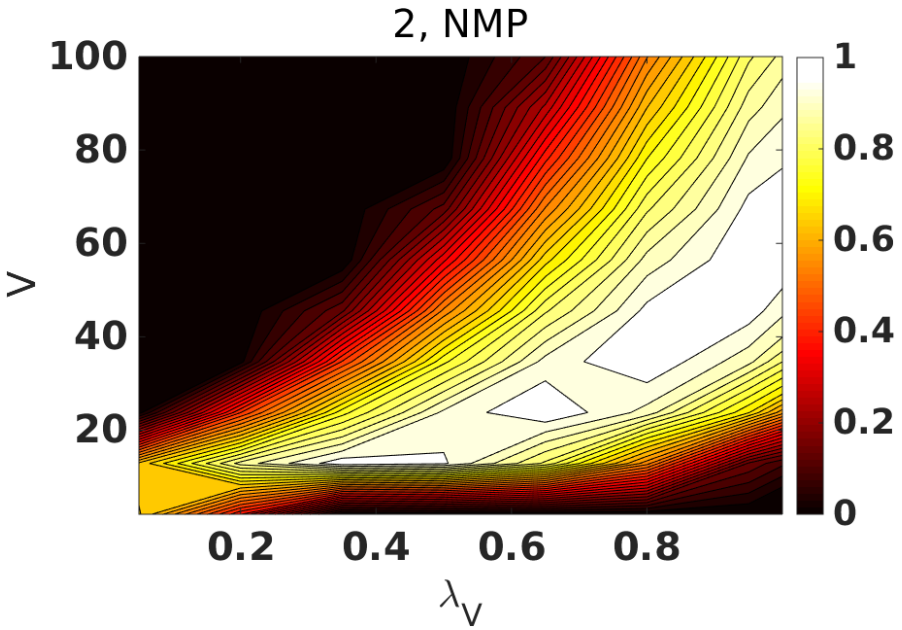

*Figure 7.12 - Contour plot of fitting parameters V and λ_v for DBA system **2** in NMP. The magnitude of the contour plot gives the R^2 values that are obtained by fitting the semi-classical equation.*

7.7.2 Control studies on bridge acceptor interactions

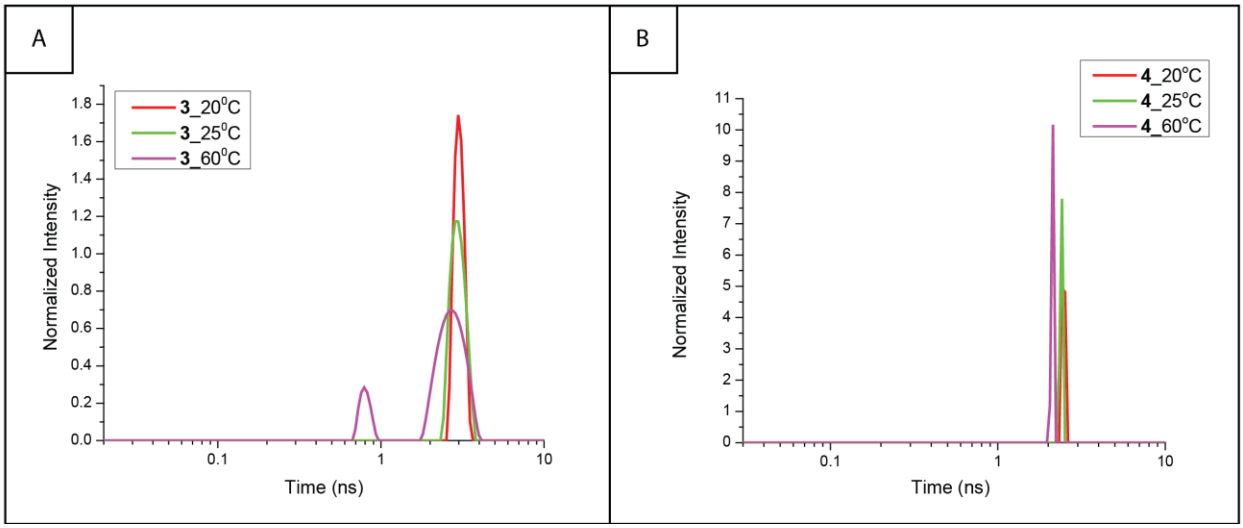

*Figure 7.13 - Distribution fits for **3** (A) and **4** (B) in DMSO at various temperatures. The broadening and the growth of the second peak for compound **3,** but not **4,** is indicative of the fact that these features exist because of the presence of the bridge; since **3** has a bridge with lysines but compound **4** does not.*

7.7.3 UPS studies of pyrene and amide substituted pyrene

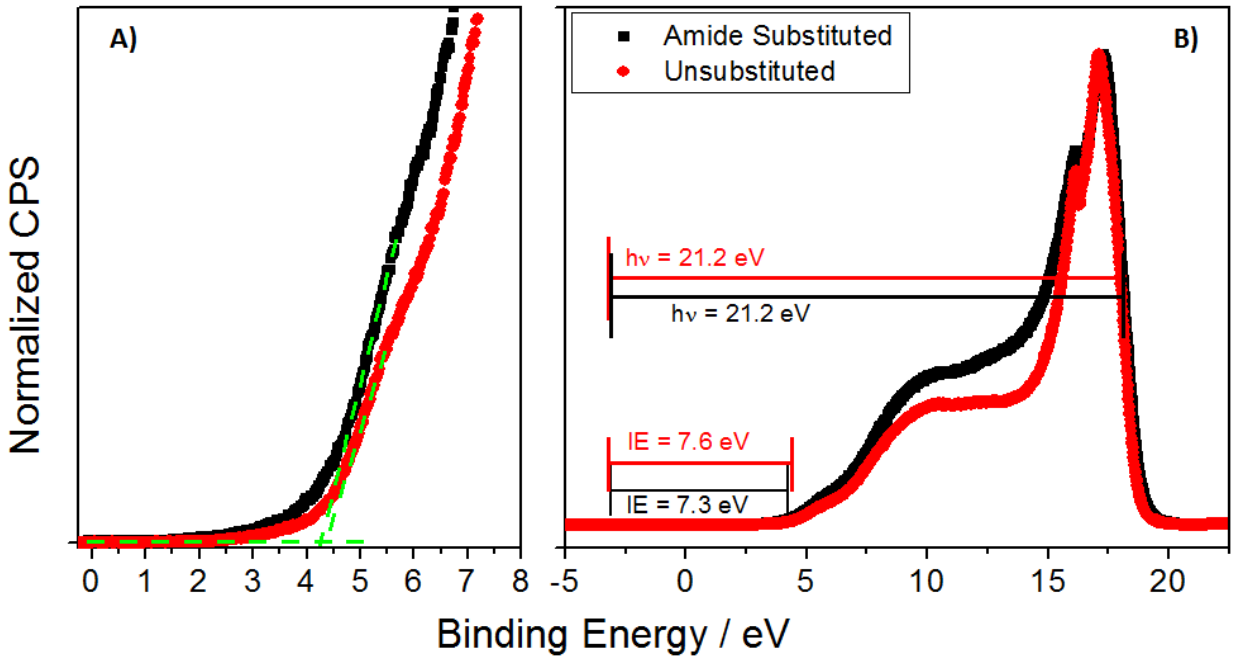

Figure 7.14 - This figure shows photoelectron spectra of amide substituted (black) and unsubstituted pyrene molecules (red). Panel A) shows the onset region of the spectra, and panel B) shows the full spectra with the calculated ionization energies (IE).

Samples were prepared by drop casting 20.0 µL of a 20.0µM ethanol solution of unsubstituted pyrene, and a 10.0 µM ethanol solution of amide substituted pyrene onto different regions of a plasma cleaned Au substrate. The different regions were separated by Kapton tape (E. I. du Pont de Nemours and Company) to prevent cross contamination. UPS measurements were then performed using an ESCALAB 250XI XPS at a base pressure of ~10^{-10} millibar. Electrical contact to the stage was made using copper tape and a -5.0 eV bias was applied. A pass energy of 1.0 eV and a dwell time of >50 s were used to increase resolution and eliminate charging respectively. A He (I) discharge lamp, 21.2 eV, was used as the ultraviolet source. The ionization energy (IE) was calculated using the following equation;

$$IE = h\nu - (\text{SECO} - \text{valence band onset}) \qquad \text{Equation 7.3}$$

where “SECO” is the secondary electron cutoff and “valence band onset” is the onset energy of the photoelectrons coming from the pyrene molecules referenced to the Fermi edge of the substrate.

7.7.4 Quantum Chemistry calculations of the cleft molecules with solvent

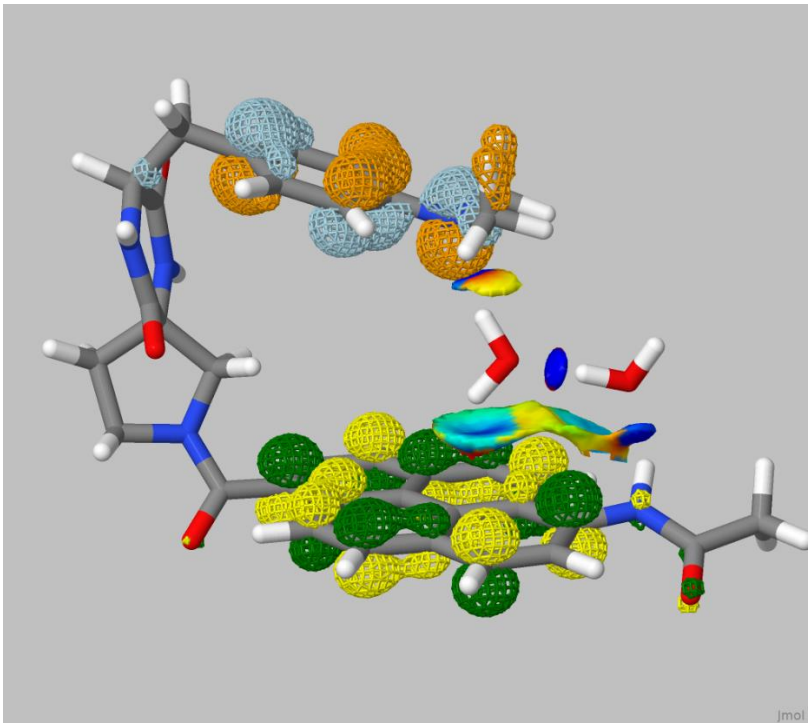

*Figure 7.15 - Frontier HOMO (grey/orange) and LUMO(yellow/green) molecular orbitals are shown for the DBA molecule **1** with two water molecules. The lysine moieties have been removed to facilitate observation of the DBA cleft region. The interaction surface of the solvent molecules is shown, as well.*

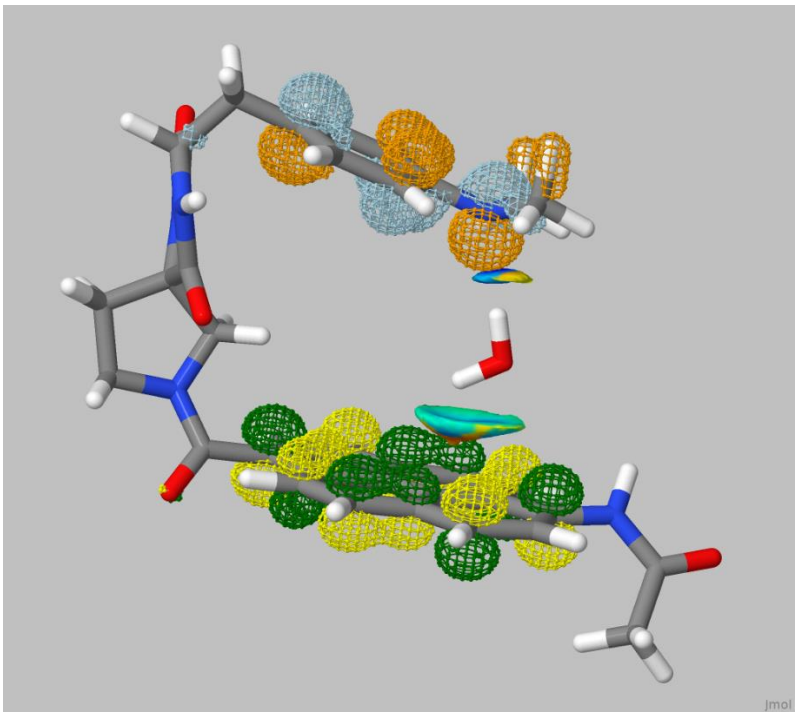

*Figure 7.16 - Frontier HOMO (grey/orange) and LUMO(yellow/green) molecular orbitals are shown for the DBA molecule **1** with one water molecule. The lysine moieties have been removed to facilitate observation of the DBA cleft region. The interaction surface of the solvent molecules is shown, as well.*

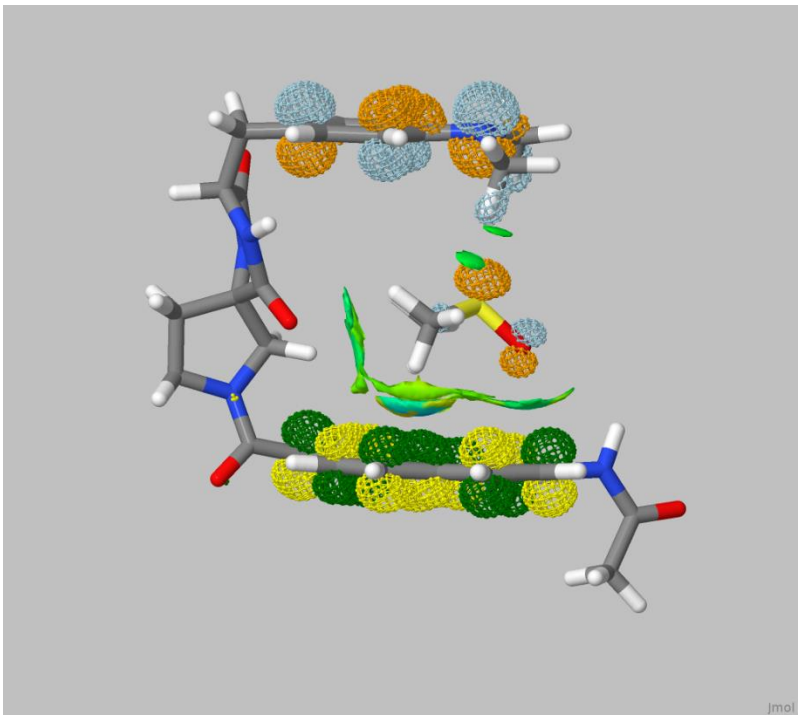

*Figure 7.17 - Frontier HOMO (grey/orange) and LUMO(yellow/green) molecular orbitals are shown for the DBA molecule **1** with one DMSO molecule. The lysine moieties have been removed to facilitate observation of the DBA cleft region. The interaction surface of the solvent molecules is shown, as well.*

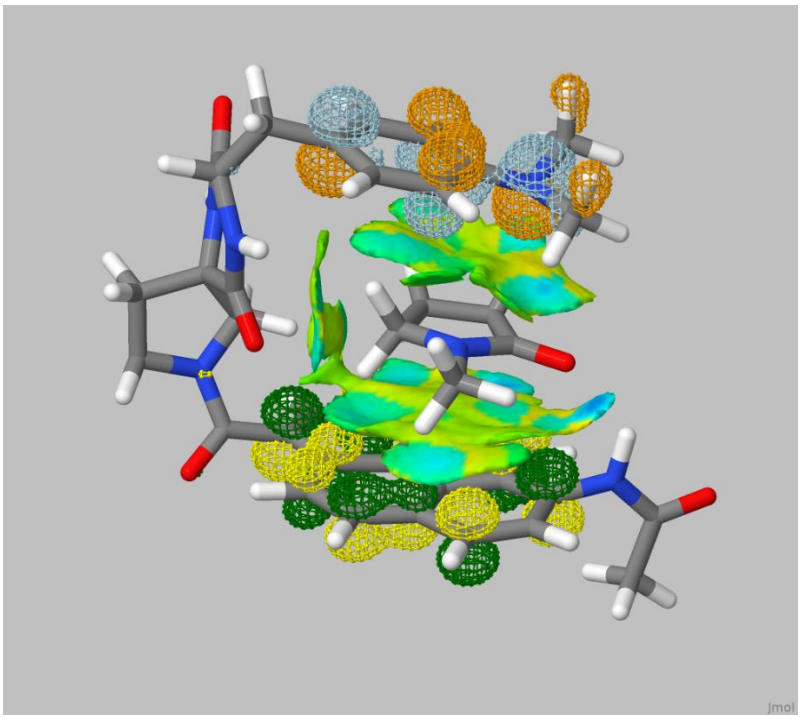

*Figure 7.18 - Frontier HOMO (grey/orange) and LUMO(yellow/green) molecular orbitals are shown for the DBA molecule **1** with one NMP molecule. The lysine moieties have been removed to facilitate observation of the DBA cleft region. The interaction surface of the solvent molecules is shown, as well*

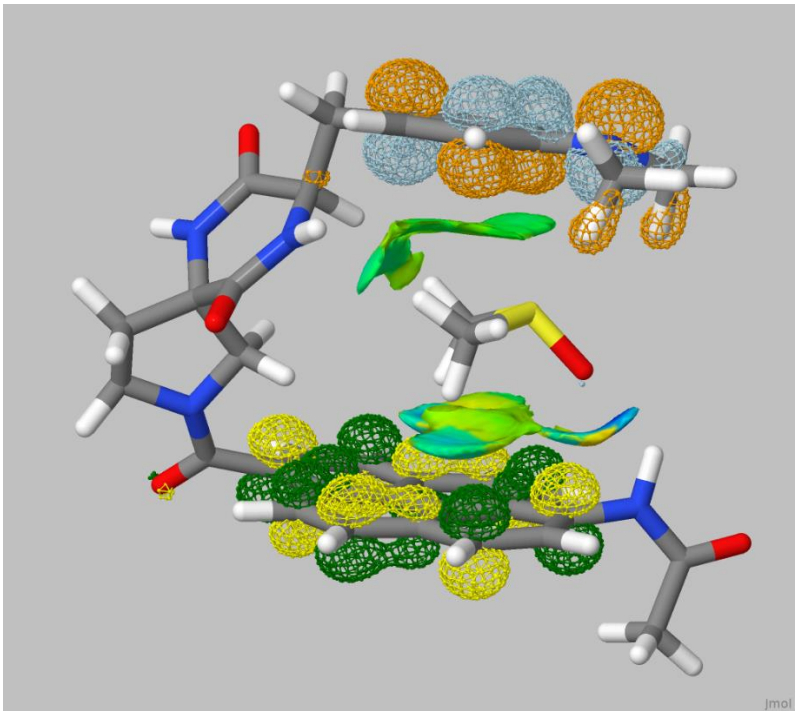

*Figure 7.19 - Frontier HOMO (grey/orange) and LUMO(yellow/green) molecular orbitals are shown for the DBA molecule **2** with one DMSO molecule. The lysine moieties have been removed to facilitate observation of the DBA cleft region. The interaction surface of the solvent molecules is shown, as well.*

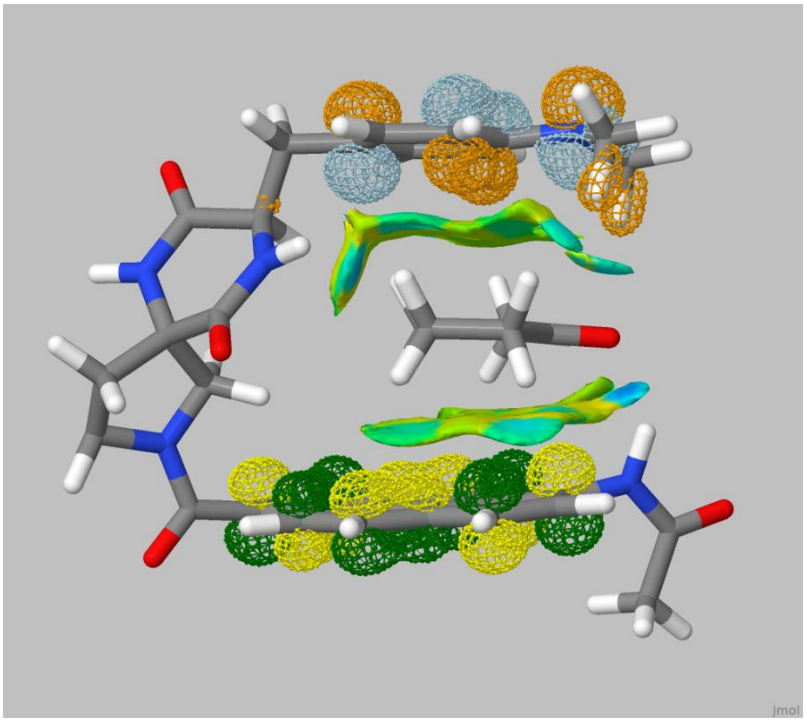

*Figure 7.20 - Frontier HOMO (grey/orange) and LUMO(yellow/green) molecular orbitals are shown for the DBA molecule **2** with one NMP molecule. The lysine moieties have been removed to facilitate observation of the DBA cleft region. The interaction surface of the solvent molecules is shown, as well.*

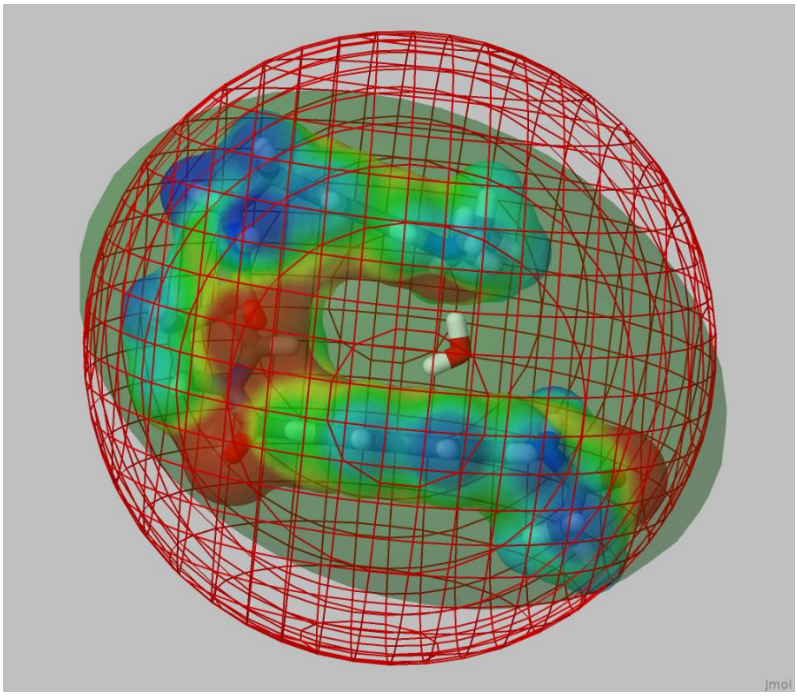

*Figure 7.21 - This figure shows van der Waals surface of **1,** the corresponding circumscribed sphere (red mesh) and prolate spheroid (green) with one water molecule in the cleft.*

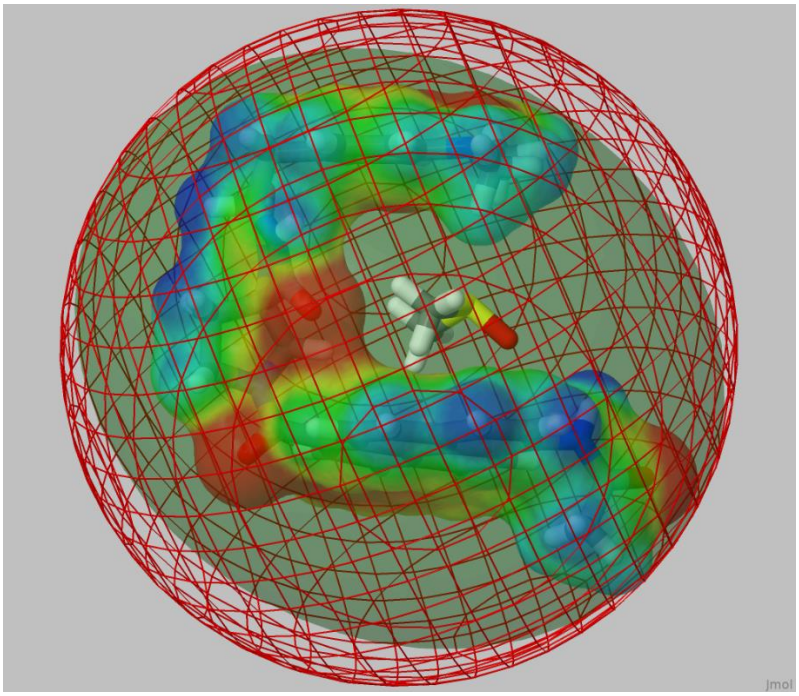

*Figure 7.22 - This figure shows van der Waals surface of **1,** the corresponding circumscribed sphere (red mesh) and prolate spheroid (green) with one DMSO molecule in the cleft.*

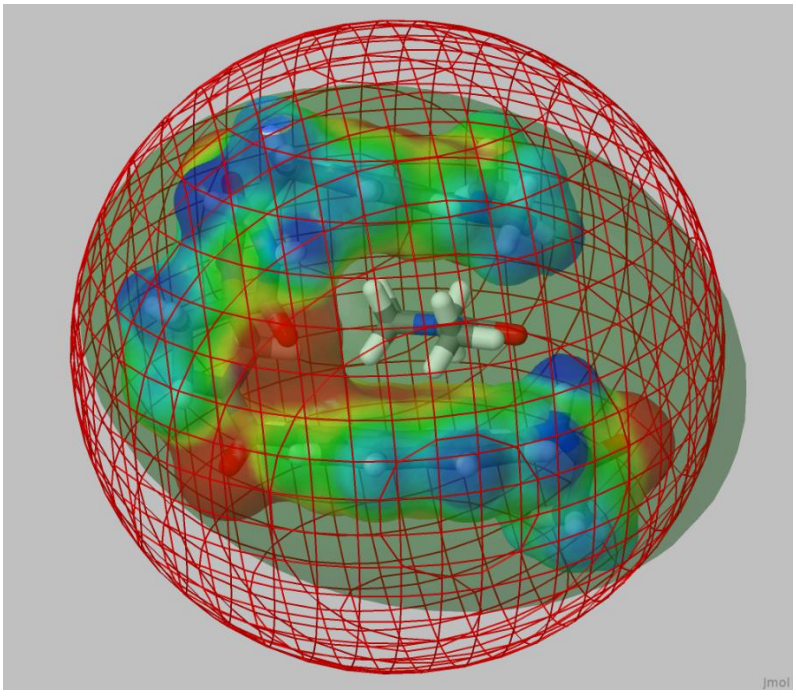

*Figure 7.23 - This figure shows van der Waals surface of **1,** the corresponding circumscribed sphere (red mesh) and prolate spheroid (green) with one NMP molecule in the cleft.*

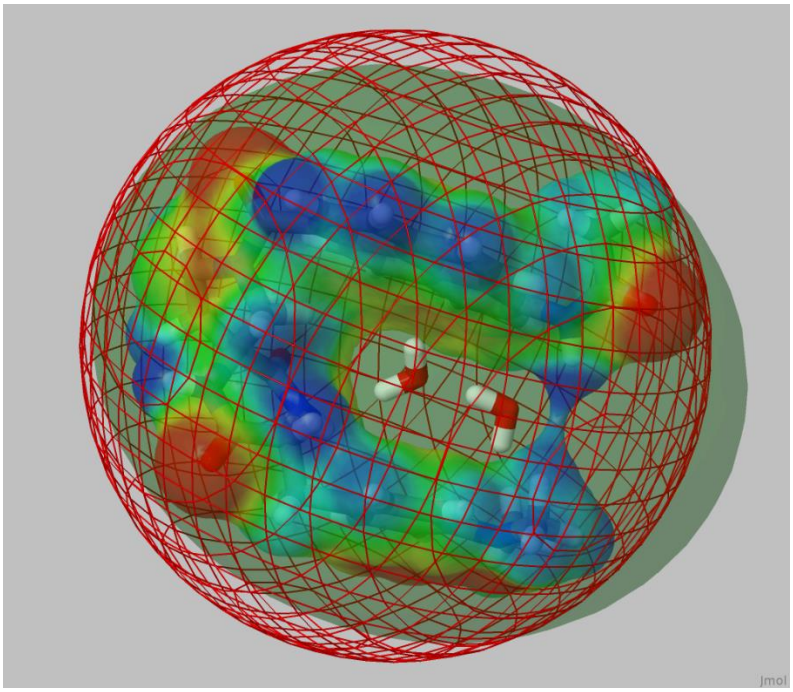

*Figure 7.24 - This figure shows van der Waals surface of **2,** the corresponding circumscribed sphere (red mesh) and prolate spheroid (green) with two water molecules in the cleft.*

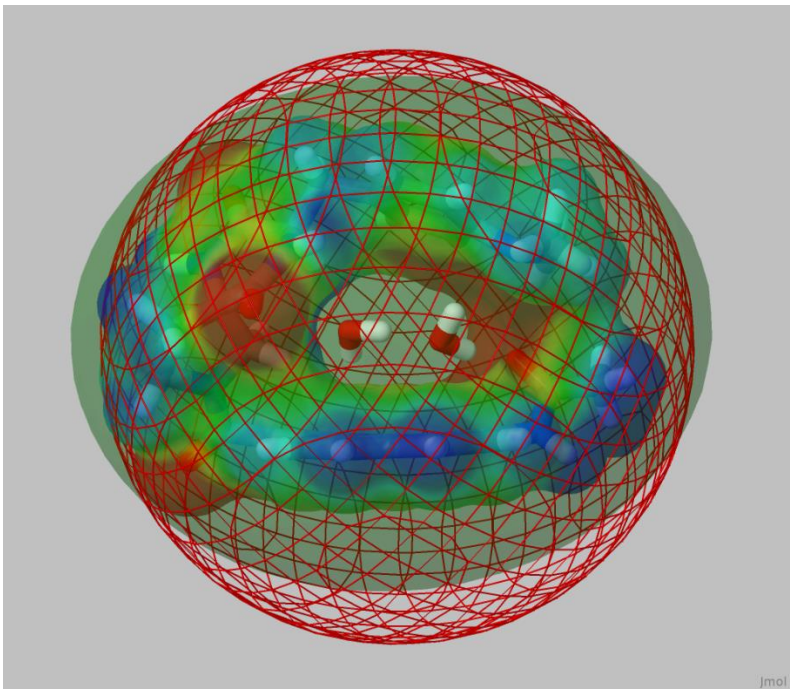

*Figure 7.25 - This figure shows van der Waals surface of **2,** the corresponding circumscribed sphere (red mesh) and prolate spheroid (green) with two water molecules in the cleft. This is the lowest energy configuration of this DBA molecule, but the orientation of the cleft is significantly different from the other DBA systems. So, Figure 7.24 (above) is also present for a more direct comparison.*

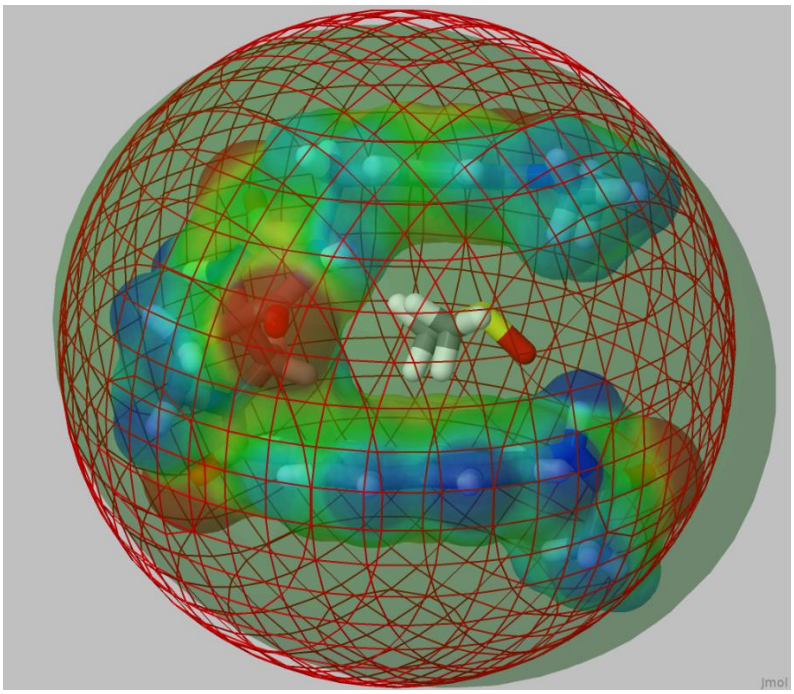

*Figure 7.26 - This figure shows van der Waals surface of **2,** the corresponding circumscribed sphere (red mesh) and prolate spheroid (green) with one DMSO molecule in the cleft.*

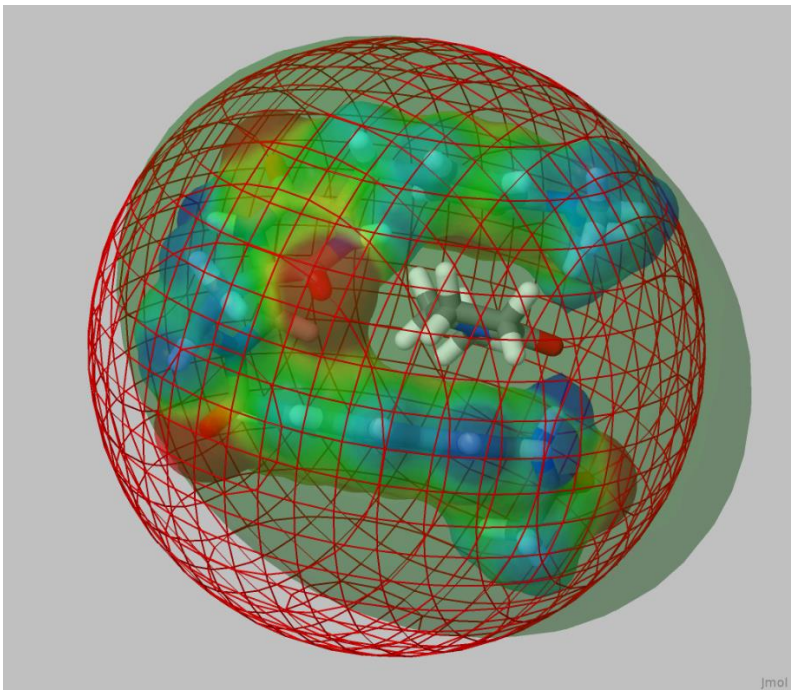

*Figure 7.27 - This figure shows van der Waals surface of **2,** the corresponding circumscribed sphere (red mesh) and prolate spheroid (green) with one NMP molecule in the cleft.*

7.8 EXAMPLES OF THE FLUORESCENCE DATA AND THE FITS ARE SHOWN FOR THE DIFFERENT MOLECULES IN THE DIFFERENT SOLVENTS

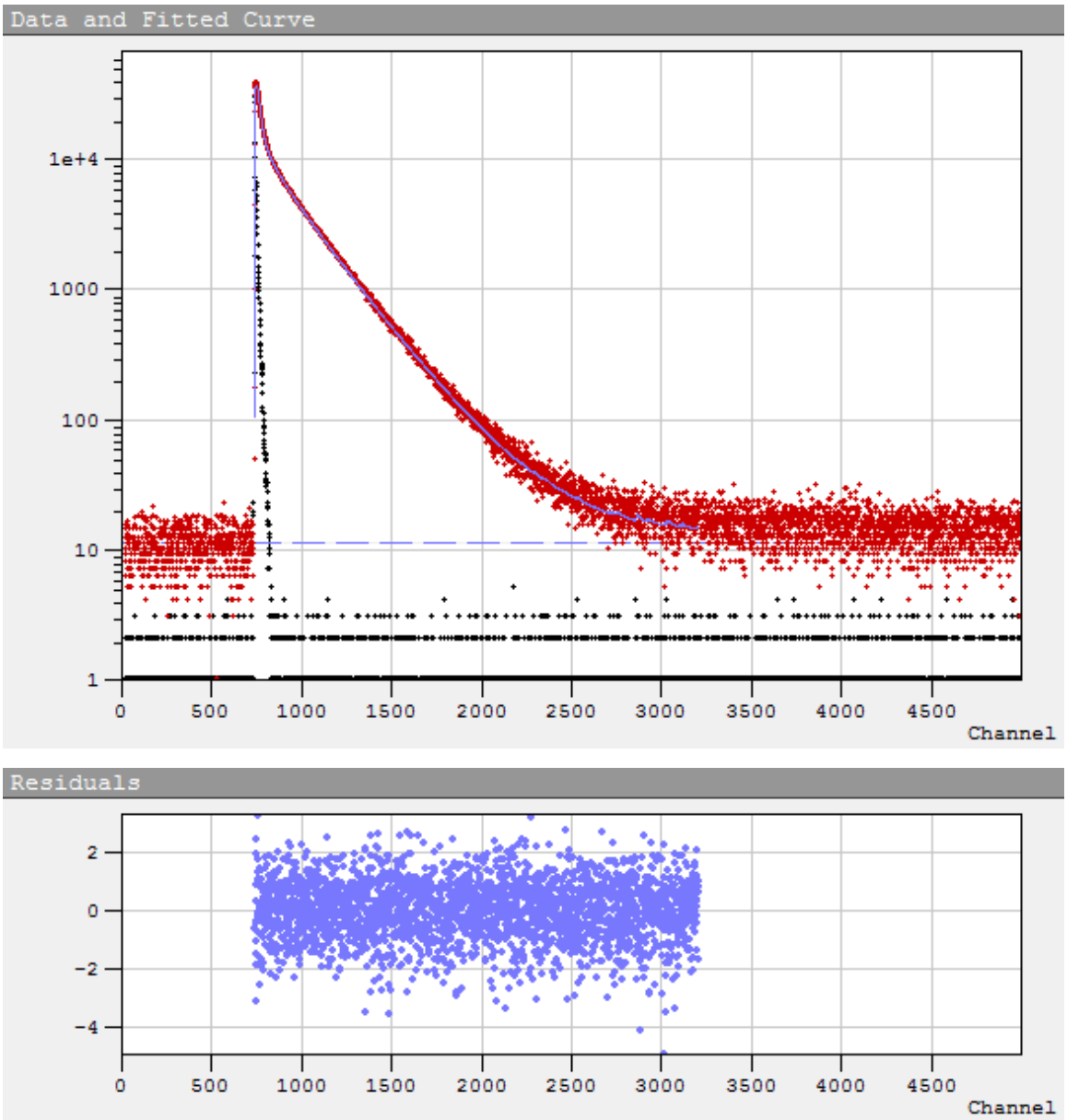

*Figure 7.28 - The figure shows a sample instrument response function (black), photoluminescence decay (red), and best fit line (blue) for **1** in pH 7 buffer at 25°C. The corresponding residuals for **1** in pH 7 buffer at 25°C is also shown.*

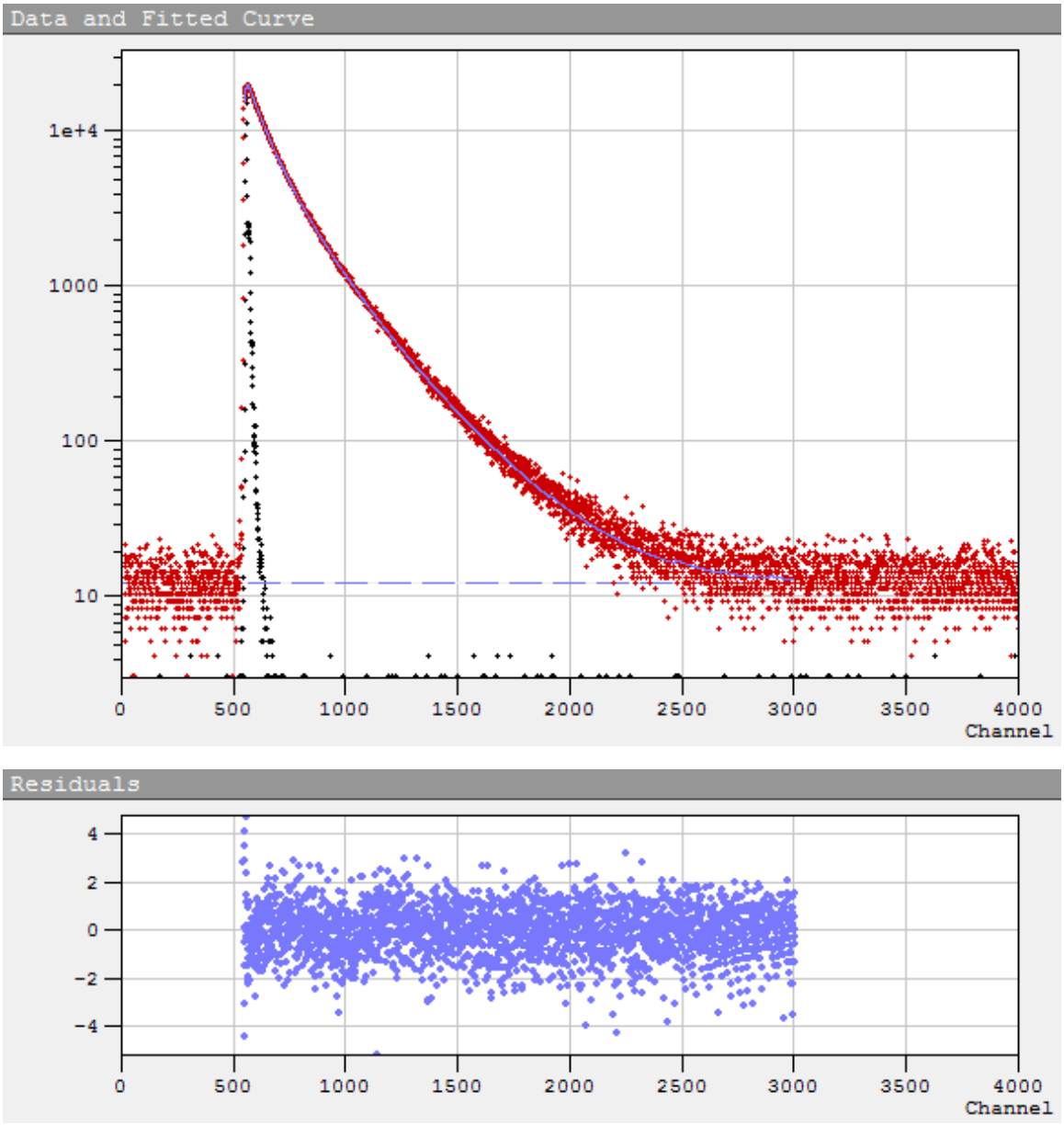

*Figure 7.29 - The figure shows a sample instrument response function (black), photoluminescence decay (red), and best fit line (blue) for **2** in pH 7 buffer at 25°C. The corresponding residuals for **2** in pH 7 buffer at 25°C is also shown.*

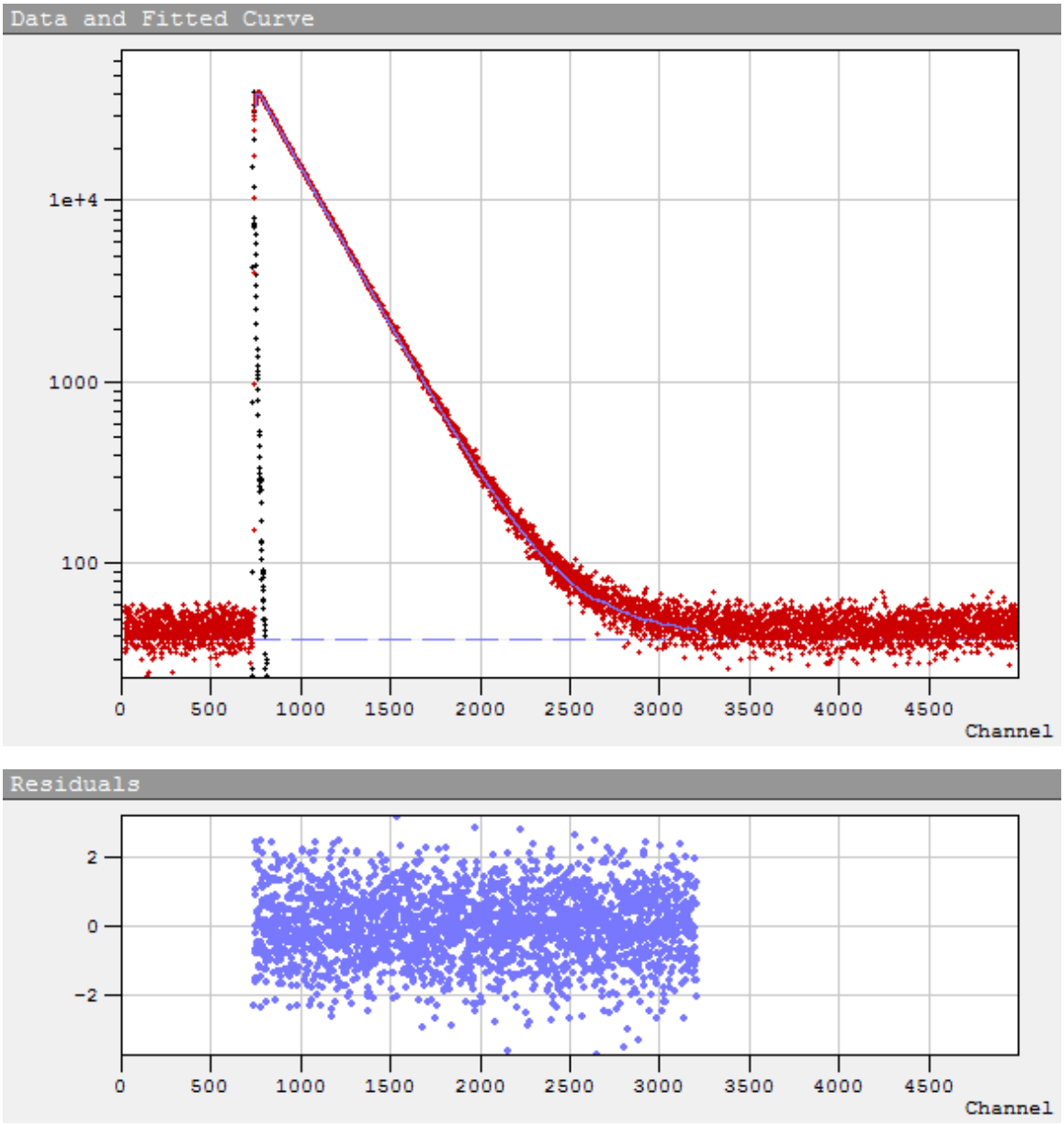

*Figure 7.30 - The figure shows a sample instrument response function (black), photoluminescence decay (red), and best fit line (blue) for **3** in pH 7 buffer at 25°C. The corresponding residuals for **3** in pH 7 buffer at 25°C is also shown.*

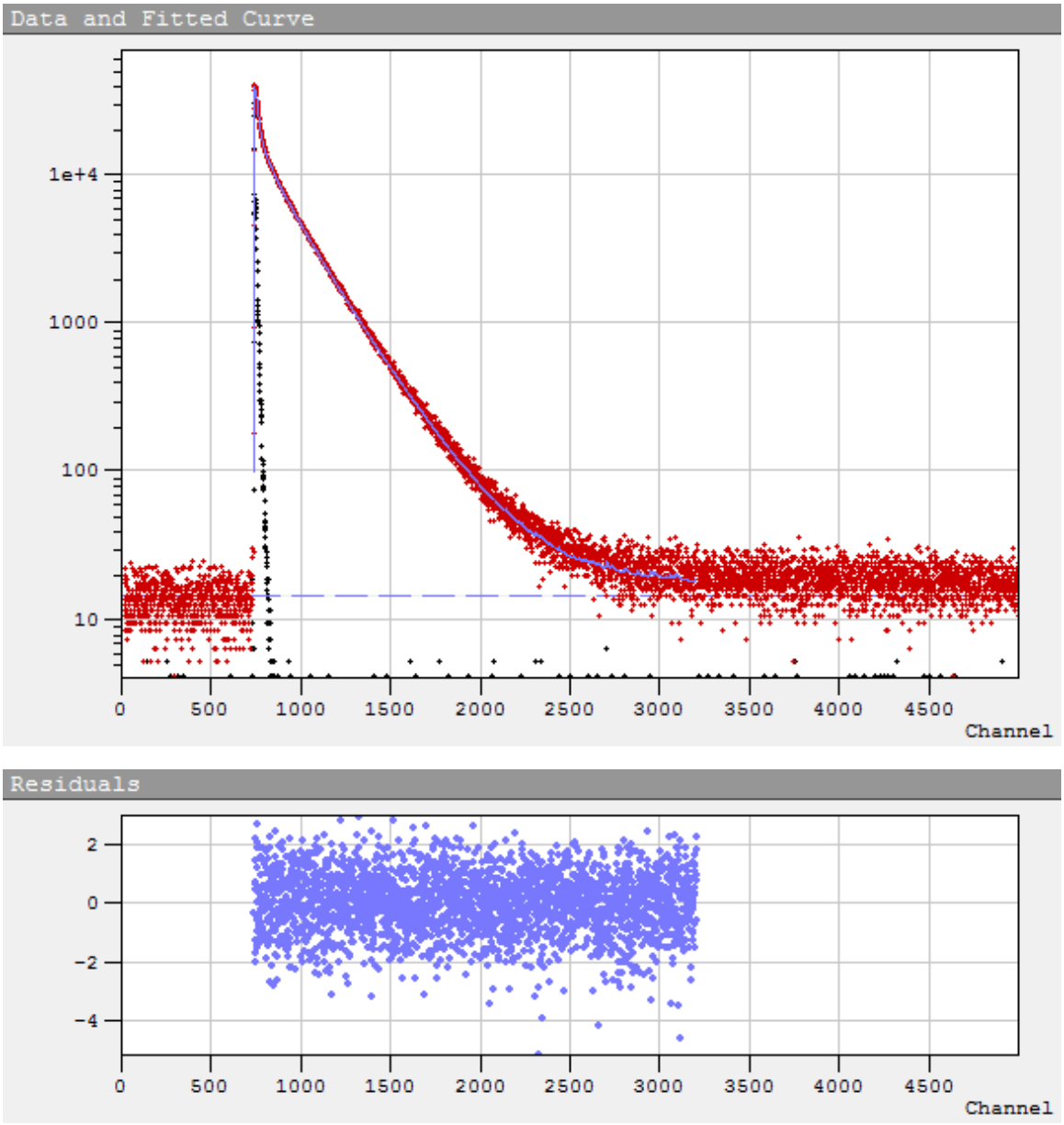

*Figure 7.31 - The figure shows a sample instrument response function (black), photoluminescence decay (red), and best fit line (blue) for **1** in pH 7 buffer at 60°C. The corresponding residuals for **1** in pH 7 buffer at 60°C is also shown.*

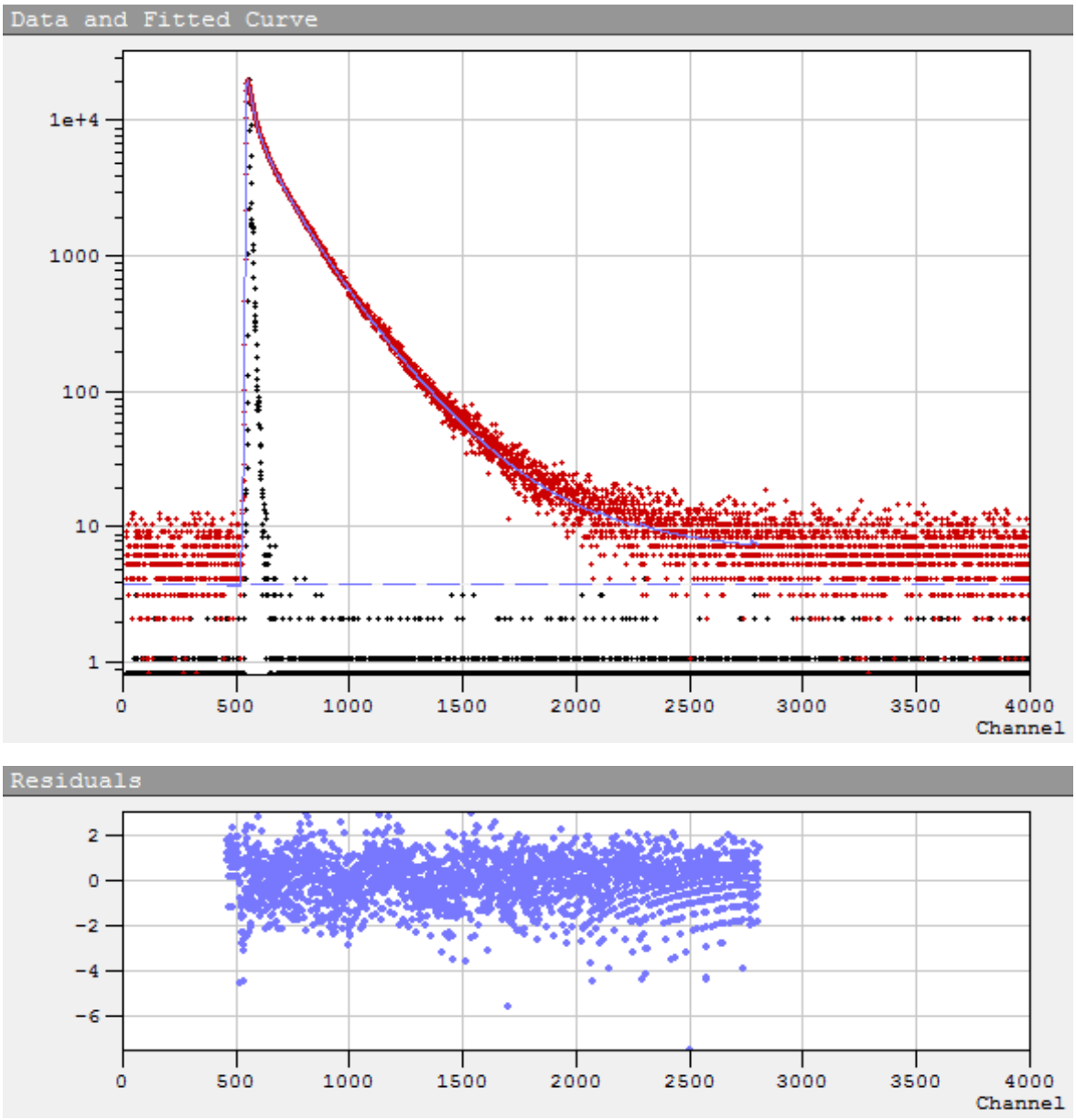

*Figure 7.32 - The figure shows a sample instrument response function (black), photoluminescence decay (red), and best fit line (blue) for **1** in DMSO at 25°C. The corresponding residuals for **1** in DMSO at 25°C is also shown.*

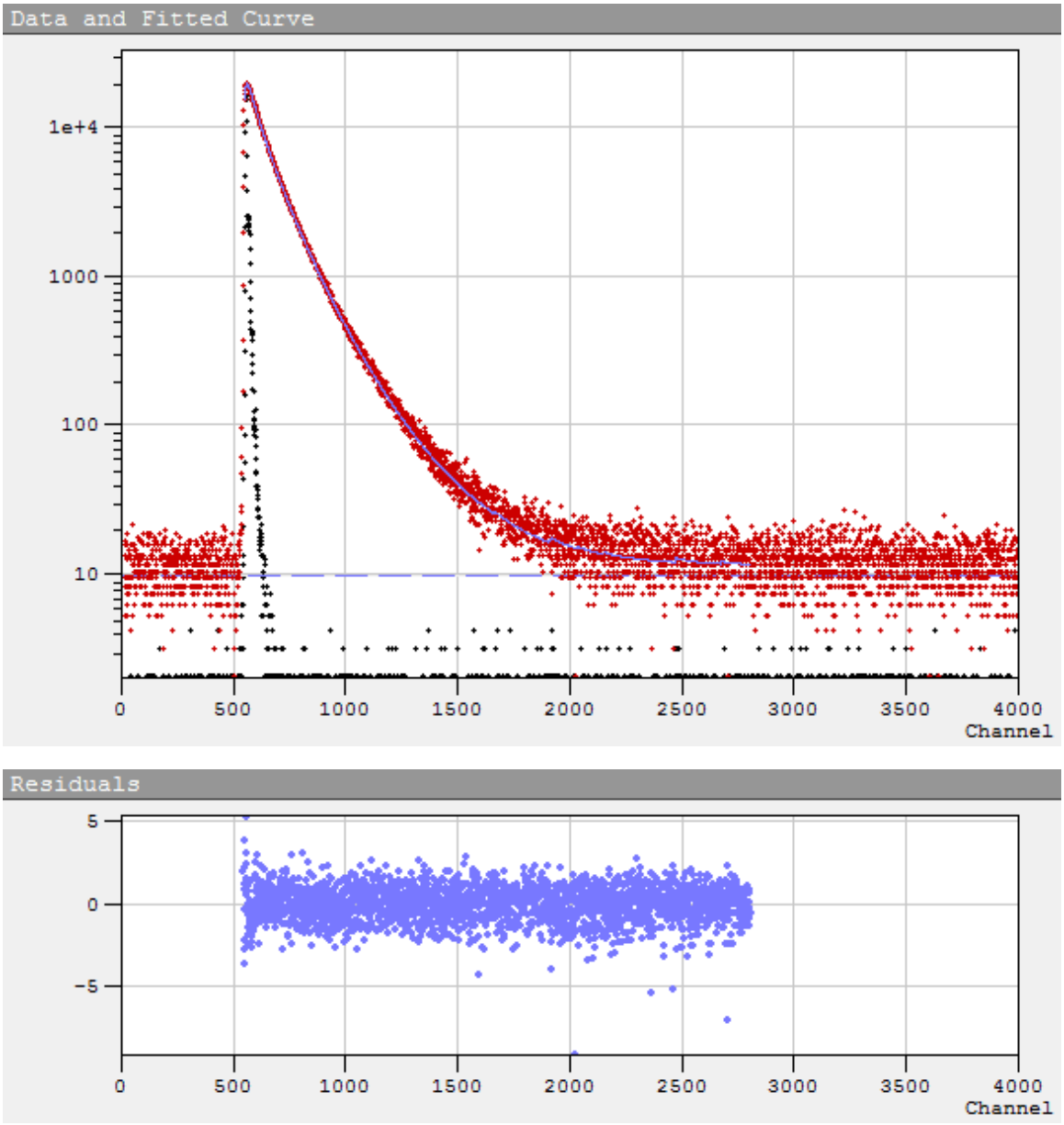

*Figure 7.33 - The figure shows a sample instrument response function (black), photoluminescence decay (red), and best fit line (blue) for **2** in DMSO at 25°C. The corresponding residuals for **2** in DMSO at 25°C is also shown.*

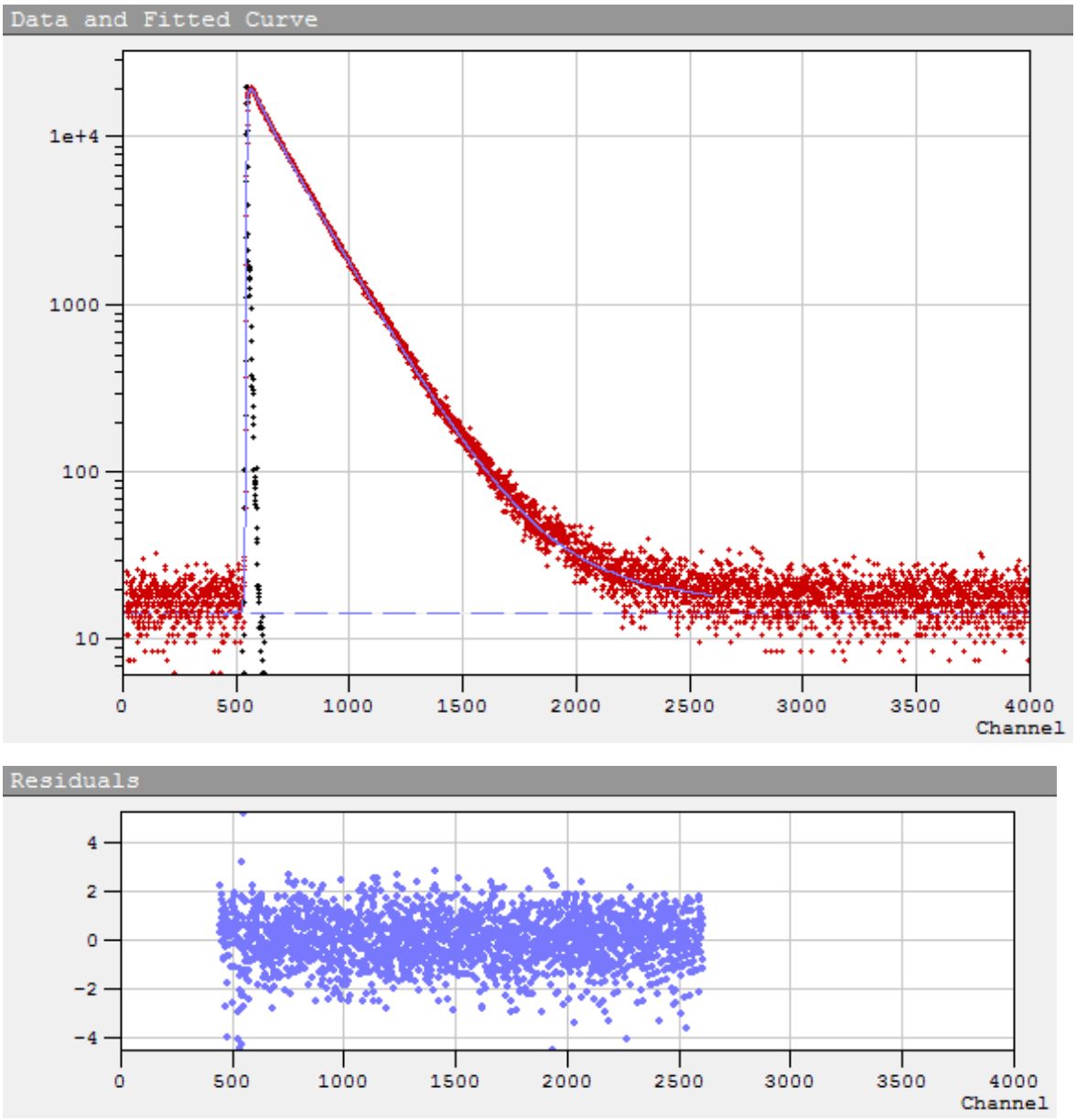

*Figure 7.34 - The figure shows a sample instrument response function (black), photoluminescence decay (red), and best fit line (blue) for **3** in DMSO at 25°C. The corresponding residuals for **3** in DMSO at 25°C is also shown.*

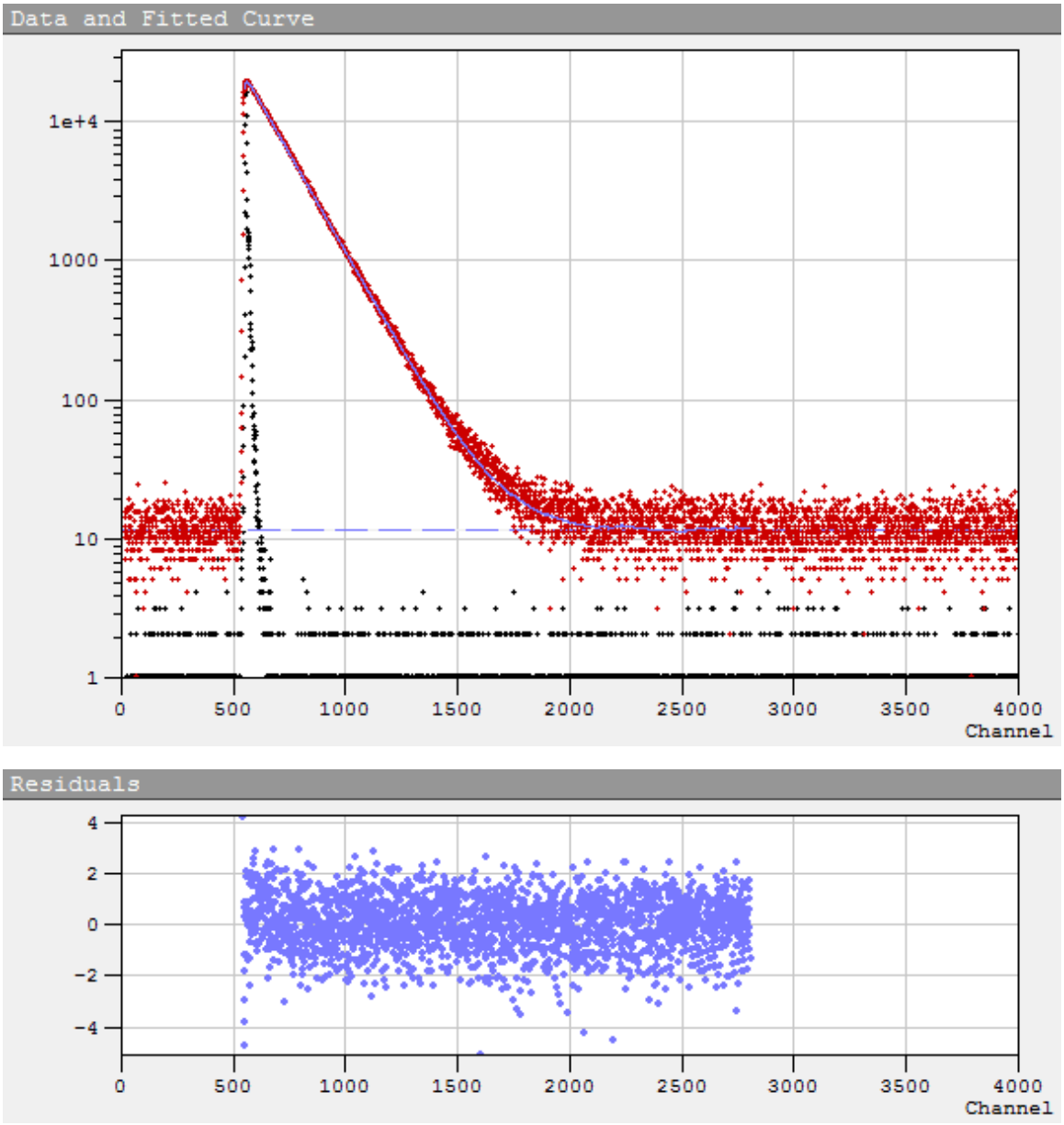

*Figure 7.35 - The figure shows a sample instrument response function (black), photoluminescence decay (red), and best fit line (blue) for **4** in DMSO at 25°C. The corresponding residuals for **4** in DMSO at 25°C is also shown.*

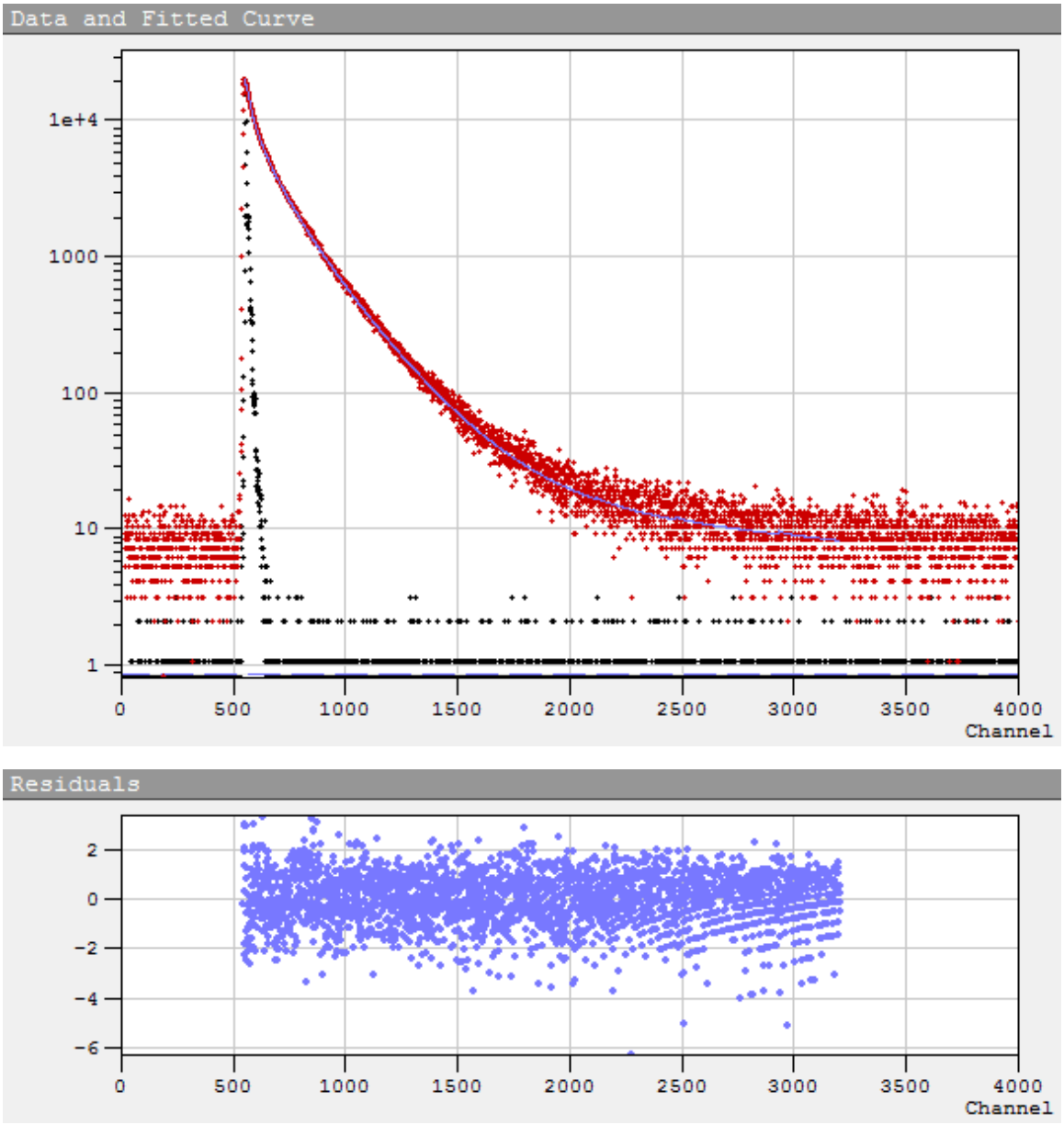

*Figure 7.36 - The figure shows a sample instrument response function (black), photoluminescence decay (red), and best fit line (blue) for **1** in NMP at 25°C. The corresponding residuals for **1** in NMP at 25°C is also shown.*

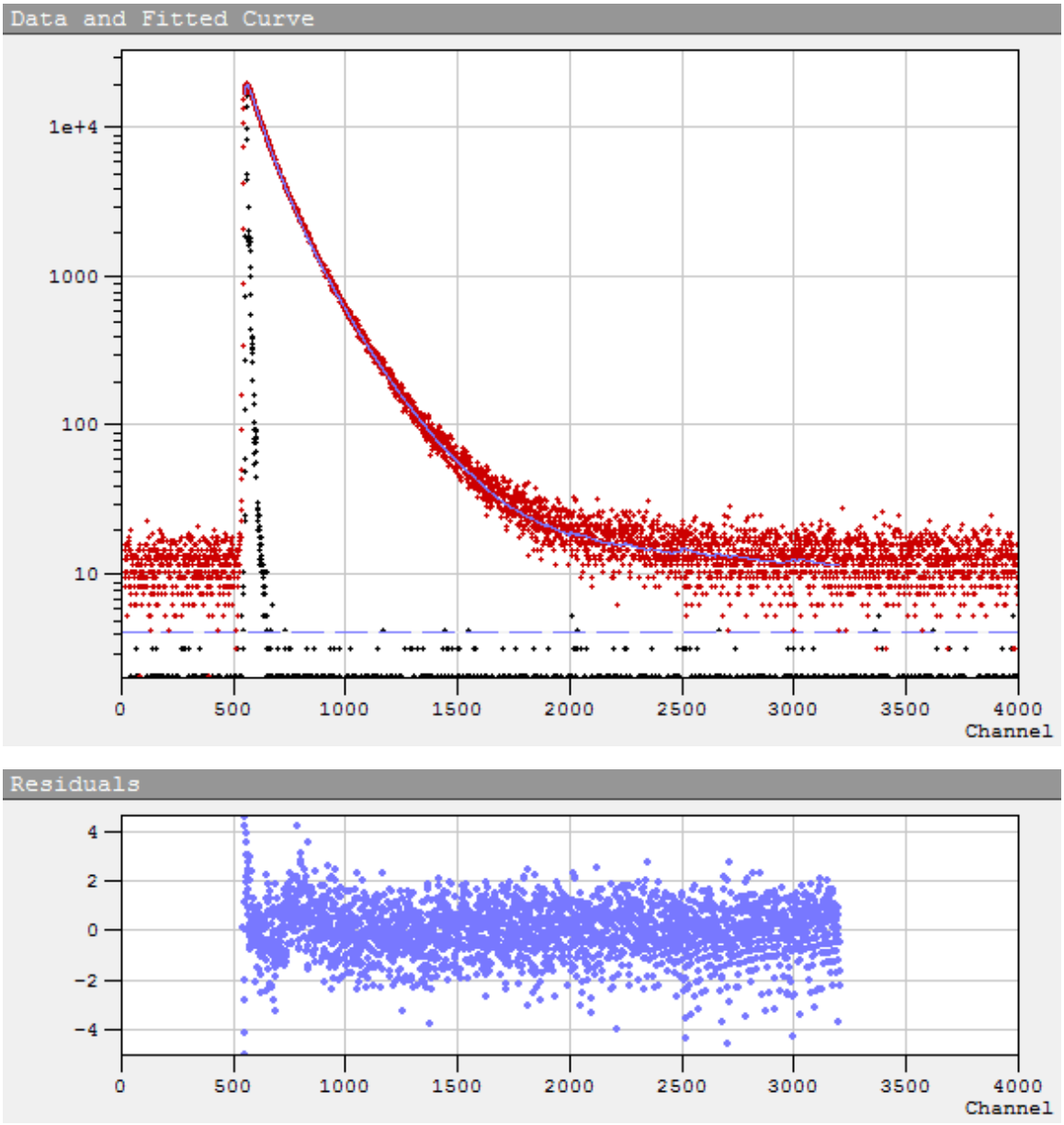

*Figure 7.37 - The figure shows a sample instrument response function (black), photoluminescence decay (red), and best fit line (blue) for **2** in NMP at 25°C. The corresponding residuals for **2** in NMP at 25°C is also shown.*

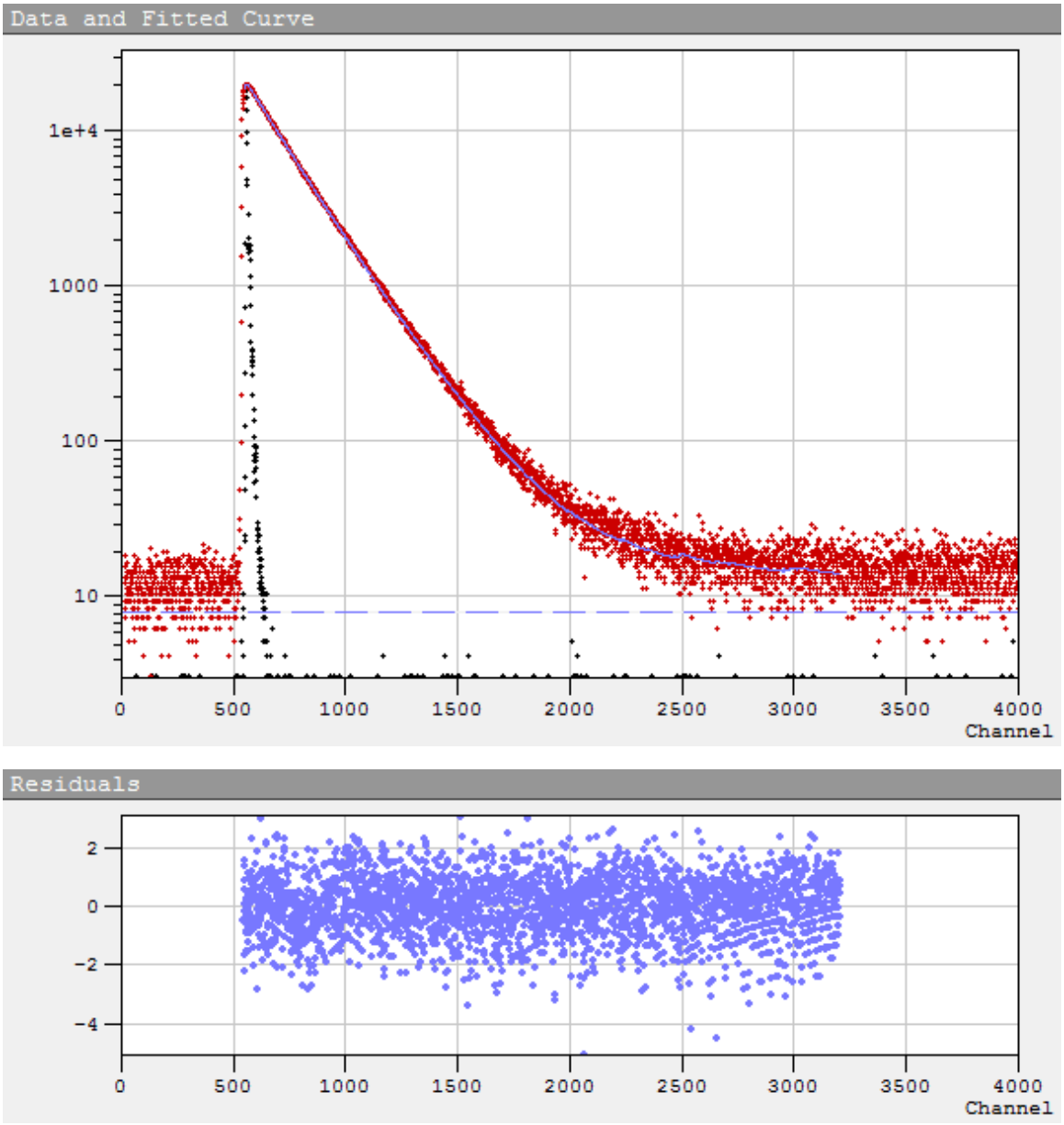

*Figure 7.38 - The figure shows a sample instrument response function (black), photoluminescence decay (red), and best fit line (blue) for **3** in NMP at 25°C. The corresponding residuals for **3** in NMP at 25°C is also shown.*

8.0 APPENDIX B

8.1 EXPLORATION INTO ORIGIN OF SECOND TIME CONSTANT PRESENT IN 3A

Questions as to the origin of time constant τ_1 in system **3A** arose. Thus, photoluminescence (PL) decay measurements were collected as a function of emission position (Table 8.1). The PL decays were fit to a sum of exponentials, minimizing the residuals and chi squared value (χ^2). A sum of exponentials was used to fit **3A** in an effort to have more control over the fitting parameters and to better understand their differences. These fits gave two distinct time constants (τ) associated with pyrene's fluorescence relaxation. The best fit time constants were determined for the emission position at 400 nm and the time constants were fixed in the fitting parameters at all other wavelengths studied. Note that the amplitude of the short and long time constants varied as the emission position was red-shifted. Generally, there was an increase in τ_1 as the emission position was moved from the blue, 400 nm, to the red, 550 nm (Table 8.1), indicating that it is more significant in the longer emission wavelengths studied.

*Table 8.1 - Best fit parameters to system **3A** in pH 7 buffer with a fixed τ1 and τ2*

Emission (nm)	α_1	τ_1 (ns)	α_2	τ_2 (ns)	$\langle\tau\rangle$ (ns)	X^2
400	0.12	2.44	0.88	5.69	5.30	1.34
425	0.12	2.44	0.88	5.69	5.30	1.25
450	0.13	2.44	0.87	5.69	5.26	1.13
525	0.20	2.44	0.80	5.69	5.04	1.29
550	0.17	2.44	0.83	5.69	5.14	2.68

8.2 COMPARISON OF 3A TO 4A

Table 8.2 shows that for three sample temperatures in DMSO, both **3A** and **4A** have two distinct time constants associated with their photoluminescence decay. This experimental evidence indicates that the source of the shorter lived lifetime component for **3A** is not a result of bridge acceptor interaction, but rather an inherent quality of the acceptor itself. Thus, to probe the origin of this de-excitation pathway, the simpler molecule, **4A**, was examined computationally. See Section 8.5 for more details on the computational study.

*Table 8.2 - Best fit parameters to either system **3A** or **4A** in DMSO at various temperatures*

Sample	Temperature (°C)	α_1	τ_1 (ns)	α_2	τ_2 (ns)	χ^2
3A	20	0.32	2.73	0.68	5.89	1.06
3A	25	0.31	2.70	0.69	5.87	1.12
3A	60	0.39	2.47	0.61	5.77	1.12
4A	20	0.24	2.36	0.76	5.70	1.09
4A	25	0.25	2.43	0.75	5.69	1.10
4A	60	0.34	2.55	0.66	5.28	1.04

8.3 DETAILS ON DETERMINATION OF k_{ET} IN THE CASE OF A SPECTATOR PATHWAY

Originally, the hypothesis was that all three substituent systems would behave similarly for the DBA molecules studied (ie. for a DBA system, one short time constant and one long time constant would exist). However, because the DBA systems with a substituent at position **A** had a total of three time constants they had to be treated differently. Various approaches were tried and the one presented in the main text gives the most sensible (self-consistent) description. An alternative approach which is consistent, but gives unusual behavior is to average the two longer time constants together. With this averaging, all three substituent systems can then be treated similarly (Figure 8.1).

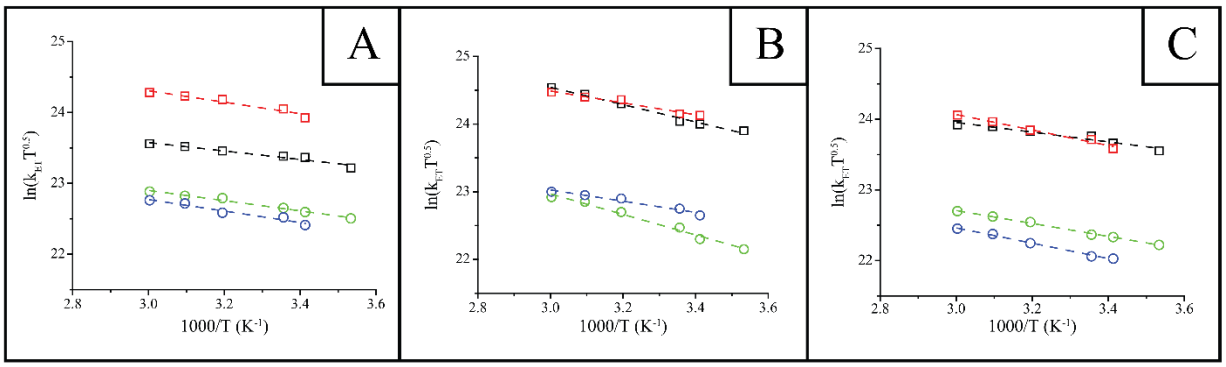

*Figure 8.1 - The temperature dependence of the electron transfer rate constant is reported for **1A**, (squares) and **2A**, (circles) in panel A, **1B** (squares) and **2B** (circles) are shown in panel B, and **1C** (squares) and **2C** (circles) are shown in panel C for pH 7 buffer corresponding to black and green and DMSO corresponds to red and blue*

Figure 8.1 shows the results of this analysis. For molecules **1B**, **1C**, **2B**, and **2C** the analysis is like that in the main text. The results for molecules **1A** and **2A** are shown in panel A of Figure 8.1. Here we found that the results for molecule **2A** were similar to **2B** and **2C**, but those for **1A** strongly differ. However, the assumption of averaging was deemed poor because the physical parameters generated for **A** were less reasonable. In particular, this analysis leads to a Gibbs' free energy, $\Delta_r G$, that is positive (ie. not favorable) and electronic coupling values that are small. This is unlikely, especially because the magnitude of electron transfer rates for all three substituent patterns were similar. Ultimately, through trial and error, it was determined that the best approach for calculating the electron transfer rate for DBA molecules with a substituent at position **A** would be to exclude one of the longer time constants, which resulted in physical parameters that were in alignment with expectations.

8.4 DISTRIBUTION FITTING AND DETERMINATION OF ERROR IN ELECTRON TRANSFER RATE

When the photoluminescence decays were fit to a distribution of lifetime components, the width of the distribution fit was used to estimate the error in the time constants. For Figure 8.2, the mean time constant is shown by the symbol and the full width at half maximum of the distribution by the error bars. When it was determined that a spectator decay constant was present and a sum of exponentials, rather than a distribution of lifetime components, was used to fit all decays. Thus, the determination of error by using the width of the distribution fit was no longer sensible.

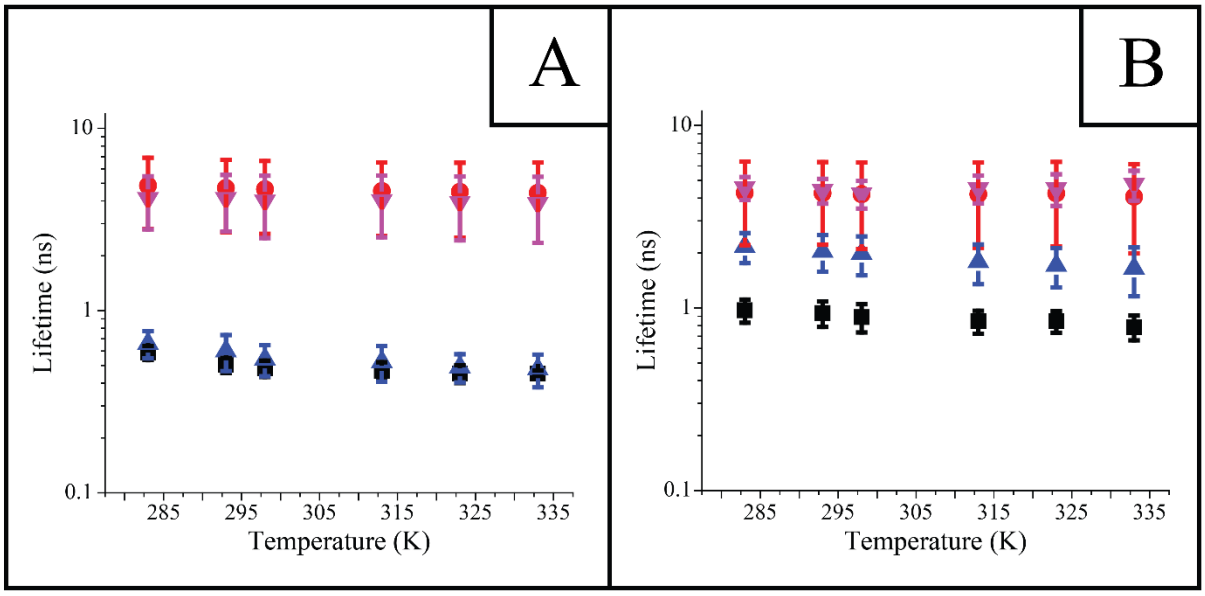

*Figure 8.2 - Time constants plotted against temperature in pH 7 buffer where the error bars indicate the width of the distribution fit for the time constants. Molecule **1** is shown in panel A while molecule **2** is shown in panel B. When the amide was located in the 3 position on the pyrene black or red symbols were utilized. Blue and pink symbols are indicative of the amide in the 8 position on the pyrene ring.*

8.5 DETAILS ON PES SCANS

The PES curves and possible geometries indicate that the PDN-ACE interaction includes both steric repulsion and attraction. The attraction likely results because of the negatively charged oxygen atom in ACE and positively charge nitrogen atom in PDN. Thus, when possible, PDN and ACE tend to stay on the same side of the pyrene plane (see the Figure 8.3 for 48°, 96° and 120° for examples of when this occurs).

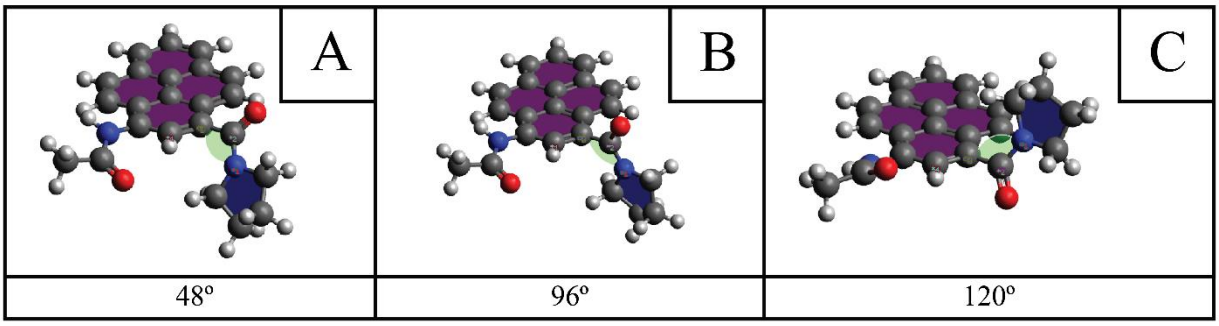

Figure 8.3 - The dihedral angle formed by the PDN plane and pyrene plane were scanned. Note that the definition is different from the torsion angle used in the molecular dynamics.

The torsion angle of PDN-Py (Figure 8.4B) stays positive (or negative) while the torsion angle of ACE-Py (Figure 8.4A) has both signs, confirming that PDN cannot rotate freely while ACE can rotate freely.

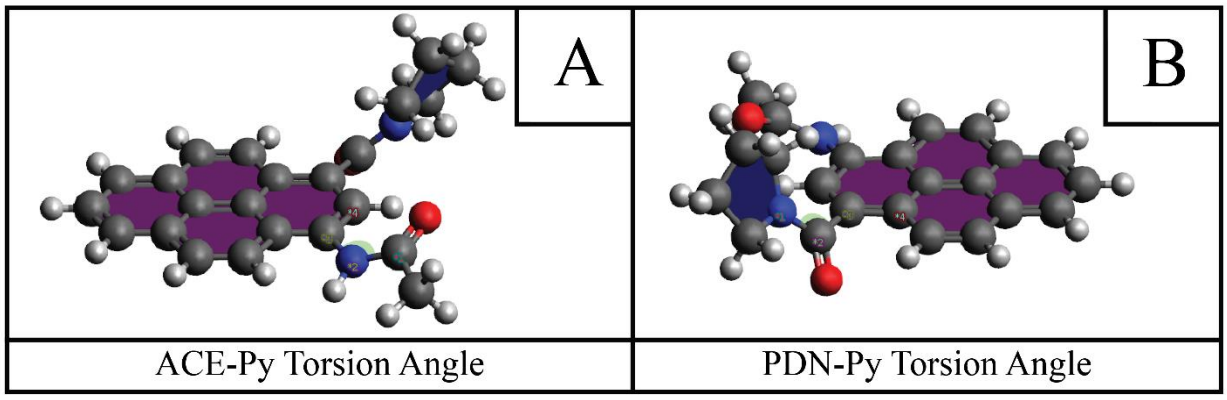

Figure 8.4 - Molecular structures indicating the change where the acetyl-pyrene (ACE-Py) angle and the pyrrolodine-pyrene (PDN-Py) angle are rotated for the MD simulations.

The PDN-Py for **4A** has the most asymmetric distribution and the frequencies of negative ACE-Py are larger than the positive ACE-Py Figure 8.5A). Note that the same sign for PDN-Py and ACE-Py means both groups are on the same side of pyrene. Conversely, the PDN-Py distribution is most symmetric for **4B** and its ACE-Py is also the most evenly distributed between positive and negative region (Figure 8.5C). They are all consistent with the PES scan in Figure 3.7.

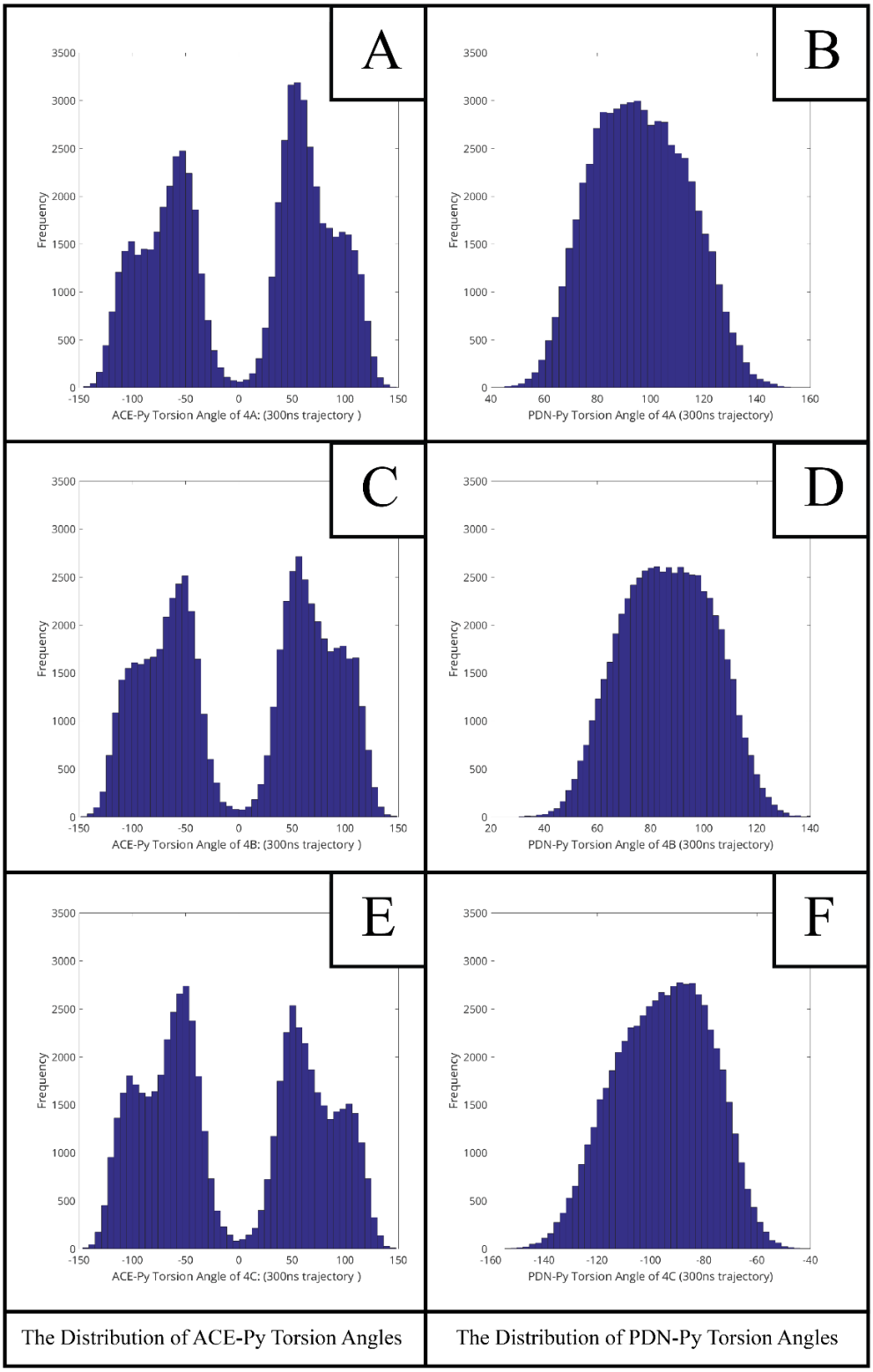

Figure 8.5 - The distribution of ACE-Py Torsion angles (left) and the distribution of PDN-Py torsion angles (right)

The potential energy scan was also run in the presence of solvent molecules for a clearer comparison to the experimental conditions. It was found that when the PES was run in the presence of solvent molecules, **4A** looked very similar to **4B** and **4C** (Figure 8.6). Figure 8.6 shows the PES found under these conditions as a function of the pyrrolidone orientation with respect to the amide. Note that the barrier height differs by approximately 0.1 eV in solvent as compared to in vacuo (Figure 3.7).

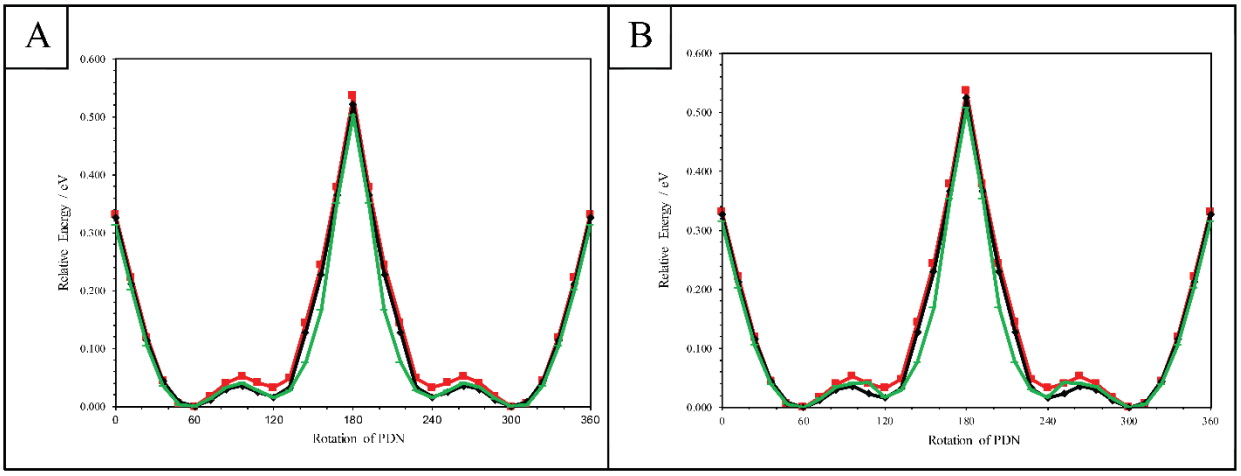

*Figure 8.6 - Potential energy scan in DMSO (A) and pH 7 buffer (B) of molecules **4A** (red), **4B** (black), and **4C** (green) while rotating the pyrrolidone group.*

Thus, while the PDN group cannot flip over the pyrene plane, the ACE group can rotate freely. Because some attraction between the PDN and ACE exists, the two substitution groups tend to stay on the same side of the pyrene plane, especially for molecule **4A** in which the distance between them is the smallest. In molecule **4A,** which shows the most unique fluorescent features, it is likely that this PDN-ACE interaction also affects the electronic structure of the whole molecule.

9.0 APPENDIX C

9.1 ASSEMBLY FORMATION

The formation of nanoparticle assemblies on a 500 nm diameter SiO_2 sphere has been confirmed by fluorescence, zeta potential, and scanning electron microscopy measurements. Figure 9.1A indicates the first fabrication step. An amine coated SiO_2 microsphere, approximately 500 nm in diameter, was the template for this assembly. Using sonication, 30 mg of the SiO_2 microspheres were dispersed in 2 mL of water. Thioglycolic acid passivated cadmium telluride, TGA-CdTe, was added in excess to the solution and the charged microsphere and nanoparticle in water were left to shake for one hour. After one hour, the assembly was purified using a stirred ultrafiltration cell. A cellulose nitrate membrane filter (Whatman), 100 nm pore size, was used in the ultrafiltration cell. Therefore, the "free" TGA-CdTe nanoparticles (4.1 nm) should go through the filter, but the SiO_2 microbead and anything attached to it, would not go through the filter. The pressure used in the filtration was 50 psi and filtrate samples were collected. After filtration, the solid on the filter paper was resuspended in 4 mL of water. An additional 2-3 filtrations were performed on this sample and the assembly was resuspended in 3 mL of water.

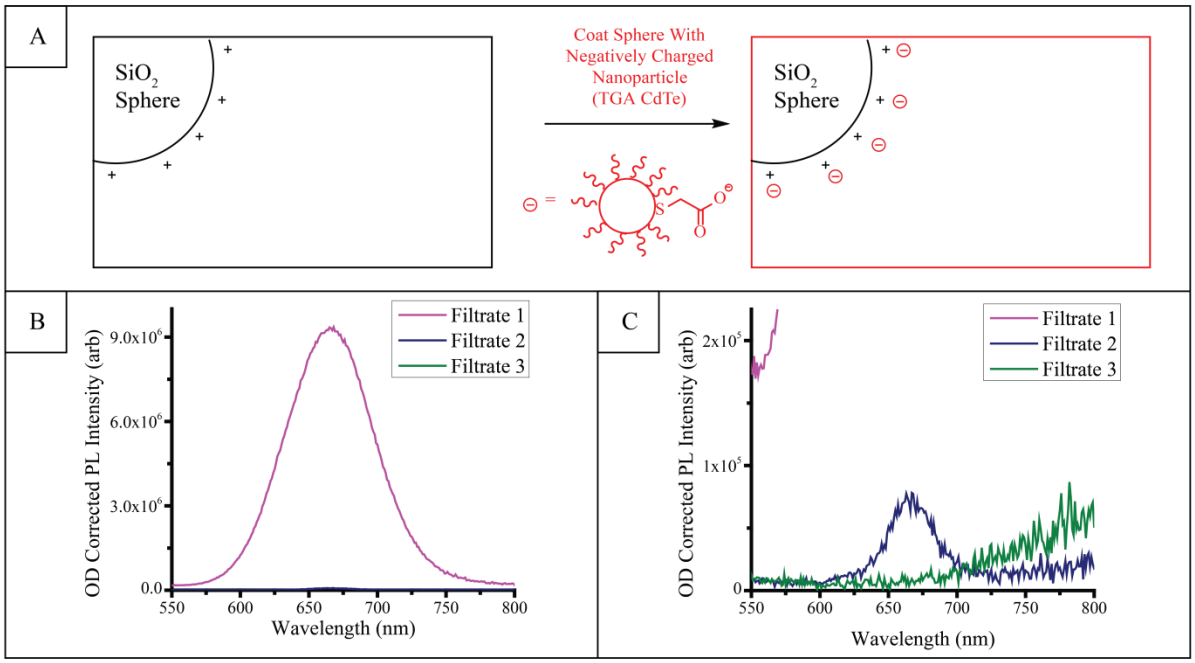

Figure 9.1 - Cartoon describing the experimental procedure used for attaching a TGA-CdTe to SiO_2 template (A). Steady state fluorescence spectra (λ_{exc}=440 nm) of collected filtrates (B) and 1B after zooming in on the data from Filter 2 and Filter 3 (C).

A positively charged SiO_2 template was placed in the presence of a negatively charged TGA-CdTe nanoparticle in water; the TGA-CdTe was electrostatically attached to the surface of the template. Figure 9.1B and Figure 9.1C show photoluminescence spectra depicting the emission intensity of the nanoparticle in the filtrate after successive filtrations. Because the assembly was resuspended in the same volume of water before each filtration, the photoluminescence intensity should be related to the concentration of free nanoparticles that are removed from the assembly solution. After each filtration the nanoparticle emission found in the filtrate decreases in intensity indicating that fewer nanoparticles are removed from solution (Figure 9.1B). In fact, after the second filtration there is no nanoparticle emission peak that is discernible from the noise (Figure 9.1C). For all of the experiments reported in this work at least two filtrations were performed to

ensure that the fluorescence from the 1NPA came from nanoparticles attached to the surface of the microsphere rather than any residual free unbound nanoparticles.

The assembly of nanoparticles on the microsphere could also be monitored by zeta potential measurements after each filtration step. Initially, the microspheres are positively charged in water and the TGA-CdTe is negatively charged; however, after the microsphere is coated with the negatively charged nanoparticle it becomes negatively charged as well. Note that the charged surface prevents aggregation of these particles.

Table 9.1 - Zeta potential measurements for microsphere, TGA CdTe, and nanoparticle assembly in water.

Sample	Zeta Potential (mV)
Microsphere (MS)	41.91 ± 0.60
Free Nanoparticle	-42.95 ± 4.13
1NPA	-19.66 ± 2.49

The surface of the acceptor nanoparticle (blue circle) can be covalently bonded to the donor nanoparticle (green circle) using an EDC and sulfo-NHS reaction. MS-Acceptor nanoparticle, EDC, and sulfo-NHS were added to a 100 mM PBS buffer solution in a 1:1000:2500 ratio, respectively.[259] The solution was stirred for 15 minutes, then donor nanoparticle (in a 1 donor:1.33 acceptor ratio) was added to the solution, and the solution was stirred overnight. The sample was cooled to 4 ^{o}C to quench the excess EDC and then purified using the same methodology as described for the assembly of the first nanoparticle. Figure 9.2 depicts the two nanoparticle assembly (MS-Acceptor Nanoparticle - Donor Nanoparticle).

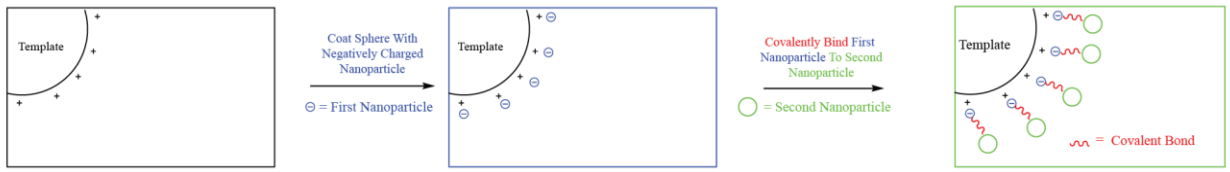

Figure 9.2 - Cartoon describing the experimental procedure for attaching a second nanoparticle covalently to first nanoparticle on the SiO_2 microsphere template.

This specific procedure was used generally for all of the two nanoparticle assemblies.

Formation of the nanoparticle assemblies on the surface of the microbeads template was further monitored with Scanning Transmission Electron Microscopy (STEM). Figure 9.3 shows several examples of original micrographs of the 1 NPA (Figure 9.3A, top row) and 2NPA (Figure 9.3B, top row), together with the images processed with a FFT bandpass filter using ImageJ software (bottom rows in Figure 9.3A and Figure 9.3B).[260] Image processing suppressed heavy contrast between the microbeads and the carbon support background, thus enhancing the contrast associated with the nanoparticles themselves (dark spots in the images). The average diameter of the particles visible in the images c.a. 5 nm is close to the average size of the particles used to form the nanoparticles assembly i.e. 4.0 nm and 5.5 nm for the first and second nanoparticle layer, respectively.

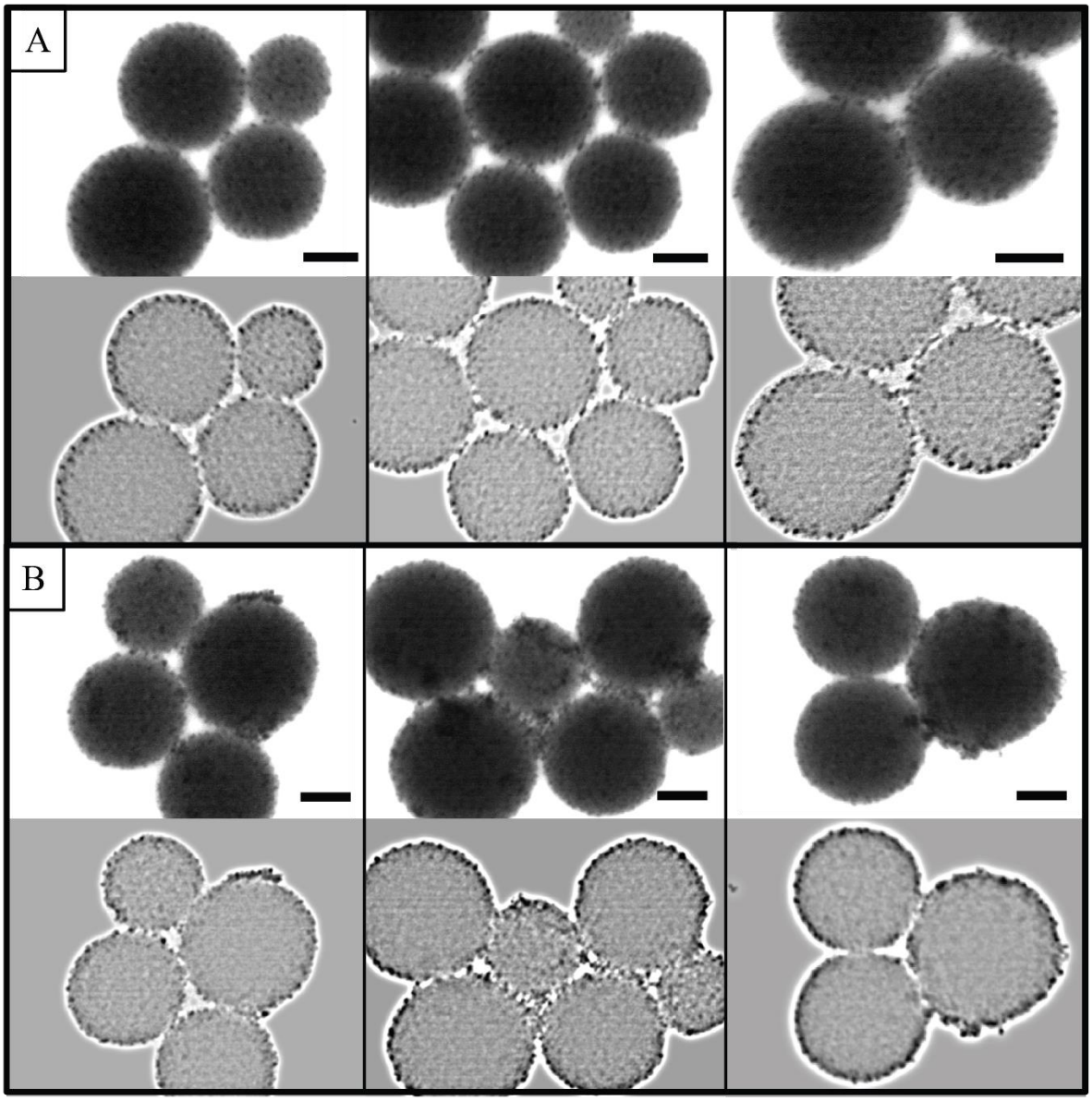

Figure 9.3 - Panels A and B show examples of STEM micrographs of 1NPA and 2NPA samples, respectively (top rows) together with data digitally processed with FFT bandpass filter (bottom rows). Images obtained for 1NPAs and 2NPAs are shown in A and B, respectively. Scale bars in all micrographs represent 50 nm. Note that the diameter of the silica spheres template and the size of the nanoparticles differs significantly from the parameters used in electron transfer studies. See main text for details.

Figure 9.4 shows more detailed analysis of the dimensions of the nanoparticles and nanoparticle clusters in the assemblies. In 1 NPA the nanoparticles are typically separated from each other by several nanometers on the surface of individual template beads, nevertheless in some cases they

are perceived in the image processing as the nanoparticle clusters due to the curvature of the bead template (separated along the electron beam axis but in the projection plane) or because of the close proximity of the particles assembled on different beads that aggregated when drop casted on the substrate. The left image in Figure 9.4A shows the size distribution of the nanoparticles (expressed as area) combined from the STEM data presented in Figure 9.3 and Figure 4.3 of the main text. The majority of particle areas vary over a broad range, which indicates that the above circumstances clearly play a role in the particle size analysis. As a result, the mean particle size value of 19.0 nm^2 calculated from the distribution is somewhat higher than that deduced from the average size of the particles used for 1NPA i.e. 12.6 nm^2. The right panel in Figure 9.4A shows an analogous size distribution for the 2NPA. The average size of the particles of 28.4 nm^2 is about fifty percent larger than that calculated for 1NPA. The larger size of the particle are as expected because of (i) larger size of the nanoparticles used to form second layer c.a. 19.6 nm^2, and (ii) the 2NPA should contain by design nanoparticle dyads of total area of 32.5 nm^2 (12.6 nm^2 + 19.6 nm^2). Both distributions in Figure 9.4A are affected by the presence of individual nanoparticles and nanoparticle clusters i.e. the distribution for 1NPA shows higher than expected average size values due to the 'presence' of the nanoparticle clusters, and distribution for 2NPA is affected by large number of individual nanoparticles, which did not form the nanoparticle dyads. In order to bias the particle analysis towards the dyads, the analysis of particle size approximated by the ellipsoids with the aspect ratio ranging from 1.7:1 to 2.5:1 was performed. Obtained results are shown in Figure 9.4B. The average size of the particles calculated for 1NPA was 30.7 nm^2, while for 2NPA 38.7 nm^2. These values are about twenty percent larger than estimated 25.4 nm^2 (two particles with area of 12.6 nm^2 each) for 1NPA and 32.5 nm^2 for 2NPA. Several factors such as non-ideal spherical shape of individual

nanoparticles, ligand shells around nanoparticles, and larger than two nanoparticles agglomerates, can contribute to a larger than the expected size of the dimer of the nanoparticles in addition to mentioned earlier factors. The protocol of STEM image processing and the outlines (ellipsoids) used for the particle size analysis are shown in Figure 9.4C and Figure 9.4D, respectively.

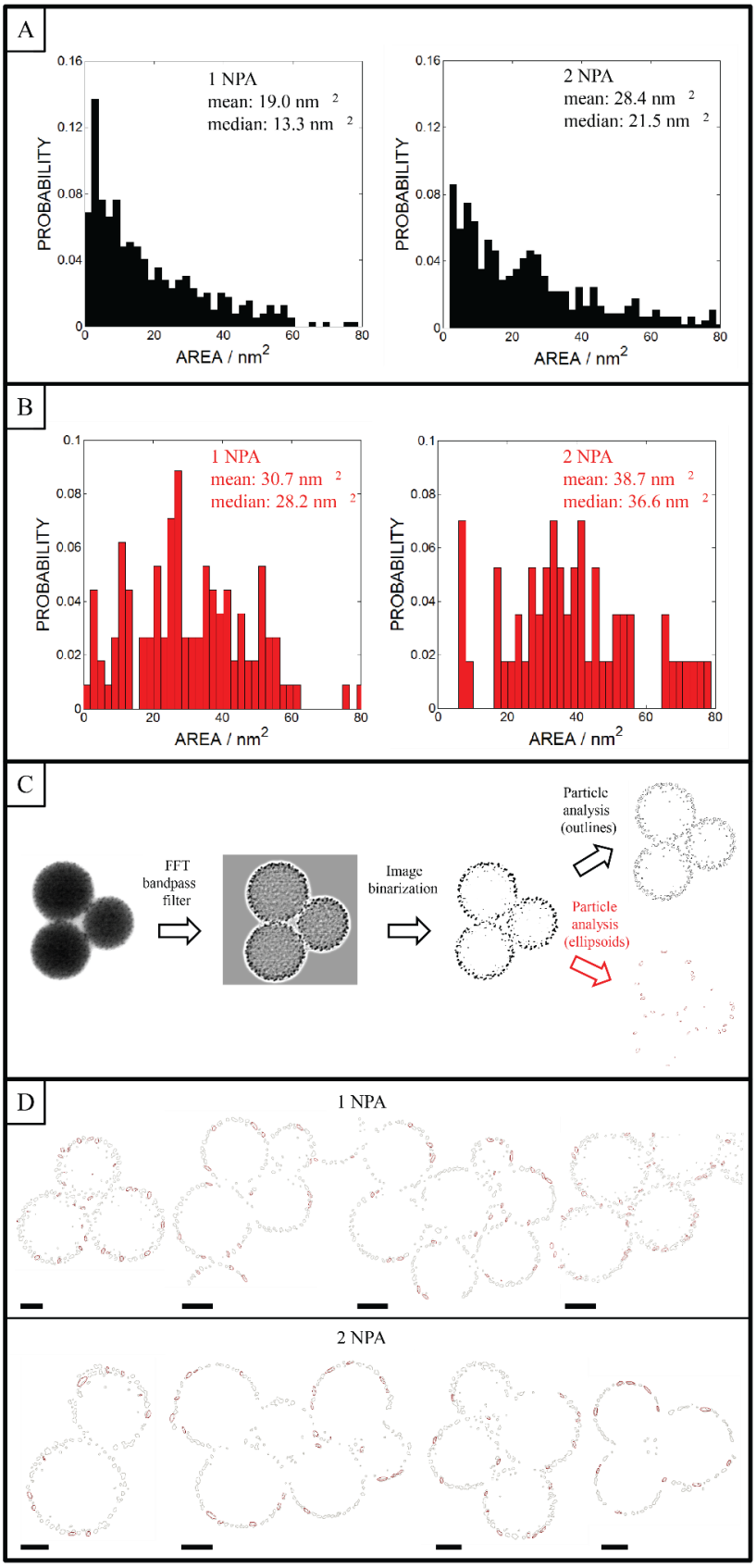
A
1 NPA
mean: 19.0 nm 2
median: 13.3 nm 2
2 NPA
mean: 28.4 nm 2
median: 21.5 nm 2
PROBABILITY
AREA / nm2
B
1 NPA
mean: 30.7 nm 2
median: 28.2 nm 2
2 NPA
mean: 38.7 nm 2
median: 36.6 nm 2
PROBABILITY
AREA / nm2
C
FFT bandpass filter
Image binarization
Particle analysis (outlines)
Particle analysis (ellipsoids)
D
1 NPA
2 NPA

Figure 9.4 - Particle size analysis. Panels A and B show the particle area distributions based on the combination of all the STEM data presented in Figure S3 and Figure 3 of the main text. Panel A presents particle size analysis based on the outlines of the nanoparticles and nanoparticle clusters in the micrographs. Panel B shows the analysis based on the ellipsoids with aspect ratio ranging from 1.7:1 to 2.5:1. The aspect ratio was chosen in order to concentrate on the two nanoparticle clusters and nanoparticle dyads (of expected ~ 2:1 dimension ratio). The protocol of the images processing for the particle size analysis is presented in Panel C and it contains FFT bandpass filtering followed by data binarization (transforming from grayscale to black and white image) prior to the particle size analysis. All the image processing steps were performed using ImageJ software.[260] Panel 4 shows the outlines of the nanoparticles and their clusters that contributed to the distributions shown in Panel A (grey lines) and the ellipsoids (shown in red) contributing to the distributions shown in Panel B.

9.2 ONE NANOPARTICLE ASSEMBLY REMOVAL

To ensure that the electrostatic assembly process was not destroying the nanoparticle, the nanoparticle was removed from the SiO_2 template and the photoluminescence decay was monitored. In order to do the removal, the nanoparticle assembly was prepared in a high ionic strength solution (NaCl, I=250 mM). The SiO_2 bead was etched by placing the 1NPA assembly in a 5% sodium hydroxide (NaOH) solution for 15 minutes at 40℃ while stirring vigorously. The sample was then run through an ultracentrifugation cell and the filtrate was collected (i.e., anything that was not microbead). Then the filtrate was concentrated down using a regenerated cellulose membrane centrifugal filter with a 10,000 molecular weight cut-off (Millipore) to remove excess solvent. The photoluminescence decay of the nanoparticle that was removed from the microbead (green) behaved identically to the nanoparticle prior to assembly formation (red).

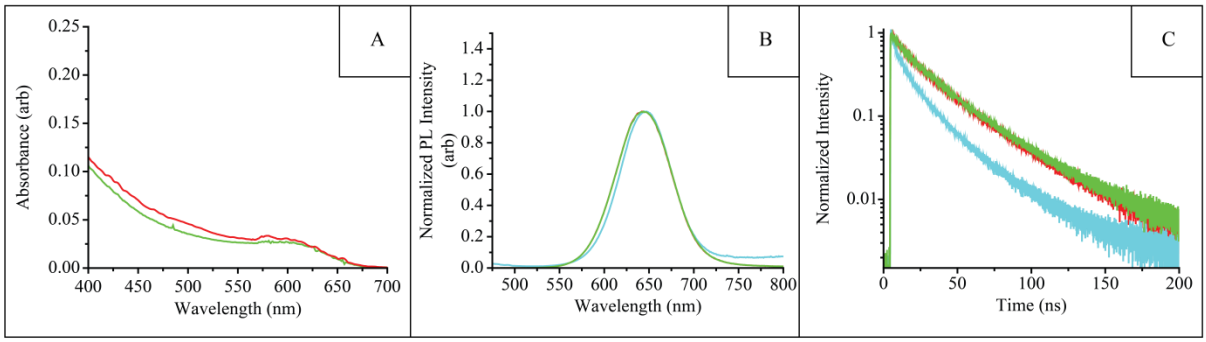

Figure 9.5 - Absorbance of nanoparticle before and after removal from the SiO_2 bead (A). Steady state fluorescence spectra (λ_{exc}=440 nm) of collected nanoparticle free in solution (red), nanoparticle bound to the microbead (cyan) and nanoparticle after removal from bead (green) (B). Photoluminescence decay of nanoparticle free in solution (red), nanoparticle bound to the microbead (cyan) and nanoparticle after removal from bead (green) Ex: 440 nm, 32 ps integration time, 1MHz repetition rate.

9.3 ELECTROCHEMISTRY

Electrochemical measurements were performed on CA-CdTe to ensure that the electric field generated from the charges on the microbeads did not change the electronic state energies of the nanoparticle by a significant amount. Figure 9.6 shows voltammetry measurements of 4.1 nm CA-CdTe nanoparticles in solution (black) and assembled on the microbead (red). A voltammogram of the microbeads without any nanoparticles was used to background subtract the CdTe-MB assembly. The onset energy (blue dashed line), corresponding to the valence band maximum of the nanoparticle, was found to occur at the same potential for both the free nanoparticle in solution and the nanoparticle assembled onto the template. The valence band maximum corresponds to an energy of -5.0 eV in good agreement with that reported by Jasieniak et al.[261] The oxidation peak at 0.2 V may arise from surface state defects on the nanoparticle. The electrochemical measurements were performed using a hexanethiol passivated Au ball working

electrode, 3M KCL AglAgCl reference electrode (CHInstruments), and a platinum auxiliary electrode. The supporting electrolyte used during the experiment was a 0.1 M KCl pH 7 solution.

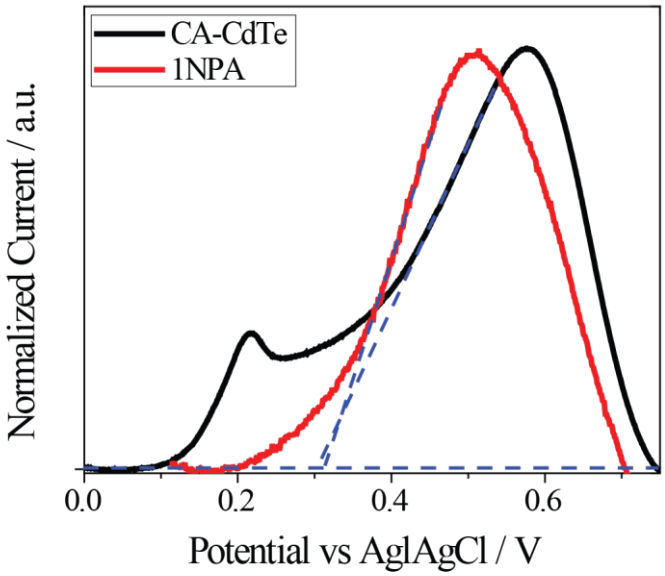

Figure 9.6 - Shows voltammetry measurements of 4.1 nm CA-CdTe in solution (black) and assembled onto the microbeads (red). The blue dashed lines correspond to the valence band maximum of CdTe and indicate that the microbeads do not greatly change the electronic states of the nanoparticles.

9.4 QUENCHING EFFECTS OF EDC AND SULFO-NHS CATALYSTS

Because the EDC has a chloride counterion, it can alter the photoluminescence decay of the nanoparticle. Thus, a 1NPA assembly in the presence of EDC and sulfo-NHS without the addition of a second nanoparticle was monitored (Figure 9.7). It was determined that while the photoluminescence decay of the nanoparticle does change in the presence of EDC. However, this

effect can be accounted for by utilizing a control system (Type I 2NPA) in which identical chemical conditions are utilized.

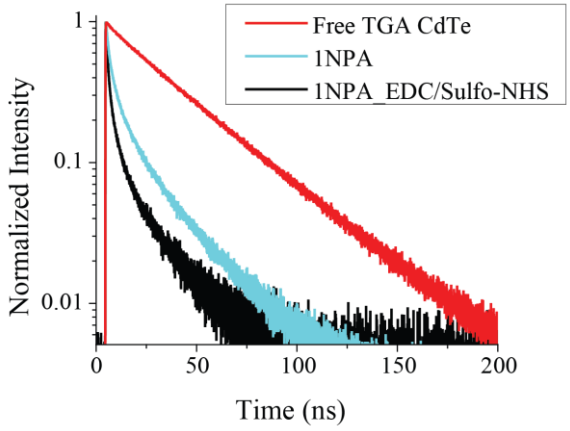

Figure 9.7 - Photoluminescence decays are for the TGA-CdTe free in solution (red), the 1NPA (blue), and the 1NPA in the presence of EDC and sulfo-NHS.

9.5 FLUORESCENCE DECAYS AND DISTRIBUTION FITTING OF ENERGY AND ELECTRON TRANSFER ASSEMBLIES

The figure shown below (Figure 9.8) is a sample of the photoluminescence decays and distribution fitting for 2NPA assemblies. In one case the systems were modeled such that energy transfer was favored (black, red) and in the other case electron transfer was favored (green, blue). In order to ensure energy transfer was favored a larger bandgap CA-CdTe nanoparticle was synthesized. Because of the difference in size, the decays of the two nanoparticles free in solution are not identical. The 2NPA assembly in the electron transfer case (blue) is more significantly quenched than the 2NPA assembly in the energy transfer case (red). The free

nanoparticles have a broad distribution with a low amplitude thus they are barely distinguishable from the baseline in Figure 9.8B.

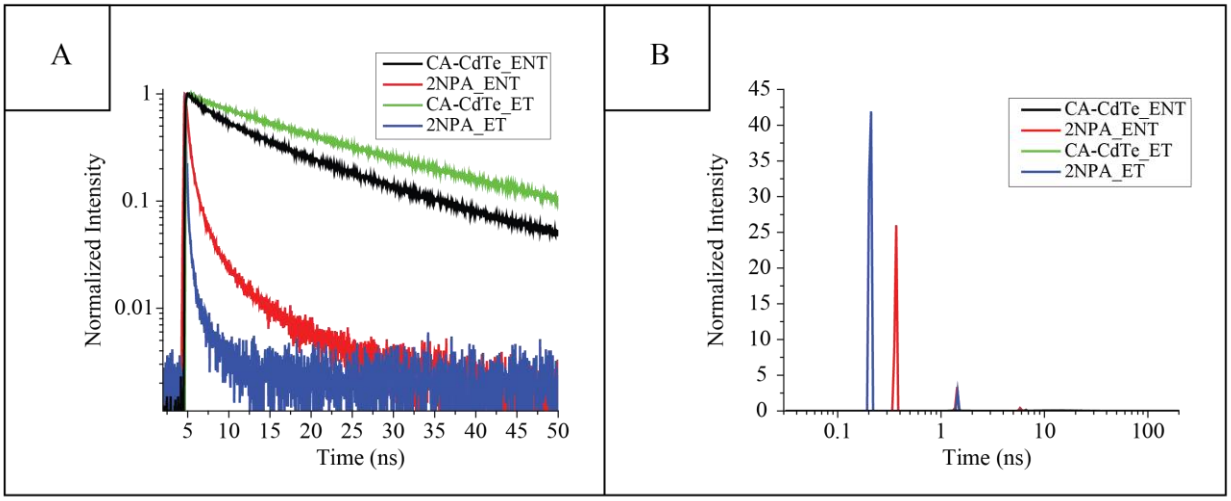

Figure 9.8 - Photoluminescence decays are shown in panel A and the lifetime distribution fitting results are shown in panel B; for the CA-CdTe free in solution (black, green), the 2NPA (red, blue). The case which facilities electron transfer is indicated by ET (green, blue) and the case which facilitates energy transfer is indicated by ENT (red,black).

9.6 FRET EFFICIENCY AND R_0

In addition to confirming the presence of two nanoparticles attached to a template, it is important to confirm that these particles interact. As an initial study, we used Förster resonance energy transfer (FRET) to assess the proximity of the nanoparticles on the microsphere. The Förster distance (R_0), which is defined as the distance at which energy transfer is 50% efficient, may be calculated by:[262]

$$R_0 = 0.211\left(\kappa^2 \eta^{-4} Q_D J(\lambda)\right)^{1/6} \qquad \text{Equation 9.1}$$

in which κ is the orientation factor related to dipole-dipole interactions between the donor and acceptor molecule (κ^2=2/3 for random orientations), η is the refractive index which was assumed to be 2, Q_D is the quantum yield of the donor, and $J(\lambda)$ is the overlap integral between the emission spectrum of the donor and the absorption spectrum of the acceptor. The overlap is given by:

$$J(\lambda) = \frac{\int_0^\infty F_D(\lambda)\varepsilon_A(\lambda)\lambda^4 d\lambda}{\int_0^\infty F_D(\lambda) d\lambda} \qquad \text{Equation 9.2}$$

where F_D is the donor's emission spectrum, ε_A is the acceptor's extinction coefficient, and λ is the wavelength. Given this relationship, the Förster distance can be calculated. It should be noted that the energy transfer probability will increase as the R_0 increases. To calculate the efficiency of energy transfer Equation 9.3 is used where r is the distance separating the two NCs.

$$E = \frac{1}{1 + \left(\frac{r}{R_0}\right)^6} \qquad \text{Equation 9.3}$$

The FRET efficiency for this two nanoparticle system is approximately 100% as evidenced by the spectral overlap of the donor (CA CdTe) emission and the acceptor (TGA CdTe) absorption, the type one heterojunction which promotes energy transfer. The R_0 value calculated for this system is 50 Å. The observation that the energy transfer does not change over our value of 6 Å, implies that the nanoparticles are within a few nanometers of each other.

9.7 FITTING PROTOCOL

The electron transfer rate (k_{et}) was determined by comparing the Type I system, which does not promote electron transfer, with the Type II system, which does promote electron transfer. The difference between these photoluminescence decays yields the k_{et}. Because the long-lived lifetime components are small in amplitude and do not shift significantly between the Type I and Type II cases in our system, it was assumed that they do not play an integral role in the k_{et}. In order to confirm that the long lived lifetime components do not play a large role in the analysis, the average lifetime of the decay was compared to the short time constant of each decay, both Type I and Type II (Figure 9.9).

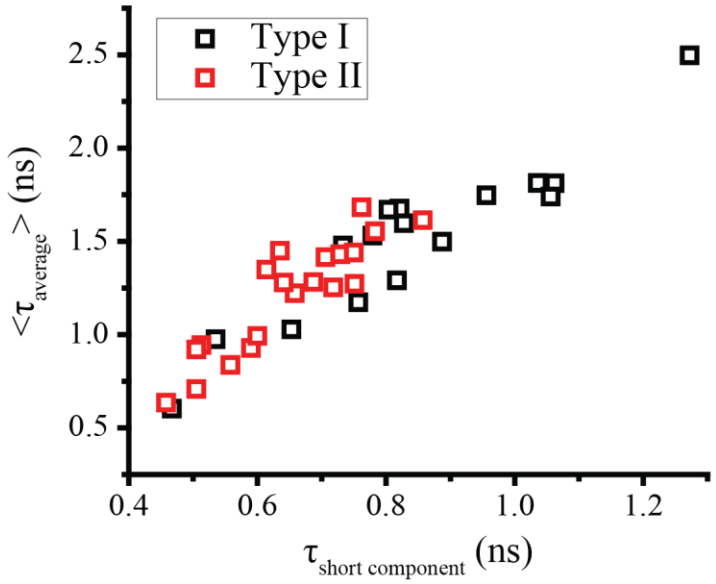

Figure 9.9 - Plot comparing the average lifetime of each decay with the short time constant of each decay for both Type I systems (black) and Type II systems (red).

It is evident that there is a correlation between the length of the short time constant and the average lifetime of the decay. Thus, while neglecting the longer time constants may affect the exact magnitude calculated for the electron transfer rate, the trends that are found in this study are consistent.

Quantum dot photoluminescence decays are frequently fit using a distribution of lifetime components. However, to ensure that the method of fitting did not skew the calculated electron transfer rates, short lifetime components were compared for two fitting methods: a sum of exponentials and a distribution of lifetime components (Figure 9.10).

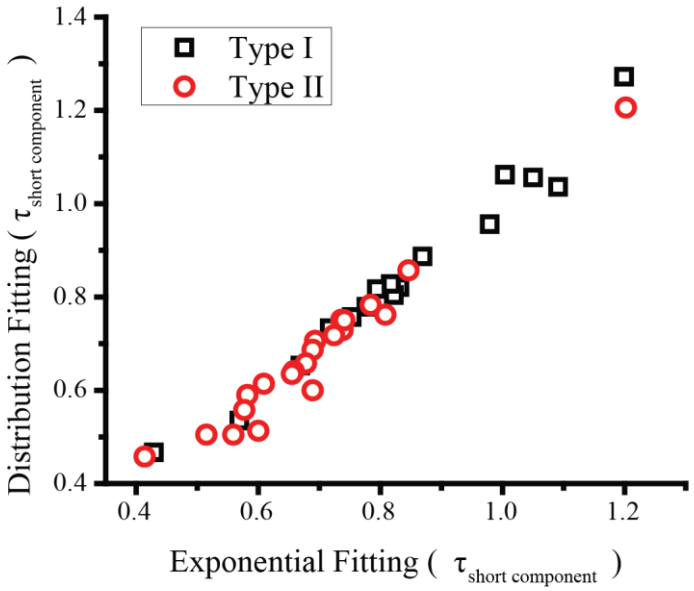

Figure 9.10 - Plot comparing the short lifetime components of each decay that were fit by two different methods for both Type I systems (black) and Type II systems (red).

It is evident that the short lifetime component does not change drastically with the method of fitting, as the slope for both the Type I and Type II systems are nearly one. Thus, fitting the nanoparticle assembly decays as a distribution of lifetime components is adequate.

In addition to the details described above a few other careful considerations were taken. Another control, a dendrimer (Figure 9.11), was utilized.

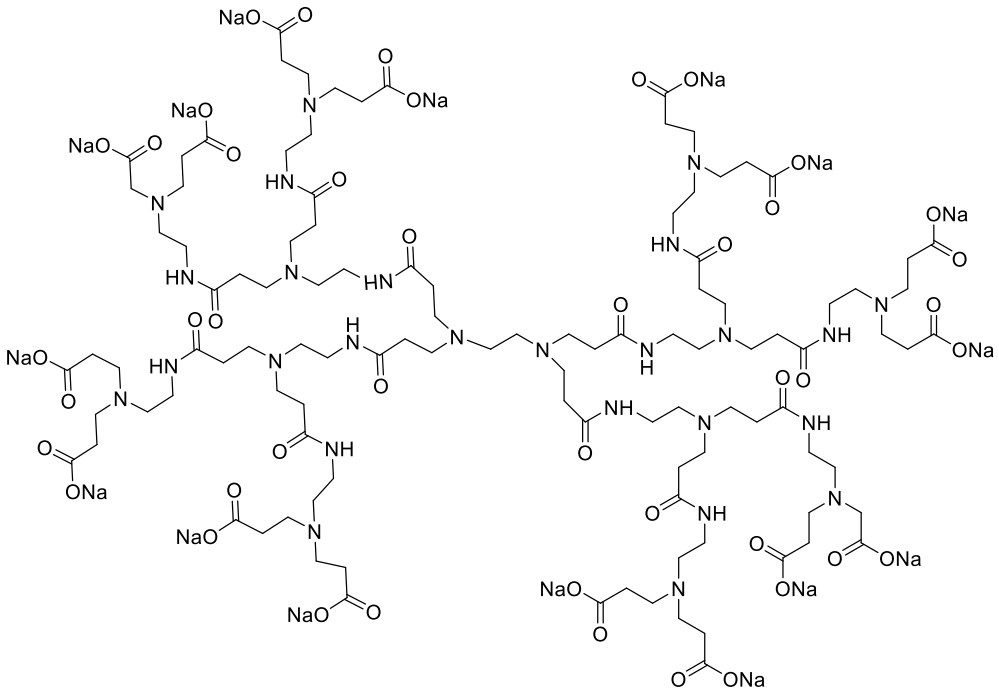

Figure 9.11 - Chemical structure of dendrimer, PAMAM Dendrimer G1.5 Carboxylate Sodium Salt, control used in this series of studies.

The dendrimer is negatively charged, is terminated with carboxylic acid units, is of similar size, and does not absorb in the regime that was studied. The carboxylic acid functional group allowed it to be covalently linked to the donor nanoparticle, and its lack of absorbance indicates that energy transfer should not be feasible. Electron transfer was also not favorable and a similar control was utilized for CdSe-CdTe aggregates in Wu et. al.[269] It was found that the dendrimer control mimics the results found for the Type I TGA-CdSe system, however, it fails to do so for the longer ligands studied. Because the microbead interacts with the donor nanoparticle as a result of the quenching observed when the donor is removed from the surface of the microbead, by introducing more methylene groups (ie. increasing the distance between the nanoparticle and the microbead), the quenching effect is changed. Thus, designing a Type I system accounts for all of the potential pathways, aside from electron transfer, that may take place.

9.8 S_E TO P_E STATE DETERMINATION

The diameter of the nanoparticle is related to the measured first excitonic peak maximum of the nanoparticle as described in the manuscript.[263] The conduction band edge was defined as the S_e state. The difference in the S_e and P_e was previously reported for CdSe.[264] Thus, the edge of the P_e state was set at this fixed difference (0.15 eV) above the S_e state. Although a fixed separation between the S_e and P_e state was utilized, this difference changes with the size of the nanoparticles and it should be considered as an approximation only.

9.9 FITTING TO THE SEMI-CLASSICAL MARCUS EQUATION

The general compact form for the semi-classical Marcus equation is listed below (Equation 9.4) and it is derived in full in the work by J. Jortner.[265]

$$k_{ET} = \frac{2\pi}{\hbar^2\omega_s}|V|^2 exp(-S)\, exp\left(-S_S(2\tilde{\nu}_S+1) - S(2\tilde{\nu}+1)\right) \sum_{m=0}^{\infty}\left(\frac{\tilde{\nu}_S+1}{\tilde{\nu}_S}\right)^{(p(m)/2)} I_{|p(m)|}\sqrt{2S_S[\tilde{\nu}_S(\tilde{\nu}_S+1)]}\left(\frac{\tilde{\nu}+1}{\tilde{\nu}}\right)^{(m/2)} I_{|m|}\sqrt{2S[\tilde{\nu}(\tilde{\nu}+1)]} \quad \text{Equation 9.4}$$

where ω is the frequency of the longitudinal optical phonon (207 cm^{-1}), S is the Huang-Rhys factor, $\tilde{\nu}$ is defined as $\left[\exp\left(\frac{\hbar\omega_l}{k_B T}\right) - 1\right]^{-1}$, $p(m)$ is defined as $\frac{(\Delta_r G - m\hbar\omega_c)}{\hbar\omega_s}$, and $I_{|m|}$ is the Bessel function. The equation listed in the manuscript, Equation 4.3, is simply one limit, in the case of high temperature. However, for the the limit of the intermediate temperature regime $kT \approx \hbar\omega_l$, Equation 9.5 is obtained[265]

$$k_{ET} = \frac{2\pi}{\hbar}|V|^2 \frac{1}{\sqrt{2\pi S\hbar\omega kT}} exp(-S) \sum_{m=0}^{\infty} \left[\exp\left(\frac{-(\Delta_r G - S\hbar\omega - m\hbar\omega)^2}{4S\hbar\omega k_B T}\right) + 3\exp\left(\frac{-(\Delta_r G - S\hbar\omega - m\hbar\omega)^2}{4S\hbar\omega k_B T}\right)\right] \left(\frac{\tilde{\nu}+1}{\tilde{\nu}}\right)^{(m/2)} I_{|m|}\sqrt{S[\tilde{\nu}(\tilde{\nu}+1)]} \quad \text{Equation 9.5}$$

If the value for S was kept consistent between the high temperature and intermediate temperature systems and only the electronic coupling was allowed to be a floating variable, the shape of the fit remained nearly identical and the electronic coupling was found to be 0.3 cm^{-1}. This indicates that while the magnitude of the electronic coupling may vary between these models, the simpler semi-classical Marcus equation describes the $\Delta_r G$ dependence of the semiconductor nanoparticle system adequately.

In addition to accounting for the temperature regime, the correlation between fitting parameters in Equation 9.3 were considered. Figure 9.12 shows a contour plot of how the quality of the fit depends on the electronic coupling and solvent reorganization energy values. The quality of fit was determined by determining the R^2 for this fit. The contour plot below (Figure 9.12) indicates

the range over which the electronic couplings and solvent reorganization energies give good fits for |V| from 2.5 cm^{-1} to 3.5 cm^{-1} and λ_s < 0.06 eV.

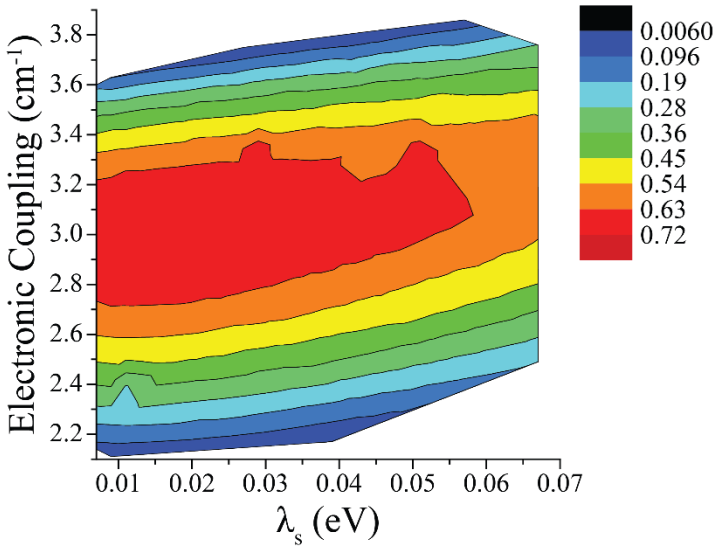

Figure 9.12 - Contour plot of fitting parameters electronic coupling and solvent reorganization energy for semiconductor nanoparticle dyad systems. The magnitude of the contours is the R^2 value, that were obtained by fitting to the semi-classical Marcus equation summing over two final states and accounting for the distribution of $\Delta_r G$ values as a result of the distribution in nanoparticle sizes.

9.10 CONFIRMATION OF COVALENTLY BOUND NANOPARTICLE AGGREGATES

Control experiments were completed to ensure that the nanoparticles were covalently linked through an amide bond (described in the literature),[266,267,268] as opposed to electrostatically linked, which is necessary for the understanding of the distance dependent study. This procedure was adapted from Wu et. al.[269] which described methods for monitoring the interaction of electrostatic donor-acceptor nanoparticle aggregates in solution. The nanoparticle aggregates

studied were of a molar ratio of 1 donor to 5 acceptor nanoparticles. The electrostatic and covalent systems were placed in nearly identical conditions. Both systems stirred in phosphate buffered saline (PBS) buffer at pH 7 for 15 hours in the dark under argon. The covalently bound system was prepared as described above with the addition of the catalyst EDC and sulfo-NHS. The donor nanoparticle was quenched in the presence of the acceptor in both the electrostatic and covalently bound systems (red) (Figure 9.13A). These data indicate that the donor nanoparticle interacted with the acceptor. Note that in the case of the covalently bound system the donor emission is more efficiently quenched than in the electrostatic case. The donor nanoparticle only was studied under identical conditions, including in the presence of EDC, and there was no change in the emission intensity.

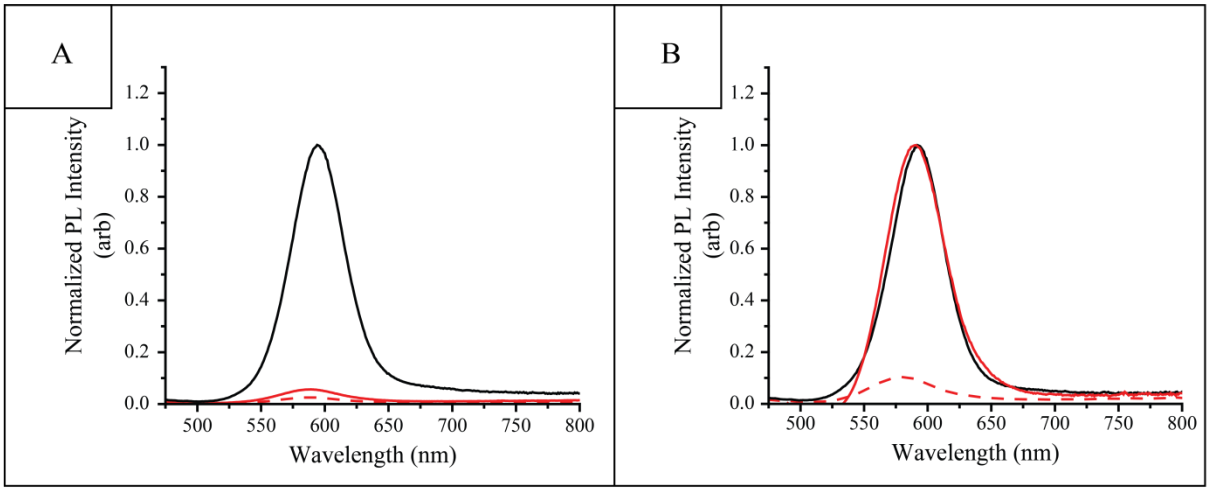

Figure 9.13 - Steady state fluorescence spectra (λ_{exc}=440 nm) of collected of the donor CdTe (black) with no acceptor in solution along with a ratio of 1 Donor: 5 Acceptor CdTe systems either bound electrostatically (red, solid line) or covalently (red, dashed line) (A). Steady state fluorescence spectra of donor CdTe (black) in high ionic strength solution and electrostatic aggregates (red) and covalent aggregates (red dash) in high ionic strength solution (B).

It has been shown that in electrostatically bound nanoparticle aggregates an increase in the ionic strength will dissociate the aggregates and increase the emission intensity coming from the donor nanoparticle.[269] Thus, the donor only, as well as the electrostatically and covalently bound systems, were placed in a solution of high ionic strength (I=660 mM). Sodium chloride (NaCl) was added to the aggregate system and stirred for 10 minutes. In the electrostatic assembly the fluorescence intensity recovered to have the same intensity as the donor only system (see Figure 9.13B). However, in the covalently bound case, while the fluorescence intensity did recover slightly, the overall emission was still significantly quenched. This indicates two important points: 1) The bond between the covalently bound aggregate system is significantly stronger than the electrostatically bound aggregate system and 2) The covalently bound aggregate system may have some electrostatic interactions, but the interaction is not dominant. This, along with the supporting literature, confirms that an amide bond covalently linking these nanoparticle aggregates is formed.

9.11 REFERENCES

259You, J.; Dou, L.; Yoshimura, K.; Takehito, K.; Ohya, K.; Moriarty, T.; Emery, K.; Chen, C.; Gao, J.; Gang, L.; Yang, Y.; *Nat. Commun.*, **2013**, 4, 1446.
260 Rasband, W.S., ImageJ, U. S. National Institutes of Health, Bethesda, Maryland, USA, http://imagej.nih.gov/ij/, 1997-2016.
261 Jasieniak, J.; Califano, M.; Watkins, S. E.; *ACS Nano*, **2011**, 5, 5888.
262 Lakowicz, J. R. *Principles of Fluorescence Spectroscopy, 3rd ed*. Springer: 2006; p. 1-61, 97-155, 331-382, 443-475.
263 Yu. W.; Qu, L.; Guo, W.; Peng, X., *Chem. Mater*. **2003**, 15, 2845.
264 Norris, D. J.; Bawendi, M. G.; *Phys. Rev. B*., **1996**, 53, 16338.
265 Jortner, J.; *J. Chem. Phys*., **1976**, 64, 4860.
266 Bartczak, B. and Kanaras, A. G.; *Langmuir*. **2011**, 27, 10119.

267 Sellers, D. G.; Button, A. A.; Nasca, J. N.; Wolfe, G. E.; Chauhan S.;Watson, D. F.; *J. Phys. Chem. C*, **2015**, 119, 27737.
268 Osovsky, R.; Shavel, A.; Gaponik, N.; Amirav, L.; Eychmuller, A.; Weller, H.; Lifshitz, E.; *J. Phys. Chem. B*, **2005**, 109, 20244.
269 Wu, M.; Mukherjee, P.; Lamont, D. N.; Waldeck, D. H.; *J. Phys. Chem. C*, **2010**, 114, 5751.

10.0 APPENDIX D

10.1 MATERIALS AND METHODS

10.1.1 Materials

Selenium powder (99.999%), tellurium powder (99.999%), cadmium chloride ($CdCl_2$; 99%) sodium borohydride ($NaBH_4$; 98%), cadmium oxide (99.999%), L-cysteine hydrochloride (99%), D-cysteine hydrochloride (98%), n-Acetyl-L-cysteine (99%), cysteamine hydrochloride (CA, 98%), 3-mercapto-1-propanol (MPOH, 95%), 1-ethyl-3-(3-dimethylaminopropyl)carbodiimide (EDC), *N*-hydroxysulfosuccinimide (S-NHS), phosphate buffered saline tablets (PBS), oleic acid (OA), trioctylphosphine oxide (99%), Tetramethylamonium hydroxide pentahydrdate (TMAH, 97%), and 1-octadecene (90%) were purchased from Sigma-Aldrich. Trioctylphospine was purchased from Strem Chemicals and octadecylphosphonic acid (ODPA, >99%) was purchased from PCI Syntheis. 30,000 molecular weight cut off centrifugal filters, 0.45 μm hydrophilic syringe filters, and 0.2 μm hydrophobic syringe filters were purchased from Millipore. Amine coated silica microbeads, 500 nm diameter, were purchased from Polysciences, Inc. All reagents and solvents were used as

received. Water used in all experiments was purified by a Barnstead Nanopure system, and its resistance was 18.2 MΩ-cm at 25 °C.

10.1.2 Preparation of CdSe and CdTe QDs

The synthesis and purification of OA and ODPA passivated CdSe QDs and CA-CdTe QDs were conducted following previously published methodologies (*16*). The purified CdSe QDs were then ligand exchanged to L-cysteine, D-cysteine, n-Acetyl-L-cysteine, and MPA using the procedure developed by Balaz *et al*. (*21*). Briefly, a 2.0 ml solution of water with 82.5 mMols of the new ligand is adjusted to a pH of 11 using concentrated TMAH or NaOH. Next, 2.0 mL of a 82.5μM OA or ODPA CdSe QD solution in chloroform are mixed with the water solution under argon in the dark overnight. The exchanged QDs were centrifuged and the top water layer solution was collected. The QDs were then purified using syringe and centrifugal filters. For the preparation of the mixed ligand shell QDs the total concentration of ligand was kept constant (82.5 mMols) and the molar ratio of L-cysteine and MPOH was varied. For the synthesis of L-cysteine or D-cysteine capped CdTe QDs, 0.916g $CdCl_2$ was dissolved in 25 mL of water and then 0.145g of the ligand was added to the solution. The pH was adjusted to 11 using a concentrated TMAH solution and the solution was purged with argon at 70 °C. In a separate 3-neck flask a tellurium precursor was prepared by dissolving 94.5 mg $NaBH_4$ and 127.5 mg of tellurium in 10 mL of water. The solution was degassed using argon and heated to 70 °C until a dark purple solution was formed. Next, 1.0 mL of the tellurium precursor solution was injected into the cadmium precursor solution. The temperature of the cadmium solution was raised to 95

°C and aliquots were taken once the desired size of QDs was reached. The QDs were then purified using centrifugation, syringe filters and centrifugal filters.

10.1.3 Assembly Formation

Quantum dot assemblies were formed by templating on a SiO_2 microsphere following previously published methodologies.[Error! Bookmark not defined.] Briefly, approximately 20 mg of 500 nm amine coated SiO_2 microspheres were dispersed in water. An excess of acceptor CdSe quantum dots were electrostatically attached to SiO_2 microspheres after shaking for one hour. The resulting solution was then purified using an ultrafiltration cell with a 100 nm pore size cellulose nitrate membrane filter. This allowed the QDs unattached to the microbead to readily pass through the filter. The QDA was fabricated by creating an amide bond between the carboxylic acid on a CdSe QD electrostatically attached to the microsphere and an amine terminated CdTe QD using EDC and S-NHS. The QDA was then purified again using the ultrafiltration.

10.1.4 Spectroscopy

Circular dichroism measurements were measured on an Olis DSM 17 CD spectrophotometer in a 3 mL quartz cuvette at an optical density of 1. An integration time of 5 s and a bandwidth of 1 nm were used for the collection. Because achiral ligand capped QDs can still exhibit some chiroptical properties[270] the achiral MPA capped CdSe was used for the background subtraction of L-cysteine, n-Acetyl-L-cysteine, and D-cysteine capped CdSe. If a slight difference in

absorption maximum was present, the MPA-CdSe circular dichroism was shifted by that difference and the circular dichroism spectra were subtracted in units of Δε so that the concentrations were equal. The magnitude of a QD sample's circular dichroism spectra was calculated by subtracting the intensity of the red part of the bisignate peak corresponding to the absorption maximum of the QD, from the blue part of the same bisignate peak. Time-resolved photoluminescence decays of the quantum dot assemblies were measured using the time correlated single photon counting (TSCPC) technique with a PicoHarp 300 TCSPC module (PicoQuant GmbH).[271] The samples were excited as close to the absorption peak maximum of the donor nanoparticle as possible and a picosecond diode laser either at 532 nm (LDH-P-FA-530L) or 635 nm (PiL063) was utilized. Measurements were collected using a 1 MHz repetition rate, 32 ps resolution, and all measurements were collected at the magic angle. The instrument response function was measured using colloidal $BaSO_4$ and in all cases the instrument response function had a full-width-at-half-maximum of ≤96 ps. The decay curves were fit to a distribution of lifetime components by a convolution and compare method using Edinburgh Instruments fluorescence analysis software technology (FAST) namely;[271,272]

$$I(t) = \int_{\tau=0}^{\infty} \alpha(\tau) \cdot \exp\left(-t/\tau\right) \mathrm{d}\tau \qquad \text{Equation 10.1}$$

In order to confirm that the quenching of the donor QD emission arises from the donor-acceptor interaction, control experiments were necessary. Figure 10.1A shows the photoluminescence (PL) decay for the donor QD, cysteamine passivated cadmium telluride (CA CdTe), free in solution when excited at the first excitonic peak maximum for three different light polarizations:

linear (black), CW (red), and CCW (green) polarized light. The corresponding distribution fitting to the PL decay is shown in panel C. The decay traces, and their subsequent distribution fits, in Figure 10.1A and Figure 10.1C do not change with light polarization indicating that the recombination kinetics of the donor QD remain unaltered. Because the photophysical properties of QDs can change when in close proximity to a SiO_2 microbead,**Error! Bookmark not defined.** additional control experiments were necessary to ensure that the decay of the donor QD in this architecture is also independent of light polarization. In this system, the CA CdTe was attached to a microbead through a non-absorbing dendrimer, with a size comparable to that of the acceptor QDs, and PL decay measurements were again collected using linear, CW, and CCW polarized light (Figure 10.1B). Both the PL decays (Figure 10.1B) and the lifetime distribution fits (Figure 10.1D) indicate that the recombination kinetics of the photoexcited donor QD in the assembly differs from that of the free QD in solution but that it does not depend on the light polarization.

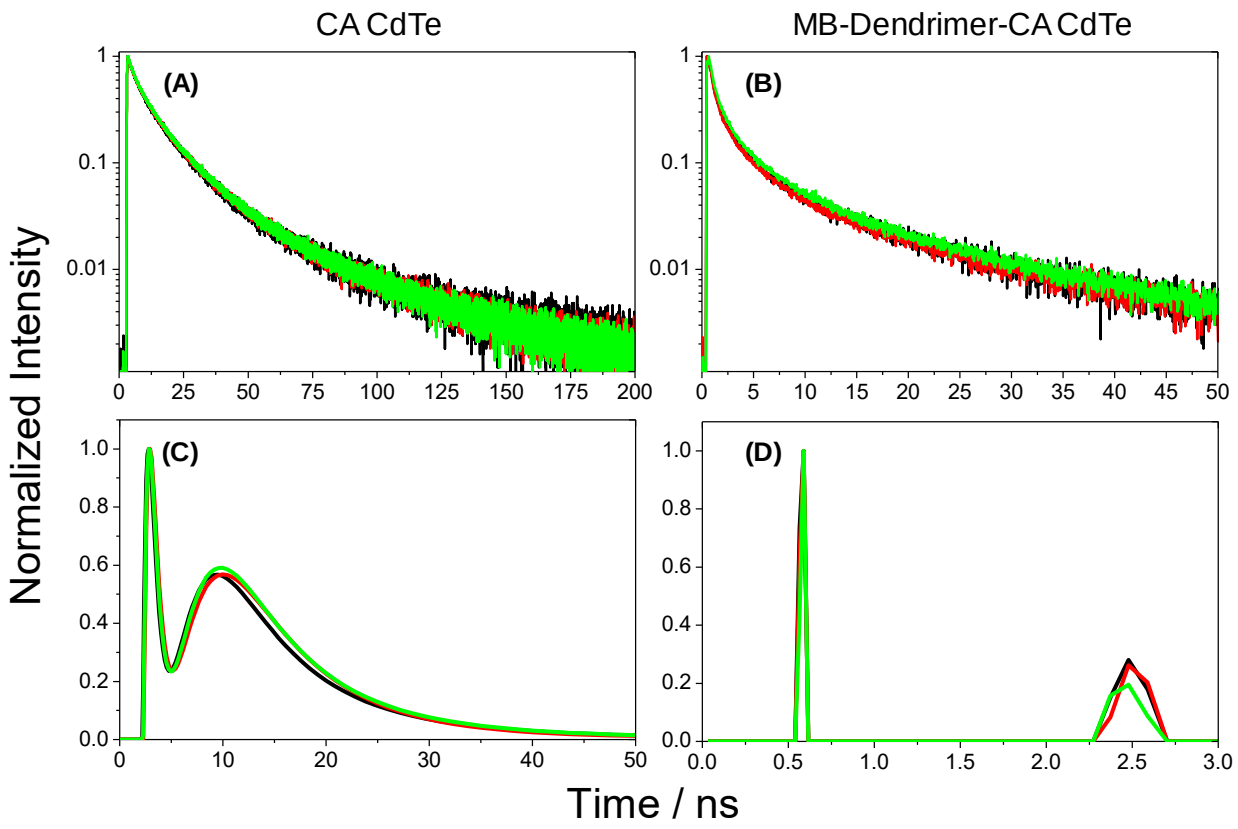

Figure 10.1 - Photoluminescence decay (A, B) and corresponding distribution fitting (C, D) of free CA CdTe (left) and MB-Dendrimer-CA CdTe (right). In each case the different colors indicate different excitation polarizations; black indicates linear, red indicates CW, and green indicates CCW polarized light.

10.2 STABILITY OF QDAS

Previous experiments by Yeom *et al.* showed that CdTe QDs can photodegrade into complex nanostructures upon long exposure to circularly polarized light.[273] To ensure that photodegradation of CdTe was not influencing the measurement, a linearly polarized PL decay was taken at the beginning (black) and end (red) of every experiment in this study. Only when the two linearly excited samples showed the same PL decay was the data set deemed unaffected

by photochemical changes and considered further. Figure 10.2. shows an example of each system studied in the manuscript; CA CdTe QDs free in solution (A), the CA CdTe and dendrimer assembly (B), the L-cysteine CdSe and CA CdTe QD assembly (C), the MPA CdSe and CA CdTe QD assembly (D), and the D-cysteine CdSe and CA CdTe QD assembly (E).

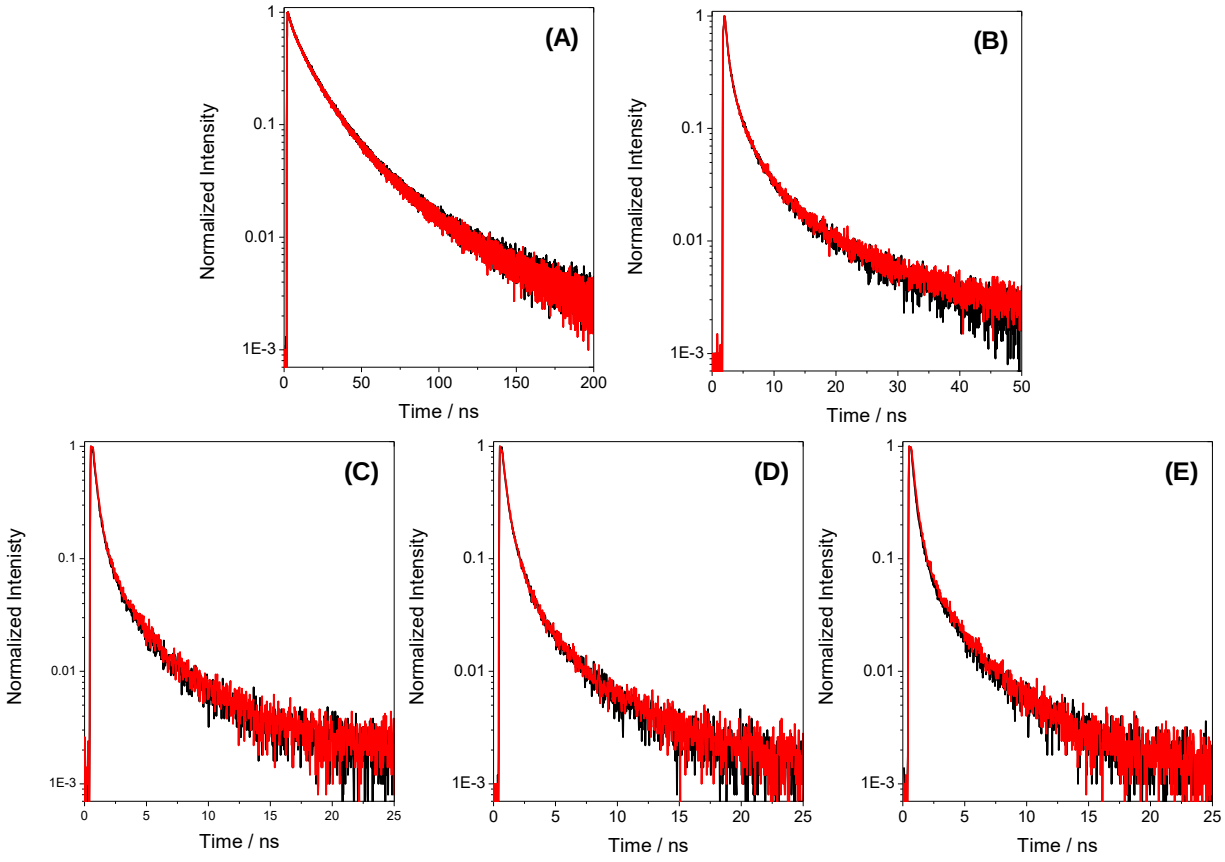

Figure 10.2 - Photoluminescence decays for CA CdTe (A), dendrimer assembly (B), QD assembly with L-cysteine CdSe (C), QD assembly with MPA CdSe (D), QD assembly with D-cysteine CdSe (E). The samples were excited with linearly polarized before (black) and after (red) the experiment.

10.3 CHIRAL CDTE QDS

To ensure that the observed spin polarization was not a result of the acceptor QD imparting chirality onto the donor QD and causing an effect, the photoluminescence decay of L- and D-cysteine capped CdTe quantum dots were measured. Figure 10.3. Shows that excitation of L-cysteine (A) and D-cysteine (B) capped CdTe QDs with linear (black, blue), CW (red), and CCW (green) polarized light do not result in changes of the photoluminescence decay measurements. This indicates that the chirality on donor CdTe QD is not responsible for the observed spin polarization.

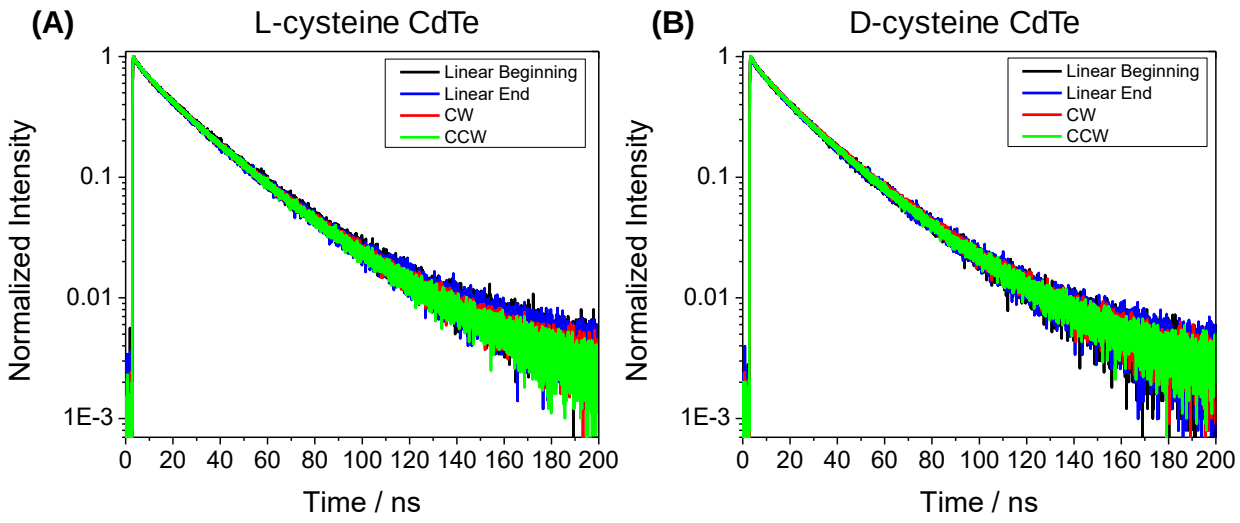

Figure 10.3 - Photoluminescence decays for L-cysteine CdTe (A) and D-cysteine CdTe (B) excited using linear (black, blue), CW (red), and CCW (green) polarized light.

10.4 EFFECT OF MIXED LIGAND SHELL QDS ON POLARIZATION

Figure 10.4 panel A shows CD spectra of CdSe acceptor QDs in which the ligand shell was prepared using different ratios of L-cysteine and 3-mercapto propanol (MPOH) surface capping ligands; 1:0 (black), 4:1 (orange), 1:1 (blue), and 1:4 (green). The spectra show a systematic decrease in intensity of the CD spectra but no significant spectral shift as the coverage of achiral ligands is increased. Because the donor CdTe can only be covalently attached to the L-cysteine ligand on the acceptor CdSe (MPOH does not have the right chemical functional group) the bridge composition is equivalent in every QD assembly. Panel B shows a distribution fitting to the short component of the photoluminescence decay measurements for the QD assemblies with

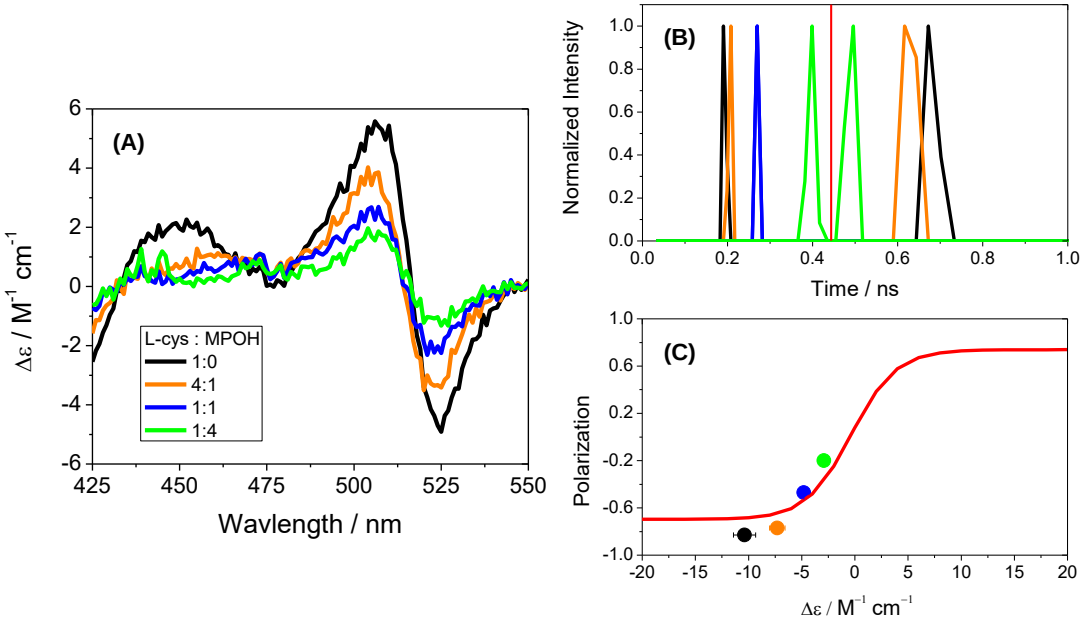

Figure 10.4 - CdSe QDs passivated with a 1:0 (black), 4:1 (orange), 1:1 (blue), and 1:4 (green) ratio of L-cysteine : MPOH ligands. Panel A shows the circular dichroism spectra of the samples. Panel B shows the short lifetime component of a distribution fitting to the photoluminescence decays of QDAs where peaks left of the red line are excited with CCW polarized light and right of the red line are excited with CW polarized light. Panel C shows the spin polarization of the different QDAs as a function of the intensity of their CD spectrum. The red line is the same sigmoidal curve in figure 5.4.

the different ligand coverages in which peaks on the left (right) half of the red line correspond to excitation with CCW (CW) polarized light. Panel C shows the calculated spin polarizations plotted against their measured CD intensity. The red line is the same sigmoidal curve used as a guide to the eye in the main text.

Figure 10.5 shows the corresponding photoluminescence decays to the data in Figure 10.4. Excitation with linear, CW, and CCW polarized light are represented by the color black, red, and green, respectively.

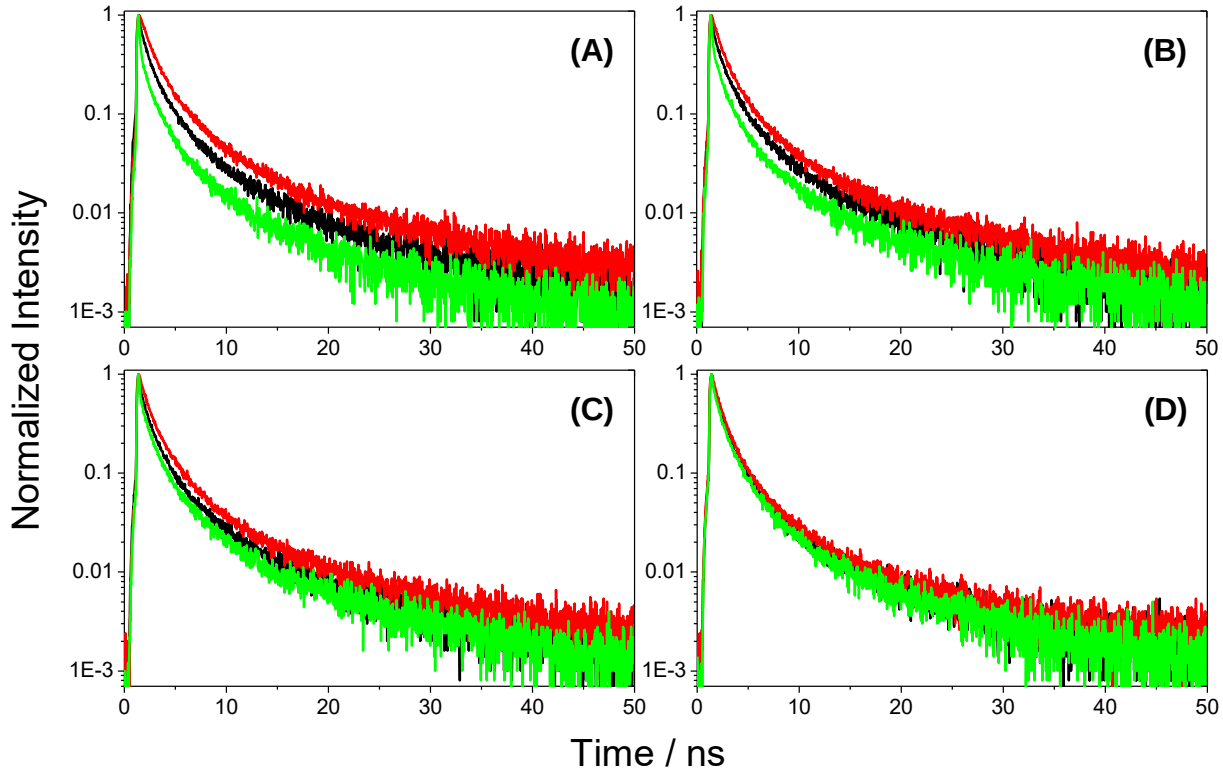

Figure 10.5 - The photoluminescence decays for QD assemblies with the acceptor CdSe ligand being a mixed ligand of chiral (L-cysteine) and achiral (MPOH) in which the ratio is varied from 1:0 (A), 4:1 (B), 1:1 (C), and 1:4 (D) and excited with linear (black), CW (red) and CCW (green) polarized light.

10.5 REFERENCES

270 D. Melnikau, D. Savateeva, N. Gaponik, A. O. Govorov and Y. P. Rakovich, *Opt. Express*, **24**, A65 (2016).
271 X. Yin, *et al*., *J Phys. Chem. B*, **118**, 9037 (2014).
272 J. R. Lakowicz, *Principles of Fluorescence Spectroscopy, 3rd ed*.; Springer: Maryland. pg. 1-61, 97-155, 331-382, 443-475 (2006).
273 J. Yeom et al. *Nat. Mater*. **14**, 66 (2015).